Stable and Radiogenic Isotope Studies of Iron-oxides as Paleoenvironmental and Tectonic Archives

Thesis by

Hayden Bryce Dutcher Miller

In Partial Fulfillment of the Requirements

for the degree of

Doctor of Philosophy

CALIFORNIA INSTITUTE OF TECHNOLOGY

Pasadena, California

2019

(Defended October 2nd, 2018)

Hayden Bryce Dutcher Miller

ORCID: 0000-0001-7305-928X

ACKNOWLEDGEMENTS

I thank my parents, Dave Miller and Katie Dutcher, along with my rest of my family, for their unwavering support and love. Through their encouragement and care, I have been able to pursue my passions. For every time you were understanding about me going to the mountains instead taking a plane flight home, I thank you.

I thank my high school chemistry teacher, Canuche Terranella. Upon finding out I would be attending Colorado College (his alma matter too), and already knowing my passion for the natural world, he encouraged me to take an Intro Geology class. At Colorado College, I thank Henry Fricke and Paul Myrow for early inspiration in my geologic journey.

I thank Sam Bowring for first introducing me to how powerful a tool geochronology can be and for encouraging me to utilize every aspect of his Radiogenic Isotope Lab at MIT rather than simply being a lab tech.

I thank Ken Farley for giving me space to pursue what interests me, for always being open to trying to measure something new, and for your availability to discuss a dataset that left me scratching my head. I thank John Eiler for giving me free reign with his first mass spectrometer, for allowing me to construct whatever eyesore was necessary for the experiment I had designed, and for his invaluable expertise when it came to interpreting the resulting stable isotope measurements. I thank Woody Fischer for helping me stay out of the geochronologic weeds and for his depth of knowledge in all things ancient. I thank George Rossman for always being willing to take the time to help determine the mineralogy of an odd sample and for being my academic advisor. I thank Paulo Vasconcelos for teaching me how to devise and undertake fieldwork campaigns designed to test geologic hypotheses utilizing iron-oxide geochronology.

In addition to my committee, I thank Lindsey Hedges for every hard-spent hour she logged with me and countless others in the basements of the GPS Division. Her decades-long support of isotope geochemistry at Caltech will not be forgotten. I thank Nami Kitchen for teaching me the dark arts of laser fluorination and for never saying 'you want to do what?' when I proposed various modifications to the existing extraction line. I thank Jonathan Treffkorn for all this daily efforts to keep Farley Lab research engine chugging along. I thank Chi Ma for his help with SEM analyses and Mike Baker for running the stepped furnace piston-cylinder press experiment. I thank the faculty of Caltech for building a community that is both creative and supportive. To each faculty member with an open door, ready and willing to talk science, I thank you. I also thank the GPS staff that keeps the Division running so smoothly, specifically Janice Grancich, Marcia Hudson, Dian Buchness, Liz Boyd, Julie Lee, and Mark Garcia.

I thank my friends at Caltech. Stephen Cox and Max Lloyd for all the inspiring conversations about science over beers. I thank Alison Piasecki, Jeff Prancevic, Sophie Hines, and Jen Buz for all the early mornings at the climbing gym and late nights at the Herm. I thank Ted Present for always reminding me it's grilling season in LA. And I thank Cody Finke for inspiring us all in his execution of the Caltech High Mountain Research Campus.

I also thank my climbing friends in Los Angeles. I thank Isamer Bilog for making me wear a helmet when I boulder instead of making me quit bouldering by dying. I thank Russell Louden for being more patient with me as a kook surfer than I ever could be with anyone learning to climb. I thank Alex Lusk for being my Seattle-Climber-Geologist doppelganger I almost never knew I had. And I thank Sean Crozier for never saying no, even when we were desperately unprepared for whatever I was proposing.

I thank the San Andreas and San Jacinto Fault for uplifting the block of Peninsular Range granite that has formed the San Jacinto Mountains. These rugged mountains, covered in boulders, cliffs and windswept Ponderosa pines out of a Dr. Suess

book have provided a necessary escape from long hours in the basement of North Mudd and the bustle of big-city Los Angeles.

Most importantly, I thank Aly Yeckes. You are the love of my life and every day I get to spend with you is a privilege. You have been my North Star through the pursuit of a PhD and I would not have gotten here today without you. I thank you for every time you put things into perspective when I came home frustrated with another day of confusing data. I thank you for every time you accompanied me on a bushwhack through the wilderness in pursuit of some rock I saw on a satellite image. I thank you for every time you sat in LA traffic on our way to try some new beer at a brewery you didn't care about. And thank you for letting me bring our sweet kitty Mia home off the street.

ABSTRACT

Geochemical records of continental weathering environments are limited despite their critical value to understanding how past climates functioned. This thesis seeks to address this limitation by drawing together innovative lines of research in geochronology, stable isotope geochemistry, and chemical weathering. Two distinct projects are described; each project designed to provide new insight into the paleoenvironmental and tectonic history of continental weathering environments. These projects, though distinct in their methods and samples, are unified by their goal: to use the stable, radiogenic, and nucleogenic isotopic composition of iron oxides to provide new constraints on the geologic history of continental weathering environments.

The weathering of Fe-bearing rocks, coupled with the extreme insolubility of iron in moderately acidic to alkaline oxic waters, causes both goethite and hematite to be abundant chemical precipitates in near-surface environments. Goethite is favored in lower temperature and more acidic or alkaline conditions, while hematite precipitates more readily in near-neutral environments. These minerals are found in soils; spring, bog, and stream deposits; oxidized chemical sediments; and hydrothermal deposits. In many cases, substantial crystalline masses occur, which can take the form of nodules, pisoliths, botryoidal, stalactitic, and radiating masses, fibrous needles, pseudomorph, veneers, or as aggregates of flakes, tabular, or anhedral crystals. Time and temperature are arguably the two most fundamental variables we as geologists seek to constrain, and iron oxide deposits can provide a valuable archive of information on low-temperature, near-surface planetary processes.

The first project investigates how the stable oxygen isotopic composition of goethite, when combined with direct He dating on the same texturally resolved scales as stable isotope analyses, can be used to interpret water sources (Chapter 1) and formation temperatures (Chapter 2). The first chapter creates a record of the paleolatitudinal gradient in the oxygen isotope composition of meteoric water. The major finding of this study is the consistency in this gradient over geologic time. This second chapter proposes a new geothermometer using the intracrystalline oxygen isotopic composition of goethite. While stable isotopic compositions of goethite have long been utilized as a tool for reconstructing paleoenvironmental conditions, previous studies have focused on the bulk concentration of stable isotopes within this phase. Since goethite has two structurally non-equivalent oxygen sites, we show it is possible to extract two isotopically unique populations of oxygen, the composition of which we interpret to be dependent on temperature at time of mineral formation. In combination with the ability to directly date goethite by the (U-Th)/He method, we may utilize goethite to constrain both the temperature and timing of goethite formation, providing a valuable archive for information on continental paleoenvironments.

The second project utilized the paired He-Ne chronometer and $^{4}He/^{3}He$ method in hematite to produce thermal histories of the ancient Kaapvaal Craton over billion-year timescales. We applied these methods to hematite ore hosted within the Transvaal Supergroup in the Griqualand West (Chapter 3) and Transvaal Basin region (Chapter 4) of the ancient Kaapvaal Craton, South Africa. The application of hematite geo- and thermochronometry to these multi-billion year-old deposits represents the most challenging environments these methods have yet been applied to. We found, in some

localities, hematite He-Ne ages provided further support of existing indirect age constraints on the timing of ore formation. In other localities, we found hematite He-Ne ages are uncorrelated with known tectono-thermal events. Modeled time-temperature histories indicate the Kaapvaal Craton has experienced exceptionally slow erosion rates over the last billion years, providing further evidence for the extreme tectonic stability of cratonic interiors over geologic timescales. This slow erosion took place over vast intervals of time, during which the craton was undergoing oxidative weathering, offering an additional constraint on understanding the history of atmospheric O_2 during Proterozoic time.

PUBLISHED CONTENT AND CONTRIBUTIONS

Miller HB, Vasconcelos PM, Eiler JM, Farley KA. (2017) A Cenozoic terrestrial paleoclimate record from He dating and stable isotope geochemistry of goethites from Western Australia. *Geology*. **45**, 895-898. DOI: 10.1130/G38989.1

H.B.D.M. designed the research project, performed laboratory measurements, and wrote the manuscript.

Farley KA, Malespin C, Mahaffy P, Grotzinger JP, Vasconcelos PM, Milliken RE, Malin M, Edgett KS, Pavlov AA, Hurowitz JA, Grant JA, Miller HBD, Arvidson R, Beegle L, et al. (2013) In Situ Radiometric and Exposure Age Dating of the Martian Surface: *Science*. 9 Dec 2013. DOI: 10.1126/science.1247166

H.B.D.M. participated in data analysis and manuscript editing.

Drignon MJ, Bechon T, Arbaret L, Burgisser A, Komorowski JC, Martel C, Miller H, Yaputra R. (2016) Preexplosive conduit conditions during the 2010 eruption of Merapi volcano (Java, Indonesia). *Geophysical Research Letters*. **43**, 11595-11602. DOI: 10.1002/2016GL071153

H.B.D.M. conducted oxygen isotope analyses and participated in manuscript editing.

TABLE OF CONTENTS

Acknowledgements……... iii
Abstract ……vi
Published Content and Contributions…….....ix
Table of Contents…… .x
List of Figures……..……xii
List of Tables……..……xiv
Chapter I: A Cenozoic terrestrial paleoclimate record from He dating and stable isotope geochemistry of goethites from Western Australia…….……..……..……...15
1.1 Introduction…….……..……..……..16
1.2 Geologic Setting and Samples…….……...17
1.3 Cenozoic Paleoclimate of Western Australia…..……..……...18
1.4 Sample Descriptions…..……..……...19
1.5 Methods…..……..……..……..……..……....22
1.6 Results…..……..……..……..……..……..…26
1.7 Discussion…..……..……..……..……..…….28
1.8 Conclusion……..……..……..……..……..…33
References…..……..……..……..……..……...…36
Appendix A: Supplemental Figures and Tables…….…...39
Chapter 2: Intracrystalline site preference of oxygen isotopes in goethite: A potential single-mineral geothermometer…….…...48
2.1 Introduction…….…….……..……..49
2.2 Background…….…….……...52
2.3 Theoretical Considerations…….……..……...57
2.4 Materials……..…..……..……..……...62
2.5 Methods…..……..……..……..……..……...66
2.6 Results and Discussion…..……...…..……..……..……72
2.7 Conclusion…..……..……..……..……..……90
References…..……..……..……..……..……...…92
Chapter 3: Combined hematite (U-Th)/He and (U-Th)/Ne ages and $^{4}He/^{3}He$ thermochronology of the iron ores of Griqualand West, South Africa…….……..…...……109
3.1 Introduction…….…….……..110
3.2 Geologic Background…….…….…….....112
3.3 Samples and Methods…….……..…….....121
3.4 Results……..…..……..……...131
3.5 Interpretations…..……..……..……..……...…….....137
3.6 Conclusion…..……..……..……..……...…149
References…..……..……..……..……..……152
Appendix B: Supplemental Figures and Tables…….....161

Chapter 4: Combined hematite (U-Th)/He and (U-Th)/Ne ages and $^{4}He/^{3}He$ thermochronology of Thabazimbi Ore, Transvaal Basin, South Africa……..……..……...……..175
4.1 Introduction……..……..……..176
4.2 Geologic Background……..…..……..……178
4.3 Sample Description……..……...…..…...186
4.4 Methods……..……..……..…….....190
4.5 Results……..…..……...……..…….....190
4.6 Discussion…..……...…….……...……..……..……..195
4.7 Conclusion…..……...……...……...……..…...201
References…..……...……...……...……..…...…...202

LIST OF FIGURES

Number *Page*

1.1 Map of Western Australia……..…17

1.2 Mean (U-Th)/He ages compared against mean $\delta^{18}O$ results…..…28

1.3 Latitudinal gradient in $\delta^{18}O$ results….....…30

2.1 Natural goethites and the meteoric water line……..…...…53

2.2 Theoretical temperature dependence between intracrystalline sites of goethite….....…58

2.3 Photographs of Colorado goethite samples……..……...…64

2.4 Schematic of reaction apparatus and dehydroxylation vessel…….68

2.5 Plot of yield vs. $\Delta^{18}O_{furnace\text{-}laser}$……..…73

2.6 Plot of dehydroxylation temperature vs. $\delta^{18}O_{dehydroxylation}$……...75

2.7 Plot of dehydroxylation yield vs. $\delta^{18}O_{dehydroxylation}$……...77

2.8 Plot of synthetic goethite precipitation temperature vs. $\delta^{18}O_{bulk}$.....79

2.9 Plot of synthetic goethite precipitation temperature vs. $\Delta^{18}O_{bulk\text{-}dehydroxylation}$.....82

2.10 Plot of dehydroxylation yield vs. $\Delta^{18}O_{bulk\text{-}dehydroxylation}$.....83

3.1 DEM of southern Africa with simplified geologic map….....112

3.2 Generalized N-S cross-section of Griqualand West……...…...115

3.3 Sample photos……121

3.4 Arrhenius arrays…….....…..130

3.5 Delta plots……..……...…..…134

3.5 $^{4}He/^{3}He$ age spectra…….……...…..…136

3.7 Generalized geologic map of Griqualand West with ages……...…137

3.8 Illustration of proposed hematite ore forming processes…….....140

3.9 Time-temperature modeling results……..….....143

4.1 DEM of southern Africa with simplified geologic map….....…176

4.2 Geologic Map of Thabazimbi area……...…180

4.3 Geologic Map and Cross section of Donkerpoort Neck……...…181

4.4 Geologic Map and Cross section of Donkerpoort West…….....…182

4.5 Sample photos……..186

4.6 FTIR spectra……..….....189

4.7 Donkerpoort Neck Arrhenius array……..…...…191

4.8 Donkerpoort Neck Delta plots……..……193

4.9 Donkerpoort Neck $^{4}He/^{3}He$ age spectrum……..…….....…194

4.10 Donkerpoort West $^{4}He/^{3}He$ age spectrum……..…….....…195

4.11 Donkerpoort Neck T-t modeling results……...…197

LIST OF TABLES

Number *Page*

1.1 Summary of Results 27
2.1 Reproducibility of bulk oxygen isotope composition 99
2.2 Dehydroxylation oxygen yield 100
2.3a Synthetic goethite bulk fluorination results 101
2.3b Synthetic goethite dehydroxylation results 101
2.4 Summary of synthetic goethite results 102
2.5 Mass balance results 103
2.6 Results of heating experiment 104
2.7 Natural goethite bulk fluorination results 105
2.8 Natural goethite dehydroxylation results 106
2.9 Summary natural goethite results 107
2.10 New (U-Th)/He results 108
3.1 Summary of (U-Th)/He and (U-Th)/Ne Results 160
4.1 Summary of (U-Th)/He and (U-Th)/Ne Results 208
4.2 Donkerpoort Neck diffusion data 209
4.3 Donkerpoort Neck step age data 210

Chapter 1

A CENOZOIC TERRESTRIAL PALEOCLIMATE RECORD FROM HE DATING AND STABLE ISOTOPE GEOCHEMISTRY OF GOETHITES FROM WESTERN AUSTRALIA

ABSTRACT

Supergene goethites from the Hamersley region of Western Australia were analyzed for $\delta^{18}O$, and the results combined with both new and previously published (U-Th)/He ages to assess the paleoenvironmental signal recorded by surficial goethite in a long-term continental archive. $\delta^{18}O_{goe}$ values increase monotonically by ~3‰ between 71 and 5 Ma and appear little affected by changes in temperature or other characteristics of depositional environment. The temporal trend likely reflects the isotopic composition of meteoric water from which the goethite formed, which varied as Australia migrated ~3000 km northward over the Cenozoic. Translating age to paleolatitude reveals that the $\delta^{18}O_{goe}$ data are consistent with a latitudinal gradient in the $\delta^{18}O_{precip}$ that, throughout the Cenozoic, remained largely unchanged from the modern gradient. There is a 5‰ offset between the latitudinal trends of $\delta^{18}O_{goe}$ and modern precipitation, approximately as expected from the water-goethite fractionation factor. Temporal variation in the $\delta^{18}O$ of local meteoric water arising from changes in moisture source or pathway is not evident in the goethites, at least in part because topography is subdued and has evolved little in this tectonically quiescent landscape. Our results provide evidence that the efficiency of water transport from equator to pole that governs the latitudinal $\delta^{18}O$ gradient of precipitation

has been roughly constant over southern temperate latitudes for the entirety of the Cenozoic.

I. INTRODUCTION

Quantitative reconstructions of continental paleoclimate are hindered by an absence of techniques for placing climate proxy material in a radiometrically dated context, but recent advances in stable isotope geochemistry and geochronology of goethite (FeOOH) offer a new potential source for such information. The oxygen isotope composition of surface and near-surface goethite largely reflects that of meteoric water, which depends on several important paleoenvironmental factors, including latitude, temperature, aridity, and elevation (Yapp, 1987, 2000). Goethite is suitable for (U-Th)/He dating (Shuster et al., 2005), and recent studies reveal that goethite (U-Th)/He (GHe) ages span at least the past 70 m.y. in Western Australia (Heim et al., 2006; Vasconcelos et al., 2013). Thus continental goethite may provide a long-lived archive by which to characterize evolving paleoenvironmental conditions, a record that has so far been little investigated (Yapp and Shuster, 2011). We selected this suite of samples for its longevity and its transition from high-latitude tropical rainforest to mid-latitude arid grassland (Martin, 2006). This transition, caused by northward motion of the Australian plate (Müller et al., 2016) and global cooling (Zachos et al. 2001), is expected to have resulted in predictable and measurable changes in goethite $\delta^{18}O$ ($\delta^{18}O_{goe}$).

II. GEOLOGIC SETTING AND SAMPLES

The Hamersley province of northwestern Australia is a passive continental margin with a moderately elevated (~800 m) interior separated from low-lying coastal plains by a series of escarpments. The elevated interior is composed of ridges and plateaus dominated by chemically resistant Archean to Paleoproterozoic banded iron formations (BIFs) and quartzites and incised valleys consisting predominantly of shales and dolomites (Figure 1.1) (Vasconcelos et al., 2013). The region has been structurally stable with little erosion

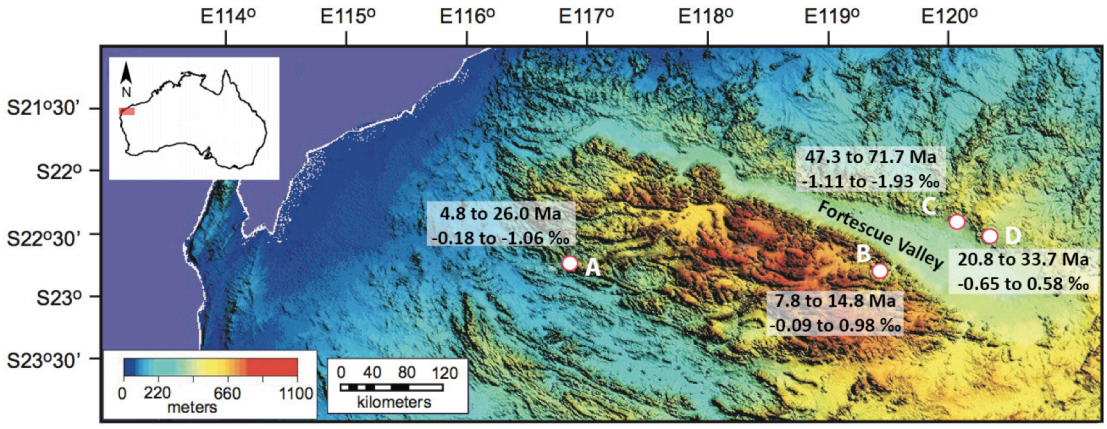

Figure 1.1. Digital terrain model of low-elevation coastal plains and elevated continental interior of Hamersley province (Western Australia), modified from Vasconcelos et al. (2013). Locations of supergene goethite deposits sampled for this study are indicated: Metawandy Valley (A), Yandi (B), Lynn Peak (C), and Roy Hill (D), each showing the range of measured goethite (U-Th)/He ages and $\delta^{18}O$.

for the entire Cenozoic (Kohn et al., 2002; Macphail and Stone, 2004; Vasconcelos et al., 2013). Much of the elevated interior is blanketed with ferruginous weathering profiles and related deposits, many of which are exposed and accessible in Fe mines or prospects.

The prolonged process of iron mobilization and precipitation, along with later cycles of dissolution and reprecipitation of existing iron oxides, has produced a thick

horizon rich in goethite with readily visible and physically separable growth zones that span many millions of years (Heim et al., 2006; Vasconcelos et al., 2013). GHe ages and oxygen isotope ratios can be obtained on the same texturally-resolved, mm-scale growth bands, allowing a time-resolved isotopic record of a single locality. With the exception of Yapp and Shuster (2011), previous studies of the stable isotope composition of goethites either assumed the age of the specimen or obtained an age from stratigraphically related materials. Both of these dating approaches are suspect in environments that experience chemical reprocessing, such as for weathering BIFs (Shuster et al., 2005; Monteiro et al., 2014).

Samples for this study (Figure 1.1) come from three localities flanking the Fortescue Valley, referred to as Yandi (Heim et al., 2006), Lynn Peak, and Roy Hill (Vasconcelos et al., 2013), and a fourth sampling site, Metawandy Valley, lying ~150 km westward and across the Hamersley Range. Although all samples are supergene, those from Yandi and Lynn Peak are from channel iron deposits (CID; Vasconcelos et al., 2013), whereas samples from Roy Hill and Metawandy Valley are from weathering profiles consisting of ferruginzed colluvium and/or ferricretes.

III. CENOZOIC PALEOCLIMATE OF WESTERN AUSTRALIA

Australia's unique climatic and tectonic evolution makes it well suited for investigating supergene goethite as a paleoclimate archive. Breakup of Gondwanaland and accelerated northward drift of Australia into low latitudes began in the early Paleogene (Müller et al., 2016). Over this same time period, global climate cooled dramatically

(Zachos et al., 2001). Thus the region likely experienced significant change in environmental conditions without complications from changing elevation or regional mountain building that might have affected the isotopic composition of meteoric water. Here we summarize constraints on the climate of northwestern Australia as a means to frame our $\delta^{18}O_{goe}$ record.

Fossil plant assemblages indicate that the region experienced a warm climate with consistently high rainfall and humidity in the Late Cretaceous and early Paleogene (Martin, 2006). Beginning in the mid-Eocene, a rise in temperature and a decrease in rainfall coincided with the early stages of Australia's shift to lower latitudes (Frakes and Barron, 2001; Martin, 2006). The initiation of the Antarctic Circumpolar Current due to the separation of Australia from Antarctica in the late Eocene triggered the onset of the Leeuwin Current, bringing warm equatorial water southward along the western margin of Australia (McGowran et al., 1997). Global circulation models (GCMs) find that by the mid- to late Miocene, significant regional aridity had begun (Frakes and Barron, 2001), with Western Australia paleodrainage systems no longer having consistent flow under a monsoon regime (Frakes and Barron, 2001; Martin, 2006).

IV. SAMPLE DESCRIPTIONS

Iron oxide environments sampled for this study fall into three groups: (i) lateritic weathering profiles; (ii) ferruginized colluvia; and (iii) channel iron deposits.

Lateritic weathering profiles sit directly on top of iron rich rock, in the case of the Hamerlsey region, on top of a banded iron formation (BIF). A lateritic ferricrust grows

downward as seasonal rainfall in combination with plant-derived organic acids triggers the dissolution of BIF minerals, leaving voids for subsequent goethite precipitation (Lascelles, 2012; Kneeshaw and Morris, 2014). This process produces a vitreous goethite cap often meters to tens of meters thick, with small fragments of remnant original hematite present (Kneeshaw and Morris, 2014). Our samples collected from Metawandy Valley represent typical lateritic weathering profile material developed on a BIF (Supplementary Figure 1.1a).

On the flanks of the BIF landforms, ferruginized colluvia encompass another iron-rich environment in the Hamersley region. These deposits are dominated by hematite alluvium with preserved original BIF textures cemented by vitreous goethite (Kneeshaw and Morris, 2014). The Roy Hill samples in this study represent such ferruginized colluvia deposits (Supplementary Figure 1.1d).

Channel iron deposits are ferruginized paleochannels, primarily found in low valleys but also extending onto surrounding plains, dominated by pisoliths, ferruginized wood, and goethite cement (Ramanaidou et al., 2003; Kneeshaw and Morris, 2014). The large stream channel size (10s of m wide), long length (sometimes hundreds of km), gentle gradients, meandering form, and wide geographic occurrence indicate these were well-developed river systems during a time Western Australia had a more active hydraulic cycle than today (Ramanaidou et al., 2003). The Lynn Peak (Supplementary Figure 1.1c) and Yandi (Supplementary Figure 1.1b) samples in this study represent typical CID material.

Natural goethites produced by weathering reactions can range widely in physical and chemical properties, from a disseminated yellowy stain to dense, compact, pure, and highly crystalline masses. Only the latter material was selected for this work. A subset of the samples reported on here was previously characterized by optical microscopy, XRD, SEM, and electron microprobe analysis (Heim et al., 2006; Heim, 2007; Vasconcelos et al., 2013). In this subset, XRD and high-resolution synchrotron analyses yield sharp symmetrical peaks, suggesting a high degree of goethite crystallinity (Heim, 2007; Vasconcelos et al., 2013). Illustrative reflected light photomicrographs and SEM images are shown in Supplementary Figure 1.2. These results are typical of the samples analyzed here.

Goethite may contain variable abundances of SiO_2 (possibly as a discrete phase), as well as substitution of Al for Fe within the mineral structure (Schwertmann, 1988). These impurities might affect either the He age or the oxygen isotope composition of our goethites. Supplementary Table 1.2 reproduces previously published Al and Si data on a subset of samples analyzed in this study, including specimens from all four studied localities. Si spot analyses range from 0.10 - 2.93 wt % (Heim, 2007; Vasconcelos et al., 2013), with the average Si content of individual samples ranging from 0.29 wt. % to 1.71 wt. % (Supplementary Table 1.2). Al spot analyses range from below detection to 5.90 wt. %, with the average Al content of individual samples ranging from 0.01 wt. % to 4.07 wt. % (Supplementary Table 1.2). We observe no correlations between Al or Si content and He age or oxygen isotope composition within our data set. For example, while the Yandi

samples have the most variable Al and Si content, they are not anomalous (nor anomalously variable) in $\delta^{18}O$ or GHe age.

V. METHODS

Goethite-dominated hand samples were cut and polished into thick sections from which vitreous goethite was drilled with a 4 mm coring bit. Cores were crushed to 0.1–3 mm fragments, sieved, and ultrasonically cleaned in ethanol. Separate, representative aliquots of the crushate were analyzed for $\delta^{18}O_{goe}$ and GHe age.

(U-Th)/He chronometry

GHe ages were determined following the procedures of Shuster et al. (2005) and Vasconcelos et al. (2013). Two to three 0.1 to 3 mm fragments (~100 ug) were selected for coarse, crystalline texture, then individually packaged in Pt tubes, heated by laser, and ^{4}He concentrations measured by quadrupole mass spectrometer following cryogenic separation of He and the addition of ^{3}He spike. After complete degassing, the goethite grains within Pt tubes were transferred to a Teflon beaker containing ^{230}Th and ^{235}U spikes and dissolved in concentrated HCl by heating for 12 hours to 90 °C. The spiked solutions were diluted and U and Th concentrations analyzed by quadrupole inductively coupled plasma–mass spectrometry (ICP-MS).

All samples were dated in duplicate or triplicate, and mean GHe ages are reported. The analytical uncertainty of ±2% underestimates the true uncertainty on formation age because most goethites lose at least a few % of their ^{4}He under earth surface conditions (Shuster et al., 2005). For example, $^{4}He/^{3}He$ experiments on Lynn Peak goethites show

that these samples experienced ~5% He loss (Vasconcelos et al., 2013). In the absence of $^{4}He/^{3}He$ experiments on all of our samples, we make an approximate correction for this effect by assuming 10% He loss and conservatively assign a ±10% uncertainty to all He ages (e.g., as in Monteiro et al., 2014).

Measurement of stable oxygen isotopes in goethite

Using the sample material recovered from the same initial 4 mm drill core that geochronometry aliquots were selected from, 10 mg of goethite was crushed to 100-300 micron size, sieved, and ultrasonically cleaned in ethanol. A ~2 mg aliquot of sample was heated to 80° C under vacuum overnight and then pretreated with BrF_5 vapor at room temperature to remove any remaining adsorbed water. The sample was then irradiated with a 10.6 μm CO_2 laser while exposed to BrF_5 vapor, driving fluorination reactions that produce O_2, HF, and iron fluoride. The O_2 was isolated and purified by cryogenic separation and passage over hot mercury, then converted to CO_2 by passage over hot graphite and analyzed by dual inlet gas source mass spectrometry in that form (Sharp et al., 1990). A garnet standard, UWG-2, was measured throughout each analytical session to monitor the accuracy of each session's measurements. When the measured $\delta^{18}O$ of UWG-2 varied from the known value, a correction was applied, typically ~0.10‰ (Valley et al., 1995). The final pressure of CO_2 produced from a sample fluorination reaction and subsequent CO_2 conversion was measured and used to check that a sample was completely fluorinated, as partial sample fluorination may induce isotopic fractionation (Valley et al., 1995). Analyses were discarded (~25% of total analyses made) when the measured moles of CO_2 differed from the mass-based prediction by more than 10%. In the case of samples

with published (U-Th)/He ages, the material prepared for $\delta^{18}O_{goe}$ was sourced from remaining crushate produced from texturally uniform bands within the 4 mm cores used for the original (U-Th)/He analyses.

Here we adopt the mean value of up to seven replicates as the best estimate for $\delta^{18}O$ of the entire sample, and report uncertainty as the standard error of the population. As discussed below, our preferred interpretation of internal $\delta^{18}O_{goe}$ variability (up to 1.3‰) within a few samples is that it reflects short-time-scale variation (i.e., daily, weekly, seasonally) in the isotopic composition of the water from which these particular goethites grew.

Stable oxygen isotope measurements of large-mass samples

The aforementioned issue of unexpectedly large $\delta^{18}O$ variability in some of our samples was investigated by the measurement of large-mass samples. The reproducibility of UWG-2 standards, the mineralogical purity of goethite in this study (Heim et al., 2006; Heim, 2007; Vasconcelos et al., 2013), and the reproducible $\delta^{18}O$ results from the remainder of our samples together suggest this variability is not inherent to the fluorination procedure or other aspects of the analytical method. As an alternative, we hypothesize that some of our samples contain isotopic heterogeneity arising from factors occurring on short timescales and therefore over small length scales of goethite growth. If so, we expect that replicate measurements of small samples (2 mg) will yield the same mean as analysis of a much larger sample mass. To test this hypothesis, we measured the $\delta^{18}O$ of two of the anomalously variable goethite samples with five times more than our typical sample mass. Weighed samples and standards are typically loaded into a nickel

disc with 36 pits. For this experiment, we loaded five adjacent pits each with the ~2 mg sample mass typical of laser fluorination measurements, then drew a proportionally larger quantity of BrF_5 to completely fluorinate the larger mass sample, and lased them all. Typical pretreatment, fluorinated species purification, and CO_2 conversion were all followed for these large-mass measurements. We allowed for a lower yield criterion in these large-mass measurements due to very slow conversion to CO_2. We suspect that the graphite rod reaches a saturation state when exposed to gas from these large mass fluorination reactions and incompletely converted our sample to CO_2.

Larger aliquots produced $\delta^{18}O_{goe}$ results consistent with the average of the smaller aliquots. Thus we interpret these observations to indicate that in some of our samples, 2 mg aliquots were too small to capture the average composition of the goethite. This fine scale heterogeneity may be due to local variations in meteoric water on time scales unresolvable by GHe dating. By averaging the $\delta^{18}O$ of the smaller aliquots, we obtain our best estimate of the composition of the goethite at the time associated with the GHe age.

(U-Th)/He age to paleolatitude transformations

(U-Th)/He ages were transformed to paleolatitude for each sample to explore the possible correlation between the modern latitudinal gradient in isotopic composition of meteoric water and our $\delta^{18}O_{goe}$ record. Absolute plate speed and direction calculated by Muller et al. (2016) for the Australian plate from 80 Ma to present was used to determine paleolatitudes. The vector along which the center of the Australian plate traveled shifted from NW to NE with a speed of 1-3 cm/yr between 80 Ma and 40 Ma then increased speed significantly to between 6 and 8 cm/yr in the NNE direction between 40 Ma and the

present (Muller et al., 2016). Supplementary Table 1.7 presents the speed and direction of the Australian plate in 10 Ma periods used to transform (U-Th)/He ages into paleolatitudes. Here we assume the ±10% uncertainty applied to the (U-Th)/He ages dominates over the error associated with determining finite plate rotations, and therefore the error assigned to sample paleolatitude is the result of propagating (U-Th)/He error through the latitude transformation. For Cenozoic plate reconstructions, where an absolute reference frame can be tied down via well-constrained subduction and hotspot locations, this assumption is likely valid (Muller et al., 2016).

VI. RESULTS

New GHe ages were measured for ten samples: four from Metawandy Valley and six from Roy Hill (Supplementary Table 1.3). These ages complement and extend those previously reported from Yandi, Lynn Peak, and Roy Hill (Heim et al., 2006; Vasconcelos et al., 2013). Single-aliquot GHe ages from the entire data set span the interval 71 ± 7 to 4 ± 0.4 Ma. Among the Fortescue Valley localities, the oldest ages were obtained at Roy Hill (72 ± 7 to 47 ± 5 Ma), with successively younger ages from Lynn Peak (34 ± 3 to 20 ± 2 Ma) and Yandi (15 ± 1.5 to 8 ± 0.8 Ma). The Metawandy Valley samples range from 26 ± 3 to 4 ± 0.4 Ma.

Summary $\delta^{18}O$ results are presented for the 21 dated samples in Table 1.1, with full analytical data in Supplementary Table 1.4. Across the entire data set, sample-mean $\delta^{18}O_{goe}$ values range by ~3‰, from -1.93‰ ± 0.02‰ to +0.98‰ ± 0.03‰. Variability of ~1‰ occurs at each sampling locality, with the lightest $\delta^{18}O_{goe}$ at Roy Hill and the

heaviest at Yandi. Among the Fortescue Valley suite, there is a positive correlation between $\delta^{18}O_{goe}$ and GHe age (Figure 1.2). The Metawandy Valley samples display a similar correlation with age, but are shifted to ~1‰ lower $\delta^{18}O_{goe}$ for a given GHe age.

TABLE 1.1: SUMMARY OF LASER FLUORINATION AND (U-TH)/HE RESULTS FROM GOETHITE SAMPLES, WESTERN AUSTRALIA

Sample	Mean $\delta^{18}O_{VSMOW}$ (‰)	±	Mean corrected age (Ma)	±	Paleolatitude (°S)
Stop1-6-A1	–0.316	0.015	4.8	0.5	26.3
Stop1-6-A7	–0.181	0.037	4.9	0.5	26.4
Stop1-6-A5	–0.370	0.024	8.5	0.9	29.1
Stop1-1-A3	–1.061	0.092	26.0	2.6	42.1
Yan-02-09	0.627	0.027	7.8*	0.8	28.6
Yan-02-02	0.703	0.022	10.4*	1.0	30.5
Yan-02-01-A	0.677	0.026	11.3*	1.1	31.0
Yan-02-03	0.976	0.028	12.0*	1.2	31.6
Yan-02-06	–0.088	0.028	13.5*	1.4	32.7
Yan-02-01-D1	0.727	0.055	14.8*	1.5	33.6
LynP-02-09-A5	0.578	0.035	20.8†	2.1	37.7
LynP-02-09-A3	–0.205	0.248	33.7†	3.4	47.2
LynP-02-09-A2	–0.645	0.069	33.7†	3.4	47.2
LynP-02-09-A1	–0.479	0.226	33.7†	3.4	47.2
Roy-02-02-Cy1	–1.477	0.133	47.3	4.7	53.0
Roy-02-02-Cy2	–1.609	0.076	61.7	6.2	55.8
Roy-02-02-Cy3	–1.682	0.028	68.0	6.8	56.1
Roy-02-02-B5	–1.283	0.035	68.0	6.8	56.1
Roy-02-02-C03	–1.630	0.001	68.8	6.9	56.2
Roy 02–02-C1	–1.113	0.076	70.5	7.1	56.2
Roy-02–02-B1	–1.928	0.020	71.7*	7.2	56.3

Note: VSMOW—Vienna standard mean ocean water.
*(U-Th)/He date from Heim et al. (2006)
†(U-Th)/He date from Vasconcelos et al. (2013)

VII. DISCUSSION

The large span of GHe ages obtained from this composite of just four sampling sites demonstrates that, at least in the Hamersley region, surficial iron-rich deposits carry a very long-lived goethite record that can be dated with uncertainty of a few million years. The key result of this study is that $\delta^{18}O_{goe}$ increases monotonically through time, independent of depositional environment, by 3‰ over the course of the Cenozoic (Figure 1.2). We seek an explanation for this correlation, and, ideally, one that can also explain the offset in $\delta^{18}O_{goe}$ between the Fortescue Valley and Metawandy Valley localities.

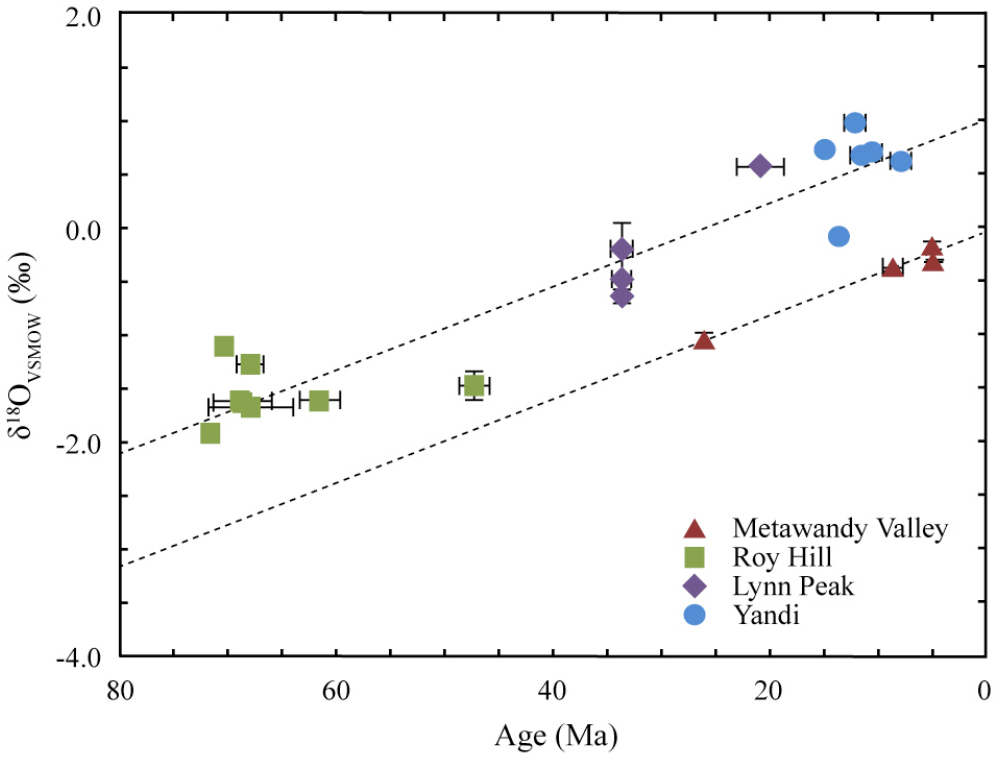

Figure 1.2. Mean (U-Th)/He ages compared against mean $\delta^{18}O$ results of goethite samples from Metawandy Valley (red triangles), Roy Hill (green squares), Lynn Peak (purple diamonds), and Yandi (blue circles), Western Australia. Metawandy Valley is separated from other samples because of its position on opposing flank of Hamersley Range from other sites. VSMOW—Vienna standard mean ocean water. Linear regressions of the Fortescue Valley suite data and Metawandy Valley data are show as dashed lines.

$\delta^{18}O_{goe}$ is not correlated with goethite formation environment: locality-mean values from the Yandi and Lynn Peak CID goethites differ from each other by ~1‰, with the weathering profile samples at Roy Hill and Metawandy Valley differing from each other by a comparable amount. Furthermore, open-system behavior of the oxygen or He in goethite can be ruled out. For samples forming at earth-surface conditions, GHe ages (Shuster et al., 2005) and $\delta^{18}O_{goe}$ (Yapp, 1991) are both established upon mineral crystallization. Over million-year time scales, there is no evidence that isotopic exchange can occur between ambient water and structural oxygen in goethite in the absence of mineral dissolution and reprecipitation (Yapp, 1991). While dissolution and reprecipitation doubtless occur in supergene environments, both GHe ages and $\delta^{18}O_{goe}$ will record only the final crystallization event.

$\delta^{18}O_{goe}$ is sensitive to formation temperature (Yapp, 2000). GCMs indicate ~10 °C of warming in northwest Australia through the Cenozoic (Frakes and Barron, 2001). Based on the $a_{goethite\text{-}water}$ temperature dependence as determined by synthesis experiments (Yapp, 2000), this amount of warming would result in a 1‰ decrease in $\delta^{18}O_{goe}$. While this effect is likely present in our data at some level, it is subordinate to and of opposite sense to the observed trend, and so must be a secondary factor.

Goethite acquires oxygen from the water in which it forms, so changes in the composition of surface or groundwater will be reflected in $\delta^{18}O_{goe}$ (Yapp, 1987). Such changes could be local, regional, or continental in scale. At the continental scale, Earth's modern climatic regime imparts a dramatic latitudinal decrease in the $\delta^{18}O$ of precipitation ($\delta^{18}O_{precip}$) as cloud water distills along its general tropics-to-pole trajectory (Dansgaard,

1964). This effect causes a roughly 3‰ decrease in $\delta^{18}O_{precip}$ from 20°S to 50°S latitude (Supplementary Table 1.8). From ca. 72 Ma to 5 Ma, the Hamersley region migrated through roughly this same latitudinal range (56°S to 26°S), with an additional 4° northward migration in the last 5 m.y. Because the northward migration was monotonic, the correlation of $\delta^{18}O_{goe}$ with GHe age is retained when plotted against paleolatitude (Figure 1.3). Interestingly, sample Roy-02-02-Cy1, which lies off of the GHe- $\delta^{18}O_{goe}$

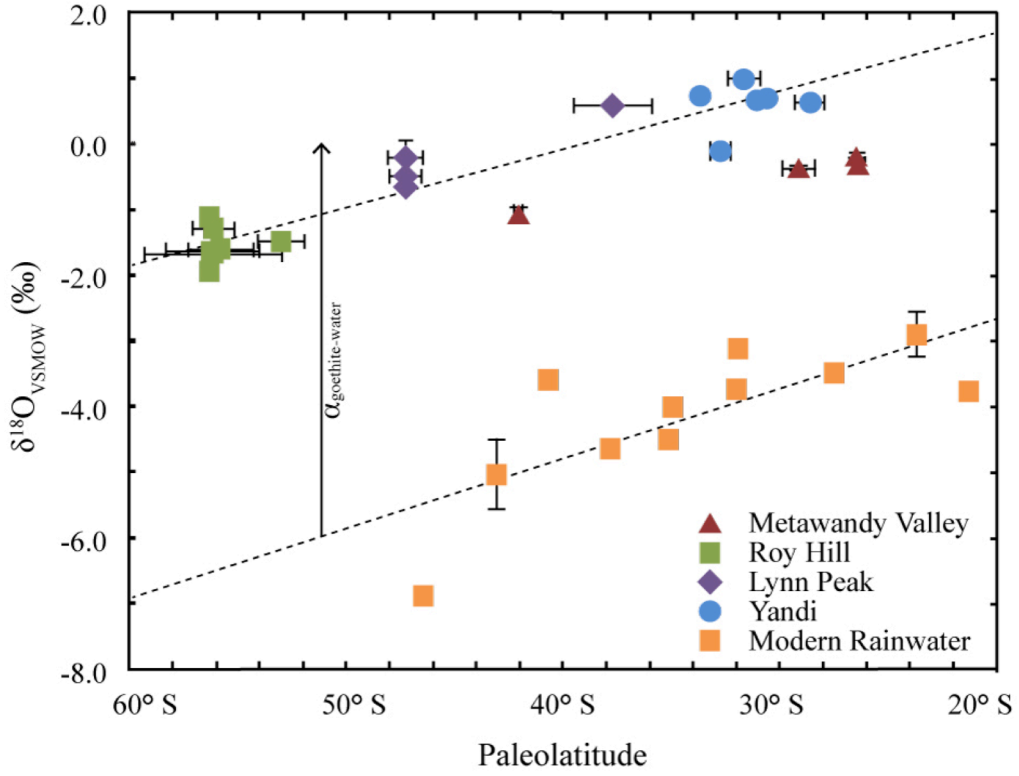

Figure 1.3. Latitudinal gradient in $\delta^{18}O$ of mean annual modern meteoric water in South Pacific region (orange squares) compared against mean $\delta^{18}O$ results of goethite samples from Metawandy Valley (red triangles), Roy Hill (green squares), Lynn Peak (purple diamonds), and Yandi (blue circles), Western Australia. (U-Th)/He ages have been transformed into paleolatitude based on Australian plate absolute motion from Müller et al. (2016). VSMOW—Vienna standard mean ocean water. Linear regressions of the Fortescue Valley suite data and of modern rainwater data are show as dashed lines.

trend (Figure 1.2), sits on the trend when plotted against paleolatitude. This occurs because the slow northward movement of Australia during the Paleogene causes the entire Roy Hill sample suite to have a similar paleolatitude despite a 25 Ma range in age.

Figure 1.3 reveals that the paleolatitude- $\delta^{18}O_{goe}$ trend defined by the Fortescue Valley group of samples has the same slope as the modern rainwater gradient, offset by approximately +5‰. This offset is in good agreement with the empirically observed +6‰ $a_{goethite\text{-}water}$ for surface weathering conditions (Yapp, 2000). Taken together, these observations strongly suggest that the first-order control on $d^{18}O_{goe}$ in our record is the evolving isotopic composition of meteoric water, which itself reflects the large-scale latitudinal pattern in $\delta^{18}O_{precip}$ coupled to Australia's northward migration.

Distillation of cloud water toward lighter $\delta^{18}O$ also occurs at the regional scale as moisture pathways traverse land and particularly mountain ranges. Because the Hamersley region, and indeed most of Western Australia, has remained tectonically stable through the entire Cenozoic (Kohn et al., 2002; Macphail and Stone, 2004), evolving topography is unlikely to have played an important role in our data set. For example, using the global average $\delta^{18}O_{precip}$-elevation relationship of -0.28‰/100 m (Poage and Chamberlain, 2002), our observed +3‰ shift would necessitate the existence of an ~1 km range at 70 Ma between the precipitation's moisture source and Hamersley, followed by its subsequent removal. We are aware of no evidence supporting the possibility of such a range.

Changes in air-mass trajectory can also lead to changes in meteoric water $\delta^{18}O$ at a given location. In Hamersley, the moisture pathway from tropical feeding zone to rainout has remained similar since at least the Miocene, with the majority of the region's moisture being delivered by summer cyclones approaching from the north (Martin, 2006; Dogramaci et al., 2012). The match between the $\delta^{18}O_{goe}$ record and the modern latitudinal gradient (Figure 1.3) suggests that the dominant pathway has not evolved substantially. This conclusion is supported by the $\delta^{18}O_{goe}$ trend from the Metawandy Valley locality, which for the last 25 m.y. has been similar to that of the Fortescue Valley sites but shifted by ~1‰ to lighter compositions. Precipitation sourced from the north or northeast must have crossed the 600 m orographic barrier of the Hamersley Range to get from the Fortescue Valley sites to Metawandy Valley. This would have promoted enhanced rainout that left the residual moisture relatively depleted in ^{18}O by the time it arrived in the Metawandy Valley region, an observation that holds true in the modern day (Dogramaci et al., 2012).

A variety of other local mechanisms related to the distillation of water could be responsible for a change in $\delta^{18}O_{goe}$. These include short-term changes in moisture source, changes in the magnitude of storm events, and factors such as humidity, runoff, surface water evaporation, and groundwater mixing and recharge. While a 25‰ range in $\delta^{18}O_{precip}$ has been observed in Fortescue Valley, large summer cyclones, which today deliver 85% of the annual precipitation, have a $\delta^{18}O$ range of just 7‰, and groundwater varies by just a few per mil (Dogramaci et al., 2012). In an overall sense, we see no evidence for such variability in our goethite record, such as deviations from the trend in Figure 1.3. Perhaps

its absence arises from the fact that suitable conditions for goethite formation within ~10 m of the surface likely only occur seasonally when adequate moisture is present. This is a period of the year when the $\delta^{18}O_{precip}$ has a narrow range, and evaporation from soil or fractured rock does not obscure the first-order latitudinal control on $\delta^{18}O_{precip}$. However, at the finer scale, such variability provides a potential explanation for the $\delta^{18}O_{goe}$ heterogeneity we observe in a few of our samples. Short-term variations in the isotopic composition of water may yield finely banded goethite generations that are unresolvable either by our sample preparation methods or by GHe dating.

VIII. CONCLUSIONS

Goethites from the Hamersley region carry a 70 m.y. record of systematic $\delta^{18}O$ variation. Although other processes undoubtedly have affected $\delta^{18}O_{goe,}$ the dominant signal in the record is that of the evolving composition of meteoric water. Specifically, the correlation between $\delta^{18}O_{goe}$ and paleolatitude arises from Australia's northward migration coupled with the global latitudinal gradient in $\delta^{18}O_{precip}$. The strength of the correlation and its match to the modern gradient argues that the latitudinal gradient in $\delta^{18}O_{precip}$ has been largely unchanged through time. The modern hydrologic cycle is dominated on the global scale by evaporation in the tropics and transport of moisture to higher latitudes (Dansgaard, 1964). The extent to which the global-scale hydrologic cycle functioned to export moisture from low to high latitude in the geologic past, when both plate configuration and global climate were significantly different from the present, is not known. Data from our goethite archive suggest that the hydrologic cycle has maintained

remarkable consistency for the past 70 m.y., with both the modern $\delta^{18}O_{precip}$ data and our $\delta^{18}O_{goe}$ record indicating a gradient of 0.10‰ per degree latitude.

A continued mismatch in $\delta^{18}O_{precip}$ between GCM predictions and proxy data from the geologic past (Poulsen et al., 2007; Carmichael et al., 2016) shows that much improvement is still required in our understanding of the global, regional, and local controls on $\delta^{18}O_{precip}$. Specifically, models predict a reduced $\delta^{18}O_{precip}$ gradient in the Eocene southern hemisphere, but proxy data by which to validate these results is lacking (Winnick et al, 2015). This study provides the new insight that the latitudinal gradient in $\delta^{18}O_{precip}$ in southern mid- to low-latitude bands has remained largely invariant during the Cenozoic despite major shifts in temperature, paleogeography, and ocean-atmosphere circulation patterns.

Measurement of $\delta^{18}O_{goe}$ on radiometrically dated milligram-size aliquots of supergene goethite provides access to a new long-term continental paleoclimate record. Further work could implement paired measurements of hydrogen and oxygen isotopes to determine temperatures during crystallization (Yapp, 1987), simultaneously permitting isolation of meteoric water composition effects on $\delta^{18}O_{goe}$. Should such data confirm the 10 °C increase in mean temperature in the Hamersley region predicted by GCMs over the Cenozoic, the resulting 1‰ decrease in $\delta^{18}O_{goe}$ may need to be considered when interpreting the present data set in terms of the latitudinal gradient of $\delta^{18}O_{precip}$. Similarly, goethite could be used to produce higher-temporal-resolution records, records pushing further back in time, or records assessing spatial gradients at a specific time. The general abundance of goethite in surface environments (e.g., in Australia, Brazil, South Africa,

and India) could allow for the construction of $\delta^{18}O_{goe}$ records from other regions in which the goethite stable isotope composition records similar or different aspects of the continental paleoenvironment.

REFERENCES

Carmichael, M.J., et al., 2016, A model–model and data–model comparison for the early Eocene hydrological cycle: Climate of the Past, v. 12, p. 455–481, doi:10.5194/cp-12-455-2016.

Dansgaard, W., 1964, Stable isotopes in precipitation: Tellus, v. 16, p. 436–468, doi:10.3402/tellusa.v16i4.8993.

Dogramaci, S., Skrzypek, G., Dodson, W., and Grierson, P.F., 2012, Stable isotope and hydrochemical evolution of groundwater in the semi-arid Hamersley Basin of subtropical northwest Australia: Journal of Hydrology (Amsterdam), v. 475, p. 281–293, doi:10.1016/j.jhydrol.2012.10.004.

Frakes, L.A., and Barron, E.J., 2001, Phanerozoic general circulation model results and quantitative climate data for Australia: Australian Journal of Earth Sciences, v. 48, p. 643–655, doi:10.1046/j.1440-0952.2001.00887.x.

Heim, Jonathan Andrew (2007). *Geochronology of weathering and landscape evolution, Hamersley Iron Province, Australia* PhD Thesis, School of Physical Sciences, University of Queensland.

Heim, J.A., Vasconcelos, P.M., Shuster, D.L., Farley, K.A., and Broadbent, G., 2006, Dating paleochannel iron ore by (U-Th)/He analysis of supergene goethite, Hamersley province, Australia: Geology, v. 34, p. 173–176, doi:10.1130/G22003.1.

Kneeshaw, M., and Morris, R.C., 2014, The Cenozoic detrital iron deposits of the Hamersley Province, Western Australia: Australian Journal of Earth Sciences, v. 61, no. 4, p. 513–586.

Kohn, B.P., Gleadow, A.J.W., Brown, R.W., Gallagher, K., O'Sullivan, P.B., and Foster, D.A., 2002, Shaping the Australian crust over the last 300 million years: Insights from fission track thermotectonic imaging and denudation studies of key terranes: Australian Journal of Earth Sciences, v. 49, p. 697–717, doi:10.1046/j.1440-0952.2002.00942.x.

Lascelles, D.F., 2012, Banded iron formation to high-grade iron ore: a critical review of supergene enrichment models: Australian Journal of Earth Sciences, v. 59, no. 8, p. 1105–1125.

Macphail, M.K., and Stone, M.S., 2004, Age and palaeoenvironmental constraints on the genesis of the Yandi channel iron deposits, Marillana Formation, Pilbara, northwestern Australia: Australian Journal of Earth Sciences, v. 51, p. 497–520, doi:10.1111/j.1400-0952.2004.01071.x.

Martin, H.A., 2006, Cenozoic climatic change and the development of the arid vegetation in Australia: Journal of Arid Environments, v. 66, p. 533–563, doi:10.1016/j.jaridenv.2006.01.009.

McGowran, B., Li, Q., Cann, J., and Padley, D., 1997, Biogeographic impact of the Leeuwin Current in southern Australia since the late middle Eocene: Palaeogeography, v. 136, p. 19–40, doi:10.1016/S0031-0182(97)00073-4.

Monteiro, H.S., Vasconcelos, P.M., Farley, K.A., Spier, C.A., and Mello, C.L., 2014, (U-Th)/He geochronology of goethite and the origin and evolution of cangas: Geochimica et Cosmochimica Acta, v. 131, p. 267–289, doi:10.1016/j.gca.2014.01.036.

Müller, R.D., Seton, M., and Zahirovic, S., 2016, Ocean basin evolution and global-scale plate reorganization events since Pangea breakup: Annual Review of Earth and Planetary Sciences, v. 44, p. 107–138, doi:10.1146/annurev-earth-060115-012211.

Poage, M.A., and Chamberlain, C.P., 2002, Stable isotopic evidence for a pre-Middle Miocene rain shadow in the western Basin and Range: Implications for the paleotopography of the Sierra Nevada: Tectonics, v. 21, p. 16-1–16-10, doi:10.1029/2001TC001303.

Poulsen, C.J., Pollard, D., and White, T.S., 2007, General circulation model simulation of the $\delta^{18}O$ content of continental precipitation in the middle Cretaceous: A model-proxy comparison: Geology, v. 35, p. 199–202, doi:10.1130/G23343A.1.

Ramanaidou, E.R., Morris, R.C., and Horwitz, R.C., 2003, Channel iron deposits of the Hamersley Province, Western Australia: Australian Journal of Earth Sciences, v. 50, no. 5, p. 669–690.

Schwertmann U. 1998. Occurrence and formation of iron oxides in various pedoenvironments, in Iron in Soils and Clay Minerals, v217, pp. 267-308.

Sharp, Z. D., 1990, A laser-based microanalytical method for the *in-situ* determination of oxygen isotope ratios of silicates and oxides: Geochimica et Cosmochimica Acta, v. 54, p. 1353-1357.

Shuster, D.L., Vasconcelos, P.M., Heim, J.A., and Farley, K.A., 2005, Weathering geochronology by (U-Th)/He dating of goethite: Geochimica et Cosmochimica Acta, v. 69, p. 659–673, doi:10.1016/j.gca.2004.07.028.

Valley, J. W., Kitchen, N., Kohn, M. J., Niendorf, C. R., & Spicuzza, M. J., 1995. UWG-2, a garnet standard for oxygen isotope ratios: strategies for high precision and accuracy with laser heating: Geochemica et Cosmochimica Acta, v. 59, p. 5223-5231.

Vasconcelos, P.M., Heim, J.A., Farley, K.A., Monteiro, H., and Waltenberg, K., 2013, $^{40}Ar/^{39}Ar$ and (U-Th)/He–$^{4}He/^{3}He$ geochronology of landscape evolution and channel iron deposit genesis at Lynn Peak, Western Australia: Geochimica et Cosmochimica Acta, v. 117, p. 283–312, doi:10.1016/j.gca.2013.03.037.

Wessel, P., and Müller, R.D., 2015, Plate Tectonics, *in Treatise on Geophysics, 2nd edition,* Schubert, Gerald ed., vol. 6, pp. 45-93.

Winnick, M. J., Caves J. K., and Chamberlain C. P., 2015, A mechanistic analysis of early Eocene latitudinal gradients of isotopes in precipitation: Geophysical Research Letters, v. 42, p. 8216– 8224, doi:10.1002/2015GL064829.

Yapp, C.J., 1987, Oxygen and hydrogen isotope variations among goethites (a-FeOOH) and the determination of paleotemperatures: Geochimica et Cosmochimica Acta, v. 51, p. 355–364, doi:10.1016/0016-7037(87)90247-X.

Yapp, C.J., 1991, Oxygen isotopes in an oolitic ironstone and the determination of goethite $\delta^{18}O$ values by selective dissolution of impurities: The 5M NaOH method: Geochimica et Cosmochimica Acta, v. 55, p. 2627–2634, doi:10.1016/0016-7037(91)90378-I.

Yapp, C.J., 2000, Climatic implications of surface domains in arrays of δD and $\delta^{18}O$ from hydroxyl minerals: Goethite as an example: Geochimica et Cosmochimica Acta, v. 64, p. 2009–2025, doi:10.1016/S0016-7037(00)00347-1.

Yapp, C.J., and Shuster, D.L., 2011, Environmental memory and a possible seasonal bias in the stable isotope composition of (U-Th)/He–dated goethite from the Canadian Arctic: Geochimica et Cosmochimica Acta, v. 75, p. 4194–4215, doi:10.1016/j.gca.2011.04.029.

Zachos, J., Pagani, M., Sloan, L., Thomas, E., and Billups, K., 2001, Trends, rhythms, and aberrations in global climate 65 Ma to present: Science, v. 292, p. 686–693, doi:10.1126/science.1059412.

APPENDIX A: SUPPLEMENTARY FIGURES AND TABLES

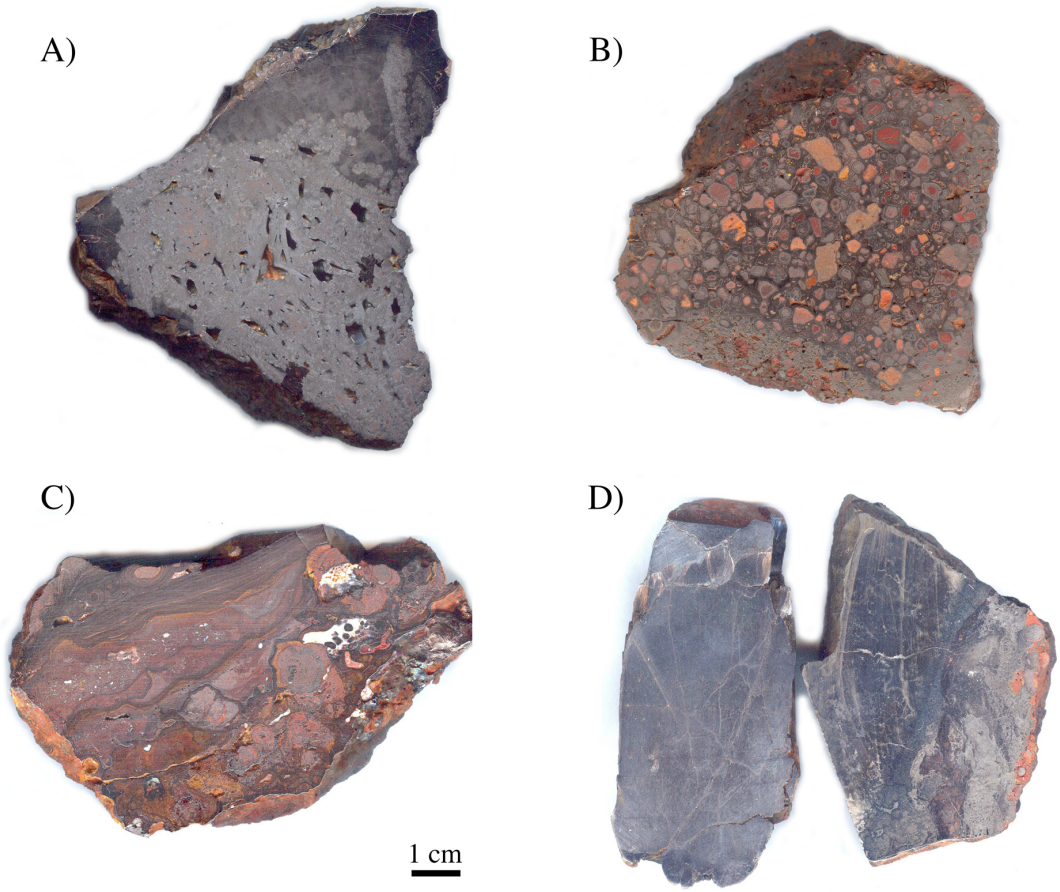

Supplementary Figure 1.1: Cut hand samples show characteristic textures of each locality from this study. (A) Botryoidal goethite crystals formed in cavities at Metawandy Valley; (B) pisolith and detrital hematite clasts supported in a goethite matrix at Yandi and (C) Lynn Peak; (D) elongate fibrous crystals of Roy Hill.

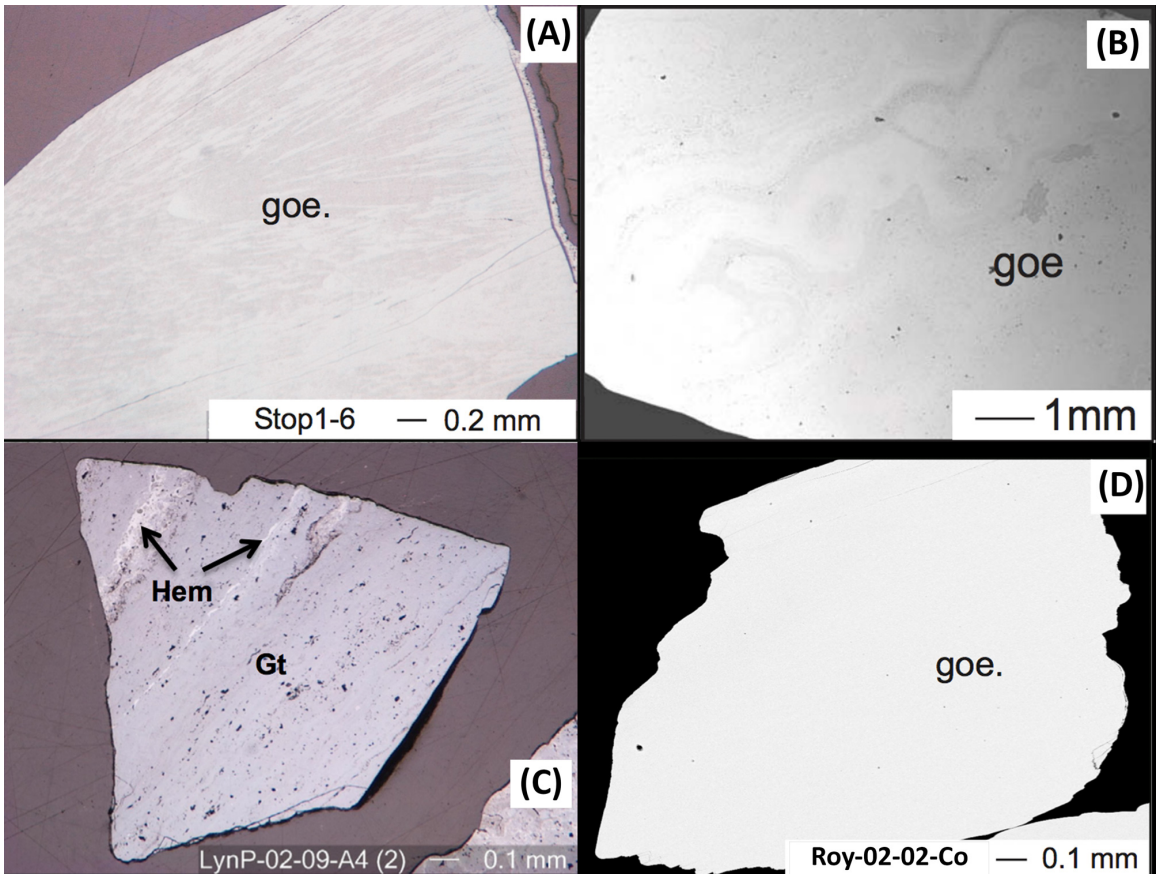

Supplementary Figure 1.2: (A) Representative reflected light photomicrograph of Metawandy Valley sample Stop-1-6, with fibrous crystal growth habit visible. (B) SEM image showing Yandi CID goethite, the darker zones represent greater Al substitution. See Supplementary Table 1.2 for measurements of Al concentration. (C) Reflected light photomicrograph of LynP-02-09-A4, showing the presence of both hematite (Hem) and goethite (Gt). Mixed mineralogy samples such as this one were not analyzed for (U-Th)/He ages or oxygen isotope composition. (D) A SEM image of Roy Hill sample Roy02-02-Co showing our preferred material for geochronology and oxygen isotope analysis: this goethite has uniform composition and low abundance of Al and Si (see Supplementary Table 1.2).

Supplementary Figure 1.3: Red circles show locations of IAEA GNIP collection sites used in this study to create a regional latitudinal gradient in the isotopic composition of rainwater.

Supplementary Table 1.1: Sample locations and brief descriptions

Sample	Northing	Easting	Host Rock	Depth
Stop1-6-A1	-22.747	116.612	Lateritic ferricrust	Surface
Stop1-6-A7	-22.747	116.612	Lateritic ferricrust	Surface
Stop1-6-A5	-22.747	116.612	Lateritic ferricrust	Surface
Stop1-1-A3	-22.747	116.612	Lateritic ferricrust	Surface
Yan-02-09	-22.721	119.080	CID	Surface
Yan-02-02	-22.721	119.080	CID	Surface
Yan-02-01-A	-22.721	119.080	CID	Surface
Yan-02-03	-22.721	119.080	CID	Surface
Yan-02-06	-22.721	119.080	CID	Surface
Yan-02-01-D1	-22.721	119.080	CID	Surface
LynP-02-09-A5	-22.50	-120.09	CID	Surface
LynP-02-09-A3	-22.50	-120.09	CID	Surface
LynP-02-09-A2	-22.50	-120.09	CID	Surface
LynP-02-09-A1	-22.50	-120.09	CID	Surface
Roy-02-02-Cy1	-22.452	119.930	Ferruginized colluvia	Surface
Roy-02-02-Cy2	-22.452	119.930	Ferruginized colluvia	Surface
Roy-02-02-Cy3	-22.452	119.930	Ferruginized colluvia	Surface
Roy-02-02-B5	-22.452	119.930	Ferruginized colluvia	Surface
Roy-02-02-Co3	-22.452	119.930	Ferruginized colluvia	Surface
Roy 02-02-C1	-22.452	119.930	Ferruginized colluvia	Surface
Roy-02-02-B1	-22.452	119.930	Ferruginized colluvia	Surface

Supplementary Table 1.2: Summary of electron microprobe analyses

Sample	Average Al (wt. %)	n	Min Al (wt. %)	Max Al (wt %)	Average Si (wt. %)	Min Si (wt. %)	Max Si (wt. %)
Stop-1-6-A1*	0.01	9	BD	0.05	1.02	0.87	1.20
Stop-1-6-A5*	0.11	4	0.09	0.14	1.71	1.67	1.79
Stop-1-6-A7*	0.05	5	0.05	0.10	1.38	1.79	1.89
Yan-02-01-A*	1.62	10	0.17	4.94	1.35	0.69	2.93
Yan-02-02*	3.62	6	2.53	4.95	0.76	0.67	0.87
Yan-02-03*	4.07	7	3.40	4.50	1.58	1.32	1.80
Yan-02-06*	0.45	15	0.11	1.45	0.56	0.08	0.88
Yan-02-09*	0.43	10	0.23	0.96	0.97	0.88	1.14
LynP-02-09-A1 †	0.64	23	0.11	2.37	0.29	0.15	0.97
LynP-02-09-A2 †	2.30	38	0.15	5.90	0.36	0.10	1.65
LynP-02-09-A3 †	1.08	20	0.26	3.24	0.42	0.13	2.79
Roy-02-02-B5*	0.03	30	0.00	0.05	0.84	0.68	0.99
Roy-02-02-B1*	0.02	30	0.00	0.03	0.86	0.69	0.95

*(Heim, 2007); † (Vasconcelos, 2013)
BD - below detection.
n - number of points analyzed.

Supplementary Table 1.3: New (U-Th)/He results

	Corrected Age (Ma)	±	U (ppm)	Th (ppm)	He (nmol/g)	Mass (µg)
Stop1-6-A1-A	4.5	0.5	5.62	0.16	0.13	72
Stop1-6-A1-B	5.6	0.6	5.15	0.09	0.14	49
Stop1-6-A1-C	4.4	0.4	5.54	0.15	0.12	64
Mean	**4.8**		**5.4**	**0.1**	**0.1**	
Stop1-6-A7-A	4.9	0.5	4.46	0.12	0.11	35
Stop1-6-A7-B	4.9	0.5	4.55	0.03	0.11	41
Mean	**4.9**		**4.5**	**0.1**	**0.1**	
Stop1-6-A5-A	7.5	0.8	5.23	0.11	0.20	19
Stop1-6-A5-B	9.6	1.0	4.94	0.07	0.24	32
Mean	**8.5**		**5.1**	**0.1**	**0.2**	
Stop1-1-A3-A	25.8	2.6	2.86	0.04	0.37	67
Stop1-1-A3-B	26.2	2.6	2.79	0.08	0.37	64
Mean	**26.0**		**2.8**	**0.1**	**0.4**	
Roy-02-02-Cy1-A	44.3	4.4	1.36	1.26	0.36	48
Roy-02-02-Cy1-B	48.3	4.8	1.28	1.27	0.38	53
Roy-02-02-Cy1-C	49.3	4.9	1.15	0.40	0.30	59
Mean	**47.3**		**1.3**	**1.0**	**0.3**	
Roy-02-02-Cy2-A	65.6	6.6	0.69	0.17	0.24	48
Roy-02-02-Cy2-B	60.8	6.1	0.75	0.26	0.25	35
Roy-02-02-Cy2-C	58.6	5.9	0.98	0.32	0.31	78
Mean	**61.7**		**0.8**	**0.3**	**0.3**	
Roy-02-02-Cy3-A	66.9	6.7	1.16	0.32	0.41	73
Roy-02-02-Cy3-B	61.1	6.1	1.55	0.21	0.49	69
Roy-02-02-Cy3-C	76.0	7.6	1.13	0.35	0.46	78
Mean	**68.0**		**1.3**	**0.3**	**0.5**	
Roy-02-02-B5-A	69.3	6.9	1.38	0.09	0.48	64
Roy-02-02-B5-B	66.7	6.7	1.18	0.08	0.40	58
Mean	**68.0**		**1.3**	**0.1**	**0.4**	
Roy-02-02-C1-A	70.5	7.1	1.19	0.04	0.42	63
Roy-02-02-C1-B	71.2	7.1	1.18	0.07	0.42	58
Roy-02-02-C1-C	69.8	7.0	1.22	0.05	0.43	51
Mean	**70.5**		**1.2**	**0.1**	**0.4**	
Roy-02-02-Co3-A	72.3	7.2	1.25	0.09	0.46	60
Roy-02-02-Co3-B	62.9	6.3	1.43	0.17	0.46	44
Roy-02-02-Co3-C	71.2	7.1	1.33	0.11	0.48	94
Mean	**68.8**		**1.3**	**0.1**	**0.5**	

Supplementary Table 1.4: All Laser Fluorination $\delta^{18}O$ results

Sample	Subsample	$\delta^{18}O_{VSMOW}$ (‰)	±
Stop1-6-A5		-0.370	0.024
Stop1-6-A1		-0.316	0.015
Stop1-6-A7		-0.207	0.033
		-0.228	0.028
		-0.107	0.041
Mean		-0.181	
Stop1-1-A3		-1.257	0.035
		-1.176	0.014
		-0.888	0.027
		-0.873	0.022
Mean		-1.049	
Yan-02-01-A		0.677	0.026
Yan-02-01-D1		0.727	0.055
Yan-02-02		0.703	0.022
Yan-02-03		0.976	0.028
Yan-02-09		0.627	0.027
Yan-02-06		-0.088	0.028
LynP-02-09-A1	A	-0.945	0.016
	A	-0.977	0.022
	B	0.324	0.019
	B	0.188	0.047
	B	-0.069	0.028
	C	-0.872	0.030
	D	-1.002	0.034
Mean		-0.479	
LynP-02-09-A2		-0.714	0.027
		-0.576	0.045
Mean		-0.645	

Supplementary Table 1. 4: All Laser Fluorination $\delta^{18}O_{VSMOW}$ results (continued)

Sample	Subsample	$\delta^{18}O_{VSMOW}$ (‰)	±
LynP-02-09-A3	A	0.569	0.037
	A	0.522	0.033
	B	-0.509	0.024
	B	-0.920	0.029
	C	-0.500	0.029
	C	-0.390	0.027
Mean		-0.205	
LynP-02-09-A5		0.613	0.038
		0.543	0.034
Mean		0.578	
Roy-02-02-Cy1		-1.855	0.030
		-1.387	0.048
		-1.231	0.060
		-1.434	0.040
Mean		-1.477	
Roy 02-02-C1		-1.037	0.039
		-1.189	0.040
Mean		-1.113	
Roy-02-02-Co3		-1.629	0.023
		-1.631	0.030
Mean		-1.630	
Roy-02-02-Cy2		-1.533	0.046
		-1.685	0.046
Mean		-1.609	
Roy-02-02-Cy3		-1.654	0.034
		-1.710	0.025
Mean		-1.682	
Roy-02-02-B5		-1.283	0.035
Roy-02-02-B1		-1.928	0.020

Supplementary Table 1.5: Large mass $\delta^{18}O_{VSMOW}$ measurements

Aliquot	Yield (%)	Mass (mg)	$\delta^{18}O_{VSMOW}$ (‰)	±
LynP-02-09-A1 (1A)	82.7	10.72	-0.615	0.018
LynP-02-09-A1 (1B)	89.8	6.96	0.024	0.038
LynP-02-09-A3 (1A)	80.4	11.04	0.270	0.019
LynP-02-09-A3 (1B)	81.3	7.52	0.031	0.015

Supplementary Table 1.6: Normal mass and large mass measurements comparison

A) LynP-02-09-A1	
Normal Mass Aliquots	
Number	7
Average $\delta^{18}O$ (‰)	-0.479
Total mass analyzed (mg)	10.78
$\delta^{18}O$ (‰) High Value	0.324
$\delta^{18}O$ (‰) Low Value	-1.002
Range $\delta^{18}O$ (‰)	1.326
Large Mass Aliquots	
Number	2
(Mass weighted) Average $\delta^{18}O$ (‰)	-0.363
Total mass analyzed (mg)	17.68
Difference between average of normal mass and large mass $\delta^{18}O$ (‰)	**0.116**
B) LynP-02-09-A3	
Normal Mass Aliquots	
Number	6
Average $\delta^{18}O$ (‰)	-0.205
Total mass analyzed (mg)	9.02
$\delta^{18}O$ (‰) High Value	0.569
$\delta^{18}O$ (‰) Low Value	-0.920
Range $\delta^{18}O$ (‰)	1.489
Large Mass Aliquots	
Number	2
(Mass weighted) Average $\delta^{18}O$ (‰)	0.173
Total mass analyzed (mg)	18.56
Difference between average of normal mass and large mass $\delta^{18}O$ (‰)	**0.378**

Supplementary Table 1.7: (U-Th)/He age to paleolatitude conversion rates

Age Range (Ma)	Centimeters per year	Plate direction (azimuth degrees)	Kilometers north per 10 Ma
0 - 10	7.5	15	724.4
10 - 20	7	15	676.1
20 - 30	8	15	772.7
30 - 40	6	20	563.8
40 - 50	3	30	259.8
50 - 60	3	50	192.8
60 - 75	1	-60	50.0

Supplementary Table 1.8: Compiled IAEA meteoric water data from South Pacific

Latitude	Long-term Mean* $\delta^{18}O_{VSMOW}$ (‰)	Standard Deviation	GNIP code
-21.23	-3.77	0.67	9184300
-23.70	-2.90	1.72	9432600
-27.47	-3.49	0.89	9457600
-31.94	-3.11	0.34	9460800
-31.99	-3.74	0.47	9460801
-34.93	-4.01	0.47	9467500
-35.12	-4.50	0.39	9301100
-37.81	-4.63	0.63	9486800
-40.68	-3.59	0.6	9495400
-43.02	-5.04	1.31	9497001
-46.43	-6.89	0.41	9384400

The Global Network of Isotopes in Precipitation (GNIP) is part of the International Atomic Energy Agency's (IAEA) efforts to monitor the distribution and transportation of rare isotopes across our planet. Long-term mean refers to the mean of the annual mean rainwater $\delta^{18}O$ over the lifespan of the collection site, which range between 6 and 54 years.

Chapter 2

INTRACRYSTALLINE SITE PREFERENCE OF OXYGEN ISOTOPES IN GOETHITE: A POTENTIAL SINGLE-MINERAL GEOTHERMOMETER

ABSTRACT

Studies of the stable isotope geochemistry of hydroxyl-bearing silicate minerals, such as kaolinite, muscovite and chlorite, have demonstrated differences in oxygen isotopic composition between structurally-non-equivalent crystal sites within a single mineral (Hamza and Epstein, 1980). First-principle predictions indicate the isotopic composition of non-equivalent oxygen sites within goethite depends on mineral growth temperature and thus goethite may be suitable for single-phase geothermometry. Two fractions of oxygen that differ from one another in isotopic composition were extracted from goethtite using a stepped-heating, furnace fluorination procedure. Using synthetic goethite precipitates, grown at known environmental conditions, we demonstrate that $\Delta^{18}O_{bulk\text{-}dehydroxylation}$ (where $\Delta^{18}O_{bulk\text{-}dehydroxylation} = \delta^{18}O_{bulk} - \delta^{18}O_{dehydroxylation}$) has a strong temperature dependence suitable for geothermometry, which in turn can be used to constrain the isotopic composition of ancient fluieds from which goethite formed in equilbirium with. Finally, we applied the temperature calibration derived from the synthetic goethite suite to eight natural goethites and calculated formation temperatures between 11 and 39 °C, values within the broad geologic expectations for these goethites.

I. INTRODUCTION

Paleoclimate records derived from lake deposits, stalagmites, soil carbonates, and siliciclastic sediments provide valuable archives of continental climatic variability in the geologic past. However, deposits of these types limit our spatial and temporal sampling to depositional environments. Weathering reactions triggered by meteoric water-rock interactions commonly produce Fe-oxyhydroxides, mainly goethite (FeOOH), at the Earth's surface, driven by dissolution of ferrous-iron bearing phases such as carbonates, silicates and oxides. The stable isotopic composition of these Fe-oxyhydroxides largely reflects that of meteoric water, thus providing a valuable target for producing paleo-hydrologic and climatic records in previously unsampled regions and/or times in Earth's history.

Goethite (FeOOH) is a ubiquitous mineral in many continental surficial environments, and its presence alone places constraints on climatic characteristics (Alpers and Brimhall, 1988). Goethite contains both hydrogen and oxygen, the stable isotope compositions of which can be used to interpret formation temperatures and water sources, especially when the two stable isotope systems are combined (Yapp, 1987, 1993, 1998, 2000; Girard et al., 2000; Pack et al., 2000; Poage et al., 2000; Yapp and Shuster, 2011; Miller et al., 2017; Yapp and Shuster, 2017). However, temperatures or water composition derived from goethite using the hydrogen, oxygen, or paired isotope system are made more difficult by the necessity of external constraints on environmental conditions at time of goethite formation. In seeking to unravel previously unknown paleoenvironmental conditions, investigators rarely have the luxury of utilizing independently known

constraints on environmental conditions. Rather, stable isotope paleoclimate studies rely on assumptions to translate measured compositions into environmental records of interest.

In an attempt to combat the aforementioned limitations, investigators have pioneered innovative lines of research into multiply substituted isotopologues (i.e., 'clumped' isotope species) and non-random distributions of isotopes between non-equivalent atomic sites (i.e., site-specific fractionation effects). In the case of clumped isotopes, there is typically an excess of multiply substituted isotopologues in a given species, at thermodynamic equilibrium, compared to a purely random distribution of all isotopologues (Eiler, 2007). The magnitude of this clumping excess is a function of temperature and, in the case of minerals forming from water-rock interactions, independent of the composition (i.e., $\delta^{18}O$) of the fluid that the new-formed mineral is in equilibrium with (Eiler, 2007). Advancements in mass spectrometry allowed for precise and accurate measurement of multiply substituted isotopologues and resulted in the development of the powerful clumped isotope thermometer for many phases, including calcite, carbonate-apatite, and dolomite (Passey and Henkes, 2012; Henkes et al., 2014; Stolper and Eiler, 2015; Lloyd and Eiler, 2017). Determining mineral formation temperature, independent of parent fluid isotopic composition, has proved an invaluable tool for advancing the study of continental paleoclimate (Quade et al., 2013; Snell et al., 2014; Tobin et al., 2014; Fan et al., 2018; Lechler et al., 2018).

A complementary approach to isotopic clumping is that of site-specific fractionation effects. The temperature dependence of site-specific fractionation can be taken advantage of in species with multiple, non-equivalent sites to yield formation

temperatures independent of the isotopic composition of the parent fluid. Studies of the stable isotope geochemistry of hydroxyl-bearing silicate minerals (e.g. kaolinite, muscovite, chlorite) have demonstrated differences in oxygen isotopic composition between structurally non-equivalent crystal sites within a single mineral (Hamza and Epstein, 1980). Intracrystalline site preference for oxygen isotopes in smectite has been demonstrated to display temperature dependence (Delgado and Reyes, 1996). Hydrogen intracrystalline site preference has also been observed in copper sulfate pentahydrate (Kita and Matsuo, 1981) and borax (Pradhananga and Matsuo, 1985).

Since goethite also has structurally non-equivalent oxygen sites, this common weathering product should be suitable for single-phase geothermometry. Yapp (1990; 2003; 2015) has shown that two or more fractions of oxygen that differ from one another in oxygen isotopic composition can be extracted from goethite. In addition, theoretical predictions indicate there should be an easily measurable temperature dependence of intracrystalline oxygen isotope site preference (Blanchard et al., 2015). Other investigators have even explicitly suggested the intracrystalline site preference in goethite could be used as a geothermometer (Oerter et al., 2017). Yet, we are unaware of any successful attempts to implement the intracrystalline site preference of oxygen isotopes in goethite as a single-phase geothermometer. Here, we present measurements from a suite of synthetic goethites, precipitated under known environmental conditions, which demonstrate the viability of goethite intracrystalline oxygen isotope geothermometry. We then applied this initial calibration to eight natural goethites, which yield geologically plausible intracrystalline temperatures.

II. BACKGROUND

Goethite often forms in acidic, iron-bearing soils and oxic ground waters, where reduced iron in solution experiences oxidation followed by precipitation of this extremely insoluble phase (Yapp, 2001). Weathering reactions triggered by meteoric water-rock interactions commonly set the stage for goethite formation in surface and near-surface environments as they dissolve ferrous-iron-bearing phases (carbonates, silicates, oxides). For this reason, the stable isotope composition of goethite largely reflects that of meteoric waters, which depends on several parameters of interest to paleoenvironmental reconstructions, including latitude, temperature, aridity, and elevation.

The work of Yapp (1987, 1993, 1997, 2000) establishes that the stable isotope composition of goethite in surficial environments is consistently offset from that of local meteoric waters. The stable oxygen and hydrogen isotope composition of most meteoric waters, in turn, generally conforms to a line in a plot of δD vs. $\delta^{18}O$ (i.e. the meteoric water line, Figure 2.1):

$$\delta D = 8 \times \delta^{18}O + 10 \quad (1)$$

where $\delta = (R_{sample}/R_{std} - 1) * 1000$, and $^{18}R=[^{18}O]/[^{16}O]$ and $^{D}R = [D]/[H]$, with 'std' denoting to which standard all measurements are referenced. For this paper, all oxygen and hydrogen measurements are referenced to VSMOW. Figure 2.1 also illustrates the relationship between the meteoric water line and stable isotope composition of goethite,

where goethites produce an array that is offset yet generally parallel to the meteoric water line. This meteoric water line trend is largely controlled by fractionations associated with condensation of water from saturated air masses — rain in low latitude marine and coastal environments lies at the upper right end, near (though not exactly coincident with) the compositional range of seawater ($\delta^{18}O_{VSMOW} = 0 \pm 1$ and $\delta D_{VSMOW} = 0 \pm 5$), and compositions move down and to the left along this trend as a result of any process that promotes further net condensation: climatic cooling; ascent to higher altitude; migration of an air mass to higher latitude or across a large land mass; or more complex large scale weather patterns such as monsoons.

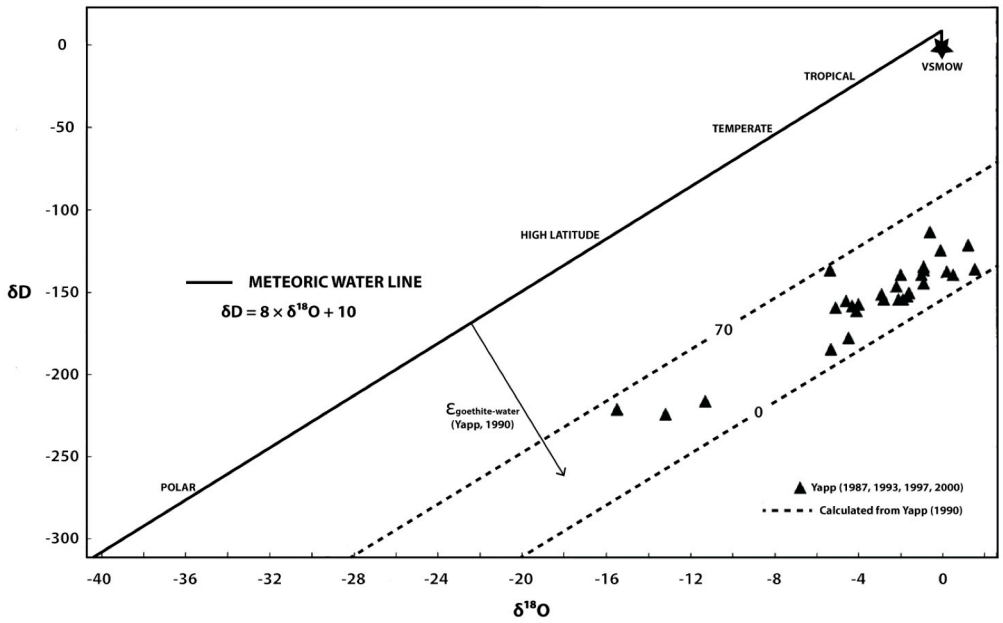

Figure 2.1: Meteoric water line is shown in solid black. VSMOW (black star) represents the composition of the ocean. Tropical meteoric waters are close to the isotopic composition of the ocean, and progressive distillation causes the residual water to become depleted in heavy isotopes. The dashed lines represent 0 °C and 70 °C goethite formation isotherms with data from natural, continental goethites shown as black triangles.

Although several factors may contribute to the composition of a given water, with sufficient contextual information it is possible to use these dependencies to interpret the stable isotope compositions of water or ice — or goethite that grows from meteoritic waters — as records of past climatic warming or cooling (Zachos et al., 2001), paleoaltimetry (Rowley and Garzione, 2007), paleolatitude (Fricke and Wing, 2004) or monsoonal strength and/or the location of a monsoonal front (Yuan et al., 2004). These principles form the foundation from which the Western Australia goethite stable oxygen isotope record was interpreted in the previous chapter.

However, the previous chapter focused on secular variation in isotopic composition of goethite under rather unique environmental conditions; the samples formed over a narrow range of temperatures, in mildly acidic soil conditions near the earth's surface, and without significant secular changes to the topographically controlled distillation of atmospheric water masses. The same circumstances are not attainable in the vast majority of paleoenvironmental studies, which ask questions requiring the interpretation of absolute stable isotope compositions that can in turn be used to produce records of interest, such as tracking changes in temperature when water source composition may simultaneously vary. This study aims to address this limitation by proposing a method that can simultaneously determine formation temperature and, from that, back out the isotopic composition of the parent fluid.

As previously discussed, the translation of bulk mineral isotopic compositions (whether hydrogen, oxygen, or the paired system) to paleoenvironmental conditions of interest requires external knowledge of both environmental and geochemical conditions at

time of mineral formation. Studies utilizing goethite to constrain the composition of water sources (in the case of goethite, often considered to be meteoric) have either assumed a formation temperature (Bird et al., 1993; Pack et al., 2000; Poage et al., 2000) or implemented the paired hydrogen-oxygen isotope system. Equation 2 expresses the expected relationship between the hydrogen and oxygen isotopic composition of goethites formed from meteoric water:

$$\delta D_{goethite} = 8\ ({}^{D}\alpha / {}^{18}\alpha)\ \delta^{18}O_{goethite} + 1000\ [8\ ({}^{D}\alpha / {}^{18}\alpha) - 1]\ - 6990\ {}^{D}\alpha, \qquad (2)$$

where ${}^{D}\alpha$ and ${}^{18}\alpha$ are the goethite-water fractionation factors defined as:

$${}^{D}\alpha_{goethite\text{-}water} = (D/H)_{goethite} / (D/H)_{water}, \qquad (3)$$

and

$${}^{18}\alpha_{goethite\text{-}water} = ({}^{18}O/{}^{16}O)_{goethite} / ({}^{18}O/{}^{16}O)_{water} \qquad (4)$$

$$= (1000 + \delta^{18}O_{goethite}) / (1000 + \delta^{18}O_{water}). \qquad (5)$$

Many mineral-water systems have fractionation factors that are dependent on temperature and this relationship can be generalized as:

$$1000 \ln \alpha_{mineral\text{-}water} = (A / T^2) + B \qquad (6)$$

where A and B are constants specific to the isotope and mineral-water system and T is the equilibrium temperature (K). Equation 2 has been implemented to constrain paleotemperatures in lateritic soils (Girard et al., 2000), oolitic ironstones (Yapp, 1993; 1998), and marine hydrothermal goethite (Yapp, 2000). However, this method of goethite geothermometry makes a number of assumptions: (a) the parent fluid of interest has a composition corresponding exactly to the meteoric water line (Equation 1), (b) water-rock ratios are sufficiently large that no compositional change occurs as goethite precipitation progresses, (c) goethite-water fractionation factors for oxygen and hydrogen are the same for all environments with the same temperature. The first two assumptions may very well hold true in many environments where goethite forms, but it cannot be known a priori. Accompanying the third assumption is the fact the temperature dependence of hydrogen and oxygen goethite-water fractionation factors, along with the associated dependency of this fractionation on such conditions as pH and trace element substitution, is not well-constrained (Yapp and Pedley, 1985; Yapp, 1987, 1990, 1993; Muller et al., 1995; Zheng 1998; Bao and Koch 1999; Yapp, 2007, 2012). For these reasons, the development of a goethite geothermometer that is independent of the isotopic composition of the parent fluid, the pH of that fluid, or the abundance of trace element substitution within goethite (e.g. Al for Fe), would be tremendously useful for constructing continental paleoclimate records.

III. THEORETICAL CONSIDERATIONS

Here, we focus on the theoretical prediction of equilibrium thermodynamic fractionations involving intracrystalline oxygen isotope variations in goethite (Section 3.1) and kinetic isotope effects associated with the dehydroxylation of goethite (Section 3.2).

3.1 Theoretical prediction of equilibrium thermodynamic fractionations

The prediction of equilibrium thermodynamic fractionations applies the first-principles calculations for reduced partition functions of goethite from Blanchard et al. (2015) to determine the theoretical intracrystalline oxygen isotope site preference. We use the reduced partition function ratios (β-factors) for oxygen in goethite, which were calculated by Blanchard et al. (2015) using density functional theory to model the vibrational frequencies of the fundamental modes of this phase. Two sets of β-factors were predicted by Blanchard et al. (2015), one using a generalized gradient approximation (GGA) and a second using GGA with a Hubbard U correction. The results vary by only 4% and thus only the β-factors predicted using the GGA plus Hubbard U correction are utilized here. We can translate the predicted β-factors into a fractionation factor (α) using Equation 7:

$$10^3 \ln \alpha_{A\text{-}B} = 10^3 \ln \beta_A - 10^3 \ln \beta_B, \quad (7)$$

For many applications, *A* and *B* would denote two phases of interest. For our purposes, *A* and *B* are the oxygen reservoirs of two structurally non-equivalent sites within the goethite crystal. The results of this first-principles calculation for oxygen isotope site preference in goethite are shown in Figure 2.2. This prediction refers to three populations of oxygen: 'O' being the 50% of oxygen atoms exclusively coordinated to three Fe atoms, 'hydroxylated' being the remaining 50% of oxygen atoms which are coordinated to three

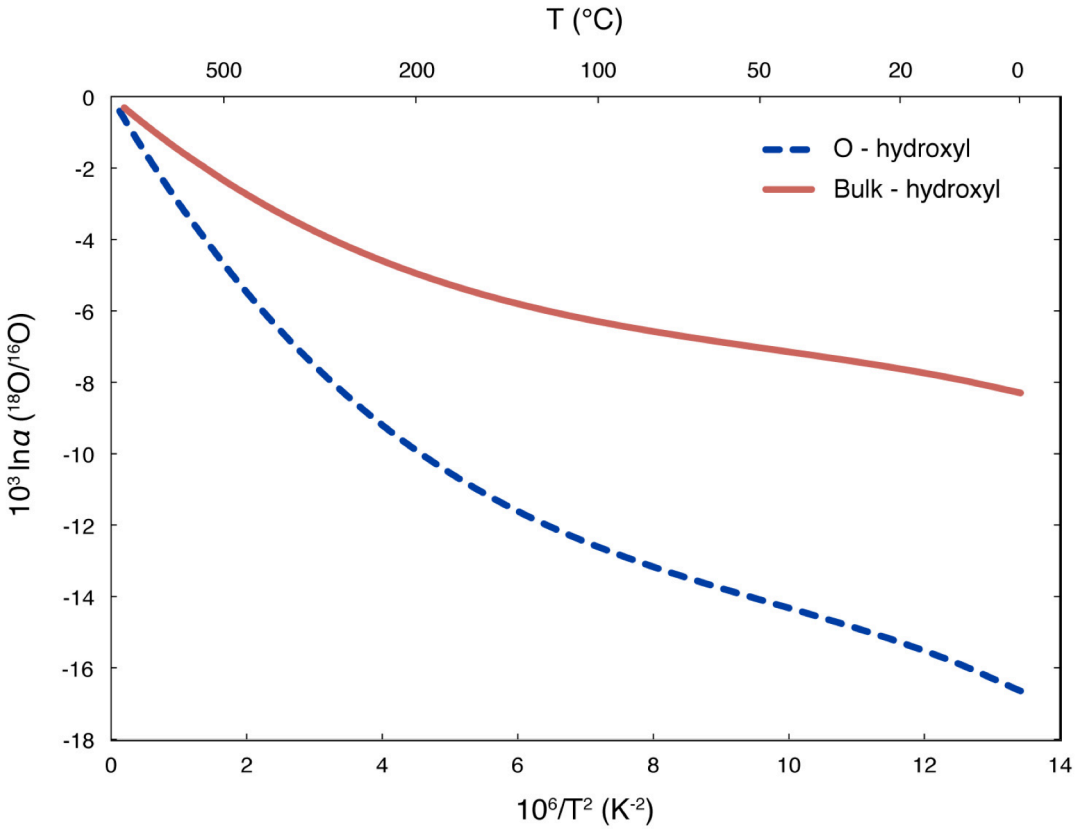

Figure 2.2: Temperature dependence of oxygen isotope fractionation ($10^3 \ln\alpha$) of structurally non-equivalent oxygen populations in goethite using the oxygen β-factors of Blanchard et al. (2015). Here, 'O' refers to the population of oxygen only bound to iron atoms, while hydroxyl refers to oxygen that is additionally bound to hydrogen. 'Bulk' refers to all the structural oxygen atoms within goethite.

Fe atoms and an additional H atom, and the 'bulk' being the combination of both populations (i.e. all structural oxygen). Note that the 'hydroxylated' population represents all oxygen atoms associated with hydroxyl sites, while the empirically measured 'dehydroxylation' population of this study only represents those oxygen atoms collected during dehydroxylation.

Figure 2.2 shows evidence for isotopically distinguishable populations of oxygen within goethite, with heavier isotopes concentrating into the hydroxylated sites of goethite at thermodynamic equilibrium. Since most fractionations are near unity, $10^3 \ln \alpha_{A\text{-}B}$ coincides numerically with the isotope fractionation shift expressed in permil (‰) such that:

$$\Delta_{A\text{-}B} = \delta^{18}O_A - \delta^{18}O_B \cong 10^3 \ln \alpha_{A\text{-}B}, \quad (8)$$

Therefore, we use Equation 8 to make a prediction of what the $\Delta^{18}O_{\text{bulk-hydroxylated}}$ in goethite may be (while remaining cognizant this value will not be equal to our observed values due to the kinetic isotope effect associated with dehydroxylation). Therefore, at 25° C, we predict a $\Delta^{18}O_{\text{bulk-hydroxylated}} \cong$ -7.5‰. A -7.5‰ difference between bulk and hydroxylated oxygen populations would be very easily measurable, should that hydroxylated oxygen population (or some reproducible portion) be recoverable.

3.2 Kinetic isotope effects associated with the dehydroxylation of goethite

All experimental results will utilize the isotopic composition of oxygen collected from dehydroxylation such that:

$$\Delta^{18}O_{\text{bulk-dehydroxylation}} = \delta^{18}O_{\text{bulk}} - \delta^{18}O_{\text{dehydroxylation}}. \quad (9)$$

Here, we must reiterate that Section 3.1 is the sole location where we reference $\Delta^{18}O_{\text{bulk-hydroxylated}}$. While the intracrystalline site preference for oxygen isotopes could be defined a number of ways, we define it as $\Delta^{18}O_{\text{bulk-dehydroxylation}}$ due to the nature of our method for measuring the two non-equivalent oxygen sites. In our procedure (see Methods section for details), we collected the oxygen freed by the dehydroxylation of goethite (i.e. the dehydration from goethite to hematite), then fluorinated the yield and measured the resulting oxygen isotopic composition. The reason this is brought up in advance of the Methods section is here we consider the possibility of a kinetic isotope effect associated with the dehydroxylation of goethite. Equation 8 depicts a generalized goethite dehydration scheme:

$$2(FeOOH) \rightarrow [\ Fe_2O_3^* + H_2O^*\ ] \rightarrow Fe_2O_3 + H_2O \quad (10)$$

goethite → transition state → hematite + water

In this reaction sequence, dehydration is proposed to occur progressively as a migrating transition state volume of 'proto-hematite' progresses from smaller to larger crystallites (Wolska and Schwertmann, 1989; Gualtieri and Venturelli, 1999; Yapp, 2003). The rate of the dehydration reaction depicted in Equation 8 likely plays an important role in controlling the oxygen isotopic composition of the water collected during dehydroxylation (i.e. it imparts a kinetic isotope effect). Isotope effects associated with the rate of dehydration may yield variation in the isotopic composition of the water collected from goethite dehydroxylation due to variable exchange between oxygen freed during dehydroxylation, oxygen temporarily held onto by the proto-hematite, and the oxygen preserved within the final hematite. For these reasons it is imperative that a consistent methodology for the liberation and collection of hydroxyl group oxygen be implemented.

As evidenced in Equation 10, 50% of the structural oxygen within goethite is initially associated with the hydroxyl group, yet only half of that hydroxylated oxygen is liberated during dehydration. The remainder is incorporated into the newly formed hematite. One would expect a strong fractionation of oxygen isotopes to occur during this transfer of atoms depicted in Equation 8. Isotope effects such as these have long been observed in other methodologies for stable isotope analyses, such as during the acid digestion of carbonates (McCrea, 1950). For this reason, we emphasize that our definition for $\Delta^{18}O$ involves the difference between $\delta^{18}O_{bulk}$ and $\delta^{18}O_{dehydroxylation}$ (i.e. $\delta^{18}O$ of water collected during dehydroxylation). One would expect $\delta^{18}O_{dehydroxylation}$ to be different from that of $\delta^{18}O_{hydroxyl}$.

IV. MATERIALS

This study utilizes two suites of goethite samples. The first suite consists of synthetic goethites precipitated under controlled environmental conditions. This suite is aimed at investigating the temperature dependence of intracrystalline oxygen isotope site preference in goethite under known conditions of formation. The second is comprised of a variety of natural goethites, selected for their own variable formation conditions, which should manifest as variable $\Delta^{18}O_{bulk\text{-}dehydroxylation}$.

4.1 Synthetic goethite suite

The laboratory-precipitated goethite suite was synthesized by Albertus Mostert as part of his PhD thesis at University of Queensland and provided to this study by Paulo Vasconcelos. Two sets of goethite precipitates were synthesized: at high-pH (>12) and low-pH (<2) (Mostert, 2014). At each pH condition, a stoichiometric and Al-doped (Fe:Al – 90:10 mol ratio) goethite was synthesized at 22, 40, and 70 °C (Mostert, 2014). The high-pH precipitates were grown from Fe-salts with KOH as the base following the methods of Glasauer et al. (1999). The low pH precipitates were grown from Fe-salts with HNO_3 as an acid following the methods of Mørup et al. (1983). Each solution was aged for 10 weeks to ensure complete transformation from ferrihydrite intermediate to final goethite precipitate (Mostert, 2014). Precipitates were analyzed by high-resolution synchrotron X-ray diffraction and found to be pure goethite (or Al-goethite in the case of the Al-doped precipitates) and free of amorphous material. The complete details of the precipitation procedure can be found in Mostert (2014).

4.2 Natural goethite suite

Two groups of natural goethites are utilized in this study. The first is a suite of secondary iron deposits produced by weathering reactions, comprised of Western Australia goethite samples from the previous chapter. The Western Australia goethite-bearing ironstones are composed of massive, chemically pure iron oxyhydroxides. These formations are often up to 93-96% FeO, with 1-2% Al_2O_3 and 3-5% SiO_2 (Ramanaidou et al., 2003). Potential mineral contaminants include kaolinite, quartz, opal, and, more rarely, Mn oxides, typically filling fractures, voids, or root cavities. Detrital grains such as quartz, ilmenite, rutile, and zircon can also occur, but are rare. In addition, detrital (mostly BIF-derived) hematite occurs within the secondary iron oxides. Careful sub-sampling of coarsely crystalline goethite growth bands allows the majority of contaminants to be avoided. Unlike in (U-Th)/He dating, where, for example, the presence of a single zircon rich in U and Th can render an age determination useless, contaminants on the ~1% level are unlikely to have a significant effect on oxygen isotope analyses. Goethite from the Roy Hill weathering profile, utilized as a standard in this study, is dominated by massive (up to 10 cm) fibrous crystals of stoichiometrically pure goethite.

This study also utilizes two morphologically unique goethite samples interpreted to be of hydrothermal origin. These goethites display massive, bladed crystal habit (Figure 2.3a and 2.3b) and form on large groups of smoky quartz crystals. This morphology is entirely different from the goethites produced by weathering reactions at or near the Earth's surface. These two samples were collected in miarolitic cavities of pegmatites in the Lake George quadrangle of the Pikes Peak granite batholith of the Colorado Front

Range, approximately 60 km west of Colorado Springs (Barry, 2001). The Pikes Peak granite is a 1060-1090 Ma batholith interpreted to have been emplaced at a shallow depth of 5 km (Barker et al., 1975).

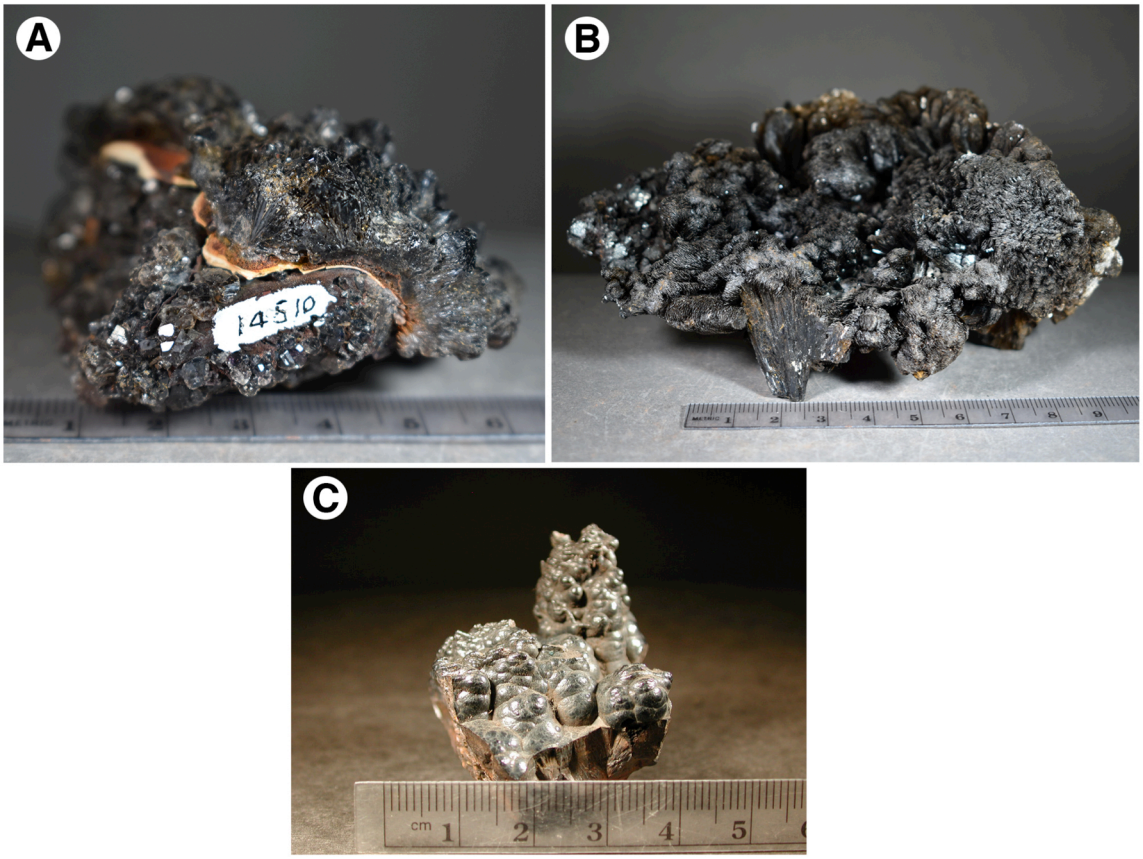

Figure 2.3: Photos of pegmatite-associated goethites from the Lake George quadrangle, Pikes Peak batholith, Colorado. DMNH-14510 (Panel A) and DMNH-10029 (Panel B) both display prismatic morphology, where radiating blades of goethite are growing on quartz crystals. Sample DMNH-14510 has mm to cm-scale smoky quartz intermixed with goethite. Sample DMNH-10029 has goethite growing onto top of massive quartz crystal faces. CIT-8809 (Panel C) displays botryoidal morphology more typical of goethite formed from weathering reactions.

The batholith hosts thousands of small pegmatites, many of which yield museum quality specimens of quartz, microcline (amonazite), topaz, fluorite, goethite, and other rare minerals (Simmons et al., 1987; Unruh et al., 1995; Barry, 2001; Gagon et al., 2004).

Multiple generations of crystallization within the miarolitic cavities are interpreted to have taken place (Levasseur, 1997). Fluid inclusion studies of primary fluorite and quartz indicate crystallization temperatures between 340 and 500 °C (Levasseur, 1997; Berry, 2001). Inclusions within secondary quartz and fluorite in the northern South Platte district of the Pikes Peak batholith have temperatures between 80 and 150 °C (Gagnon et al., 2004). Fluid inclusions within secondary quartz intergrown with goethite indicate these late stage crystals formed at ~40 °C (Berry, 2001). Regional uplift of the Colorado Front Range, associated with the Laramide Orogeny, began locally at 70 Ma (Kelly, 2002). If the goethite is co-genetic with quartz as the intergrown relationship suggests, these late stage crystals may have formed post-Laramide. These two hydrothermal goethite samples (DMNH-14510 and DMNH-10029) were obtained from the Denver Museum of Natural History mineral collection. These samples were selected for the likelihood these goethites may record intracrystalline thermometry temperatures above that associated with weathering reactions at the Earth's surface.

We also analyzed a third sample from the Pikes Peak region. This sample was sourced from the Caltech mineral collection (CIT-8809) and is only identified as "Pikes Peak Goethite." Many of the museum quality goethite specimens associated with Pikes Peak come from the Lake George pegmatites; however, we cannot be certain of this sample's exact locality. CIT-8809 has a botryoidal morphology (Figure 2.3c), typical of goethite produced by weathering reactions. One surface of the sample has a stalactitic form suggesting this goethite grew in a void space.

V. METHODS

This study implemented three related fluorination procedures for the measurement of stable oxygen isotopes of goethite. This trio of methods was necessary both because we aimed to extract two chemically unique populations of oxygen and due to the extremely fine-grained nature of our synthetic precipitates. Since Fe-oxyhydroxides easily adsorb atmosphere-derived water onto their surfaces, this potential contaminant reservoir of non-structural oxygen was removed following the goethite pre-treatment methods of Yapp (1987). The laser fluorination method is suitable for the determination of bulk goethite stable oxygen isotope compositions when samples are sufficiently coarse such that structural oxygen is not partially reacted during this pre-treatment procedure. However, laboratory goethite synthesis produces goethite crystallites no greater than 1 micron in size, and often less than 30 nm in size (Mostert, 2014). Exceptionally fine materials were too reactive for laser fluorination and therefore required a different analysis method. To work around this difficulty, we resurrected a fluorination method utilizing a resistance-heated nickel reaction cell (Taylor and Epstein, 1962; Clayton and Mayeda, 1963). While cumbersome compared to laser fluorination, a resistance-heated furnace proved the only workable method for analyzing the oxygen isotope composition of synthetic powders. The structural oxygen collected during dehydroxylation was analyzed by a modified resistance-heated furnace method. The details of these three methods are described below.

5.1 Bulk $\delta^{18}O$ by laser fluorination

The methods for measurement of stable oxygen isotopes of bulk goethite by laser fluorination are identical to those described in the previous chapter. Briefly, samples were

heated to 80 °C under vacuum overnight and then pretreated with BrF_5 vapor at room temperature to remove adsorbed water (Yapp 1987). Following pre-treatment, ~2 mg aliquots of sample material were irradiated with a 10.6 μm CO_2 laser while exposed to BrF_5 vapor, driving fluorination reactions that produced O_2, HF, and iron fluoride. The O_2 was isolated and purified by cryogenic separation and passage over hot mercury. At this stage, the gas was converted to CO_2 by passage over hot graphite and then analyzed by dual inlet gas source mass spectrometry in that form. The final CO_2 pressure yielded from the sample fluorination reaction and subsequent CO_2 conversion was measured. This measurement was used to check that a sample was completely fluorinated, as partial sample fluorination may induce isotopic fractionation (Valley et al., 1995). Furthermore, yields above that associated with complete sample reaction are indicative of incomplete removal of adsorbed species during pre-treatment. Laser fluorination analyses were discarded when the CO_2 yield differed from the mass-based prediction by more than 10%. A garnet standard (UWG-2) was measured daily to monitor the accuracy of each session's measurements. When the measured $\delta^{18}O$ of the standard varied from the known value, a correction was applied, typically ~0.10‰ (Valley et al., 1995).

5.2 Bulk $\delta^{18}O$ by resistance-heated furnace

Laser fluorination effectively rendered the methods of Taylor and Epstein (1962) and Clayton and Mayeda (1963) defunct. However, for the reasons outlined above, these methods were implemented to measure the bulk oxygen isotopic composition of synthetic goethite powders. Several modifications to the existing Caltech laser fluorination line were required and are shown in Figure 2.4. In this new configuration, a nickel reaction

vessel is prefluorinated to develop a metal fluoride coating, which protects the nickel from further reaction during sample heating (Taylor and Epstein, 1962). Since this metal fluoride coating is highly reactive with water, sample introduction must be accomplished without exposing the reaction vessel to atmosphere (Taylor and Epstein, 1962). To accomplish this, we bleed N_2 through a U-trap held at liquid nitrogen temperature into our

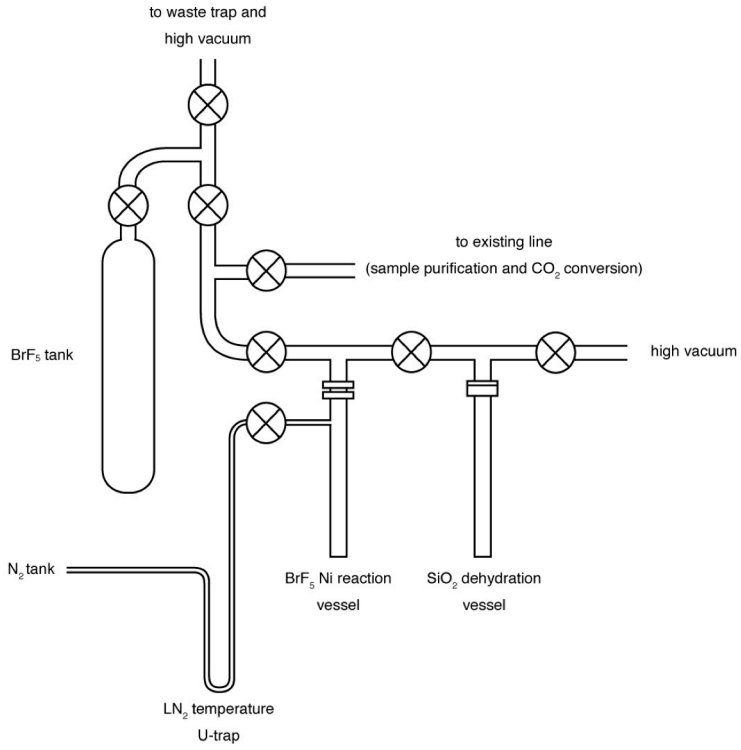

Figure 2.4: Schematic of BrF_5 reaction apparatus and dehydroxylation vessel. A Ni vessel and electrically heated, resistance furnace was used for bulk fluorination of goethite samples. A N_2 bleed was installed below the Ni reaction vessel ferrule connection to prevent atmospheric derived water from contaminating vessel surfaces. Dehydroxylation reactions were performed using an electrically heated, resistance furnace and quartz vessel.

Ni reaction vessel (Figure 2.4). This allowed for a positive pressure of dry N_2 to flush the reaction vessel for the short duration the line was open to atmosphere during sample

loading. Due to this positive pressure of dry N_2, samples were weighed into pure silver capsules and loosely pinched shut to prevent loss of any fine-grained material.

Once the sample was loaded into the Ni reaction vessel, the N_2 bleed was closed and the reaction vessel outgassed for 1 hour at room temperature. As an initial treatment, the nickel reaction vessel was held at liquid nitrogen temperature and an aliquot of BrF_5 was frozen into the vessel. The vessel was then warmed to room temperature for 10 minutes to react away any adsorbed water before transferring the reaction products and any unreacted BrF_5 to the waste trap. Following this, an electrical-resistance heated furnace was placed around the nickel reaction vessel and heated to 80° C, the held at that temperature overnight (typically 12-14 hours) with the vessel open to the high vacuum pump. This was hot enough to remove the majority of adsorbed water without inducing sample dehydration. After the overnight bake, a second BrF_5 treatment was performed, this time for 20 minutes. Finally, a 20-minute, room temperature, procedural blank was run in which O_2 produced by BrF_5 reagent was purified and converted to CO_2. If the procedural blank measured above 1 torr on the manometer, a second blank was performed.

After the procedural blank, the reaction vessel was evacuated and then charged with an aliquot of BrF_5. The resistance furnace was preheated to 550° C, then placed on the reaction vessel for 20 minutes. After the reaction period, the nickel vessel was cooled to liquid nitrogen temperature. The same procedure as for laser fluorination was then followed; the O_2 is isolated and purified by cryogenic separation and passage over hot mercury then converted to CO_2 by passage over hot graphite and analyzed by dual inlet gas source mass spectrometry in that form (Sharp et al., 1990). A re-extraction following

the same procedure was performed at 575 °C to confirm all sample associated oxygen was reacted and no contribution to the following sample would occur. A goethite standard (Roy Hill 02-02-B3) was analyzed weekly to monitor sample measurement accuracy. Measured $\delta^{18}O_{bulk}$ values for this Roy Hill goethite standard (-1.96‰ $\delta^{18}O_{bulk}$ by laser fluorination) varied by ~0.1‰ over the duration of the synthetic goethite measurement campaign. No correction was made to our reported synthetic goethite $\delta^{18}O_{dehydroxylation}$ and $\delta^{18}O_{bulk}$ because (a) no secular trend was apparent in the measured Roy Hill 02-02-B3 standards and (b) deviations in the measured $\delta^{18}O_{bulk}$ of this standard were much smaller than observed sample reproducibility. Future work should include modification to the sample introduction setup where multiple quartz dehydration and Ni reaction vessels would allow for increased sample throughput and daily analysis of the Roy Hill 02-02-B3 goethite standard.

5.3 Hydroxylated site $\delta^{18}O$ by resistance-heated furnace

A quartz vessel was added to the sample introduction line (Figure 2.4) to allow for the structural oxygen associated with the hydroxylated sites in goethite to be analyzed. In this setup, hydroxyl group oxygen is liberated via dehydration, that water is collected, fluorinated, purified, and converted to CO_2 for isotopic analysis. No metal capsule was used in this procedure. Rather, samples were loaded directly into the quartz vessel, as water produced at goethite dehydration temperatures will react with native metals to form metal oxides before cryogenic isolation is possible. The vessel was then evacuated for 1 hour at room temperature. Following this, the electrical-resistance heated furnace was placed around the quartz reaction vessel and heated to 80 °C, while open to the high vacuum pump, and held at that temperature overnight (typically 12-14 hours). This pre-

treatment baking was aimed at removing the majority of adsorbed water without inducing any sample dehydration.

The resistance furnace was then removed the following day, and a 20-minute, 80 °C procedural blank was run. In this procedural blank, an aliquot of BrF_5 was frozen into the nickel reaction vessel and held there at liquid nitrogen temperature. The valve between the nickel and quartz reaction vessels remained open while the quartz vessel was held at 80 °C for 45 minutes. The open valve was then closed to isolate the nickel reaction vessel and the reaction vessel warmed to room temperature to induce fluorination reactions. The results of which were purified, converted to CO_2, and the yield measured. If the procedural blank measured above 1 torr on the manometer, the procedural blank was repeated.

Following the procedural blank, both the nickel and quartz vessels were evacuated, and the nickel vessel charged with an aliquot of BrF_5. The same procedure as the blank was followed, except this time the sample is heated to 250 °C. At this temperature, goethite dehydration must occur in an open system, where any water produced can immediately and continuously be removed as isotopic exchange can take place between the water and residual iron oxide (hematite) in closed systems (Yapp, 1990). Upon completion of the 45-minute dehydration reaction, the nickel reaction vessel was isolated and warmed to room temperature. The O_2 produced by fluorination reactions was purified, converted to CO_2, and then analyzed by dual inlet gas source mass spectrometry in that form (Sharp et al., 1990). A second heating to 300 °C was performed to confirm all hydroxyl-associated oxygen was liberated.

VI. RESULTS AND DISCUSSION

Here we break the presentation of our results and following discussion into three sub-sections: (6.1) method development, (6.2) the observation of intracrystalline oxygen isotope fractionation temperature dependence in synthetic goethites, and (6.3) intracrystalline oxygen isotope measurements of eight natural goethite samples.

6.1 Experimental reproducibility

Prior to undertaking oxygen isotope measurements of unknown composition synthetic or natural goethite, a series of tests were performed to assess the reproducibility of bulk sample analysis by resistance furnace fluorination. In addition, we present experimental evidence that an isotopically unique population of hydroxylated oxygen can be reproducibly extracted from goethite by dehydration.

6.1.1 Reproducibility of bulk goethite fluorination by resistance furnace

Here, we aimed to select a suitable goethite of known composition to refine the methodology for bulk fluorination by resistance furnace. Relying on the knowledge gained from the laser fluorination measurements presented in the previous chapter, we selected two specimens to be used as a potential standard: Yandi (02-01-a) and Roy Hill (02-02-B3). These samples were chosen due to their reproducible oxygen isotope composition when measured by laser fluorination. The resistance furnace fluorination method (re)development focused on determining a suitable procedure in which the proportion of analyzed oxygen originating from non-structural sources (likely dominated by adsorbed atmospheric water) could be limited. After a suitable method for sample loading and

pretreatment was determined, these two potential standards yielded reasonably reproducible results, presented in Table 2.1 and shown in Figure 2.5. The Yandi sample consistently yielded isotopically light values compared to those derived from laser fluorination. Furthermore, the offset between furnace- and laser-derived oxygen isotope measurements ($\Delta^{18}O_{furnace\text{-}laser}$) is correlated to yield in the Yandi (02-01-a) measurements (Figure 2.5), with the two lowest yield measurements corresponding to the largest $\Delta^{18}O_{furnace\text{-}laser}$. We interpret this trend to be the result of a kinetic isotope effect associated with incomplete sample reaction.

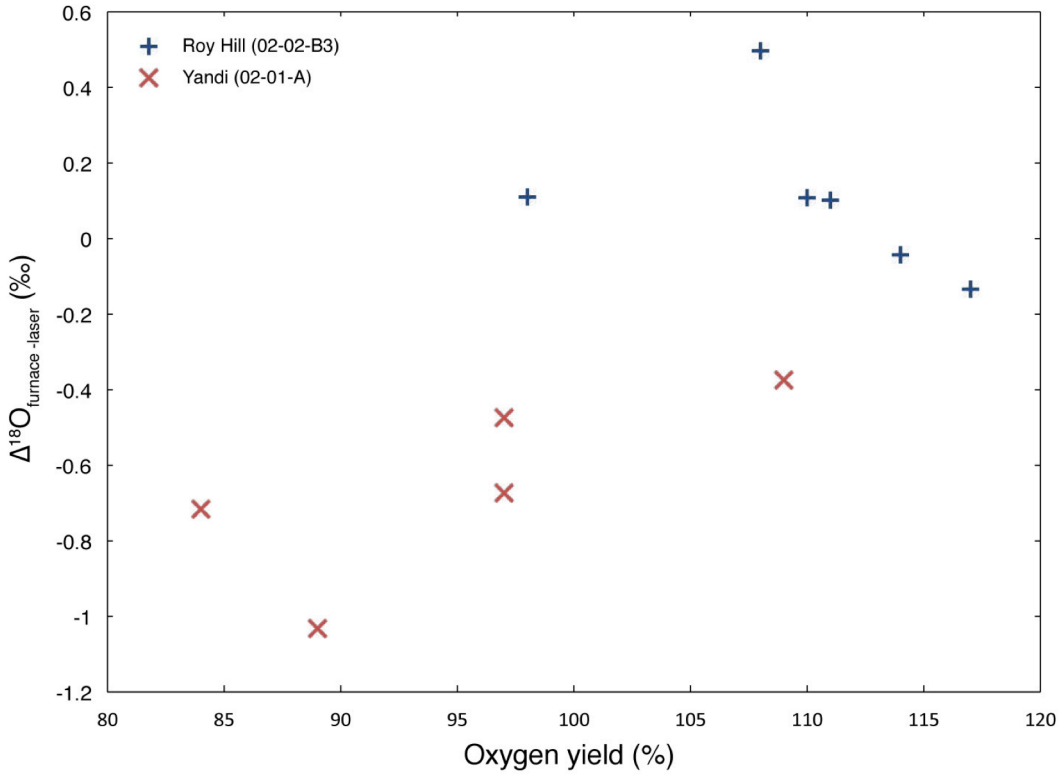

Figure 2.5: Relationship between oxygen yield (%) and $\Delta^{18}O_{furnace\text{-}laser}$.

Following the Yandi (02-02-a) measurement campaign, we began a second set of analyses on the Roy Hill (02-02-B3) goethite. We aimed to test whether the negative $\Delta^{18}O_{furnace\text{-}laser}$ values observed in the Yandi measurements were an artifact of the furnace fluorination methodology or specific to this Yandi sample. The Roy Hill samples, with the exception of one particularly light $\delta^{18}O_{furnace}$ measurement ($\Delta^{18}O_{furnace\text{-}laser}$ = 0.497‰), yielded values within ~0.1‰ of the laser derived value. At this point in time, we had also begun measuring oxygen collected during dehydroxylation of natural goethites and observed a large $\Delta^{18}O_{bulk\text{-}dehydroxylation}$. For this reason, after the three initial Roy Hill furnace measurements (measurements are listed chronologically in Table 2.1), we concluded our $\delta^{18}O_{furnace}$ measurement method was acceptably reproducible to ±0.5‰ and began measuring synthetic goethites of unknown isotopic composition. The final three Roy Hill furnace measurements, listed in Table 2.1, were made though the synthetic goethite measurement campaign.

6.1.2 Reproducibility of oxygen extraction by goethite dehydroxylation

In this experiment, we tested the reproducibility of our $\delta^{18}O_{dehydroxylation}$ measurement method. As previously discussed, goethite dehydration releases 25% of the total structural oxygen (see Section 3 - Theoretical Considerations). In these experiments, we analyzed aliquots of freshly prepared Roy Hill (02-02)[1] sample. The first experiment conducted was aimed at determining a temperature for dehydroxylation experiments.

[1] Roy Hill 02-02 refers to a hand sample goethite specimen (~10 cm), which was subsampled along the inferred growth axis for the analyses presented in the previous chapter. In this test of the reproducibility of our dehydroxylation measurement, each measurement involved tens of grams of sample. This quantity of material would have consumed a significant proportion of the remaining mineral crushate from the majority of samples previously prepared. Rather than deplete the reserve crushate, a new subsample of Roy Hill 02-02 was prepared specifically for this experiment and is referred to here simply as Roy Hill (02-02).

[2] Separate furnace temperature calibrations were measured for the Ni reaction vessel and quartz dehydroxylation vessel. These calibration curves were determined by recording both the temperature measured by placing a thermocouple

Here, we heated aliquots of Roy Hill (02-02) to temperatures between 200 and 250 °C and measured the oxygen collected from dehydroxylation. The results of this experiment are shown in Figure 2.6. Here we note that experiments conducted between 225 and 235 °C produce $\delta^{18}O_{dehydroxylation}$ values that range by 8‰. The yield of these measurements does not correlate with temperature. However, at 250 °C, much more reproducible $\delta^{18}O_{dehydroxylation}$ values are measured.

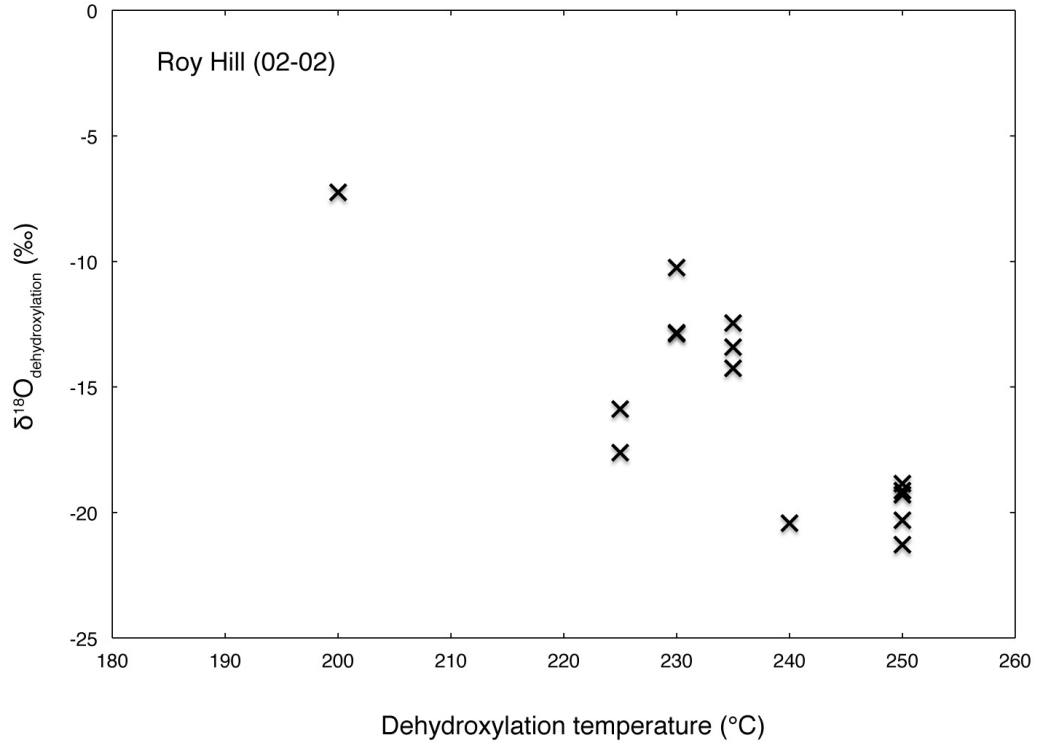

Figure 2.6: Variation in the temperature at which the dehydroxylation reaction was carried out produced highly variable $\delta^{18}O_{dehydroxylation}$ values at temperatures below 250 °C.

Table 2.2 and Figure 2.7 present the results from the five measurements conducted at 250 °C. Of these, three measurements produce oxygen yields within 3% of the expected value (25%). The mean $\delta^{18}O_{dehydroxylation}$ is -19.094‰ ± 0.129, suggesting reproducible results when oxygen yields are within a close range of the expected value. However, two low-yield measurements produce isotopically lighter $\delta^{18}O_{dehydroxylation}$ values. While only two data points, a correlation between oxygen yields and $\delta^{18}O_{dehydroxylation}$ is clearly evident, with lower yields corresponding with isotopically lighter compositions. This trend is consistent with the trend observed in the bulk Yandi samples measured by furnace fluorination (Figure 2.5). Again, we interpret this to be a result of a kinetic isotope effect associated with the preferential release of isotopically light oxygen during the initial reaction (in this case, dehydroxylation) process.

Unfortunately, there is no readily available explanation for why two of the five experiments produced low oxygen yields despite utilizing the same pre-treatment and reaction procedure. It is possible that variations in heating scheme produced these observed effects given the accuracy of the electrical-resistance furnace was only tested a single time, and heating rate is manually controlled in each experiment. Here, the user aims to rapidly reach the 250 °C dehydration setpoint then maintain the setpoint for the duration of the experiment using a variable voltage Variac transformer. However, the thermal lag time associated with heating a large-mass resistance furnace makes following a precise temperature scheme difficult. Improvement to the reproducibility of the heating scheme through automation may prove an easy avenue to improving yield and $\delta^{18}O_{dehydroxylation}$ reproducibility.

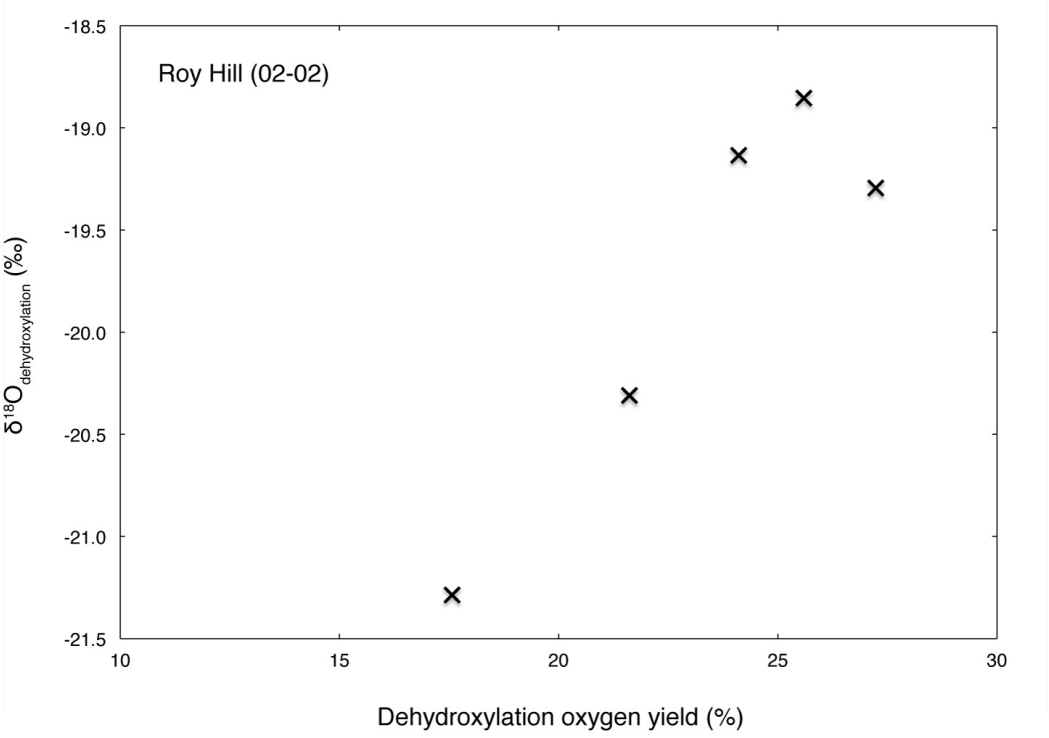

Figure 2.7: Oxygen yield plotted against the isotopic composition of oxygen collected during dehydroxylation at 250 °C.

6.2 Calibration of a goethite intracrystalline isotope thermometer

In this section, we present the results of our intracrystalline oxygen isotope measurements of goethites precipitated under known environmental conditions. We aim to use this suite of synthetic goethites as an initial calibration of the potential intracrystalline oxygen isotope thermometer.

6.2.1 Synthetics

Following the reproducibility tests discussed above, we embarked upon a measurement campaign to determine the intracrystalline oxygen isotope composition of

synthetic goethite precipitates. Bulk oxygen isotope compositions were determined by resistance-furnace fluorination while the oxygen associated with goethite dehydroxylation was collected and analyzed on a separate aliquot, the methods of which are detailed in Sections 5.2 and 5.3, respectively. Table 2.3a presents the results of the synthetic goethite bulk oxygen isotope measurements and Table 2.3b presents the dehydroxylation oxygen isotope measurements.

The results presented in Table 2.3a show a number of noteworthy trends. The first trend is that heavier oxygen isotopic compositions are associated with colder precipitation temperatures in samples grown under like environmental conditions. This trend holds in all three pairs of samples formed under variable temperature but comparable stoichiometry or pH (S22-GOE-H-5 vs. S40-GOE-H-1; S22-GOE-K-5 vs. S70-GOE-K-5; S40-GOA-H-3 vs. S70-GOA-H-3) and aligns with the expectation of heavier oxygen isotopic composition in goethites with colder formation temperatures (Yapp, 1990; Muller et al., 1995; Zheng 1998; Bao and Koch 1999: Yapp, 2007; Yapp, 2012). However, the bulk oxygen isotope composition is not well correlated with temperature because variation in the pH and stoichiometry at time of formation obscures this trend (Figure 2.8). These synthetic goethites were precipitated from water of the same initial oxygen isotope composition and therefore the scatter observed in Figure 2.8 includes no additional effect from variability in the isotopic composition of the parent fluid. Unfortunately, the isotopic composition of the parent fluid from which the synthetic goethites utilized in this study is unknown. Future work may include analyzing synthetic goethites precipitated from known isotopic composition fluid, such as those from Monteiro (2017).

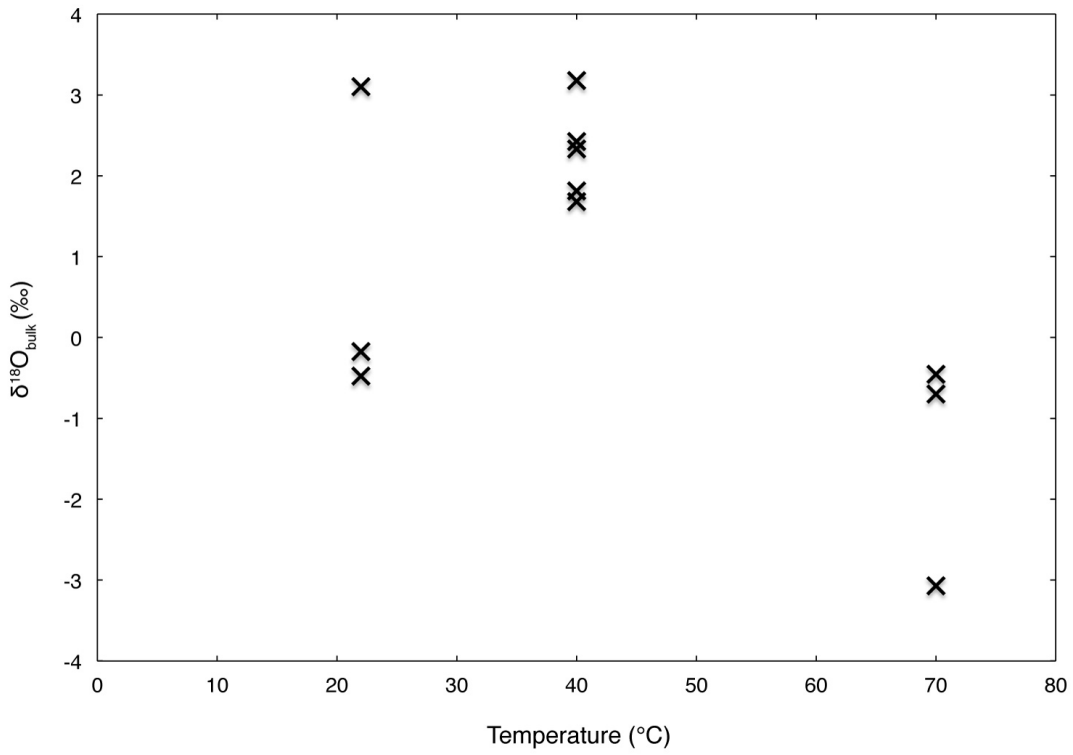

Figure 2.8: Synthetic goethite precipitation temperature plotted against the bulk oxygen isotopic composition.

We also note the variability in the oxygen yield of these synthetic goethite bulk fluorination measurements. In this study, we cull any measurement with a bulk yield more than ±20% of the expectation (100%) value, since low yields indicate incomplete sample reaction (thus potentially imparting a kinetic isotope effect), and high yields indicate contamination of non-structural oxygen. We recognize the arbitrary nature of this ±20% threshold. Only with more measurements and an improved understanding of any systematic relationship between yield and oxygen isotope measurement variation may we more rigorously determine a yield threshold for culling data. Even among the three S40-

GOA-H-3 measurements, where each fluorination reaction produced 98% of the predicted oxygen yield, the $\delta^{18}O_{bulk}$ varies by 0.85‰.

We now move to the results from dehydroxylation experiments of synthetic goethites (Table 3b). The most apparent trend observed is the relationship between temperature of precipitation and the isotopic composition of oxygen collected during dehydroxylation, with isotopically light oxygen concentrated at colder temperatures. This trend is opposite of the theoretical prediction presented in Section 3. Either this theoretical prediction is incorrect or our assumption that the oxygen produced from dehydroxylation is sourced from the population of atoms associated with hydroxylated sites is incorrect. We have no way to empirically or a priori know which oxygen atoms are collected during dehydroxylation. Therefore, we make no determination as to whether heavy oxygen does in fact concentrate in the hydroxylated sites, as the theoretical calculations of Blanchard et al. (2015) suggest. Rather, we acknowledge empirical findings are suggestive of an opposing fractionation trend and argue that regardless of the source of the oxygen extracted during dehydroxylation, strong temperature dependence is observed.

Additionally, we note that the dehydroxylation experiments of synthetic goethites produce low oxygen yields. Given that high-resolution synchrotron X-ray diffraction found precipitates were pure goethite (Mostert, 2014), mineralogical impurities (such as hematite) cannot account for low yields. We present two possible explanations, which may be functioning in conjunction. First, the large surface area to volume ratio of the very fine grain precipitates may carry a significant mass of adsorbed water. Vacuum and thermal-induced desorption during the sample pre-treatment procedure may result in a

smaller pool of available structural oxygen than predicted from mass as measured on the balance prior to pre-treatment. Second, goethite is susceptible to vacuum dehydration, with dehydration of natural goethites observed at temperatures as low as 145 °C under vacuum (Yapp and Pedley, 1985). For the majority of samples, the required goethite dehydration temperature ranges between 190 and 240 °C (Yapp and Poths, 1993). We hypothesize that the dehydration temperature necessary for a given goethite may be a function of the crystallite domain distribution of that specific sample. Therefore, it is possible that the very fine-grain precipitates are more susceptible to vacuum dehydration, and the pretreatment procedure of vacuum baking at 80 °C may induce partial dehydration.

Finally, we present a summary of the synthetic goethite intracrystalline oxygen isotope measurements in Table 2.4. S22-GOE-H-5 was never analyzed for $\delta^{18}O_{dehydroxylation}$. The temperature trend in $\Delta^{18}O_{bulk\text{-}dehydroxylation}$ is immediately apparent (Figure 2.9). Beyond the temperature dependence, we also note that oxygen isotope variations observed in the $\delta^{18}O_{bulk}$ measurements (likely related to pH and trace element effects on bulk mineral oxygen isotope fractionation) are erased. The linear regression though the synthetic goethite data presented in Figure 2.9 has the equation $\Delta^{18}O_{bulk\text{-}dehydroxylation}=5.0055(10^6/T^2)-40.091$, where T is in Kelvin.

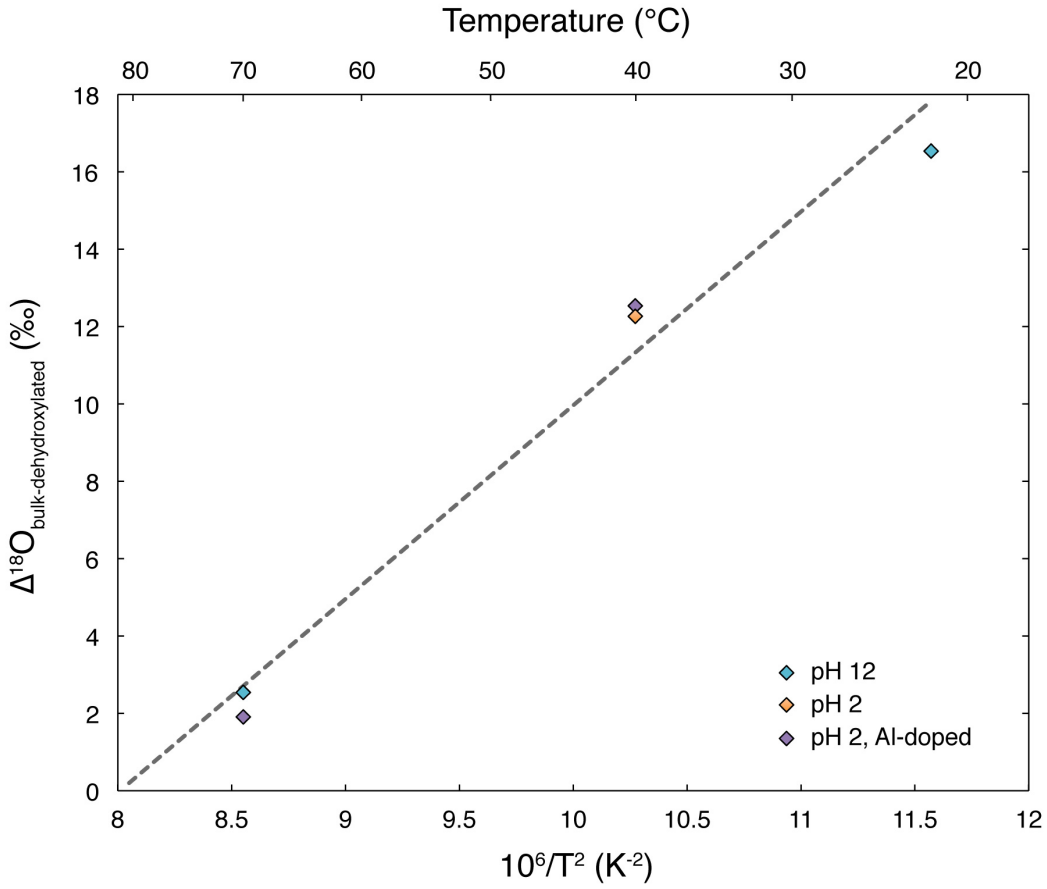

Figure 2.9: Experimentally derived $\Delta^{18}O_{bulk\text{-}dehydroxylation}$ vs. temperature of precipitation.

We also considered if yield might correlate with $\Delta^{18}O_{bulk\text{-}dehydroxylation}$. Figure 2.10 presents a plot of the yield of the dehydroxylation measurement against $\Delta^{18}O_{bulk\text{-}dehydroxylation}$. The fact that the isotopically lightest sample (the 22 °C, pH 12 measurement) has the highest yield is opposite the previously observed trend between isotopically light measurements and low yield (Figure 2.5 and Figure 2.7). Furthermore, the magnitude of the variation in $\Delta^{18}O_{bulk\text{-}dehydroxylation}$ is far greater than that observed in previous low yield measurements (Figure 2.5 and Figure 2.7). Given the lack of correlation between other

measured quantities and $\Delta^{18}O_{bulk\text{-}dehydroxylation}$, we conclude temperature is in fact the control on the intracrystalline isotopic composition of synthetic goethite precipitates, regardless of pH or Al-substitution.

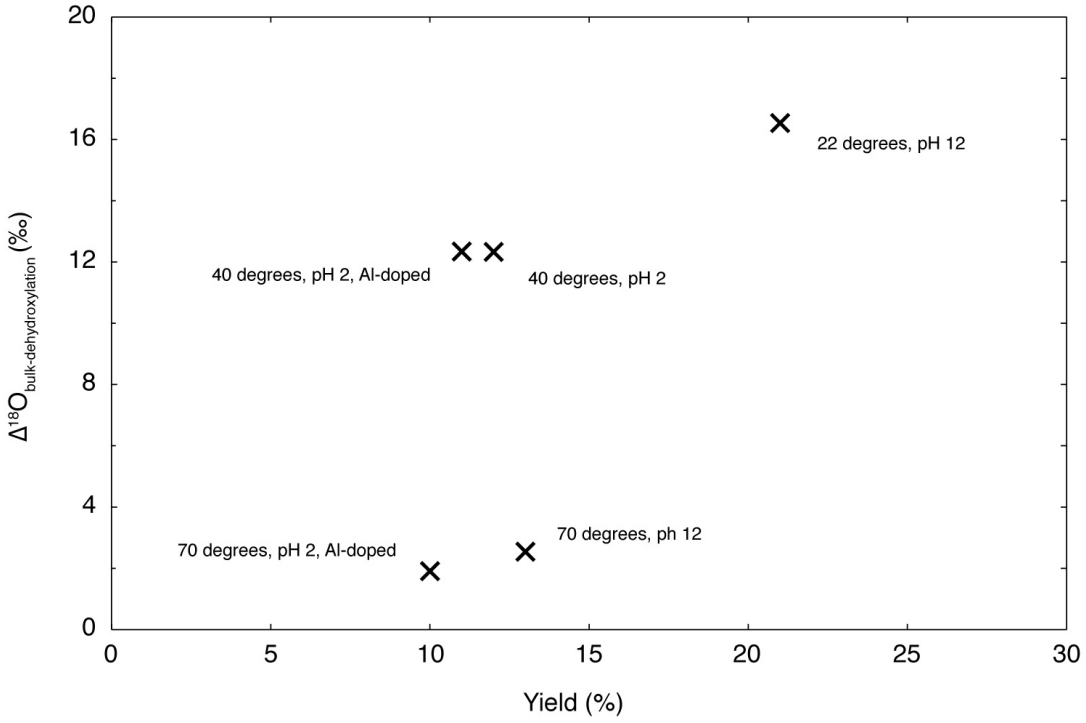

Figure 2.10: Plot of dehydroxylation oxygen yield vs. $\Delta^{18}O_{bulk\text{-}dehydroxylation}$.

In our initial calibration of the goethite intracrystalline thermometer, we place no confidence interval on the temperature dependence of $\Delta^{18}O_{bulk\text{-}dehydroxylation}$ (Figure 2.9). This is largely because the error associated with $\delta^{18}O_{bulk}$ and $\delta^{18}O_{dehydroxylation}$ measurements is not well known. Each $\Delta^{18}O_{bulk\text{-}dehydroxylation}$ value in our temperature calibration involves a single $\delta\ ^{18}O_{dehydroxylation}$ measurement and, given the range in $\delta^{18}O_{furnace}$ measurements (Table 2.1), the precision of our $\Delta^{18}O_{bulk\text{-}dehydroxylation}$ is not well

constrained. Future work should focus on fully documenting the real precision in our synthetic goethite calibrated intracrystalline thermometer.

6.2.2 Closure of mass balance

A single experiment was carried out in which the residual material produced from the dehydroxylation process was recovered from the quartz vessel, weighed, then fluorinated by resistance furnace. The result of this experiment is presented in Table 2.5. Most noticeably, the isotopic composition of the dehydroxylation experiment plus residual does not equal that of the bulk. The oxygen yield associated with the dehydroxylation measurement (expected value = 25%) and residual measurement (expected value = 75%) is low. Given the intrasample oxygen isotope variation observed in other bulk synthetic measurements, along with possible oxygen isotope yield dependence, the observed 0.453‰ difference between $\delta^{18}O_{bulk}$ and $\delta^{18}O_{dehydroxylation+residual}$ may well be within the errors of the methodology. We also note that the recovered mass (4.64 mg) is well below the expected mass (6.40 mg) assuming stoichiometric transformation from goethite to hematite. Given the fine-grain nature of the synthetic precipitates, two possibilities exist: a significant proportion of the initial mass is in fact adsorbed species (likely water) and/or some proportion of the material clung to the walls of the quartz vessel used for dehydroxylation. We assume the mass discrepancy is a combination of both factors. Future tests to verify the mass balance of our method should be undertaken.

6.2.3 Internal isotopic re-equilibration

In this experiment, we aim to internally equilibrate the oxygen isotopes of goethite at known temperature in an effort to provide a high-temperature calibration point for our intracrystalline goethite thermometer. This experiment may also be used as a first step towards determining the kinetic rate constants of high-temperature solid-state internal isotope-exchange reactions that may occur over geologic timescales. Previous laboratory heating experiments of carbonates require temperatures greater than 400 °C to generate observable changes in the clumped isotope composition of these samples (Stolper and Elier, 2015). Since the dehydration process from goethite to hematite typically occurs at ~225 °C, we utilized a stepped furnace piston-cylinder press to extend the temperature stability field of goethite. At 2.5 gigapascal (GPa), the goethite-hematite phase transition is pushed to ~300 °C (Majzlan et al., 2003; Gleason et al., 2008). To prevent the chance of initiating any dehydroxylation, we set our equilibration experiment to 275 °C and 2.5 GPa. We held 50 mg of Roy Hill (02-02-B3) at these conditions for 2 weeks.

Following the heating experiment, the FTIR spectra of the sample clearly displayed the expected infrared active modes of the hydroxyl group (the OH doublet observed at ~800 cm^{-1}, see Figure 4.6 for example), indicating no dehydration occurred. We then measured the $\Delta^{18}O_{bulk\text{-}hydroxylated}$ of this sample to determine if any internal oxygen isotope reordering had occurred. The results of this experiment are presented in Table 2.6. This experiment provides clear evidence for solid state re-ordering. The $\Delta^{18}O_{bulk\text{-}hydroxylated}$ from the heating experiment sample is 13.529‰, a decrease of 5.153‰ from the un-heated sample, corresponding to an intracrystalline temperature of 33 °C. This represents

an incomplete internal re-ordering of oxygen isotopes, a result that is not surprising given the slow kinetics of similar solid-state equilibration experiments performed at these temperatures over laboratory timescales.

6.3 Natural Samples

Finally, we applied the temperature calibration produced from the synthetic goethite suite and calculated temperatures of formation from eight natural goethite samples. This portion of our study aimed to answer two questions. First, do natural samples produce intracrystalline oxygen isotope temperatures consistent with geologic expectations? Second, if so, can we learn anything new about the environmental conditions at time of formation?

The results from bulk fluorination of natural goethites are presented in Table 2.7. The Yandi (02-01-a) and Roy Hill (02-02-B3) standards discussed in Section 6.1.1 are included. During the interpretation of these results, we cull bulk measurements with a oxygen yield greater than ±20% from the mass-calculated yield. At this threshold, no measurements were culled from the bulk fluorination of natural goethites. Table 2.7 also reports $\delta^{18}O_{laser}$ measurements. We utilize $\delta^{18}O_{laser}$ measurements in the calculation of $\Delta^{18}O_{bulk\text{-}hydroxylated}$ intracrystalline temperatures whenever possible. Only the DMNH-14510 sample was not measured utilizing the laser methodology.

Table 2.8 presents the corresponding $\delta^{18}O_{dehydroxylation}$ measurements. Here we observe a larger total variation in $\delta^{18}O_{dehydroxylation}$ (16.84‰) than in $\delta^{18}O_{bulk}$ (5.78‰). The variation in yield is also much larger than in the bulk measurements. A single

measurement of both the Yandi (02-01-a) and Roy Hill (02-02-B3) samples utilized the incorrect vessel-specific temperature calibration[2] and therefore resulted in a significantly low oxygen isotope yield. We cull these measurements. Furthermore, we cull any $\delta^{18}O_{dehydroxylation}$ measurement with a yield more than 20% different from the mass-calculated expectation (expectation = 25% of total oxygen, thus we cull any dehydroxylation measurement with a yield ±5% of the total -- the same % threshold as with bulk furnace fluorination of natural goethites). Therefore, we cull the Yandi (02-02) and (02-01-a) measurements and make no further interpretation of the $\delta^{18}O_{dehydroxylation}$ or $\Delta^{18}O_{bulk\text{-}dehydroxylation}$ values.

The intracrystalline temperatures resulting from the measured $\Delta^{18}O_{bulk\text{-}dehydroxylation}$ values are also shown in Table 2.9. The first-order finding, using the synthetic precipitate calibration, is the intracrystalline temperatures of these natural goethites are geologically reasonable, with no sample producing a temperature well beyond that of the expectation. We will now consider the sample specific intracrystalline temperatures and discuss potential interpretations.

The suite of weathering-reaction goethites from Western Australia formed between 72 Ma and present (Table 1.1) at, or very near, the surface of the Earth (Heim et al., 2006; Vasconcelos et al., 2013). The intracrystalline temperatures of the two Roy Hill samples are 19 and 20 °C, broadly consistent with the environmental conditions at the Earth's

[2] Separate furnace temperature calibrations were measured for the Ni reaction vessel and quartz dehydroxylation vessel. These calibration curves were determined by recording both the temperature measured by placing a thermocouple directly within a given vessel and the temperature measured from a thermocouple mounted within and near the base of the resistance furnace. A combination of higher thermal conductivity of the Ni vessel (which a large portion of protrudes from the furnace) and shorter quartz vessel (thus samples within this vessel rest less deeply within the furnace) produce two unique calibration curves for each vessel. In this case, the implementation of the Ni vessel curve to quartz vessel likely resulted in experimental temperatures ~60 °C below expectation.

surface. We are unaware of any paleoclimate records that report paleotemperatures specific to the Hamersley region of Western Australia. However, mean annual temperature estimates for southern high latitudes in the late Cretaceous are typically <15 °C (Greenwood and Wing, 1995; Frakes and Barron, 2001). These warmer intracrystalline temperatures may provide further evidence that weathering-reaction goethites tend to form seasonally in warm and/or wet conditions.

As discussed in the previous chapter, climate models for the Australian continent predict 10 °C of warming through the Cenozoic (Frakes and Barron, 2001). Therefore we would expect the Yandi sample (12 ± 1.2 Ma) to record warmer intracrystalline temperatures than the Roy Hill samples. However, we observe the opposite trend, with Yandi 02-03 yielding an intracrystalline temperature of 11 °C. This potentially represents a new finding about the conditions in the Hamersley region circa 12 Ma yet requires confirmation by other samples. We also consider this cooler formation temperature may speak to the environmental conditions of channel iron deposits, and we suggest intracrystalline temperatures should also be measured for Lynn Peak goethites, another Western Australia channel iron deposit.

We also measured the intracrystalline temperature of three goethites from the Pikes Peak region of the Colorado Front Range. DMNH-14510 and DMNH-10029 provide the highest intracrystalline temperatures of our natural goethite sample suite, 39 and 32 °C, respectively (Table 2.9). Fluid inclusion thermometry on quartz intergrown with massive, bladed goethite indicates these late stage crystals formed at 40 °C (Berry, 2001). The morphology of our DMNH-14510 goethite is very similar to that described by Berry

(2001), and we measure an intracrystalline temperature only 1 °C different. The DMNH-10029 sample produces a cooler temperature of 32 °C. Combined, these two intracrystalline temperatures indicate that the cm-scale bladed goethites hosted within Pike Peak pegmatites are not of hydrothermal origin. Given exhumation of the Pikes Peak batholith is associated with the Laramide Orogeny, which initiated regionally at ~70 Ma (Kelly, 2002), it is possible these goethites formed post-Laramide given their cool temperatures.

A third Colorado goethite, CIT-8809, was selected for intracrystalline thermometry. This sample was selected because the more common botryoidal morphology of this sample suggested it is unlikely to be co-genetic with the pegmatite hosted, bladed goethites (DMNH-14510 and DMNH-10029). Four aliquots of this sample were dated following the methods of the previous chapter and a mean (U-Th)/He age of 3.0 ± 0.3 Ma was determined (Table 2.10). The modern Pikes Peak land surface almost entirely exists above 2000 meters elevation (with the summit at 4301.95 m) and therefore we hypothesized this young sample may provide a cold intracrystalline temperature. Subsequent analysis produced a $\Delta^{18}O_{bulk\text{-}dehydroxylation}$ temperature of 15 °C (Table 2.9). This temperature is geologically reasonable given what we know about this sample. However, without locality specific context (which we do not have for this sample), it is difficult to interpret the intracrystalline temperature further.

We will conclude our discussion with a note on uncertainty. As the reader is likely aware, we assigned no uncertainty interval to the $\Delta^{18}O_{bulk\text{-}dehydroxylation}$ derived intracrystalline temperatures of natural goethites. This is because the $\Delta^{18}O_{bulk\text{-}dehydroxylation}$

value of many samples is comprised of just single measurements of $\delta^{18}O_{bulk}$ and/or $\delta^{18}O_{dehydroxylation}$. Variation in the measured oxygen isotope composition of replicate aliquots of natural goethite is typically far greater than the instrument error associated with a given oxygen isotope measurement (typically <0.05‰), and therefore instrument error alone would likely vastly underestimate the true uncertainty in intracrystalline temperatures. Given the reproducibility of our $\delta^{18}O_{furnace}$ measurements on the Yandi and Roy Hill standards is not better than 0.5‰ (Table 2.1), we can treat this as a lower limit to the expected sample reproducibility. Assuming both the $\delta^{18}O_{bulk}$ and $\delta^{18}O_{furnace}$ measurements have a minimum uncertainty of 0.5‰, and the uncertainty in each of these values is uncorrelated, we can estimate intracrystalline temperatures likely have uncertainties of 2-3 °C. Future experiments are necessary to fully document the actual precision of our measurements.

7. CONCLUSION

Previous studies have observed intracrystalline isotopic variation between structurally-non-equivalent crystal sites within a single phases, including kaolinite, muscovite and chlorite (Hamza and Epstein, 1980), smectite (Delgado and Reyes, 1996), copper sulfate pentahydrate (Kita and Matsuo, 1981) and borax (Pradhananga and Matsuo, 1985). We set out to extract two structurally non-equivalent reservoirs of oxygen from goethite, then assess the potential temperature dependence in their isotopic composition and determine if goethite is suitable for single-phase geothermometry. To do so, we utilized a suite of synthetic goethite precipitates, grown with known chemical

composition, and at known temperature and pH. We found the $\Delta^{18}O_{bulk\text{-}dehydroxylation}$ both correlated with formation temperature and had a temperature dependence suitable for geothermometry. Noteably, Al-substitution and pH does not seem to affect $\Delta^{18}O_{bulk\text{-}dehydroxylation}$, even though these factors influence $\delta^{18}O_{bulk}$ values of goethite (Yapp, 2007; Yapp; 2012). Future work should include documenting measurement precision to constrain the uncertainty in calculated instracrystalline temperatures, along with developing a more systematic understanding of the relationship between oxygen yield and $\delta^{18}O_{dehydroxylation}$ values.

Using this initial temperature calibration derived from the synthetic goethite suite, we calculated the instracrystalline temperature of eight natural goethites. Samples produced by weathering reactions at, or near, the Earth's surface in Western Australia yielded instracrystalline temperatures ranging between 11 and 20 °C. However, the observed temperature trend is opposite of the expectation, with cooling observed through the Cenozoic. Analysis of additional samples is necessary to confirm this finding. In addition, three samples from the Pikes Peak region of Colorado were analyzed. The resulting intracrystalline temperatures range between 15 and 39 °C. These temperatures are also within geologic expectations. These results are highly encouraging that, through further refinement of the $\Delta^{18}O_{bulk\text{-}dehydroxylation}$ temperature dependence, along with full documentation of measurement precision, goethite intracrystalline thermometry can become a useful tool for geochemists aiming to acces the wealth of paleoclimate information stored within Fe-oxyhydroxide deposits.

References

Alpers CN, and Brimhall GH. (1988) Middle Miocene climatic change in the Atacama Desert, northern Chile: Evidence from supergene mineralization at La Escondida. *Geological Society of America Bulletin*. **100**, 1640–1656.

Bao H, and Koch PL. (1999) Oxygen isotope fractionation in ferric oxide-water systems: low temperature synthesis. *Geochimica et cosmochimica acta*. **63**, 599-613.

Barker F, Wones DR, Sharp WN, and Desborough GA. (1975) The Pikes Peak batholith, Colorado Front Range, and a model for the origin of the gabbro—anorthosite—syenite—potassic granite suite. *Precambrian Research*. **2**, 97-160.

Berry RR. (2001) Goethite inclusions in quartz from the Pikes Peak Granite. *Rocks & Minerals*. **76**, 228-32.

Bird MI, Longstaffe FJ, Fyfe WS, Kronberg BI, and Kishida A. (1993) An oxygen-isotope study of weathering in the eastern Amazon Basin, Brazil. In *Climate Change in Continental Isotopic Records, Geophys*. *Monogr. 78*, ed. PK Swart, KC Lohman, J McKenzie, S Savin, pp. 295–307. Washington, DC: American Geophysical Union.

Blanchard M, Dauphas N, Hu MY, Roskosz M, Alp EE, Golden DC, Sio CK, Tissot FL, Zhao J, Gao L, and Morris RV. (2015) Reduced partition function ratios of iron and oxygen in goethite. *Geochimica et Cosmochimica Acta*. **151**, 19-33.

Clayton RN, Mayeda TK. (1963) The use of bromine pentafluoride in the extraction of oxygen from oxides and silicates for isotopic analysis. *Geochimica et cosmochimica acta*. **27**, 43-52.

Delgado A, and Reyes E. (1996) Oxygen and hydrogen isotope compositions in clay minerals: A potential single-mineral geothermometer. *Geochimica et Cosmochimica Acta*. **60**, 4285-9.

Eiler JM. (2007) "Clumped-isotope" geochemistry—The study of naturally-occurring, multiply-substituted isotopologues. *Earth and Planetary Science Letters*. **262**, 309-27.

Fan M, Ayyash SA, Tripati A, Passey BH, and Griffith EM. (2018) Terrestrial cooling and changes in hydroclimate in the continental interior of the United States across the Eocene-Oligocene boundary. *GSA Bulletin*. **130**, 1073–1084.

Farley KA. (2018) Helium diffusion parameters of hematite from a single-diffusiondomain crystal. *Earth and Planetary Science Letters*, **231**, 117-129.

Frakes LA, and Barron EJ. (2001) Phanerozoic general circulation model results and quantitative climate data for Australia. *Australian Journal of Earth Sciences*. **48**, 643-55.

Fricke HC, and Wing SL. (2004) Oxygen isotope and paleobotanical estimates of temperature and δ18O–latitude gradients over North America during the early Eocene. *American Journal of Science*. **304**, 612–635.

Gagnon JE, Samson IM, Fryer BJ, and Williams-Jones AE. (2004) The composition and origin of hydrothermal fluids in a NYF-type granitic pegmatite, South Platte District, Colorado: evidence from LA–ICP–MS analysis of fluorite-and quartz-hosted fluid inclusions. *The Canadian Mineralogist*. **42**, 1331-55.

Girard JP, Freyssinet P, and Chazot G. (2000) Unraveling climatic change from intra-profile variation in oxygen and hydrogen isotopic composition of goethite and kaolinite in laterites: an integrated study from Yaou, French Guiana. *Geochim. Cosmochim. Acta* **64**, 409–26.

Glasauer S, Friedl J, Schwertmann U. (1999) Properties of Goethites Prepared under Acidic and Basic conditions in the Presence of Silica. *Journal of Colloid and Interface Science*. **216**, 106-115.

Gleason AE, Jeanloz R, and Kunz M. (2008) Pressure-temperature stability studies of FeOOH using X-ray diffraction. *American Mineralogist*. **93**, 1882-5.

Greenwood DR, Wing SL. (1995) Eocene continental climates and latitudinal temperature gradients. *Geology*. **23**, 1044-8.

Gualtieri AF, and Venturelli P. (1999) In situ study of the goethite-hematite phase transformation by real time synchrotron powder diffraction. *American Mineralogist*. **84**, 895-904.

Hamza MS, and Epstein S. (1980) Oxygen isotopic fractionation between oxygen of different sites in hydroxyl-bearing silicate minerals. *Geochimica et Cosmochimica Acta*. **44**, 173-82.

Heim, JA, Vasconcelos PM, Shuster DL, Farley KA, and Broadbent G. (2006) Dating paleochannel iron ore by (U-Th)/He analysis of supergene goethite, Hamersley province, Australia. *Geology*. **34**, 173-176.

Henkes GA, Passey BH, Grossman EL, Shenton BJ, Pérez-Huerta A, abd Yancey TE. (2014) Temperature limits for preservation of primary calcite clumped isotope paleotemperatures. *Geochimica et Cosmochimica Acta*. **139**, 362-82.

Kelley SA. (2002) Unroofing of the southern Front Range, Colorado: A view from the Denver Basin. *Rocky Mountain Geology*. **37**, 189-200.

Kita I, and Matsuo S. (1981) Intracrystalline site preference of hydrogen isotopes in the water of crystallization of copper sulfate pentahydrate. *The Journal of Physical Chemistry*. **85**, 792-7.

Lechler AR, Huntington KW, Breecker DO, Sweeney MR, and Schauer AJ. (2018) Loess–paleosol carbonate clumped isotope record of late Pleistocene–Holocene climate change in the Palouse region, Washington State, USA. *Quaternary Research*.

Levasseur R. (1997) Fluid inclusion studies of rare element pegmatites, South Platte District, Colorado (Doctoral dissertation, University of Windsor).

Lloyd MK, Eiler JM, and Nabelek PI. (2017) Clumped isotope thermometry of calcite and dolomite in a contact metamorphic environment. *Geochimica et Cosmochimica Acta*. **197**, 323-44.

Majzlan J, Grevel KD, Navrotsky A. (2003) Thermodynamics of Fe oxides: Part II. Enthalpies of formation and relative stability of goethite (α-FeOOH), lepidocrocite (γ-FeOOH), and maghemite (γ-Fe2O3). *American Mineralogist*. **88**, 855-9.

McCrea, JM. (1950) On the Isotopic Chemistry of Carbonates and a Paleotemperature Scale. *The Journal of Chemical Physics*. **18**, 849-857.

Miller HB, Vasconcelos PM, Eiler JM, Farley KA. (2017) A Cenozoic terrestrial paleoclimate record from He dating and stable isotope geochemistry of goethites from Western Australia. *Geology*. **45**, 895-898.

Monteiro HS. (2017) Paleoenvironmental evolution of continental landscapes through combined high-resolution geochronology and $\delta^{18}O$ ion microprobe analyses of goethite (Doctoral dissertation, University of Queensland).

Monteiro HS, Vasconcelos PM, Farley KA, Spier CA, and Mello CL. (2014) (U–Th)/He geochronology of goethite and the origin and evolution of cangas. *Geochimica Et Cosmochimica Acta*. **131**, 267–289

Mørup, S, Madsen MB, Franck J, Villadsen J, Koch CJW. (1983) A new interpretation of Mössbauer spectra of microcrystalline goethite: "super-ferromagnetism" or super-spin-glass" behaviour? *Journal of Magnetism and Magnetic Materials*. **40**, 163-174.

Mostert AB. (2014) Variation in Goethite Crystallography with Reference to Ravensthorpe Ni-laterite (Doctoral dissertation, University of Queensland).

Muller JP, Manceau A, Calas G, Allard T, Ildefonse P, and Hazemann JL. (1995) Crystal chemistry of kaolinite and Fe-Mn oxides: relation with formation conditions of low temperature systems. *American Journal of Science.* **295**, 1115-1155.

Oerter E, Singleton M, and Davisson L. (2017) Hydrogen and oxygen stable isotope signatures of goethite hydration waters by thermogravimetry-enabled laser spectroscopy. *Chemical Geology*. **475**, 14-23.

Pack A, Gutzmer J, Beukes NJ, Van Niekerk HS. (2000) Supergene ferromanganese wad deposits derived from Permian Karoo strata along the Late Cretaceous-Mid- Tertiary African land surface, Ryedale, South Africa. *Economic Geology.* **95**, 203–20.

Passey BH and Henkes GA. (2012) Carbonate clumped isotope bond reordering and geospeedometry. *Earth and Planetary Science Letters*. **351**, 223-36.

Poage MA, Sjostrom DJ, Goldberg J, Chamberlain CP, and Furniss G. (2000) Isotopic evidence for Holocene climate change in the northern Rockies from a goethite-rich ferricrete chronosequence. *Chemical Geology*. **166**, 327–40**.**

Pradhananga TM, and Matsuo S. (1985) Intracrystalline site preference of hydrogen isotopes in borax. *The Journal of Physical Chemistry*. **89**, 72-6.

Quade J, Eiler J, Daeron M, and Achyuthan H. (2013) The clumped isotope geothermometer in soil and paleosol carbonate. *Geochimica et Cosmochimica Acta.* **15**, 92-107.

Ramanaidou ER, Morris RC, and Horwitz RC. (2003) Channel iron deposits of the Hamersley Province, Western Australia. *Australian Journal of Earth Sciences*. **50**, 669–690.

Rowley DB, and Garzione CN. (2007) Stable Isotope-Based Paleoaltimetry. *Annual Review of Earth and Planetary Sciences**. 35***, 463–508.

Sharp ZD. (1990) A laser-based microanalytical method for the in situ determination of oxygen isotope ratios of silicates and oxides. *Geochimica et Cosmochimica Acta*. **54**, 1353-7.

Shuster DL, Vasconcelos, PM, Heim JA, and Farley KA. (2005) Weathering geochronology by (U-Th)/He dating of goethite. *Geochimica Et Cosmochimica Acta*. **69**, 659–673.

Simmons WB, Lee MT, and Brewster RH. (1987) Geochemistry and evolution of the South Platte granite-pegmatite system, Jefferson County, Colorado. *Geochimica et Cosmochimica Acta*. **51**, 455-71.

Snell KE, Koch PL, Druschke P, Foreman BZ, and Eiler JM. (2014) High elevation of the 'Nevadaplano'during the Late Cretaceous. *Earth and Planetary Science Letters*. **386**, 52-63.

Stolper DA and Eiler JM. (2015) The kinetics of solid-state isotope-exchange reactions for clumped isotopes: A study of inorganic calcites and apatites from natural and experimental samples. *American Journal of Science*. **315**, 363-411.

Taylor HP, and Epstein S. (1962) Relationship between O18/O16 ratios in coexisting minerals of igneous and metamorphic rocks: part 1: principles and experimental results. *Geological Society of America Bulletin*. **73**, 461-80.

Tobin TS, Wilson GP, Eiler JM, and Hartman JH. (2014) Environmental change across a terrestrial Cretaceous-Paleogene boundary section in eastern Montana, USA, constrained by carbonate clumped isotope paleothermometry. *Geology*. **42**, 351-4.

Unruh DM, Snee LW, Foord EE, and Simmons WB. (1995) Age and cooling history of the Pikes Peak batholith and associated pegmatites. In Geological Society of America Abstracts. **27**, 468.

Valley JW, Kitchen N, Kohn MJ, Niendorf CR, and Spicuzza MJ. (1995) UWG-2, a garnet standard for oxygen isotope ratios: strategies for high precision and accuracy with laser heating. *Geochimica et Cosmochimica Acta*. **59**, 5223-31.

Vasconcelos, PM, Heim JA, Farley KA, Monteiro H, and Waltenberg K. (2013) $^{40}Ar/^{39}Ar$ and (U–Th)/He – $^{4}He/^{3}He$ geochronology of landscape evolution and channel iron deposit genesis at Lynn Peak, Western Australia. *Geochimica Et Cosmochimica Acta*. **117**, 283–312.

Wolska E, and Schwertmann U. (1989) Nonstoichiometric structures during dehydroxylation of goethite. *Crystalline Materials*. **189**, 223-38.

Yapp CJ. (1983) Stable hydrogen isotopes in iron oxides—isotope effects associated with the dehydration of a natural goethite. *Geochimica et Cosmochimica Acta*. **47**, 1277-87.

Yapp CJ. (1987) Oxygen and hydrogen isotope variations among goethites (α-FeOOH) and the determination of paleotemperatures. *Geochimica Et Cosmochimica Acta*. **51**, 355–364.

Yapp CJ. (1990) Oxygen isotope effects associated with the solid-state α-FeOOH to α-Fe2O3 phase transformation. *Geochimica et Cosmochimica Acta.* **54**, 229-36.

Yapp CJ. (1993) Paleoenvironment and the oxygen isotope geochemistry of ironstone of the Upper Ordovician Neda Formation, Wisconsin, USA. *Geochim. Cosmochim. Acta.* **57**, 2319–27.

Yapp CJ. (1997) An assessment of isotopic equilibrium in goethites from a bog iron deposit and a lateritic regolith. *Chemical Geology*. **135**, 159–171.

Yapp CJ. (1998) Paleoenvironmental interpretations of oxygen isotope ratios in oolitic ironstones. *Geochim. Cosmochim Acta*. **62**, 2409– 20.

Yapp CJ. (2000) Climatic implications of surface domains in arrays of δD and $\delta^{18}O$ from hydroxyl minerals: goethite as an example. *Geochim. Cosmochim. Acta*. **64**, 20009–25.

Yapp CJ. (2003) A model for $^{18}O/^{16}O$ variations in CO_2 evolved from goethite during the solid-state α-FeOOH to α-Fe_2O_3 phase transition. *Geochimica et cosmochimica acta*. **67**, 1991-2004.

Yapp CJ. (2007) Oxygen isotopes in synthetic goethite and a model for the apparent pH dependence of goethite–water 18O/16O fractionation. *Geochimica et Cosmochimica Acta*. **71**, 1115–1129.

Yapp CJ. (2012) Oxygen isotope effects associated with substitution of Al for Fe in synthetic goethite: Some experimental evidence and the. *Geochimica et Cosmochimica Acta*. **97**, 200–212.

Yapp CJ. (2015) $^{18}O/^{16}O$ in CO_2 evolved from goethite during some unusually rapid solid state. *Geochimica et Cosmochimica Acta*. **170**, 1–16.

Yapp CJ, and Pedley MD. (1985) Yapp isotopes in iron oxides—II. variations among natural goethites. *Geochimica Et Cosmochimica Acta*. **49**, 487– 495.

Yapp CJ, and Poths H. (1993) The carbon isotope geochemistry of goethite (α-FeOOH) in ironstone of the Upper Ordovician Neda Formation, Wisconsin, USA: Implications for early Paleozoic continental environments. *Geochimica et Cosmochimica Acta*. **57**, 2599-611.

Yapp CJ, and Shuster DL. (2011) Environmental memory and a possible seasonal bias in the stable isotope composition of (U–Th)/He-dated goethite fromthe Canadian Arctic. *Geochimica Et Cosmochimica Acta*. **75**, 4194–4215.

Yapp CJ, and Shuster DL. (2017) D/H of late Miocene meteoric waters in Western Australia: Paleoenvironmental conditions inferred from the δD of (U-Th)/He-dated CID goethite. *Geochimica et Cosmochimica Acta*. **213**, 110-36.

Yuan D, Cheng H, Edwards RL, Dykoski CA, Kelly MJ, Zhang, M, and Cai Y. (2004) Timing, duration, and transitions of the last interglacial Asian monsoon. *Science*. **304**, 575-578.

Zachos J, Pagani M, Sloan L, Thomas E, an Billups K. (2001) Trends, rhythms, and aberrations in global climate 65 Ma to present. *Science*. **292**, 686–693.

Zheng YF. (1998) Oxygen isotope fractionation between hydroxide minerals and water. *Physics and chemistry of minerals*. **25**, 213-221.

Table 2.1: Reproducibility of bulk goethite oxygen isotope composition by resistance furnace heated fluorination

Sample	Mass (mg)	Yield* (%)	Blank† (%)	$\delta^{18}O_{furnace}$ (‰)	+/- (‰)	$\delta^{18}O_{laser}$ (‰)	± (‰)	$\delta^{18}O_{furnace-laser}$ (‰)
Yandi (02-01-A)	1.95	101	1.15	0.166	0.023	0.677	0.026	-0.511
	1.97	109	1.07	0.303	0.020			-0.374
	2.23	84	1.04	-0.039	0.028			-0.716
	2.74	89	0.82	-0.355	0.059			-1.032
	2.09	97	2.03	0.004	0.048			-0.673
	2.47	97	1.10	0.203	0.029			-0.474
Roy Hill (02-02-B3)	2.20	111	0.56	-1.859	0.022	-1.961	0.020	0.102
	2.37	108	0.36	-1.464	0.009			0.497
	1.84	114	1.05	-2.004	0.021			-0.043
	1.53	117	1.18	-2.095	0.032			-0.134
	2.49	98	0.57	-1.851	0.032			0.110
	2.12	110	3.14	-1.853	0.022			0.108

*Moles oxygen produced by sample fluorination expressed as a percentage of total moles oxygen prediced from sample mass

†Moles oxygen produced in procedural blank expressed as percentage of total moles oxygen produced in sample fluorination

Table 2.2: Dehydroxylation oxygen yield

Sample	Mass (mg)	Yield (%)	Blank (%)	$\delta^{18}O_{dehydroxylation}$ (‰)	+/- (‰)
Roy-02-02	18.6	25.6	1.93	-18.854	0.033
	16.1	24.1	2.36	-19.134	0.048
	10.1	17.6	5.02	-21.286	0.027
	16.8	27.2	2.01	-19.294	0.018
	15.3	21.6	2.75	-20.310	0.058

Table 2.3a: synthetic goethite bulk fluorination

Sample	Notes	Mass (mg)	Yield (%)	Blank (%)	$\delta^{18}O_{bulk}$ (‰)	+/- (‰)
S22-GOE-H-5	22 degrees, pH 2	2.07	68	2.85	3.655	0.022
		1.95	76	1.44	4.881	0.020
		2.29	63	2.51	2.982	0.012
		1.63	112	1.95	3.102	0.028
S22-GOE-K-5	22 degrees, pH 12	1.63	110	1.88	-0.175	0.034
		1.50	84	2.68	-0.477	0.041
S40-GOE-H-1	40 degrees, pH 2	1.68	95	1.56	1.682	0.025
S40-GOA-H-3	40 degrees, pH 2, Al-doped	2.08	98	1.17	3.178	0.033
		1.87	98	1.63	2.425	0.044
		1.93	81	2.71	1.812	0.021
		2.19	98	1.43	2.333	0.025
S70-GOA-H-3	70 degrees, pH 2, Al-doped	2.32	81	3.35	-0.700	0.039
		2.03	82	0.79	-0.455	0.020
S70-GOE-K-5	70 degrees, ph 12	1.87	103	2.29	-3.070	0.047

Table 2.3b: synthetic goethite dehydroxylation

Sample	Notes	Mass (mg)	Yield (%)	Blank (%)	$\delta^{18}O_{dehydroxylation}$ (‰)	+/- (‰)
S22-GOE-H-5	22 degrees, pH 2					
S22-GOE-K-5	22 degrees, pH 12	10.22	21	0.63	-16.860	0.020
S40-GOE-H-1	40 degrees, pH 2	7.11	12	6.61	-10.648	0.010
S40-GOA-H-3	40 degrees, pH 2, Al-doped	8.81	11	1.38	-9.907	0.033
S70-GOA-H-3	70 degrees, pH 2, Al-doped	7.87	10	2.44	-2.489	0.025
S70-GOE-K-5	70 degrees, ph 12	7.12	13	4.37	-5.611	0.027

Sample naming conventions:
S = temperature (celsius)
GOE = pure goethite
GOA = Al doped goehite (90:10 - Fe:Al)
K = precipitated in KOH base (pH 12)
H = precipitated in HNO_3 acid (pH 2)

Table 2.4: Synthetic goethite summary

Sample	Notes	Mean $\delta^{18}O_{bulk}$ (‰)	+/-* (‰)	$\delta^{18}O_{dehydroxylation}$ (‰)	+/- (‰)	$\Delta^{18}O_{bulk\text{-}dehydroxylation}$ (‰)
S22-GOE-H-5	22° C, pH 2	3.102	0.028			
S22-GOE-K-5	22° C, pH 12	-0.326	0.151*	-16.860	0.020	16.534
S40-GOE-H-1	40° C, pH 2	1.682	0.025	-10.648	0.010	12.330
S40-GOA-H-3	40° C , pH 2, Al-doped	2.437	0.281*	-9.907	0.033	12.344
S70-GOA-H-3	70° C, pH 2, Al-doped	-0.578	0.123*	-2.489	0.025	1.912
S70-GOE-K-5	70° C, ph 12	-3.070	0.047	-5.611	0.027	2.541

*Standard Error reported (Standard Error = Standard deviation of the population / Square root of the number of measurements)

Sample naming conventions:

S = temperature (celsius)

GOE = pure goethite

GOA = Al doped goehite (90:10 - Fe:Al)

K = precipitated in KOH base (pH 12)

H = precipitated in HNO_3 acid (pH 2)

Table 2.5: Mass balance

Sample S40GOEH1	Mass (mg)	Yield (%)	$\delta^{18}O$ (‰)	+/- (‰)
Dehydroxylation	7.11	12	-10.648	0.010
Residual	4.64	69*	5.188	0.018
Dehydroxylation+Residual			1.229	0.016
Bulk	1.68	95	1.682	0.025

Dehydroxylation+Residual calculation utilizes a value for VSMOW = 0.0020052 ($^{18}O/^{16}O$)

*Oxygen yield determined assuming hematite (Fe_2O_3) stoichiometry and normalized to origional goehite mass (i.e. stoitchiometric residulal = 75% yield).

Table 2.6: 275 Heating experiment

Sample Roy Hill (02-02-B3)	$\delta^{18}O_{bulk}$ (‰)	+/- (‰)	$\delta^{18}O_{dehydroxylation}$ (‰)	+/- (‰)	$\Delta^{18}O_{bulk\text{-}dehydroxylation}$ 2	$\Delta^{18}O$ Temperature (° C)	+/- (° C)
Un-equilibrated	-1.961*	0.020	-20.643	0.030	18.682	19	1.5
Equilibrated	-2.361†	0.020	-15.89	0.069	13.529	33	1.7

* Measured by laser fluorination

† Measured by furnace fluorinaton

Table 2.7: Natural goethite bulk fluorination

Sample	Mass (mg)	Yield (%)	Blank (%)	$\delta^{18}O_{furnace}$ (‰)	+/- (‰)	$\delta^{18}O_{laser}$ (‰)	± (‰)	$\delta^{18}O_{furnace-laser}$ (‰)
Yandi (02-01-A)	1.95	101	1.15	0.166	0.023	0.677	0.026	-0.511
	1.97	109	1.07	0.303	0.020			-0.374
	2.23	84	1.04	-0.039	0.028			-0.716
	2.74	89	0.82	-0.355	0.059			-1.032
	2.09	97	2.03	0.004	0.048			-0.673
	2.47	97	1.10	0.203	0.029			-0.474
Roy Hill (02-02-B3)	2.20	111	0.56	-1.859	0.022	-1.961	0.020	0.102
	2.37	108	0.36	-1.464	0.009			0.497
	1.84	114	1.05	-2.004	0.021			-0.043
	1.53	117	1.18	-2.095	0.032			-0.134
	2.49	98	0.57	-1.851	0.032			0.110
	2.12	110	3.14	-1.853	0.022			0.108
Roy Hill (02-02-Cy3)	2.24	not recorded	n/a	-1.811	0.019	-1.682	0.028	-0.129
	1.95	120	3.59	-1.721	0.028			-0.039
Yandi (02-02)						0.703	0.022	
Yandi (02-03)						0.976	0.028	
CIT-8809	2.86	99	1.19	-4.804	0.014			
DMNH-10029						2.124	0.074	
DMNH-14510	2.62	117	0.21	2.720	0.016			

Table 2.8: Natural goethite dehydroxylation

Sample	Mass (mg)	Yield (%)	Blank (%)	$\delta^{18}O_{dehydroxylation}$ (‰)	+/- (‰)
Yandi (02-02)	18.5	15	3.29	-20.806	0.031
	13.7	15	4.25	-19.999	0.017
Yandi (02-03)	16.2	24	2.31	-20.879	0.054
Yandi (02-01-A)	12.7	4*	2.25	-19.527	0.082
	6.2	17	0.88	-20.679	0.025
Roy Hill (02-02-B3)	10.1	7*	3.07	-19.556	0.019
	7.5	28	3.09	-20.643	0.030
Roy Hill (02-02-Cy3)	6.9	27	1.28	-20.040	0.010
CIT-8809	7.6	21	2.27	-25.017	0.02
DMNH-10029	25.8	20	2.64	-11.761	0.014
DMNH-14510	14.9	20	0.67	-8.535	0.025

*Heated to 190° C. See discussion.

Table 2.9: Natural goethite summary

Sample	Mean $\delta^{18}O_{bulk}$ (‰)	+/- (‰)	$\delta^{18}O_{dehydroxylation}$ (‰)	+/- (‰)	$\Delta^{18}O_{bulk\text{-}dehydroxylation}$ (‰)	$\Delta^{18}O$ Temperature (° C)	Age (Ma)	+/- (Ma)
DMNH-14510	2.720	0.016	-8.535	0.025	11.255	39	not dated	
DMNH-10029	2.124	0.074	-11.761	0.014	13.885	32	not dated	
CIT-8809	-4.804	0.014	-25.017	0.02	20.213	15	3.0	0.3
Yandi (02-03)	0.976	0.028	-20.879	0.054	21.855	11	12.0	1.2
Roy Hill (02-02-B3)	-1.961	0.020	-20.643	0.030	18.682	19	not dated	
Roy Hill (02-02-Cy3)	-1.682	0.028	-20.040	0.100	18.358	20	68.8	6.8
The following measurments are discarded due to low dehydroxylation yield:								
Yandi (02-01-a)	0.677	0.026	-20.679	0.025	21.356	12	11.3	1.1
Yandi (02-02)	0.703	0.022	-20.403	0.404	21.106	13	10.4	1.0

Table 2.10: New (U-Th)/He ages

	Corrected Age (Ma)	±	U (ppm)	Th (ppm)	He (nmol/g)	Mass (ug)
CIT-8809 A	3.1	0.3	35.31	0.03	0.59	43
CIT-8809 B	3.0	0.3	35.35	0.12	0.58	30
CIT-8809 C	2.7	0.3	34.68	0.03	0.51	59
CIT-8809 D	3.3	0.3	37.23	0.04	0.66	64
Mean	**3.0**		**35.6**	**0.1**	**0.6**	

Chapter 3

COMBINED HEMATITE (U-TH)/HE AND (U-TH)/NE AGES AND ^{4}HE/^{3}HE THERMOCHRONOLOGY OF THE IRON ORES OF GRIQUALAND WEST, SOUTH AFRICA

ABSTRACT

We have implemented the combined (U-Th)/He and (U-Th)/Ne chronometers to hematite from five different iron ore localities along a ~200 km transect paralleling the Blackridge thrust fault in the Griqualand West region of the Kaapvaal Craton, South Africa. Diverse hematite ages for Khumani (Ne 2018 ± 114 Ma, He 2048 ± 87 Ma), Beeshoek (Ne 1776 ± 97 Ma, He 1761 ± 39 Ma), Black Rock (Ne 1706 ± 141 Ma, He 1523 ± 61 Ma), Rooinekke (Ne 1497 ± 112 Ma, He 912 ± 42 Ma), and Belgravia (Ne 1234 ± 47 Ma, He 740 ± 15 Ma) indicate these samples do not share a single, regional history. These bulk Ne and He ages, when combined with the ^{4}He/^{3}He age spectra from the Beeshoek, Black Rock, and Belgravia localities, indicate there were at least three distinct Proterozoic events of supergene and hydrothermal Fe-enrichment. The earliest enrichment dates back to 2.2 to 2.0 Ga, which is recorded by the Khumani and Belgravia ore bodies. These He-Ne ages indicate remarkable preservation at these localities and represent the oldest published hematite He-Ne ages thus far. The dissolution of silica and carbonate phases from parent BIF, along with Fe oxidation and hematite mineralization, are indicative of oxidative weathering occurring during a 2.2 – 2.0 Ga (pre-Gamagara) erosional unconformity. Following this initial hematite ore formation, time-temperature

modeling and He-Ne ages suggest deposition of 4-7 km of sediment that resulted in burial heating and possible fluid-mediated recrystallization in our northern samples. A second phase of hematite ore formation by hydrothermal fluid circulation occurred during the Kheis Orogeny. Time-temperature modeling indicates very slow erosion rates and extreme tectonic stability in the Griqualand West region of the Kaapvaal Craton over the last billion years, leading to the preservation of age constraints for low-temperature mineralization processes for over 2 billion years.

I. INTRODUCTION

The Transvaal Supergroup is a sequence of sedimentary and volcanic rocks providing some of the best-preserved geologic records from the late Archean through early Paleoproterozoic (2.67 – 2.05 Ga) (Eriksson et al., 2006; Sumner and Beukes, 2006; Beukes and Gutzmer, 2008). The Transvaal Supergroup documents a period of significant, global environmental change, including the Great Oxidation Event and Snowball Earth style glaciations (Holland and Beukes, 1990; Evans et al., 1997; Hoffman, 2013; Gumsley et al., 2017). Furthermore, the Transvaal Supergroup contains vast reserves of mineable resources, including abundant Fe-upgraded banded iron formations (BIFs) and ~78% of the world's subaerially accessible Mn ore (Beukes and Gutzmer, 2008; Beukes et al., 2016; Smith and Beukes, 2016).

The formation of Fe-upgraded hematite orebodies has been linked to extensive terrestrial weathering of underlying Archean-Paleoproterozoic boundary BIFs, thought to have taken place shortly after the rise of atmospheric oxygen (Rye and Holland, 1998;

Gutzmer and Beukes, 1998; Evans et al., 2001; 2002; Beukes and Gutzmer, 2008; Smith and Beukes, 2016; Gumsley et al., 2017). Despite considerable efforts, the timing of environmental change and related Fe ore formation is poorly constrained and contentious due to sparse and conflicting geochronometric measurements (Cornell et al., 1996; Cornell et al., 1998; Bau et al., 1999; Evans et al., 2001; 2002; Gnos et al., 2003; Moore et al., 2011; Hoffman, 2013; Gumsley et al., 2017). This study utilizes orebody hematite samples produced by supergene and metamorphic/hydrothermal Fe-upgrading of BIFs in the Griqualand West region to investigate the timing of ore formation as well as the long-term thermal history of this ancient craton.

The implementation of hematite geo- and thermochronometry is possible due to the incorporation of ~ppm levels of uranium and thorium and the high He – Ne retentivity of hematite (Farley, 2018). The combination of (U-Th)/He and (U-Th)/Ne chronometry allow for two related ages to be obtained, where the Ne system provides a valuable higher temperature constraint, potentially a formation age, on the age of a specimen and the He system provides a cooling age (Farley and Flowers, 2012; Farley and McKeon, 2015). Additionally, the hematite $^{4}He/^{3}He$ method can be applied to constrain the time-temperature history of that sample. Hematite typically consists of an aggregate of crystallites that vary in size by orders of magnitude, and each crystallite has a corresponding He closure temperature that is size dependent (Farley, 2018). Utilizing this variation in closure temperature, the $^{4}He/^{3}He$ method can constrain the thermal history of a hematite sample over a wide range of geologic temperatures. For the application of these methods, the following assumptions must apply: partial recrystallization cannot have taken

place as that would lead to partial loss of daughter He, crystallite size distribution cannot change through time, the system must remain closed with respect to U and Th, the distribution of U and Th cannot correlate to crystallite size, and mineralogically pure hematite specimens are required. Here, we apply these methods to hematites from the Griqualand West region of the Kaapvaal Craton. Billions of years of tectonic activity on the margin of an ancient craton, including a period of deep and prolonged burial, is the most challenging environment yet studied with these methods.

II. GEOLOGIC BACKGROUND

The Transvaal Supergroup consists of siliciclastic, carbonate, and iron formation-bearing strata in three major areas on the Kaapvaal craton, namely Griqualand West, Transvaal, and Kanye regions (Figure 3.1). The deposition of the Transvaal Supergroup

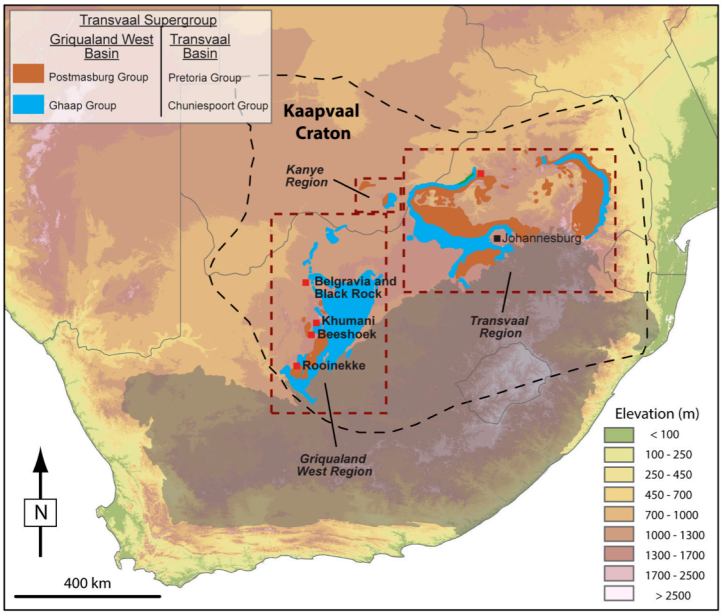

Figure 3.1: DEM of southern Africa showing a simplified geological map of the Transvaal Supergroup and sample locations (Adapted from Eriksson et al., 2006; Smith and Beukes, 2016; Smith, 2018).

was preceded by a period of intense crustal melting, plutonism, and extensional tectonics around 2.7 Ga, which produced the Ventersdorp Supergroup (Schmitz and Bowring, 2003). This intracratonic lithospheric thinning provided space for Transvaal sediment accumulation (Schmitz and Bowring, 2003). This exceptionally well-preserved succession has been of great economic significance and scientific interest, largely due to its record of the initial rise in atmospheric oxygen (Holland and Beukes, 1990; Gutzmer and Beukes, 1998; Bekker et al., 2004; Gumsley et al., 2017).

The Paleoproterozoic portion of the Transvaal Supergroup consists of a series of basin-scale iron formations, punctuated by volcanic and siliciclastic units, most notably a possible Snowball Earth glacial diamictite (Makganyene Formation; ≤2436 ± 14 Ma) (Evans et al, 1997; Gumsley et al., 2017) and the Ongeluk lava (2424 ± 32 Ma) (Gumsley et al., 2017). The Kuruman and Griquatown Iron Formations lie within the Asbestos Hills Subgroup (2521 ± 3 to ≥2426 ± 1 Ma), while the Rooinekke Iron Formation (≥2436 ± 14 Ma) resides within the overlying Koegas Subgroup, all within the Ghaap Group (Sumner and Beukes, 2006; Beukes and Gutzmer, 2008; Gumsley et al., 2017; Smith, 2018).

The Ghaap Group is overlain by the Postmasburg Group, which includes the aforementioned Makganyene Formation glacial diamictite and Ongeluk Formation lava, along with the iron and manganese Hotazel Formation (≥2292 ± 23 Ma) (Sumner and Beukes, 2006; Beukes and Gutzmer, 2008; Gumsley et al., 2017). As our hematite samples are epigenetic to the deposition of parent BIF, we restrict our focus to the post-depositional geologic history of the Transvaal Supergroup. Depositional models of Archean-Paleoproterozoic supracratonic BIFs can be found in Klein (2005) and Beukes

and Gutzmer (2008). A thorough review of the depositional timing of the units within the Transvaal Supergroup can be found in Nelson et al. (1999) and Sumner and Bowring (1996).

After its initial deposition, the Transvaal Supergroup was subjected to a series of significant Paleoproterozoic tectonic and thermal events. The oldest of these is the Bushveld Igneous Complex (BIC) centered in the Transvaal region (Figure 3.1), a massive 2.05 Ga layered intrusion that imparted a significant thermal signature on the surrounding region (Eglington and Armstrong, 2004). Mineralization associated with hydrothermal fluid flow is prevalent in the Transvaal and Witwatersrand Supergroups, at distances up to a hundred kilometers from the margin of the BIC, based on monazite and xenotime U/Pb ages (Rasmussen et al., 2007). Furthermore, Mississippi Valley type (MVT) deposits are found in the Griqualand West region, over 700 km from the margins of the BIC (Gleason et al., 2011). Paleomagnetic study of MVT deposits in Griqualand West document a widespread 2050-2000 Ma remagnetization event (de Kock et al., 2009). Whether these MVT deposits are the result of BIC-related hydrothermal fluid flow traveling through the Transvaal Supergroup (Gleason et al., 2011), the result of brines sourced from the underlying Ventersdorp Supergroup with little magmatic contribution (Duane et al., 2004), or some combination thereof, is debated. The BIC produced an elevated paleo-geothermal gradient in the Transvaal region (Figure 3.1) (Jones, 1988; Gibson and Jones, 2002). However, a shallow cratonic geothermal gradient of 15-20 °C has been interpreted for the Griqualand West region (Jones, 1988; Gibson and Jones, 2002; Schmitz and Bowring, 2003).

The Griqualand West region, while containing BIC signatures, more dominantly records a ~2.2 to ~2.0 Ga erosional unconformity, called the pre-Gamagara unconformity (Dalstra and Rosiere, 2008; Smith and Beukes, 2016). The development of this unconformity produced a Fe-rich weathering profile in the rocks immediately below. Due to the gently folded nature of the underlying strata, this paleo-weathering surface cuts across a wide variety of Transvaal units. Where the unconformity transected BIF, high-grade hematite ore developed (Figure 3.2) (Smith and Beukes, 2016). Following this pre-

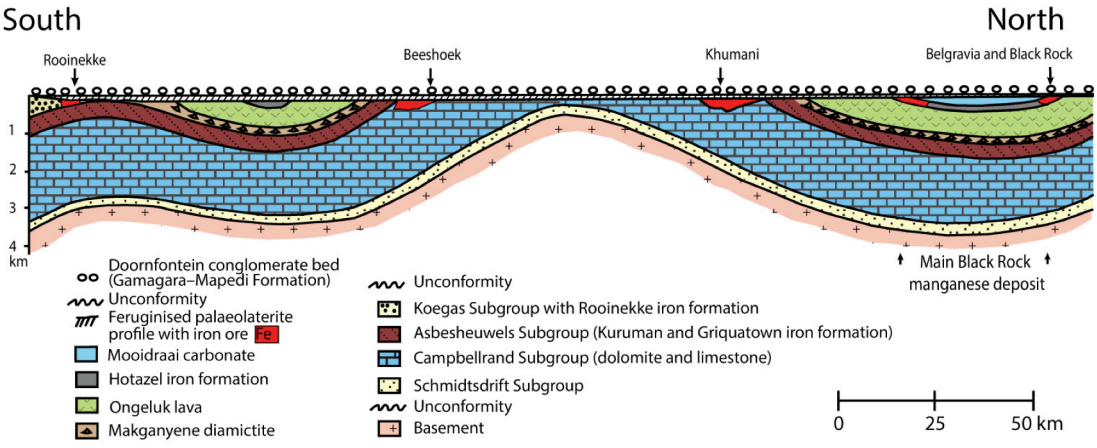

Figure 3.2: Generalized North-South cross-section of the Griqualand West sequence paralleling the Black Ridge thrust fault. Subsurface dips are exaggerated for illustrative purposes. This study's samples all source from iron ore bodies where significant Fe-upgrading has occurred.

Gamagara supergene Fe-upgrading, a final succession of Transvaal Supergroup rocks, the Elim Group, was deposited atop the folded and lateritized Transvaal sequence. The Elim includes the Gamagara-Mapedi and Lucknow formations, with a total estimated thickness of ~2 km (Van Niekerk, 2006). Following the Transvaal Supergroup is the Keis Supergroup, a series of units accumulated along a passive continental margin on the western edge of the Kaapvaal Craton (Eglington, 2006; Van Niekerk, 2006). Note that

here we use Keis to denote the Supergroup sequence, while we refer to the tectonic terrain west of the Kaapvaal as the Kheis Province.

The Keis is comprised of the Olifantshoek, Groblershoop, and Wilgenhoutsdrif groups (Van Niekerk, 2006). The Olifantshoek is dominated by fluvial red beds, deposited off the western margin of the Kaapvaal Craton as rifting initiated (Cornell et al., 1987; Moen, 2006; Van Niekerk, 2006). The total thickness of the Olifantshoek Group is estimated to have been 4-5 km in the Kheis Province, although possibly thinner atop the western Kaapvaal where this study's samples originate. The Olifantshoek is correlative to the Waterberg red bed succession that likely covered much of the Kaapvaal at some stage by a similar 4-5 km thickness (Barker et al., 2006; McCarthy et al., 2018). The Hartley Formation, a basalt unit near the base of the Olifantshoek Group, provides one of the few age constraints for the deposition of this sequence. Zircons from thin quartz-porphyry lavas interbedded with the basalt have a U/Pb age of 1915.6 ± 1.4 Ma (Cornell et al., 2016).

The Groblershoop Group overlies the Olifantshoek and represents further rifting of the basin, where a thick succession of shallow and near-shore, quartz dominated sediments was deposited (Van Niekerk, 2006). Estimates for the total thickness of the Groblershoop Group is upwards of 12 km (Van Niekerk, 2006). The Wilgenhoutsdrif Group lies unconformably on the Groblershoop and is comprised of a sequence of carbonates, siliciclastics, and volcanics (Van Niekerk, 2006). This back-arc basin sequence is estimated to have had a total thickness of nearly 4 km (Van Niekerk, 2006).

The Keis Supergroup and Kheis Province have remained enigmatic to investigators. The terrane itself is a thin-skinned fold and thrust belt that forms a transition zone between the Kaapvaal Craton and the highly metamorphosed Namaqua-Natal orogenic belt, whose western portion we here refer to as Namaqualand (Beukes and Smit, 1987; Eglington and Armstrong, 2004; Van Niekerk, 2006). The exact boundary between the Kaapvaal Craton and the Kheis terrane is disputed, historically drawn at the Blackridge Thrust (Beukes and Smit, 1987; Cornell et al., 1998; Van Niekerk, 2006), but often considered the Dabep fault (Moen, 1999; Cornell et al 2006), located to the west of the Blackridge Thrust. However, recent geophysical investigations have shown there is no indication of a major structural boundary at the Dabep (Corner and Durrheim, 2018).

The timing of deposition, deformation, and metamorphism within both the Kheis Province and Namaqualand also remain debated. Early investigators reported an Ar-Ar age of 1780 Ma for the Keis Groblershoop Group (Burger and Coertze, 1975). Later investigators also reported 1.8 Ga ages suggestive of deformation and metamorphism in the Kheis at this time (Cornell et al., 1998; Moen, 1999). However, the majority of chronometers record much younger ages in the Kheis Province. Moen and Armstrong (2008) report a zircon U-Pb age of 1290 ± 8 Ma from a deformed rhyolite in the Wilgenhoutsdrif Group. Furthermore, the 1293 ± 9 Ma Kalkwerf Gneiss intrudes the rocks of the Groblershoop Group and shares the same deformation fabric as the surrounding metasediments (Van Niekerk, 2006; Moen and Armstrong, 2008). 1293 Ma can therefore be considered an upper age constraint on this generation of Kheisian deformation. Unconformably overlying the Keis Supergroup is the 1171 ± 7 Ma, undeformed Koras

Group, which provides a lower limit on the timing of this deformation (Gutzmer et al., 2000). However, it remains a possibility that the 1293 - 1171 Ma deformation overprints a prior period of tectonism.

The most significant Proterozoic tectono-thermal event is associated with the orogeny accompanying the assembly of Rodinia as recorded by the Mesoproterozoic Namaqua-Natal Belt (Van Niekerk, 2006; Eglington, 2006). The crust was thickened by 20-25 km from structural stacking and regional-scale intrusions (Coliston et al., 2017). The Namaqualand igneous units intruded between ~1.3 and ~1.2 Ga (Eglington, 2006). This was followed by the initiation of subduction-related metamorphism, which produced a suite of supracrustal gneisses (Jacobs et al., 1993) during a period of high-grade metamorphism at ~1.16 Ga (Eglington, 2006). A suite of muscovite Rb-Sr ages collected across the Kheis Province cluster around 1160 Ma, with notable outliers at 1572 and 1390 (Moen and Armstrong, 2008). Ar-Ar age determinations on muscovites from both Kheis Province and Namaqualand consistently cluster at 1116 Ma (Van Niekerk, 2006).

The accretionary process appears to have been completed in Namaqualand between 1.1 and 1.0 Ga (Eglington, 2006; Van Niekerk, 2006; Moen and Armstrong, 2008). Recent interpretations of the chronology of units within the Kheis Province consider this terrain a precursor to the more significant period of tectonism associated with the Namaqua-Natal Belt (Van Niekerk, 2006; Eglington, 2006; Moen and Armstrong, 2008). Following a period of quiescence, Rodinia began to breakup by ~700 Ma (Hoffman, 1991; Powell et al., 1993). The assembly of Gondwana occurred between 570-

530 Ma and placed the Kaapvaal Craton at the center of the supercontinent (Hoffman, 1991; Meert, 2003).

Early Paleozoic rifting at the margins of southern Africa resulted in the deposition of a thick succession of continental and marine clastic sediments known as the Cape Supergroup (Tankard et al., 1982). Subduction-related orogenesis produced the Cape Fold Belt that was responsible for the coincident development of a retroarc foreland system, which accommodated the space for the deposition of the Karoo Supergroup (Catuneanu et al., 2005). The Karoo blanketed much of South Africa in a thick succession of fluvial and shallow marine deposits between the Late Carboniferous and Middle Jurassic (Catuneanu et al., 2005). Laterally continuous, silt-dominated marine diamictites with glacial dropstones indicate a shallow, low energy seaway extended all the way to the western edge of the Kaapvaal Craton in the Late Carboniferous (Catuneanu, 2004). Continental rifting associated with the breakup of Gondwana produced the Karoo volcanism at 185-180 Ma (Jourdan et al., 2005). (U-Th)/He dating of accessory phases in kimberlites finds these unique features to have been emplaced between ~140-70 Ma (Stanley et al., 2013; Stanley and Flowers, 2016). These (U-Th)/He ages are in agreement with Rb-Sr (Allsopp and Barrett, 1975), U-Pb (Smith et al., 1994), and $^{40}Ar/^{39}Ar$ (Phillips et al., 1998) ages for kimberlite emplacement. The southern African Plateau exists today with an elevated, low-relief interior, and a high-relief boundary surrounded by a passive continental margin (Flowers and Schoene, 2010). The mechanism responsible for producing this high-elevation, relatively undeformed plateau is still debated (Maud and Partridge, 1987; Gurnis et al., 2000; de Wit, 2007; Braun et al., 2014; Green et al., 2017).

While a great deal of effort has focused on understanding the evolution of the high-relief plateau margin, coined the Great Escarpment, there is a much smaller body of work aimed at understanding the evolution of the plateau interior. Flowers and Schoene (2010) found that apatite (U-Th)/He ages along the eastern margin of the craton permit less than 850 meters of Cenozoic unroofing. Apatite (U-Th)/He ages from kimberlites at the edge of the Kaapvaal Craton indicate spatially variable erosion (Stanley et al., 2013). The apatite data permit 1.0 – 1.5 km localized unroofing post-45 Ma along the paleo-Koa River, located on the SW margin of the craton (Stanley et al., 2013). Finally, Braun et al. (2014) estimated 2 – 3 km of denudation has occurred since the Cretaceous by estimating the quantity of Kaapvaal sediments found in offshore, marine sequences.

This lengthy geologic summary speaks to the complex history of Griqualand West and surrounding regions. The aim of this study is to obtain formation and/or cooling ages of BIF hosted iron deposits within the late Archean through early Paleoproterozoic Transvaal Supergroup. In addition, we seek to utilize the $^{4}He/^{3}He$ method in conjunction with existing geologic constrains to further reveal the geologic history of the region. These deposits are interpreted to have formed by supergene and/or metamorphic/hydrothermal leaching of silica under oxidizing conditions (Smith and Beukes, 2016). While this section is meant to serve as a useful framework for interpreting the geo- and thermochronologic results of this study, we remain cognizant that the Fe-upgrading of hematite ore bodies may have occurred at any point in this history and need not be correlated to known tectono-thermal events (Farley and McKeon, 2015).

III. SAMPLES AND METHODS

3.1 Samples

All samples were collected either from mining operations or borehole exploration in the Griqualand West region. Figure 3.3 shows the laminated texture of the Khumani

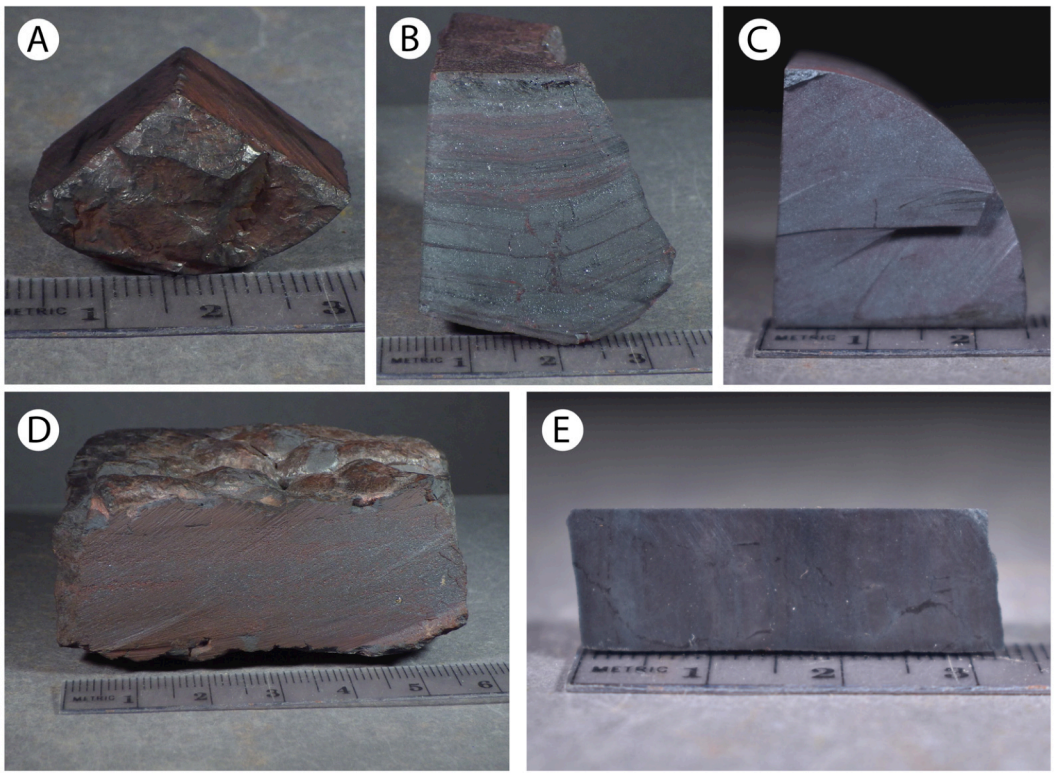

Figure 3.3: Photos of the Belgravia (A), Khumani (B), Beeshoek (C), Rooinekke (D), and Black Rock (E) hand samples used in this study.

sample (panel B), while the remaining samples (panel A, C, D, and E) consist of massive ore, interpreted to have formed from the Fe-upgrading of muddy BIFs (e.g. Fe-lutite) (Beukes and Gutzmer, 2008). The Khumani sample was collected in the open pit of the Khumani mine (GPS: -27.864 S, 23.013 E). The Beeshoek sample comes from borehole QK2/90 at 105 meters depth (-28.284, 23.011). The Rooinekke sample was collected in

the open pit of the Rooinekke Mine (-28.872, 22.718). The Black Rock sample comes from borehole N64 (-27.139, 22.862) at 699 meters depth. The Belgravia sample comes from borehole 99H at the Belgravia Farm locality (-27.162, 22.852) at 584 meters depth. At these depths, both the Belgravia and Black Rock core samples came from the footwall of the Blackridge Thrust (Beukes and Smit, 1987).

We utilized a Scanning Electron Microscope (SEM) with an attached X-ray energy dispersive spectrometer (EDS) to assess sample purity. We determined our samples to be dominated by stoichiometric hematite (69.94 wt% Fe), with Fe contents of 70 ± 2 wt% in all samples. EDS elemental analysis provides relative accuracy of a few wt% and small deviations in measured Fe contents from that of stoichiometric hematite should not, alone, cause concern for the He-Ne method. In the Black Rock and Beeshoek sample, we detected Si and Al content below the 1 wt% level. The Belgravia sample had a dispersed Mn content of 1-2 wt%. The Khumani sample is dominated by stoichiometric hematite, although we identified regions with Si-rich banding. Supplementary Figure 3.6 illustrates one such region, which has an EDS mapped Si content of 7.5% wt% (the band itself presumably much higher). He-Ne measurements utilize ~100 mg aliquots, drawn from grams of prepared crushate (see Methods below), and it is likely that even through careful sample preparation, some of these Si rich zones were sampled.

3.2 Methods

The (U-Th)/He chronometer has been developed for multiple Fe-oxide phases, including hematite (Lippolt et al., 1993), goethite (Shuster et al., 2005), and magnetite

(Blackburn et al., 2007). In oxygen-bearing minerals, the production of ^{4}He by α decay is accompanied by the far less common production of nucleogenic ^{21}Ne by the reaction $^{18}O(\alpha,n)^{21}Ne$. The yield of this reaction is governed by the α particle capture cross section of ^{18}O and the α particle stopping power of the mineral. Production rate estimates (Gautheron et al., 2006) and subsequent experimental confirmation (Cox et al., 2015) predict a $^{21}Ne/^{4}He$ production ratio of 2.8×10^{-8} in hematite and allows for the implementation of the (U-Th)/Ne chronometer.

In minerals where the (U-Th)/He system has been extensively applied for thermochronology (e.g. apatite, zircon), the temperature-dependent loss of He by diffusion is governed by the size of the analyzed specimen (Farley, 2000). However, most hematite samples consist of an aggregate of crystallites, which can vary in size by orders of magnitude within a single sample (Farley, 2018). In this case, the crystallites act as individual diffusion domains while the crystallite grain boundaries can be considered infinitely fast pathways for diffusive loss. Therefore, in addition to temperature, the size distribution of crystallite domains within a hematite sample controls He diffusion. By applying the $^{4}He/^{3}He$ method to hematite samples, we can model the crystallite domain size distribution within a sample, then, in combination with an age spectrum, model the time-temperature history of that sample (Farley and Flowers 2012).

The analytical methods of this study closely follow those of Farley and Flowers (2012) and Farley and McKeon (2015). A large initial aliquot (tens of grams) of each hematite sample was crushed with a mortar and pestle then wet sieved to separate the 100

– 500 μm size fraction. A few cm scale pieces of sample were cut, mounted, and polished for secondary electron microscope (SEM) analysis.

3.2.1 He and Ne dating

We implemented a two-aliquot method for He and Ne dating where noble gas concentrations are measured on a separate aliquot from U and Th determinations. We encapsulated ~100 mg of the 100 – 500 μm size fraction hematite crushate in a tin foil ball and placed it in the sample introduction system of a double walled vacuum furnace. Samples were evacuated overnight (>12 hours), but not baked. Within the double wall furnace, a molybdenum crucible was filled with 5 grams of 50:50 lithium metaborate:lithium tetraborate flux to aid in the extraction of the noble gases. Previous use of this flux method in hematite He and Ne analyses show quantitative extraction of both gases from samples with no meaningful increase in procedural blank He or Ne (Farley and McKeon, 2015). The flux-loaded liner was slowly ramped to 1000° C then held there for ~30 minutes. This slow ramp helps prevent bubbling and splashing of the flux. Once initially degassed, the flux can tolerate rapid temperature changes without consequence. Samples were loaded into a side arm of the vacuum system with a 12 sample cup, magnetically driven linear motion feedthrough. This allows for samples to be held at ultrahigh vacuum yet remain isolated from the hot furnace before being successively dropped into the degassed flux for He and Ne extraction. Sample degassing occurred by heating to 1000° C over 20 minutes then an additional hold time at 1000° C for 15 minutes while exposed to a pass-through, charcoal trap held at liquid nitrogen temperature.

The extracted gas was then introduced to the vacuum processing line where it was split 75:25 for neon and helium analysis, respectively. The neon analysis split was exposed to hot and cold SAES NP10 getters and a second charcoal trap held at liquid nitrogen temperature. The neon was cryofocused on charcoal at 21 K before being desorbed at 68 K and inlet into a GV Helix-SFT mass spectrometer. ^{20}Ne and ^{21}Ne were measured on a pulse-counting electron multiplier by accelerating-voltage controlled peak-hopping at a fixed magnetic field. No isobaric correction was made for ^{20}Ne (pseudo-resolved from $^{40}Ar^{+2}$) or ^{21}Ne. Once the neon split was inlet to the GV Helix-SFT, the remaining gas in the extraction line was introduced to the vacuum processing line. Following exposure to hot and cold SAES NP10 getters, He was cryofocused at 14 K and released at 34 K before being inlet for analysis on a MAP 215-50 mass spectrometer.

Instrument sensitivity and isotopic fractionation were determined using a manometrically calibrated standard of terrestrial atmosphere doped with commercial He. All standard analyses are treated identically to samples, including the split fraction used for Ne and He analyses. Cold blanks were subtracted from hot blanks, standards, and sample analyses. No hot blank correction was made for Ne because the nucleogenic neon ($^{21}Ne^*$) component of sample neon was determined by subtraction of the air derived ^{21}Ne based on the measured atmospheric air standard composition and assuming all sample-derived ^{20}Ne is atmospheric. Typical neon hot blanks ranged from 5 - 10 pcc ^{20}Ne, and 0.01 to 0.05 pcc ^{21}Ne (1% to 2% of sample measurements). Hot blanks, when corrected for cold blanks and the atmospheric component, yield no detectable $^{21}Ne^*$. No hot blank correction was needed for helium analyses due to the extraordinarily high abundance of

^{4}He in ~100 mg sample aliquots. Given that these samples were all collected in mines below the attenuation depth of cosmic rays, no correction is made for cosmogenic ^{21}Ne or ^{3}He, and He age calculations assume no excess ^{4}He was contributed by fluid or mineral inclusions. Age uncertainties were calculated using a Monte Carlo approach that combines the uncertainty associated with the noble gas concentrations (in decreasing order of importance: sensitivity calibration of the mass spectrometer measurements, the volume fraction used for Ne and He gas splits, the blanks, and the mass spectrometer peak heights), with the parent isotope concentrations. In the case of Ne ages, the 3% uncertainty in the nucleogenic neon production rate is also incorporated (Cox et al., 2015).

3.2.2 ^{4}He/^{3}He analysis

The ^{4}He/^{3}He method requires both an age spectrum and diffusion kinetics. Here, a separate aliquot of sample (~20 mg) was crushed, rinsed in ethanol to remove fines, then proton irradiated to produce a uniform, artificial distribution of ^{3}He (Shuster et al., 2004). The samples were irradiated at the Frances Burr Proton Therapy Center at Massachusetts General Hospital with a 220 MeV proton beam and received a total fluence of ~4x10^{15} protons/cm^{2}. We utilized two aliquots of 2-5 mg irradiated material for the ^{4}He/^{3}He hematite method. The first aliquot was placed in a copper packet and mounted directly on a thermocouple wire and heated using a projector lamp apparatus (Farley et al., 1999) to temperatures not exceeding 500° C, including both prograde and retrograde steps. The temperature range achievable with the projector lamp apparatus produces the majority of data points shown in the Arrhenius plot of any given sample. For steps exceeding 500° C, a diode laser was used to heat the sample. In this setup, the sample remains within the

original copper packet but is placed within a 5 mm diameter alumina capsule through which the thermocouple penetrated. This capsule serves to distribute heat produced from the diode laser to more uniformly heat the sample packet to the desired temperature. Near-complete extraction of helium occurred by laser heating up to 1000° C, but a final, furnace step was performed following the step-heating procedure described above to ensure complete He extraction. Extracted He was purified and analyzed as previously described.

A second aliquot of irradiated material was heated using the double-walled vacuum furnace to produce a $^{4}He/^{3}He$ age spectrum. The sample-specific diffusion kinetics were determined from our first aliquot, then forward-modeled to design a heating scheme that would produce subequal ^{3}He yields from each heating step. While the temperature range most useful for determining diffusion coefficients is low (<500° C), the majority of our sample's ^{3}He and ^{4}He reside in domains retentive to He diffusion over laboratory time scales at these temperatures. By using the furnace on this second aliquot, we can produce a ~20 step, near equal-yield $^{4}He/^{3}He$ age spectrum based on the sample-specific diffusion kinetics in ~24 hours and up to 1200° C, all without changing heating methods from lamp to laser to furnace. We also take advantage of the far higher temperature accuracy of the lamp cell compared to the furnace when establishing the diffusion parameters.

$^{4}He/^{3}He$ data were converted to step ages using the bulk $^{4}He/^{3}He$ ratio observed from all steps and the bulk He age (the result of the previously described method utilizing unirradiated sample). Step-age uncertainties were calculated using a Monte Carlo

approach factoring in observed uncertainty of the He bulk age, the cold blank, and the mass spectrometer peak height measurements.

3.2.3 U and Th analysis and He and Ne Ages

A pair of separate aliquots of the 100 – 500 μm crushate was analyzed for U, Th, and Sm concentration by isotope dilution inductively-coupled mass spectrometry following the procedure of Farley and Flowers (2012). Aliquots of ~25 mg were dissolved in boiling HCl overnight, diluted with ultrapure water, volumetrically split, and spiked with ^{230}Th and ^{235}U. We implemented this large aliquot procedure to appropriately average over a quantity of sample comparable to our aliquots used for He and Ne analysis. A small quantity of transparent, skeletal residue was present following HCl dissolution of the Khumani sample. We interpret this material to be the phase contributing the ~7% Si content identified in SEM EDS mapping. Neon ages were computed using the production rates of Cox et al. (2015). We made no corrections for alpha or ^{21}Ne redistribution (Gautheron et al., 2006) given the mineralogical purity and large size (>10 cm) from which the samples were prepard.

3.2.4 Extracting a time-temperature history

3.2.4.1 Determining the domain size distribution

The simultaneous degassing of polycrystalline systems will produce non-linear Arrhenius arrays dependent on heating schedule (Farley and Flowers, 2012; Farley, 2018). This manifests as a reduction in diffusivity at any given temperature as the diffusion experiment proceeds while activation energy remains constant (Farley, 2018). The offset in diffusivity between a reference line with a slope corresponding to the activation energy

of the material and a given step can be plotted against cumulative fraction of ^{3}He released to produce a Delta plot (Farley, 2018). Implementing a hematite PCD model (Farley 2018), allows for the calculation of a distribution of domain sizes and corresponding closure temperatures that would produce the experimentally observed Delta plot.

Following the methods described by Farley and Flowers (2012), the fractional yield of each heating step, in combination with the cumulative yield, can be used to define a small number of discrete-sized domains using the standard diffusion equations of Fechtig and Kalbitzer (1966). We fit our experimental data using contributions modeled from 8 domains. In some cases, fewer domains would have been adequate (see later discussion). We also tested fitting our data with more domains, but saw insignificant improvements in the goodness of fit.

The PCD model is used to determine D_o/a^2, the activation energy (E_a), and the domain size distribution. When modeling time-temperature paths, we implemented a fixed activation energy of 171 kJ/mol for all our samples. This specific activation energy was determined on a unique, single domain crystal of hematite (Farley, 2018) and is consistent, within error, with the activation energy determined from the majority of hematite diffusion experiments. E_a, as determined by regressing through retrograde heating steps from individual hematite samples in this study, is shown for comparison in Figure 3.4. Furthermore, we ran our time-temperature model using both sample-specific E_a and the single crystal hematite value of 171 kJ/mol and found no meaningful variation in the results (see description of T-t modeling methods below).

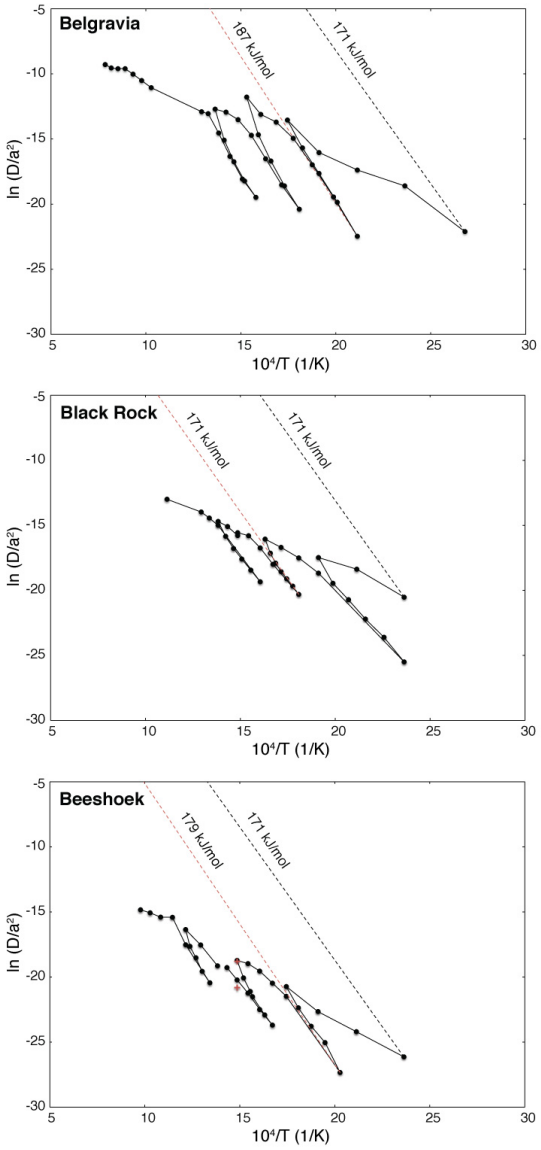

Figure 3.4: Arrhenius arrays from ^{3}He diffusion experiments for the Belgravia, Black Rock, and Beeshoek samples. The experiment progresses from lower right, along the solid black line connecting the calculated diffusivity from each heating step. The series of prograde and retrograde heating steps produces a zig-zag pattern. However, the retrograde sequences within each sample's Arrhenius array have a nearly identical slope (activation energy). The first few heating steps, where diffusivity rapidly changes, and the final fusion step are omitted. The dashed black line originating from the first plotted diffusion measurement reflects the activation energy from Farley (2018). This can be compared to the sample-derived activation energy shown as a dashed red line. The Belgravia array also illustrates the quantity Delta, measured as the vertical offset between a reference line and data point. The red crosses represent poor temperature control while switching from lamp to diode laser heating schemes and therefore are omitted from the Beeshoek Arrhenius array.

3.2.4.2 Forward modeling of time-temperature paths

Following the principles of Farley and Flowers (2012), we combined the data from the domain-size distribution and age spectrum to forward model our experimental results into a time-temperature path. This was accomplished using a slightly modified version of the $^{40}Ar/^{39}Ar$ function of QTQt. QTQt implements a Bayesian transdimensional Markov Chain Monte Carlo method to inverse model a best fitting time-temperature path (Gallagher, 2012). The $^{40}Ar/^{39}Ar$ function of QTQt is equipped to model multiple domains within a single sample following the feldspar MDD model (Lovera et al., 1989). The model inputs are D_o/a^2, E_a, and domain distribution, along with the age spectrum. The modeling function for MDD $^{40}Ar/^{39}Ar$ age spectrum data in QTQt was initially equipped to accumulate daughter product Ar using the ^{40}K decay constant. At the first author's request, Kerry Gallagher added a function to implement the ^{238}U decay constant and accumulation of daughter ^{4}He. Given the close similarity in results between thermal histories generated using the ^{40}K decay constant and those resulting from the ^{238}U decay constant, we considered the addition of code to accommodate ^{232}Th, which contributes modestly to both ^{4}He and ^{21}Ne, to be unnecessary (Supplemental Figures 3 and 4).

IV. RESULTS

4.1 He and Ne ages

Results from He, Ne, U, and Th concentration measurements are shown in Table 3.1. 16 aliquots from 5 samples were analyzed for He and Ne concentrations, along with a separate pair of aliquots from each sample for U and Th concentration. Replicate U and

Th concentrations were within 2s for each sample. Samples had U and Th concentrations between 0.25 and 1.1 ppm each. When combined with He concentrations of 3.3 to 14 nmol/g, Ne ages of 2048 Ma, 1761 Ma, 1523 Ma, 912 Ma, and 740 Ma were determined for samples from Khumani, Beeshoek, Black Rock, Rooinekke, and Belgravia, respectively.

All aliquots analyzed for He were also analyzed for Ne. These measurements yielded ^{21}Ne concentrations consisting of a high percentage of nucleogenic ^{21}Ne (^{21}Ne*), ranging from 60-81% ^{21}Ne* for all but the Black Rock sample, which ranged from 20-23%. Combining the above-mentioned parent isotope concentrations with ^{21}Ne* concentrations of 0.13 to 0.45 fmol/g, ages of 2018 Ma, 1776 Ma, 1706 Ma, 1497 Ma, and 1234 Ma were determined for samples from Khumani, Beeshoek, Black Rock, Rooinekke, and Belgravia, respectively. Ne ages ranged from almost identical to their corresponding He age, to hundreds of millions of years older. The younger He ages are as expected given the lower closure temperature of the He system.

4.2 He diffusivity

Belgravia, Black Rock, and Beeshoek ^{3}He diffusion experiment results are shown in the form of Arrhenius plots in Figure 3.4. The Rooinekke sample was collected in a later field campaign and was not available for proton irradiation and associated ^{4}He/^{3}He analysis. The Khumani sample produced results not compatible with the application of the ^{4}He/^{3}He method and therefore is not included here (see discussion in Interpretation section and Supplementary Figure 3.5). The Arrhenius plots (Figure 3.4) show systematically declining diffusivity at any given temperature as the experiment progresses, the hallmark

of PCD diffusion (Farley 2018). A series of prograde and retrograde heating steps produce a series of linear segments in Arrhenius space with nearly equal slopes and thus a nearly uniform He diffusion activation energy for all domains. Plotted through the first point of each array is a dashed, black line corresponding to an activation energy of 171 kJ/mol, as determined for hematite by Farley (2018). For comparison we also plot a line fit through an initial prograde and subsequent retrograde heating sequence, corresponding to an activation energy specific to that sample. These ranged from 171 to 187 kJ/mol.

To obtain the domain-size distribution for each sample, the step-heat data were transformed into a Delta plot (Figure 3.5), in which the vertical deviation from the 171 kJ/mol reference line is plotted against cumulative fraction of ^{3}He released (Farley 2018). Each sample presents a distinctive pattern in this space, indicating a distribution of crystallite sizes unique to each sample. While fractional yield data was fit using contributions from 8 domains, domains with <2° C difference in closure temperature were combined and domains contributing <0.5% of the total yield ignored. In the supplemental material, we assess the consequences of assuming the sample-specific activation energy for each sample.

Closure temperatures ranging between ~15° C to ~260° C were modeled for the three samples in this study. This is comparable to the range observed in previous work on PCD hematite (Farley and Flowers, 2012; Farley and McKeon, 2015), though the present samples have a substantially higher percentage of larger, more He-retentive crystallites. The highest closure temperatures observed here correspond to crystallite domains

approaching 1 mm when compared with the single domain hematite studied by Farley (2018).

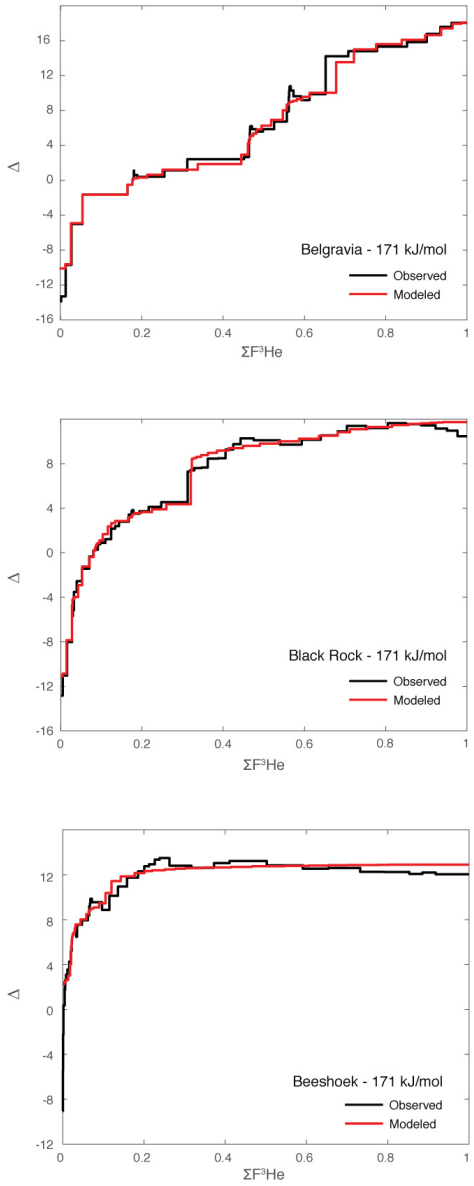

Figure 3.5: Delta plots for the Belgravia, Black Rock, and Beeshoek samples. The black line shows the experimentally observed Delta array, while the red line is a best-fit model using hematite diffusion kinetics and 8 discrete diffusion domains. Delta (Δ) = $2\ln(r/r_0)$ of Lovera et al. (1989).

Figure 3.6 shows the $^{4}He/^{3}He$ age spectra for the Belgravia, Black Rock, and Beeshoek samples along with the corresponding bulk (U-Th)/Ne age and 2s error. The Belgravia hematite shows increasing step-age until $\Sigma F^{3}He \sim 0.65$, and then an unexpected decrease in step-age above $\Sigma F^{3}He \sim 0.9$. The Black Rock sample sharply increases in step-age until $\Sigma F^{3}He \sim 0.15$, then plateaus for the duration of the experiment. The Beeshoek sample sharply increases in step-age until $\Sigma F^{3}He \sim 0.20$, then more slowly continues to increase for the duration of the experiment. All age spectrum data is presented in Supplemental Table 3.1.

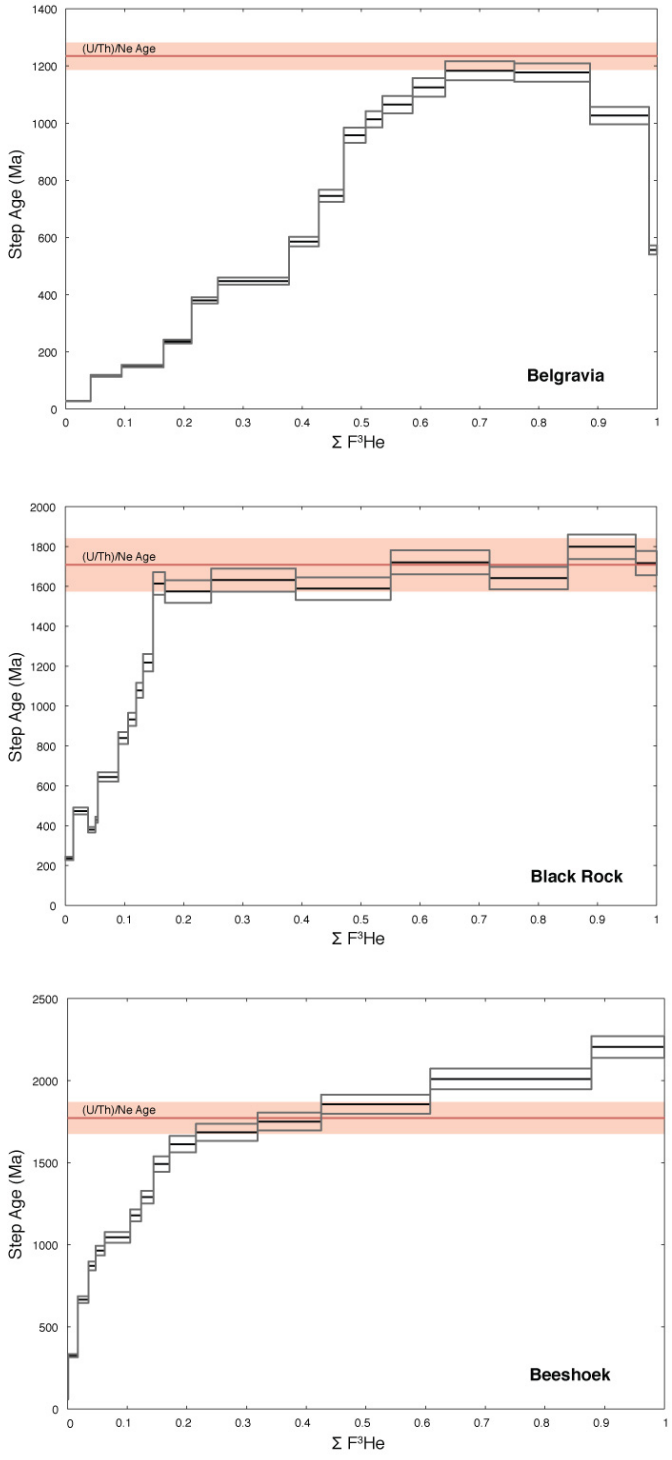

Figure 3.6: $^{4}He/^{3}He$ age spectra for the Belgravia, Black Rock, and Beeshoek samples. Each sample's (U-Th)/Ne age with 2s uncertainty is shown for reference.

V. INTERPRETATIONS

The overall range in Ne and He ages across our five sample suite, along with approximately concordant Ne and He ages for Khumani and Beeshoek but discordant Ne and He ages for Belgravia, Black Rock, and Rooinekke, indicates these hematite ores do not originate from a single, regional formation event. Figure 3.7 presents our Ne and He

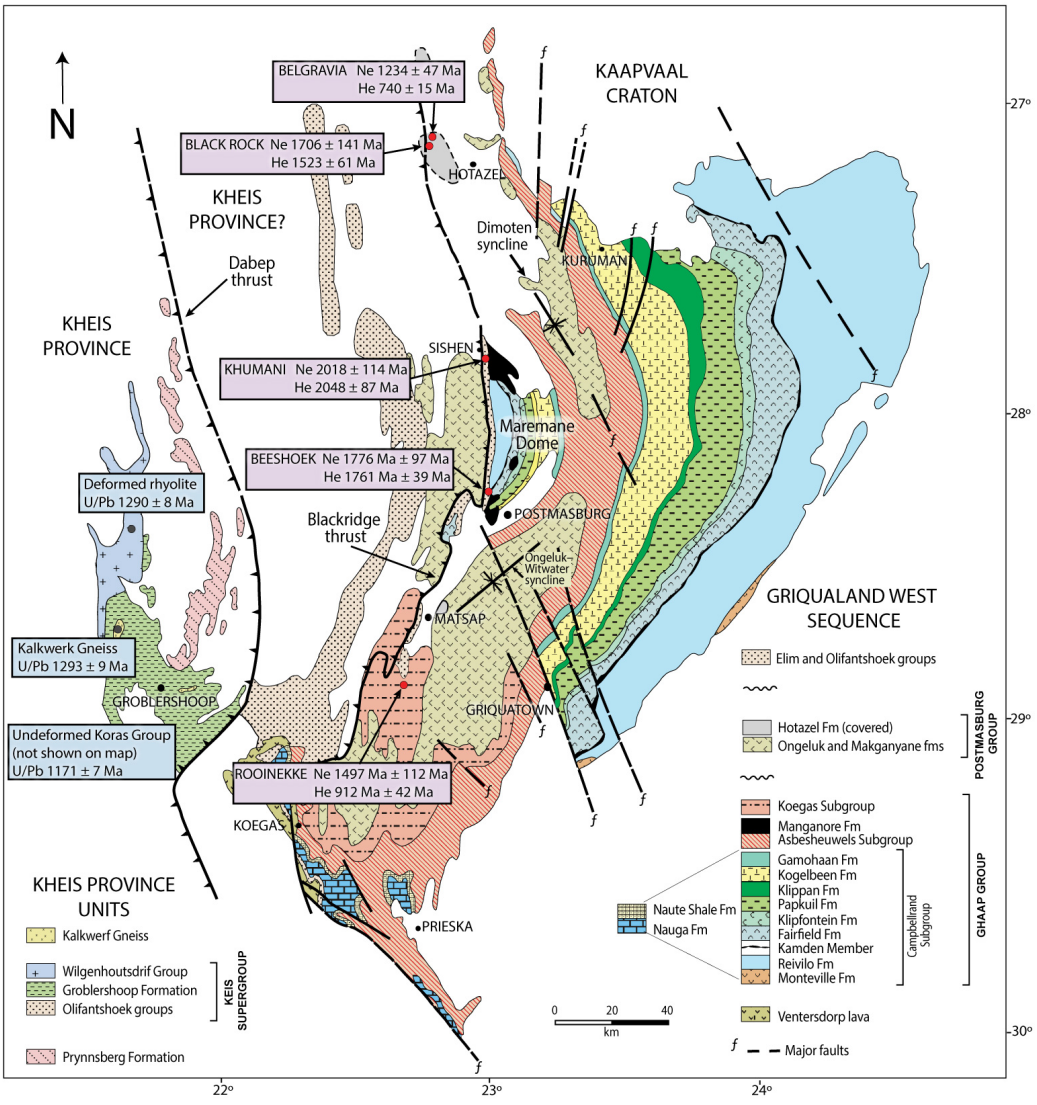

Figure 3.7: Generalized geologic map of the Griqualand West region. The five sample localities, as well as their bulk (U-Th)/Ne and (U-Th)/He ages are shown. Kheis Province U/Pb ages shown for context (Gutzmer et al., 2000;Van Niekerk, 2006; Moen and Armstrong, 2008).

ages in the context of a simplified geologic map of the Griqualand West region. Sample localities are all found on the footwall of the Black Ridge thrust fault, with our southern and northern localities separated by ~200 km.

The combined He-Ne chronology and $^{4}He/^{3}He$ thermochronology may provide new constraints on the formation of these ore bodies and the erosional history of the Griqualand West region. The Kuruman and Griquatown Iron Formations of the Asbestos Hills Subgroup are the parent units for Khumani and Beeshoek ore bodies, while Rooinekke ore sources from the Rooinekke Iron Formation of the Koegas Subgroup and the Belgravia and Black Rock samples come from the Hotazel Iron formation of the Postmasburg Group (Smith, 2018). The Khumani, Beeshoek, and Rooinekke ore bodies are developed where their parent BIFs intersect the pre-Gamagara erosional unconformity (Figure 3.2). Paleomagnetic studies place the age of this unconformity at 2.22 to 2.06 Ga (Evans et al., 2002; De Kock et al., 2008). This is in agreement with geochronologic bracketing of the unconformity (Cornell et al., 1998). Previous investigators have proposed that the Khumani, Beeshoek, and Rooinekke ore developed through supergene enrichment of parent BIF at the time of the pre-Gamagara weathering surface (Smith and Beukes, 2016).

A second Fe-upgrading mechanism must be invoked to explain the occurrence of tabular ore bodies, which are developed along faults, since their geometry cannot be explained by surface-derived, supergene fluid flow (Dixon, 1989; Grobbelaar et al., 1995) requires. In the Black Rock region, these tabular ore bodies are interpreted to be the result

of hydrothermal upgrading of parent BIF (Beukes et al., 2016). The Black Rock and Belgravia hematite are typical examples of the hydrothermally Fe-upgraded Hotazel BIF found in the Black Rock region (Grobbelaar et al., 1995; Beukes et al., 2016; Gumsley et al. 2017). Peak metamorphic conditions at Black Rock and Belgravia have been proposed to range between 270° and 420° C (Dixon 1989; Gutzmer and Beukes 1998), and we use this constraint as an upper limit in our time-temperature modeling at these localities. Ar/Ar dating of hydrothermal sugilite, hosted in adjacent Mn ore, yields a crystallization age of 1048 ± 6 Ma, interpreted as the timing for the main hydrothermal Mn-ore enrichment (Gnos et al., 2003). Norrishite collected at the same localities has a crystallization age of 1010 Ma, with subsequent alteration at 850 Ma (Gnos et al., 2003). Hydrothermal sugilite from the Maremane Dome area (between our Khumani and Beeshoek localities) has an Ar/Ar age of 620 ± 3 Ma, significantly younger than other ages proposed for hydrothermal mineralization in the Griqualand West region (Moore et al., 2011). The range in Ar ages illustrates the complex and localized nature of hydrothermal alteration in the Black Rock region.

These two proposed mechanisms for Fe-ore formation are schematically illustrated in Figure 3.8 and used as a framework for interpreting our bulk ages and as constraints on the starting conditions for time-temperature modeling.

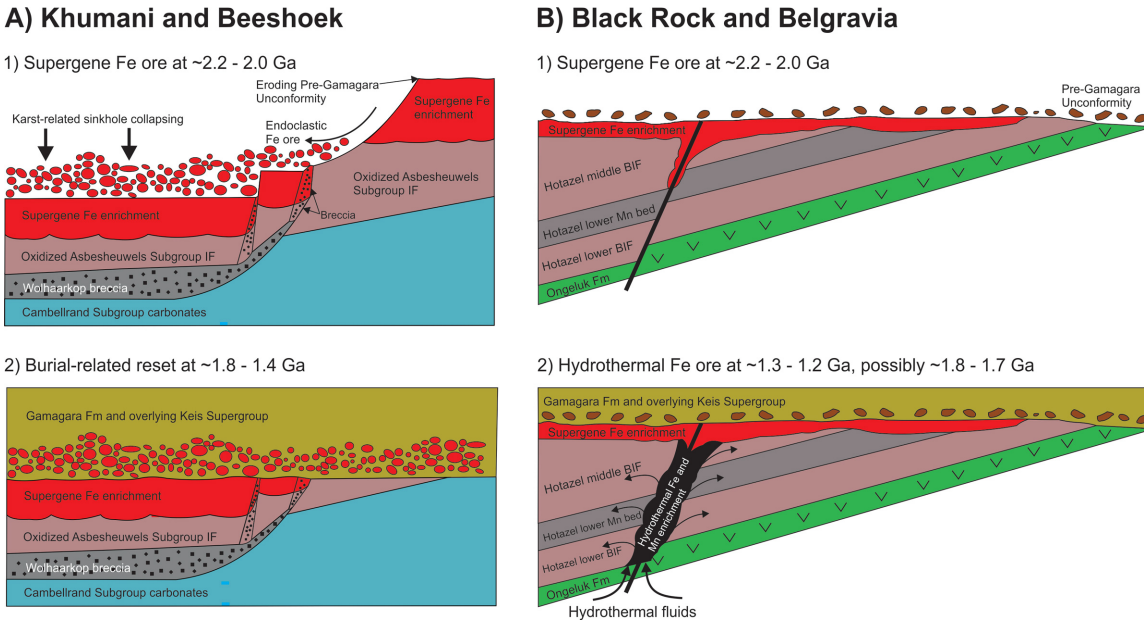

Figure 3.8: Schematic illustration of the two proposed hematite ore forming processes. (1) shows Fe-upgrading through the dissolution of non-iron bearing phases such as chert and carbonates where banded iron formation intersected the pre-Gamagara unconformity. This regional scale unconformity is the result of a 2.2 – 2.0 Ga paleoweathering surface, which allowed for supergene Fe-enrichment by meteoric fluid percolation. (2) shows subsequent Fe-upgrading by hydrothermal fluid circulation, primarily along fault planes.

KUHMANI AND BEESHOEK

The Khumani locality hematite (Ne 2018 ± 114 Ma, He 2048 ± 87 Ma) represents the oldest bulk ages in our Griqualand West suite, and furthermore the oldest published hematite He-Ne ages thus far. These ages alone speak to the retentivity of He and Ne in hematite. However, the interpretation of concordant He-Ne ages is non-unique. The simplest interpretations are either the hematite sample formed at cold temperatures (i.e. supergene processes) or very rapidly cooled below both the Ne and He closure temperature and remained fairly cool ever since. The Khumani He-Ne ages fall within the period of proposed pre-Gamagara Fe-upgrading associated with a regional-scale, paleoweathering horizon (Evans et al., 2002; Smith and Beukes, 2016). Thus, we

tentatively interpret this Khumani sample to have formed at or very near the Earth's surface from supergene Fe-enrichment of the parent BIF at ~2.0 Ga, an interpretation consistent with sample morphology (Smith and Beukes, 2016). The dissolution of silica and carbonate phases by meteoric fluids, along with Fe-upgrading and oxidation, are indicative of oxidative weathering reactions as commonly observed in the oxygenated Phanerozoic.

The Khumani sample was proton irradiated for the $^{4}He/^{3}He$ method, yet multiple $^{4}He/^{3}He$ step heating experiments produced an anomalous age spectrum, with geologically implausible ages for nearly 50% of heating steps (Supplemental Figure 5). Subsequent U-Th analyses of 22 replicate chips indicate a heterogeneous distribution in parent isotope concentration on the sub-milligram scale (Supplemental Table 5). A fundamental requirement of the $^{4}He/^{3}He$ method and hematite PCD model is U-Th homogeneity across domains. The age spectrum displayed by the Khumani sample suggests a higher parent isotope concentration in the more retentive domains. It is important to note that while we cannot utilize the $^{4}He/^{3}He$ method to interpret the time-temperature history at the Khumani locality, U-Th heterogeneity between different crystallite domains does not invalidate the bulk He-Ne ages determined from large-mass sample aliquots (100 mg for He-Ne measurements, 25 mg for U-Th measurements). Given the problematic $^{4}He/^{3}He$ age spectra produced from the Khumani sample (Supplemental Figure 5), confirmation of our interpretation of the bulk Khumani He-He ages with samples that produce reasonable $^{4}He/^{3}He$ spectra is needed.

Bulk ages for the Beeshoek hematite (Ne 1776 ± 97 Ma, He 1761 ± 39 Ma) are also concordant with each other, and their interpretation can be resolved with the $^{4}He/^{3}He$ method and time-temperature modeling. Sloping age spectra (Figure 3.6) indicate some He loss has occurred in the less retentive hematite domains. The final two heating steps yield ages of 2010 ± 63 Ma and 2205 ± 66 Ma (Supplementary Table 3.1). These two steps fall within the 2.0 – 2.2 Ga period of pre-Gamagara supergene enrichment. The presence of pre-Gamagara age domains within the Beeshoek hematite implies a much more complicated history than the concordant bulk He-Ne ages alone would suggest or a possible violation of 4He/3He method assumptions. We interpret these results while holding the underlying assumptions of the He-Ne and $^{4}He/^{3}He$ methodology to be true.

When using our Beeshoek $^{4}He/^{3}He$ data to model a time-temperature history, we constrain the starting condition of our model to 25 °C ± 25 °C at 2200 Ma. Figure 3.9 shows the results of this time-temperature model. For the Beeshoek hematite, all acceptable T-t paths indicate initial heating, followed by near monotonic cooling from ~1500 Ma until the present. A peak temperature of ~200 °C was modeled to have occurred at 1600 +/- 200 Ma. Here, the Beeshoek $^{4}He/^{3}He$ time-temperature modeling suggests deep burial in the Maremane Dome area (Figure 3.7), a finding consistent with geologic expectations. He loss would be expected from some Beeshoek domains at 200 °C, thus producing a He age younger than the Ne age. At 2s, the Ne age may be up to 136 Ma older than the He age. Therefore, our preferred explanation is that the $^{4}He/^{3}He$ modeled time-temperature history accurately portrays that of the true T-t history of the Beeshoek sample,

and the uncertainty associated with our He-Ne age determinations has produced numerically concordant ages.

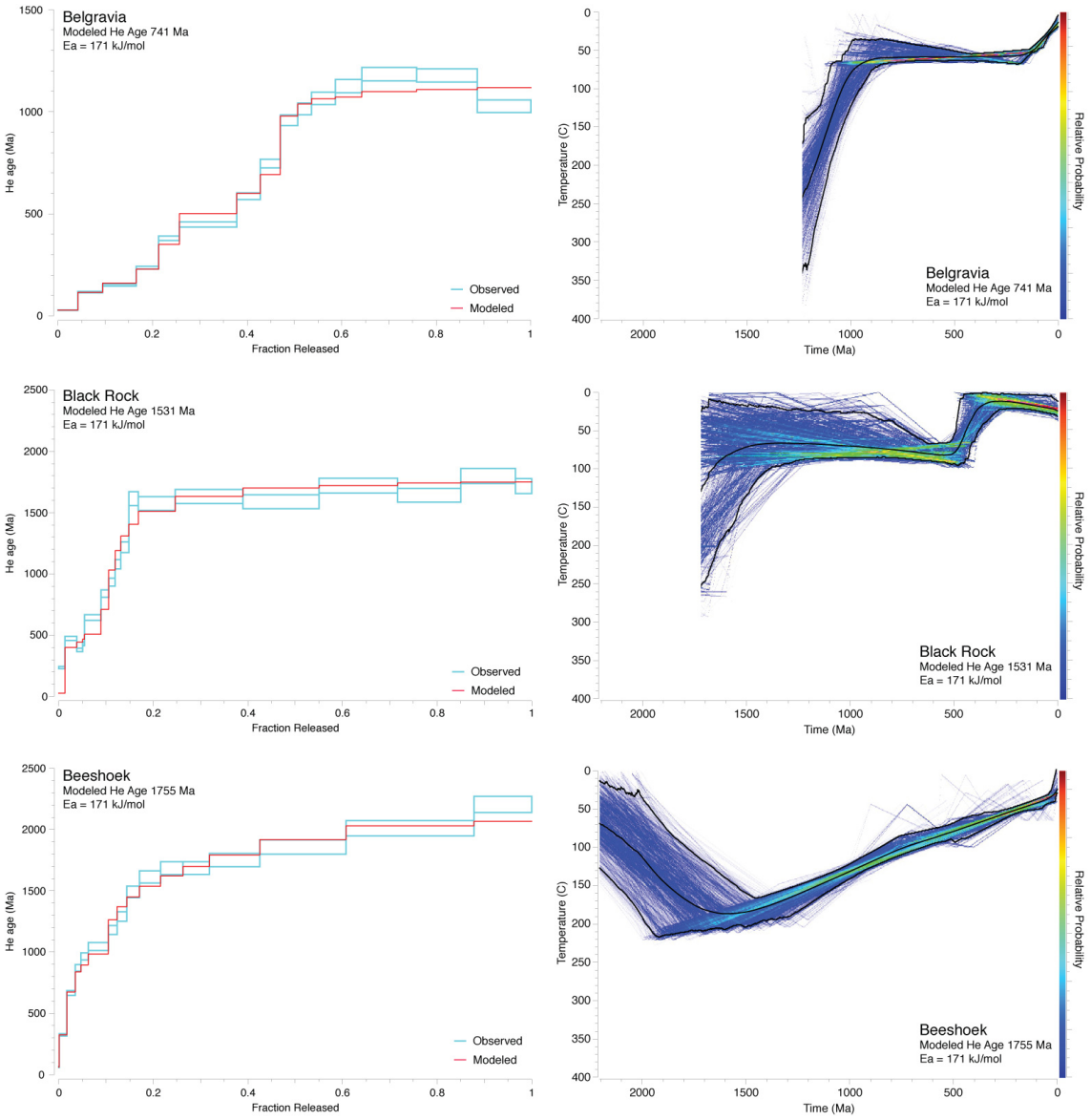

Figure 3.9: Time-temperature modeling results for the Belgravia, Black Rock, and Beeshoek samples. The left panel shows the age spectrum with measured data uncertainty bounds (blue lines) and the best-fit model age spectrum (red lines) obtained from the average (black line) time-temperature path shown in the right panel.

This explanation illustrates the importance of constraining a sample's history with the $^{4}He/^{3}He$ method whenever possible. It also invites the chance that the 2.0 Ga bulk He-Ne ages from Khumani may hide similar complications. The interpreted geologic history of the Maremane Dome area indicates the Khumani and Beeshoek localities must have experienced very similar burial histories (Grobbelaar et al., 1995; Van Niekert, 2006). The uncertainty in the Khumani bulk He-Ne ages allows for the Ne age to be up to 201 Ma older (2s). Given the strong probability that Khumani was as deeply buried as Beeshoek, it may be necessary to invoke the He-Ne age uncertainly to explain the concordant ages.

Within the Kheis Province, the Groblershoop Formation has a whole-rock Ar-Ar age of 1780 Ma, likely reflecting greenschist facies burial metamorphism at that time (Burger and Coertze, 1975). This age is in close agreement with our reported Beeshoek He-Ne ages, with higher peak metamorphic conditions likely the result of burial by a thicker succession of Keis Supergroup sediments in the central Kheis Province. At the margin of the Kaapvaal Craton, the ~2 km Transvaal Elim Group and up to 5 km of Olifantshoek sediments were likely present atop the Beeshoek and Khumani localities (Barker et al., 2006; Van Niekerk, 2006). Therefore, we interpret the Beeshoek sample, and tentatively the Khumani sample, to have initially formed from pre-Gamagara supergene Fe-upgrading, followed by burial heating to ~200° C, then slow unroofing through the Proterozoic.

A combination of a coarser crystallite domain distribution in the Khumani sample (thus higher He and Ne retentivity), differences in burial depth by several kilometers, or

additional heating at the Beeshoek locality by hydrothermal fluid could explain the difference in hematite He-Ne ages at Khumani and Beeshoek. While deformation associated with the Kheis Orogeny is typically considered to have occurred between ~1.3 to ~1.2 Ga (Moen and Armstrong, 2008), field relationships indicate an older deformation event, largely overprinted, must have occurred (Van Niekerk, 2006), and localized fluid flow along fault surfaces could have affected the Beeshoek ore body without imparting a chronologic signature on the hematite found at Khumani. The above interpretations are all made assuming no partial recrystallization and a closed system with respect to U and Th. However, the mobility of U and Th, changes to the crystallite domain-distribution, or a combination of the two, could produce spurious results that lead to geologically meaningless ages. Dating another sample, potentially hematite from the nearby Khuman-adjacent Sishen Mine, could add confidence to our results.

ROOINEKKE

Moving to the southernmost locality in our sample suite, field relationships indicate the Rooinekke ore body formed from supergene Fe-upgrading of the Rooinekke Iron Formation at pre-Gamagara time (Smith and Beukes, 2016). However, bulk ages (Ne 1497 ± 112 Ma, He 912 ± 42 Ma) significantly younger than the pre-Gamagara unconformity suggest significant heating and/or recrystallization must have occurred if this sample did in fact initially form from supergene weathering at ~2.0 Ga. As previously mentioned, one of the central assumptions of the He-Ne method is that, should recrystallization have occurred, it occurred completely. Our interpretation of the

Rooinekke sample holds this underlying assumption to be true. The younger age observed in Rooinekke hematite suggests several possibilities: a thicker succession of Olifantshoek sediments was deposited here and/or the Rooinekke hematite crystallite domain distribution is more sensitive to He diffusion; or complete recrystallization of the Rooinekke deposit occurred by Mesoproterozoic hydrothermal fluid flow around ~1500 Ma. Given the lack of prior evidence for a hydrothermal event at this time and the structural position of this deposit along the pre-Gamagara unconformity, our preferred interpretation is Rooinekke experienced protracted heating by burial. Application of the $^{4}He/^{3}He$ method on this sample could determine the closure temperature for this sample's crystallite domain distribution along with whether modeled T-t paths at this locality fit a protracted (burial) or rapid (hydrothermal recrystallization) heating history.

BLACK ROCK AND BELGRAVIA

Finally, we consider our northern two samples, Black Rock and Belgravia. As previously discussed, these samples come from an area of the Griqualand West region with considerable evidence for hydrothermal activity. When searching for time-temperature paths that honor our $^{4}He/^{3}He$ age spectra, we used the existing fluid inclusion thermometry and allowed for the initial sample temperature to range up to 400° C. Two ages, 1270 ± 30 Ma (Dixon, 1989) and 1048 ± 6 Ma (Gnos et al., 2003), have been determined for different zones of hydrothermal sugilite from the nearby Wessels mine. The Black Rock hematite (Ne 1706 ± 141 Ma, He 1523 ± 61 Ma) has bulk ages

significantly older than previously identified hydrothermal fluid circulation as recorded by sugilite crystallization, thereby providing a new age constraint on this sample's history.

Examining the $^{4}He/^{3}He$ age spectrum produced from Black Rock hematite, the Ne bulk age agrees with the He step ages from $\Sigma F^{3}He=\sim0.20$ to $\Sigma F^{3}He=1$, within error. If we only attempt to honor the Ne age and $^{4}He/^{3}He$ age spectra, the simplest explanation is this 1706 Ma Ne age represents a formation age for the Black Rock hematite and subsequent unroofing of the Elim and Olifantshoek succession produced the cooling history observed in the modeled T-t path. Another possibility that must be considered given the geologic context (Figure 3.2) is the Black Rock hematite formed from supergene Fe-enrichment at pre-Gamagara time. Modeling of the Black Rock crystallite size distribution indicates >70% of the domains have a closure temperature between 200 and 240° C (Supplemental Table 3a). Pre-Gamagara Fe-enrichment, followed by burial heating to ~250° C is geologically permissible and could account for the observed $^{4}He/^{3}He$ age spectrum plateau if the sample was quickly unroofed to ~100° C by 1500 Ma (where only <30% of the domains would be experiencing He loss). However, this scenario is inconsistent with the observed 1706 Ma Ne age because it is geologically implausible to accumulate enough sediment on the Black Rock locality to completely diffuse Ne from the most retentive domains (Cox, 2016). For this reason, our preferred interpretation is that recrystallization occurred at ~1.7 Ga, thereby resetting the He-Ne age.

Following this event, unroofing of the Elim and Olifantshoek groups cooled the Black Rock hematite sample to ~100° C by 1500 Ma, where our modeled T-t history

indicates it remained for nearly a billion years. Given the close spatial proximity between Black Rock hematite and nearby Mn ore, which has reported ages much younger than our Black Rock He-Ne ages (Evans et al., 2001; Gnos et al., 2003), hydrothermal heating may have occurred in multiple, relatively localized events in this area. Another notable feature in our modeled Black Rock T-t history is the sudden cooling observed at ~500 Ma, a feature unique within our T-t models to Black Rock. A planar erosion surface cuts across deformed Namaqualand, which the late Neoproterozoic-Cambrian Nama sediments unconformably overlie, suggesting an erosive regime in the region at the time. Further Kaapvaal erosion would have taken place prior to the deposition of the Ordovician Cape Supergroup. Therefore, we interpret the rapid ~500 Ma cooling in our Black Rock T-t model to be the result of several km of overburden being removed as Nama or Cape Supergroup sediments.

The last sample in our suite, Belgravia, comes from the same Black Rock region, yet reveals a slightly different history from the main Black Rock ore body. Again we observe normally discordant bulk ages (Ne 1234 ± 47 Ma, He 740 ± 15 Ma) that suggest protracted cooling. $^{4}He/^{3}He$ step ages approach that of the Ne age, suggesting ~1.2 Ga ore formation related to the Kheis Orogeny. By 1.0 Ga, the Belgravia hematite had cooled to ~60° C, where it resided until a phase of cooling beginning at ~150 Ma, likely related to Cretaceous unroofing as observed in Kaapvaal craton erosional histories derived from apatite thermochronology (Flowers and Schoene, 2010; Stanley et al., 2013; Stanley and Flowers, 2016). If any 2.0 Ga supergene Fe-enrichment occurred, complete hematite recrystallization must have taken place to erase any chronologic record in the Black Rock

or Belgravia samples. Another possibility is no pre-Gamagara supergene hematite is represented within our small sample suite from these localities. Application of the $^{4}He/^{3}He$ method to other ore localities in the area, such as at the Wessels mine, could provide further insight into the complex history of this area along with providing a better understanding to differences in cooling paths between Black Rock and Belgravia through the Phanerozoic.

VI. CONCLUSIONS

Combined (U-Th)/Ne and (U-Th)/He chronometry of hematite from five ore localities along a ~200 km transect paralleling the Blackridge thrust fault in Griqualand West, in combination with the application of the $^{4}He/^{3}He$ method to hematite from three of these localities, indicates locality-specific formation and thermal histories. This study represents an early exploration of the potential, as well as the associated challenges, of constraining thermal and erosional histories using hematite thermochronology. These methods allow us to examine the timing of ore formation and exhumation in the Kaapvaal Craton well into the Proterozoic. Despite differences in formation age and exhumation history, this suite of samples is linked together by the extreme longevity of this landscape.

Our samples provide further support for a regionally developed paleo-weathering surface, known as the pre-Gamagara unconformity, that was responsible for the initial Fe-upgrading of parent BIF between 2.2 and 2.0 Ga. Fe-oxidation from percolation of meteoric fluids at the Earth's surface is indicative of oxidative weathering reactions common in the Phanerozoic. Following this initial supergene ore formation event, we

identify evidence for burial heating in the Paleo- and Mesoproterozoic from our modeled Beeshoek time-temperature history and Rooinekke He-Ne ages. This is followed by a ~1.3 to 1.2 Ga hydrothermal event associated with the Kheis orogeny (Moen and Armstrong, 2008), likely concurrent with the initiation of Blackridge thrusting (Beukes and Smit, 1987). The identification of hydrothermal Fe-upgrading prior to the Namaqua-Natal hydrothermal Mn ore formation previously recognized at 1.1 to 1.0 Ga (Evans et al., 2001; Gnos et al., 2003) indicates the importance of multi-method investigations sensitive to a variety of temperatures.

The BIF-hosted Fe ore bodies of Griqualand West provide a particularly difficult environment to apply the paired He-Ne chronometers and $^{4}He/^{3}He$ method due to the long and complex geologic history. Hematite formation and possible recrystallization may occur at nearly any time and previous studies have found hematite formation need not be correlated to known regional, tectono-thermal events (Farley and McKeon, 2015). This sample suite includes two samples, Khumani and Beeshoek, with concordant He-Ne ages that are difficult to interpret in light of the geologic expectations and Beeshoek $^{4}He/^{3}He$ results. Slow-cooling settings, such as exhumation from deep burial, should produce discordant He-Ne ages, based on the understanding of higher hematite Ne retentivity. The violation of any of the underlying assumptions of our method (such as the occurrence of partial recrystallization or mobility of U and Th) could produce geologically meaningless results. The consequences of partial recrystallization on He and Ne age systematics have, to our knowledge, not yet been investigated.

A significant advantage of hematite thermochronology is that the multi-domain structure inherently makes it well suited to probing a wide range of temperature histories. Belgravia hematite records both the higher temperature (≥ 200° C) ore forming processes and the much more recent Cretaceous exhumation. At this locality, a ~1.3 Ga time-temperature history is produced that independently fits the geologic expectations of Mesoproterozoic hydrothermal Fe-ore formation and Cretaceous exhumation. On a regional scale, our time-temperature modeling, assuming a ~20° C/km geothermal, indicates these samples have been within ~6 km of the surface of the Earth for at least the last billion years, providing further evidence for the exceptionally slow erosion of cratonic interiors.

References

Allsopp HL, and Barrett (1975) Rb–Sr age determinations on South Africa Kimberlite Pipes. *Physics and Chemistry of the Earth*. 605-617.

Barker OB, Brandl G, Callaghan CC, Eriksson PG, and van Der Neut M. (2006) The Soutpansberg and Waterberg groups and the Blouberg formation. *The Geology of South Africa.* Geological Society of South Africa, Johannesburg/Council for Geoscience, Pretoria. 301-318.

Bau M, Romer RL, Luders V, and Beukes NJ. (1999) Pb, O, and C isotopes in silicified Mooidraai dolomite (Transvaal Supergroup, South Africa): implications for the composition of Paleoproterozoic seawater and "dating" the increase of oxygen in the Precambrian atmosphere. *Earth and Planetary Science Letters*. **174**, 43–57.

Bekker A, Holland HD, Wang P-L, Rumble D, Stein, HJ, Hannah JL, Coetzee LL, and Beukes NJ. (2004) Dating the rise of atmospheric oxygen. *Nature*. **427**, 117–120.

Beukes, NJ and Smit CA. (1987) New evidence for thrust faulting in Griqualand West, South Africa: implications for stratigraphy and the age of red beds. *South African Journal of Geology*. **90**, 378-394.

Beukes NJ, and Gutzmer J. (2008) Origin and paleoenvironmental significance of major iron formations at the Archean-Paleoproterozoic boundary. *Reviews in Economic Geology*. **15**, 5-47.

Beukes NJ, Swindell EPW, and Wabo H. (2016) Manganese deposits of Africa. *Episodes* **39.2**, 285-317.

Blackburn TJ, Stockli DF, Walker JD. (2007) Magnetite (U-Th)/He dating and its application to the geochronology of intermediate to mafic volcanic rocks. *Earth and Planetary Science Letters*. **259**, 360–371

Braun J, Guillocheau F, Robin C, Baby G, and Jelsma H. (2014) Rapid erosion of the Southern African Plateau as it climbs over a mantle superswell. *Journal of Geophysical Research: Solid Earth*. **119**, 6093-6112.

Bowring SA, and Schmitz MD. (2003) Ultrahigh-temperature metamorphism in the lower crust during Neoarchean Ventersdorp rifting and magmatism, Kaapvaal Craton, southern Africa. *GSA Bulletin*. **115**, 533–548.

Burger AJ, and Coertze FJ. (1975) Summary of age determinations carried out during the period April 1974 to March 1975. *Ann. Geologic Survey of South Africa*. **11**, 317-321.

Catuneanu O. (2004) Basement control on flexural profiles and the distribution of foreland facies: The Dwyka Group of the Karoo Basin, South Africa. *Geology*. **32**, 517-520.

Catuneanu O, Wopfner H, Eriksson PG, Cairncross B, Rubidge BS, Smith RMH, and Hancox PJ. (2005) The Karoo basins of south-central Africa. *Journal of African Earth Sciences*. **43**, 211-253.

Colliston WP, Schoch AE, and Cole J. (2017) The Grenvillian Namaqua fold belt adjacent to the western Kaapvaal Craton: 2. Archaean Craton and supercontinent connections. *Precambrian Research*. **300**, 289-314.

Corner B, and Durrheim RJ. (2018) An Integrated Geophysical and Geological Interpretation of the Southern African Lithosphere. In: Siegesmund S, Basei M, Oyhantçabal P, and Oriolo S (eds) *Geology of Southwest Gondwana*. Regional Geology Reviews.19-61.

Cornell DH. (1987) A field and petrographic study of the Hartley Basalt Formation, Northern Cape Province of South Africa. Transactions of the Geological Society of South Africa, 90, 7-24.

Cornell DH, Schutte SS, and Eglington BL. (1996) The Ongeluk basaltic andesite formation in Griqualand West, South Africa: submarine alteration in a 2222 Ma Proterozoic sea. *Precambrian Research*. **79**, 101–123.

Cornell, DH, Armstrong RA, and Walraven F. (1998) Geochronology of the Proterozoic Hartley Basalt formation, South Africa: constraints on the Kheis tectogenesis and the Kaapvaal Craton's earliest Wilson Cycle. *Journal of African Earth Sciences.* **26**, 5-27.

Cornell DH, Thomas RJ, Gibson R, Moen HF, Reid DL, Moore JM, Gibson RL. (2006) The Namaqua-Natal Province. In: Johnson MR, Anhausser CR, and Thomas RJ (eds.) *The Geology of South Africa*. Johannesburg, South Africa, Geological Society of South Africa, 325-379.

Cornell DH, Zack T, Andersen T, Corfu F, Frei D, and Van Schijndel V. (2016) Th-U-Pb zircon geochronology of the Palaeoproterozoic Hartley Formation porphyry by six methods, with age uncertainty approaching 1 Ma. *South African Journal of Geology*. **119**, 473-494.

Cox SE, Farley KA, and Cherniak DJ. (2015) Direct measurement of neon production rates by (a,n) reactions in minerals. *Geochimica et Cosmochimica Acta*. **148**, 130–144, doi: 10.1016/j.gca.2014.08.036.

Cox, SE. (2016) New techniques for noble gas geochronometry and thermochronometry. (Doctoral dissertation, California Institute of Technology).

Dalstra HJ, and Rosière CA. (2008) Structural controls on high- grade iron ores hosted by banded iron formation: a global perspective. In: Hagemann S, Rosière CA, Gutzmer J, and Beukes NJ (Eds), *Reviews in Economic Geology*. **15**, 73-106.

De Kock MO, Evans DAD, Kirschvink JL, Beukes NJ, Rose E, and Hilburn I. (2009) Paleomagnetism of a Neoarchean-Paleoproterozoic carbonate ramp and carbonate platform succession (Transvaal Supergroup) from surface outcrop and drill core, Griqualand West region, South Africa. *Precambrian Research.* **169**, 80-99.

De Wit M. (2007) The Kalahari Epeirogeny and climate change: differentiating cause and effect from core to space. *South African Journal of Geology*. **110**, 367-392.

Dixon, RD. (1989) Sugilite and associated metamorphic silicate minerals from Wessels mine, Kalahari manganese field. *Bulletin of the Geologic Survey South Africa*. **93**, 1-47.

Duane MJ, Kruger FJ, Turner AM, Whitelaw HT, Coetzee H, and Verhagen BT. (2004) The timing and isotopic character of regional hydrothermal alteration and associated epigenetic mineralization in the western sector of the Kaapvaal Craton (South Africa). *Journal of African Earth Sciences*. **38**, 461–476, doi: 10.1016/j.jafrearsci.2004.03.002.

Eglington BM. (2006) Evolution of the Namaqua-Natal Belt, southern Africa–A geochronological and isotope geochemical review. *Journal of African Earth Sciences*. **46**, 93-111.

Eglington BM, and Armstrong RA. (2004) The Kaapvaal Craton and adjacent orogens, southern Africa: a geochronological database and overview of the geological development of the craton. *South African Journal of Geology*. **107**, 13-32.

Eriksson PG, Altermann W, and Hartzer FJ. (2006) The Transvaal Supergroup and its precursors. In: Johnson MR, Anhaeusser CR, and Thomas RJ (Eds), The Geology of South Africa, *Geological Society of South Africa and Council for Geoscience*, Johannesburg, 237-260.

Evans DAD, Beukes NJ, and Kirschvink JL. (1997) Low-latitude glaciation in the Paleoproterozoic era. *Nature*. **386**, 262-266.

Evans DAD, Gutzmer J, Beukes NJ, and Kirschvink JL. (2001) Paleomagnetic constraints on ages of mineralization in the Kalahari manganese field, South Africa. *Economic Geology*. **96**, 621-631.

Evans DAD, Beukes NJ, and Kirschvink JL. (2002) Paleomagnetism of a lateritic paleoweathering horizon and overlying Paleoproterozoic red beds from South Africa: Implications for the Kaapvaal apparent polar wander path and a confirmation of atmospheric oxygen enrichment. *Journal of Geophysical Research*. **107**, 1-22.

Farley KA. (2000) Helium diffusion from apatite: General behavior as illustrated by Durango fluorapatite. *Journal of Geophysical Research*. **105**, 2903–2914.

Farley KA. (2018) Helium diffusion parameters of hematite from a single-diffusion-domain crystal. *Geochimica et Cosmochimica Acta*. **231**, 117-29.

Farley KA, and Flowers R. M. (2012) (U-Th)/Ne and multidomain (U-Th)/He systematics of a hydrothermal hematite from eastern Grand Canyon. *Earth Planet. Sci. Lett.* **359**, 131–140.

Farley KA, and McKeon R. (2015) Radiometric dating and temperature history of banded iron formation–associated hematite, Gogebic iron range, Michigan, USA. *Geology*. **43**, 1083–1086.

Farley KA, Reiners P, Nenow V. (1999) An apparatus for high-precision helium diffusion measurements from minerals. *Anal Chem*. **71**, 2059-2061.

Fechtig H, and Kalbitzer S. (1966) The diffusion of argon in potassium-bearing solids. In: *Potassium argon dating*. 68-107.

Flowers RM, and Schoene B. (2010) (U-Th)/He thermochronometry constraints on unroofing of the eastern Kaapvaal craton and significance for uplift of the southern African Plateau. *Geology*. **38**, 827–830, doi: 10.1130/G30980.1.

Gallagher K. (2012) Transdimensional inverse thermal history modeling for quantitative thermochronology: Journal of Geophysical Research. **117**, B02408, doi: 10.2475/ajs.297.10.939.

Gautheron, CE, Tassan-Got L, and Farley KA. (2006) (U–Th)/Ne chronometry. *Earth and Planetary Science Letters*. **243**, 520–535, doi: 10.1016/j.epsl.2006.01.025.

Gibson RL, and Jones MQ. (2002) Late Archaean to Palaeoproterozoic geotherms in the Kaapvaal Craton, South Africa: constraints on the thermal evolution of the Witwatersrand Basin. *Basin Research*. **14**, 169-81.

Gleason JD, Gutzmer J, Kesler SE, and Zwingmann H. (2011) 2.05-Ga Isotopic Ages for Transvaal Mississippi Valley–Type Deposits: Evidence for Large-Scale Hydrothermal Circulation around the Bushveld Igneous Complex, South Africa. *The Journal of Geology*. **119**, 69-80.

Gnos E, Armbruster T, Villa IM. (2003) Norrishite, K (Mn23+ Li) Si4O10 (O) 2, an oxymica associated with sugilite from the Wessels Mine, South Africa: Crystal chemistry and 40Ar-39Ar dating. *American Mineralogist*. **88**, 189-94.

Grobbelaar WS, Burger MA, Pretorius AI, Marais M, and Van Niekerk I. (1995) Stratigraphic and Structural Setting of the Griqualand West and the Olifantshoek Sequences at Black Rock, Beeshoek and Rooinekke Mines, Griqualand West, South-Africa. *Mineralium Deposita*. **30**, 152–161.

Green PF, Duddy IR, Japsen P, Bonow JM, and Malan JA. (2017) Post-breakup burial and exhumation of the southern margin of Africa. *Basin Research*. **29**, 96–127.

Gumsley AP, Chamberlain KR, Bleeker W, Söderlund U, de Kock MO, Larsson ER, Bekker A. (2017) Timing and tempo of the Great Oxidation Event. *Proceedings of the National Academy of Sciences.* **114**, 1811-6.

Gurnis M, Mitrovica JX, Ritsema J, and van Heijst HJ. (2000) Constraining mantle density structure using geological evidence of surface uplift rates: The case of the African superplume. *Geochemistry, Geophysics, Geosystems*. **105**, 11063-11082.

Gutzmer J, and Beukes NJ. (1998) Earliest laterites and possible evidence for terrestrial vegetation in the Early Proterozoic. *Geology*. **26**, 263-266.

Gutzmer J, and Beukes NJ. (1998) The manganese formation of the Neoproterozoic Penganga Group, India-revision of an enigma. *Economic Geology*. **93**, 1091–1102.

Gutzmer J, Beukes NJ, Pickard A, Barley ME. (2000) 1170 Ma SHRIMP age for Koras Group bimodal volcanism, northern Cape Province. *South African Journal of Geology*. **103**, 32-7.

Hoffman PF. (2013) The Great Oxidation Event and a Siderian Snowball Earth: MIF based correlation of Paleoproterozoic glaciations. *Chemical Geology*. **362**, 1–34. doi: 10.1016/j.chemgeo.2013.04.018.

Hoffman PF. (1991) Did the breakout of Laurentia turn Gondwanaland inside-out? *Science*. ***252***, 1409-1412.

Holland HD, and Beukes NJ. (1990) A paleoweathering profile from Griqualand West, South Africa: evidence for a dramatic rise in atmospheric oxygen between 2.2 and 1.9 bybp. *American Journal of Science*. **290**, 1–34.

Jacobs J, Thomas RJ, and Weber K. (1993) Accretion and indentation tectonics at the southern edge of the Kaapvaal craton during the Kibaran (Grenville) orogeny. *Geology*. **21**, 203-206.

Jones MQ. (1998) Heat flow in the Witwatersrand Basin and environs and its significance for the South African shield geotherm and lithosphere thickness. *Journal of Geophysical Research: Solid Earth*. **93**, 3243-60.

Jourdan F, Féraud G, Bertrand H, Kampunzu AB, Tshoso G, Watkeys MK, and Le Gall B. (2005) Karoo large igneous province: Brevity, origin, and relation to mass extinction questioned by new 40Ar/39Ar age data. *Geology*. **33**, 745-748.

Klein C. (2005) Some Precambrian banded iron-formations (BIFs) from around the world: Their age, geologic setting, mineralogy, metamorphism, geochemistry, and origins. *American Mineralogist*. **90**, 1473–1499, doi: 10.2138/am.2005.1871.

Lippolt HJ, Wernicke RS, and Boschmann W. (1993) 4He diffusion in specular hematite. *Physics and Chemistry of Minerals*. **20**, 415–418.

Lovera OM, Richter FM, and Harrison TM. (1989) The $^{40}Ar/^{39}Ar$ thermochronometry for slowly cooled samples having a distribution of diffusion domain sizes. *Journal of Geophysical Research*. **94**, 17–935.

Lovera OM, Richter FM, and Harrison TM. (1991) Diffusion domains determined by ^{39}Ar released during step heating. *J. Geophys. Res.* **96**, 2057–2069.

McCarthy TS, Corner B, Lombard H, Beukes NJ, Armstrong RA, and Cawthorn RG. (2018) The pre-Karoo geology of the southern portion of the Kaapvaal Craton, South Africa. *South African Journal of Geology*. **121**, 1-22.

Meert JG. (2003) A synopsis of events related to the assembly of eastern Gondwana. *Tectonophysics*. **362**, 1-40.

Moen HFG. (1999) The Kheis tectonic subprovince, southern Africa: A lithostratigraphic perspective. *South African Journal of Geology*. **102**, 27-42.

Moen HFG. (2006) The Olifantshoek Supergroup. *The Geology of South Africa. Geological Society of South Africa/Council for Geoscience*. 319-324.

Moen HFG, and Armstrong RA. (2008) New age constraints on the tectogenesis of the Kheis Subprovince and the evolution of the eastern Namaqua Province. *South African Journal of Geology*. **111**, 79-88.

Moore JM, Kuhn BK, Mark DF, and Tsikos, H. (2011) A sugilite-bearing assemblage from the Wolhaarkop breccia, Bruce iron-ore mine, South Africa: Evidence for alkali metasomatism and 40Ar-39Ar dating. *European Journal of Mineralogy*. **23**, 661–673, doi: 10.1127/0935-1221/2011/0023-2117.

Nelson DR, Trendall AF, and Altermann W. (1999) Chronological correlations between the Pilbara and Kaapvaal cratons. *Precambrian Research*. **97**, 165–189, doi: 10.1016/S0301-9268(99)00031-5.

Maud RR, and Partridge TC. (1987) Regional geomorphic evidence for climatic change in southern Africa since the Mesozoic. *Palaeoecology of Africa*. **18**, 337-348.

Phillips D, Machin KJ, Kiviets GB, Fourie LF, Roberts MA, and Skinner EMW. (1998) A petrographic and $^{40}Ar/^{39}Ar$ geochronological study of the Voorspoed Kimberlite, South Africa; implications for the origin of Group II kimberlite magmatism. *South African Journal of Geology*. **101**, 299–306.

Powell CM, Li ZX, McElhinny MW, Meert JG, and Park JK. (1993) Paleomagnetic constraints on timing of the Neoproterozoic breakup of Rodinia and the Cambrian formation of Gondwana. *Geology*. **21**, 889-892.

Rasmussen B, Fletcher IR, Muhling JR, Mueller AG, and Hall GC. (2007) Bushveld-aged fluid flow, peak metamorphism, and gold mobilization in the Witwatersrand basin, South Africa: Constraints from in situ SHRIMP U-Pb dating of monazite and xenotime. *Geology*. **35**, 931-934, doi: 10.1130/G23588A.1.

Rye R, Holland HD. (1998) Paleosols and the evolution of atmospheric oxygen: a critical review. *American Journal of Science*. **298**, 621-72.

Shuster DL, and Farley KA. (2004) $^{4}He/^{3}He$ thermochronometry. *Earth and Planetary Science Letters*. **217**, 1–17, doi: 10.1016/S0012-821X(03)00595-8.

Shuster DL, Vasconcelos PM, Heim JA, and Farley KA. (2005) Weathering geochronology by (U-Th)/He dating of goethite: *Geochimica et Cosmochimica Acta*. **69**, 659–673, doi: 10.1016/j.gca.2004.07.028.

Smith AJB. (2018) The Iron Formations of Southern Africa. In: Siegesmund S, Basei M, Oyhantçabal P, and Oriolo S (eds) *Geology of Southwest Gondwana*. Regional Geology Reviews. 469-491.

Smith AJB, and Beukes NJ. (2016) Paleoproterozoic Banded Iron formation-Hosted High Grade Hematite Iron Ore Deposits of Transvaal Supergroup, South Africa. *Episodes*. **39**, 269-284, doi: 10.18814/epiiugs/2016/v39i2/95778.

Smith CB, Clark TC, Barton ES, and Bristow JW. (1994) Emplacement ages of kimberlite occurrences in the Prieska region, southwest border of the Kaapvaal Craton, South Africa. *Chemical Geology*. **113**, 149-169.

Stanley JR, and Flowers RM. (2016) Dating kimberlite emplacement with zircon and perovskite (U-Th)/He geochronology. *Geochemistry, Geophysics, Geosystems*. **17**, 4517–4533, doi: 10.1002/2016GC006519.

Stanley JR, Flowers RM, and Bell DR. (2013) Kimberlite (U-Th)/He dating links surface erosion with lithospheric heating, thinning, and metasomatism in the southern African Plateau. *Geology*. **41**, 1243–1246, doi: 10.1130/G34797.1.

Sumner DY, and Beukes NJ. (2006) Sequence stratigraphic development of the Neoarchean Transvaal carbonate platform, Kaapvaal Craton, South Africa. *South African Journal of Geology*. **109**, 11-22.

Sumner DY, and Bowring SA. (1996) U/Pb geochronologic constraints on deposition of the Campbellrand Subgroup, Transvaal Supergroup, South Africa. *Precambrian Research*. **79**, 25-35.

Tankard AJ, Jackson MPA, Eriksson KA, Hobday DK, Hunter, DR, and Minter WEL. (1982) The Cape trough: an aborted rift. In *Crustal evolution of Southern Africa*. 333-363.

Tinker J, de Wit M, and Grotzinger J. (2002) Seismic stratigraphic constraints on Neoarchean-Paleoproterozoic evolution of the western margin of the Kaapvaal Craton, South Africa. *South African Journal of Geology*. **105**, 107-134.

Trendall AF. (2002) The significance of iron-formation in the Precambrian stratigraphic record. In: Altermann W, and Corcoran PL (Eds), *Precambrian sedimentary environments: A modern approach to ancient depositional systems*. 133-66.

Van Niekerk HS. (2006) The origin of the Kheis Terrane and its relationship with the Archean Kaapvaal Craton and the Grenvillian Namaqua Province in southern Africa. (Doctoral dissertation, University of Johannesburg).

Table 3.1:

Aliquot	Degassed mass (mg)	[4He] nmol/g	+/-	[21Ne*] fmol/g	+/-	Nucleogenic $^{21}Ne^*$ (%)	$^{21}Ne^*/^4He$	Ne age (Ma)	+/-	He age (Ma)	+/-
Khumani											
10-11KH	103.0	4.70	0.03	0.157	0.001	65.59	3.34E-08	2041	115	1937	62
11KH-b	105.6	4.98	0.09	0.154	0.002	63.87	3.09E-08	2012	119	2029	83
10-11KH-N1	100.4	5.05	0.03	0.149	0.001	65.37	2.95E-08	1960	113	2052	65
10-11KH-N2	101.9	5.43	0.04	0.159	0.001	66.44	2.93E-08	2063	117	2173	70
	Mean	5.04		0.155		65.32	3.08E-08	2018		2048	
	2s	0.26		0.004				114		87	
	% 2s	5.16		2.58				5.65		4.25	
Black Rock											
13-N64	102.3	3.32	0.02	0.132	0.003	20.45	3.99E-08	1715	129	1440	50
13-N64-1	105.8	3.64	0.04	0.131	0.007	21.44	3.61E-08	1705	164	1562	61
13-N64-2	99.5	3.66	0.04	0.131	0.006	22.59	3.57E-08	1698	160	1568	62
	Mean	3.54		0.131		21.50	3.72E-08	1706		1523	
	2s	0.15		0.004				141		61	
	% 2s	4.24		3.04				8.26		4.00	
Belgravia											
BEL99H	106.2	3.25	0.02	0.187	0.001	78.16	5.75E-08	1275	66	729	17
BEL99H-a	107.7	3.28	0.06	0.170	0.002	65.89	5.20E-08	1173	63	734	25
BEL99H-b	130.3	3.29	0.06	0.182	0.002	59.86	5.55E-08	1247	67	736	25
BEL99H-4-N1	102.1	3.44	0.03	0.182	0.001	81.27	5.29E-08	1243	64	767	20
BEL99H-4-N2	102.2	3.28	0.03	0.180	0.001	81.20	5.49E-08	1234	62	735	20
	Mean	3.31		0.180		73.28	5.45E-08	1234		740	
	2s	0.06		0.004				47		15	
	% 2s	1.69		2.22				3.81		2.03	
Beeshoek											
03QK-90-1	104.56	14.40	0.04	0.455	0.003	69.23	3.16E-08	1774	83	1759	33
03QK-90-2	98.21	14.44	0.04	0.456	0.003	70.06	3.16E-08	1778	83	1762	34
	Mean	14.42		0.456		69.64	3.16E-08	1776		1761	
	2s	0.05		0.004				97		39	
	% 2s	0.33		0.88				5.46		2.22	
Rooinekke											
Rooin_A	326.46	4.93	0.07	0.267	0.004	67.58	5.42E-08	1493	96	894	35
Rooin_B	332.06	5.14	0.07	0.269	0.004	69.42	5.23E-08	1501	96	930	37
	Mean	5.04		0.268		68.50	5.33E-08	1497		912	
	2s	0.12		0.005				112		42	
	% 2s	2.42		1.75				7.48		4.61	

Aliquot	Digested mass (mg)	U (ppm)	+/-	Th (ppm)	+/-	Sm (ppm)	+/-
Khumani							
09KH1	26.65	0.31	0.01	0.32	0.01	0.16	0.01
09KH2	27.04	0.29	0.01	0.29	0.01	0.14	0.01
	Mean ppm	0.30	0.01	0.31	0.01	0.15	0.01
	2s	0.01		0.01		0.01	
	% 2s	2.98		4.58		6.57	
Black Rock							
09N64A	25.25	0.25	0.01	0.50	0.01	0.65	0.01
09N64B	25.33	0.28	0.01	0.50	0.01	0.61	0.01
	Mean ppm	0.26	0.01	0.50	0.01	0.63	0.01
	2s	0.01		0.00		0.02	
	% 2s	4.30		0.38		2.90	
Belgravia							
09BEL1	27.12	0.61	0.01	0.68	0.02	2.58	0.02
09BEL2	26.48	0.62	0.01	0.71	0.02	1.81	0.02
	Mean ppm	0.61	0.01	0.69	0.02	2.20	0.02
	2s	0.01		0.01		0.38	
	% 2s	0.92		1.64		17.49	
Beeshoek							
09QK1	28.14	1.03	0.02	1.08	0.02	0.27	0.02
09QK2	32.31	1.02	0.02	1.09	0.02	0.25	0.02
	Mean ppm	1.03	0.02	1.08	0.02	0.26	0.02
	2s	0.01		0.01		0.01	
	% 2s	0.78		0.65		2.78	
Rooinekke							
Rooin A	24.54	0.78	0.02	0.58	0.03	0.63	0.04
Rooin B	25.48	0.82	0.01	0.59	0.03	0.61	0.04
	Mean ppm	0.80	0.02	0.59	0.03	0.62	0.04
	2s	0.02		0.01		0.01	
	% 2s	2.50		0.85		1.61	

APPENDIX B: SUPPLEMENTARY FIGURES AND TABLES

Supplementary Figure 3.1: Delta plots for the Belgravia, Black Rock, and Beeshoek samples modeled using the sample derived activation energy. The black line shows the experimentally observed Delta array, while the red line is a best-fit model using hematite diffusion kinetics and 8 discrete diffusion domains. Delta (Δ) = $2\ln(r/r_0)$.

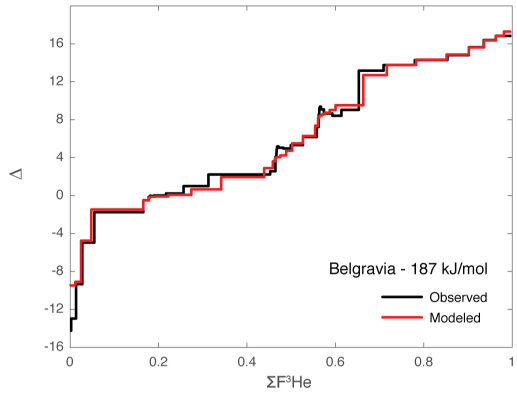

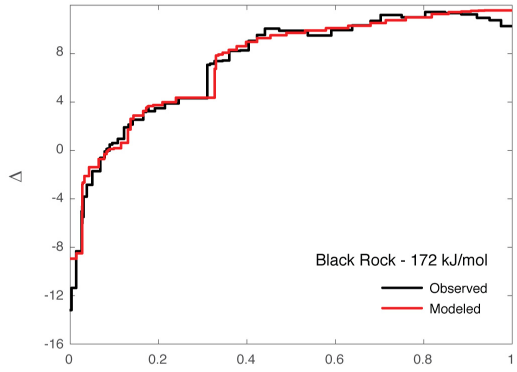

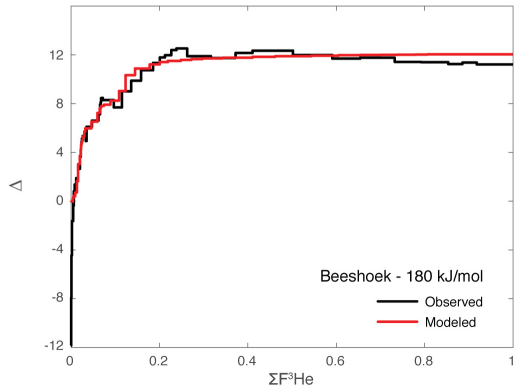

Supplementary Figure 3.2: Here we include the results of our time-temperature modeling in which we tested the sensitivity of our modeled results to varying input parameters. These time-temperature paths were generated using sample-specific activation energies and the ^{238}U decay constant.

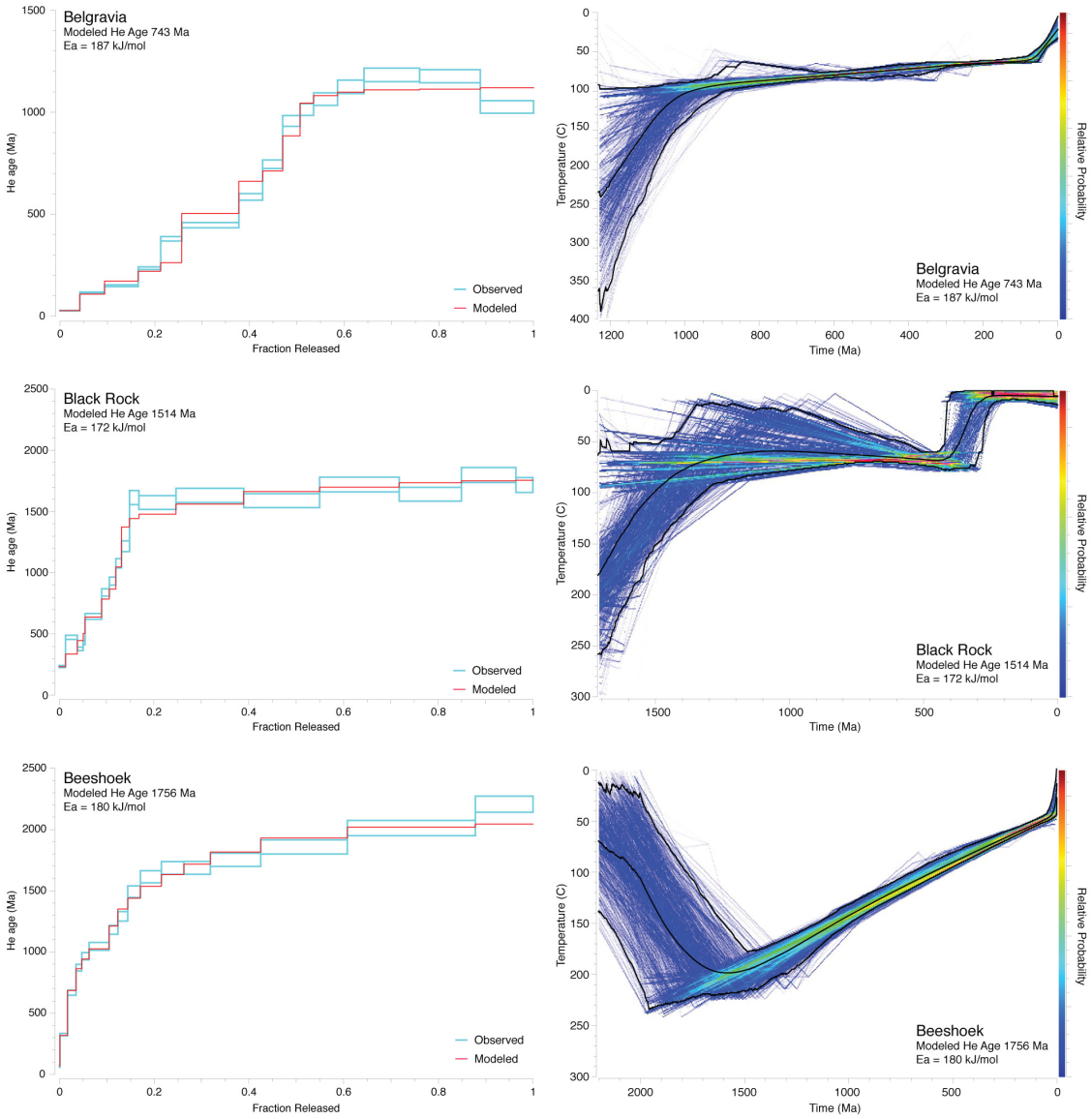

Supplementary Figure 3.3: Here we include the results of our time-temperature modeling in which we tested the sensitivity of our modeled results to varying input parameters. These time-temperature paths were generated using a fixed activation energy of 171 kJ/mol (Farley, 2018) and the ^{40}K decay constant.

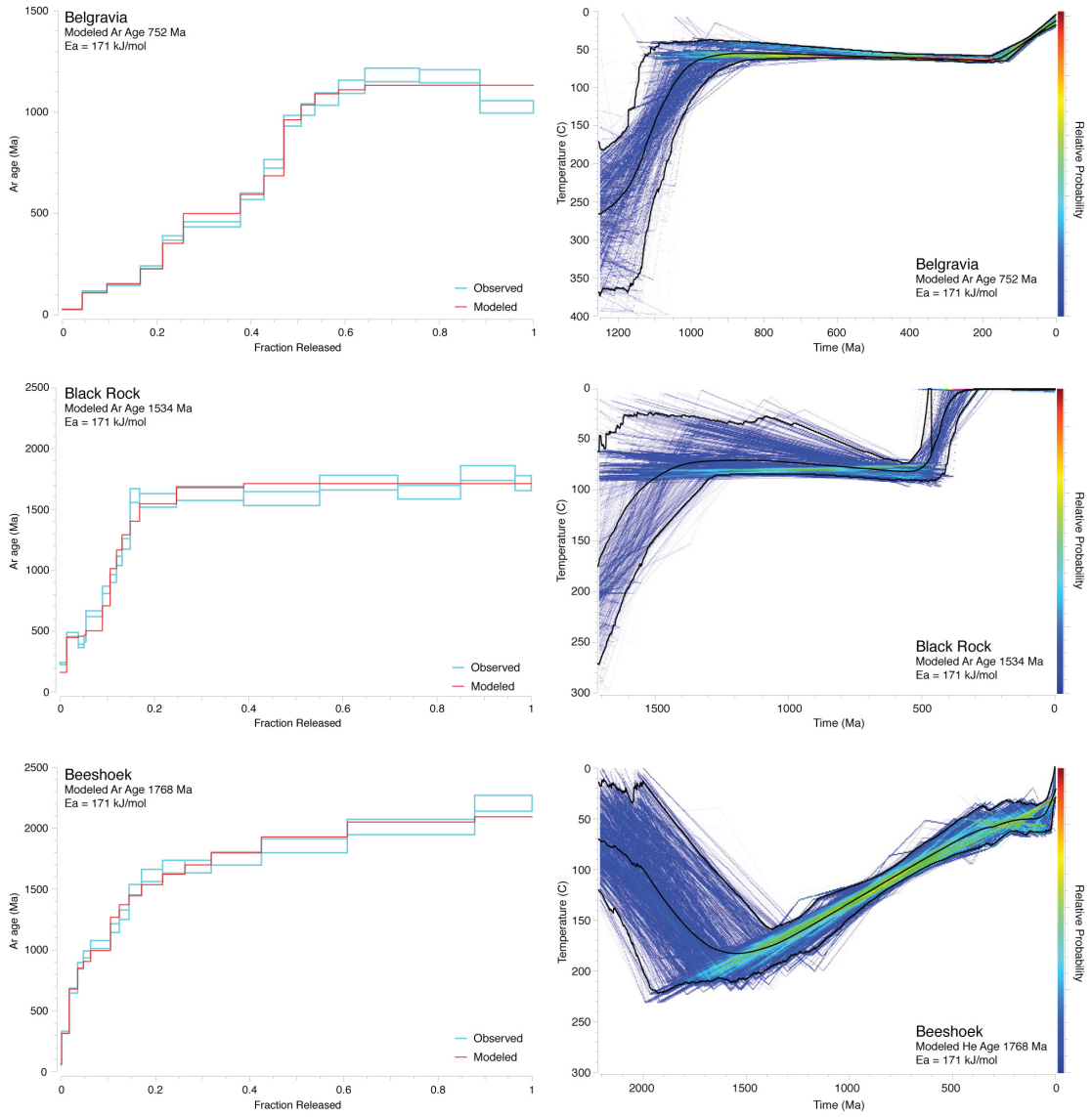

Supplementary Figure 3.4: Here we include the results of our time-temperature modeling in which we tested the sensitivity of our modeled results to varying input parameters. These time-temperature paths were generated using sample-specific activation energies and the ^{40}K decay constant.

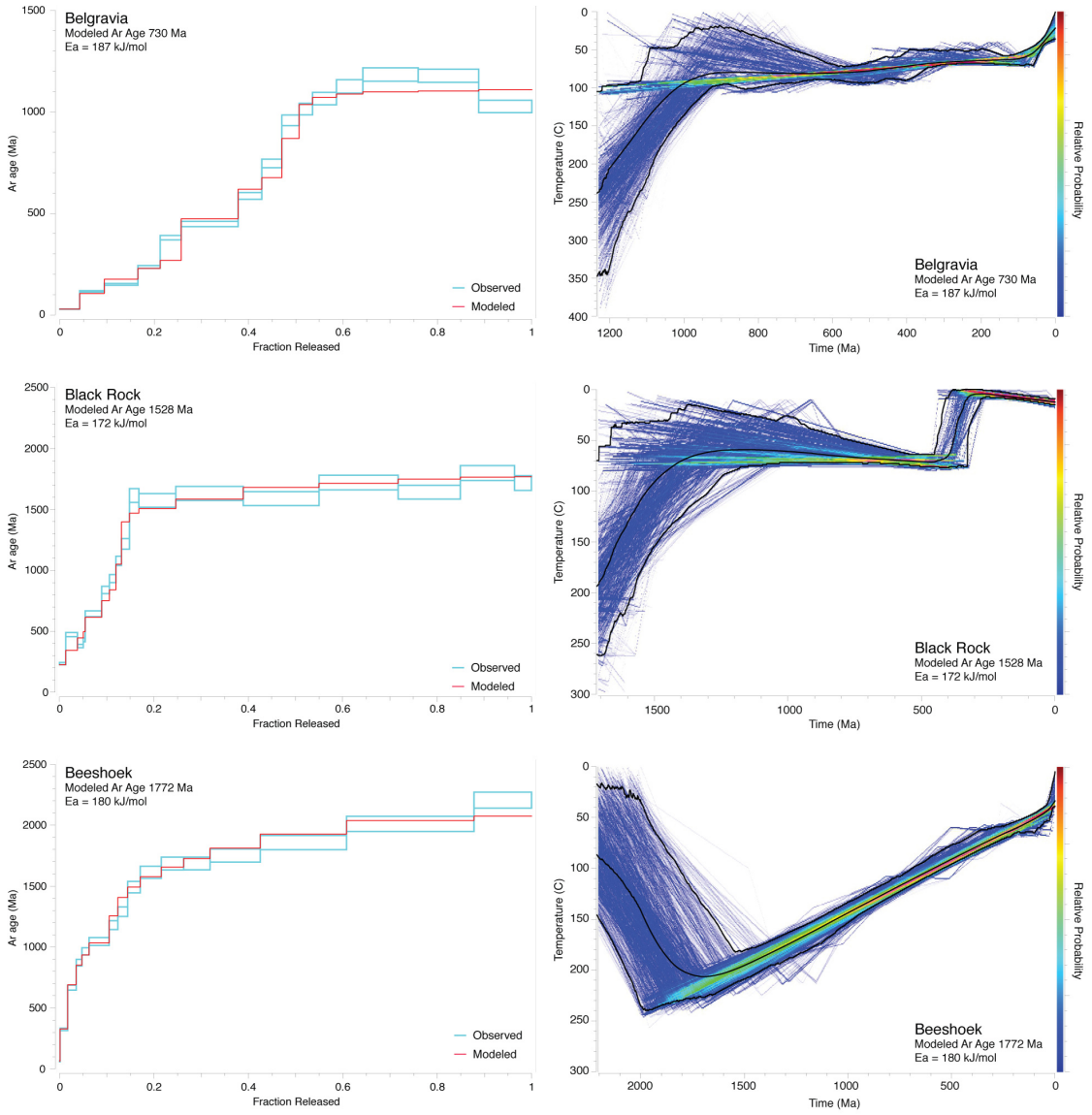

Supplementary Figure 3.5: $^{4}He/^{3}He$ age spectra produced from two different step-heating experiments. The (U-Th)/Ne age is shown for reference. We interpret this pattern to be the result of U-Th inhomogeneity, where larger (i.e. more retentive) domains have a higher U-Th concentration.

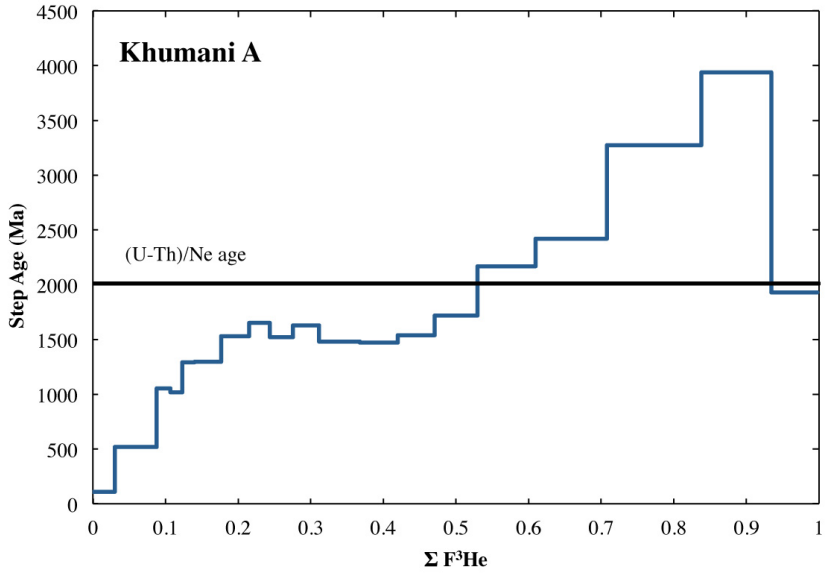

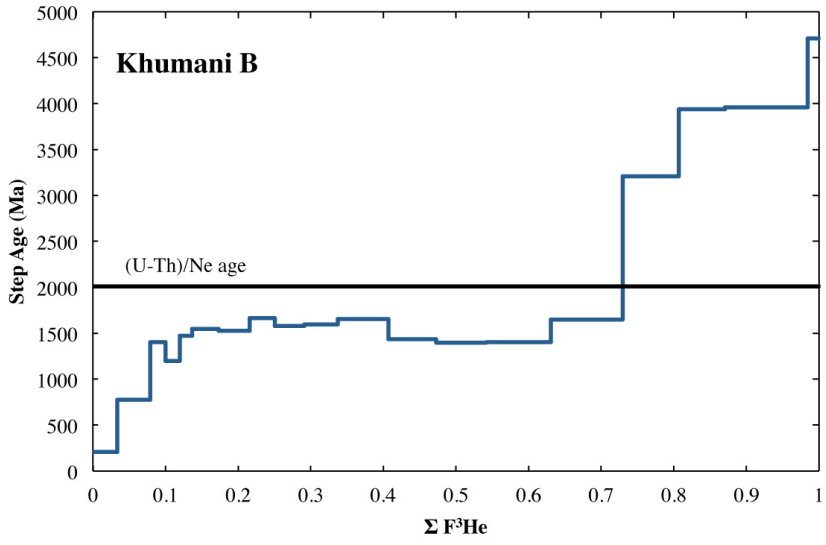

Supplementary Figure 3.6: SEM image (A) and corresponding EDS map (B) indicative of the regions within the Khumani sample which have an elevated Si content. This particular map has a Si content of 7.5 wt.%.

(A)

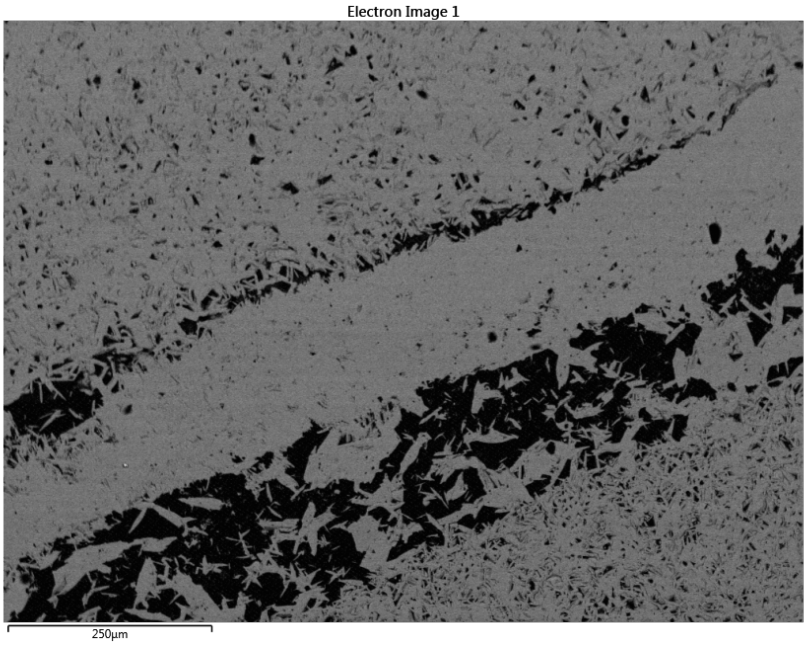

(B)

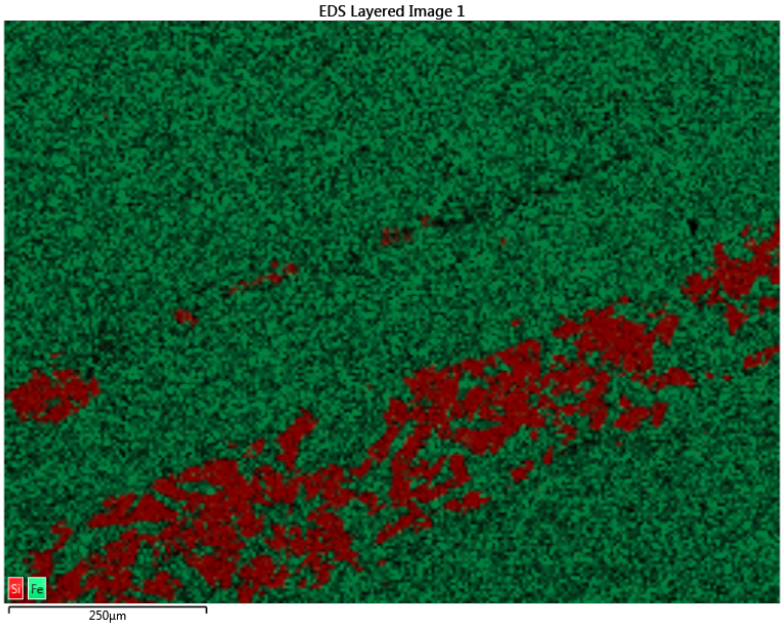

Supplementary Table 1: Step Age plot data. Ages in Ma.

Black Rock

^{4}He Fcum	R_{step}/R_{bulk}	± R_{step}/R_{bulk}	Step Age	± Step Age
0.0134	0.1546	0.0043	236	8.7
0.0382	0.3116	0.0084	474	16.9
0.0506	0.2491	0.0068	380	13.8
0.0546	0.2820	0.0075	429	15.3
0.0894	0.4228	0.0114	644	23.6
0.1058	0.5510	0.0147	840	30.0
0.1195	0.6121	0.0164	933	32.8
0.1313	0.7081	0.0181	1078	37.5
0.1484	0.7996	0.0215	1217	43.7
0.1683	1.0597	0.0280	1615	57.0
0.2465	1.0329	0.0270	1574	56.4
0.3896	1.0701	0.0288	1632	57.9
0.5500	1.0434	0.0284	1589	56.9
0.7172	1.1309	0.0293	1721	60.3
0.8499	1.0791	0.0290	1642	56.2
0.9646	1.1810	0.0300	1799	61.5
1.0000	1.1275	0.0291	1717	60.8

Belgravia

^{4}He Fcum	R_{step}/R_{bulk}	± R_{step}/R_{bulk}	Step Age	± Step Age
0.0420	0.0386	0.0011	28.5	0.9
0.0943	0.1574	0.0041	116	3.3
0.1654	0.2038	0.0055	151	4.4
0.2127	0.3195	0.0082	236	6.5
0.2570	0.5142	0.0135	381	10.9
0.3775	0.6049	0.0156	448	12.7
0.4280	0.7917	0.0209	586	16.4
0.4703	1.0084	0.0267	746	21.1
0.5072	1.2948	0.0328	958	26.3
0.5356	1.3693	0.0352	1014	28.7
0.5864	1.4397	0.0376	1065	30.5
0.6417	1.5205	0.0407	1125	32.7
0.7586	1.5990	0.0413	1184	33.0
0.8867	1.5906	0.0408	1177	32.3
0.9865	1.3871	0.0376	1027	30.6
1.0000	0.7523	0.0201	557	16.1

Beeshoek

^{4}He Fcum	R_{step}/R_{bulk}	± R_{step}/R_{bulk}	Step Age	± Step Age
0.0011	0.0355	0.0023	62.6	4.0
0.0172	0.1843	0.0055	324	9.7
0.0351	0.3786	0.0114	667	20.1
0.0471	0.4949	0.0153	871	26.9
0.0625	0.5478	0.0165	965	29.1
0.1050	0.5937	0.0184	1045	32.5
0.1235	0.6701	0.0206	1180	36.2
0.1441	0.7328	0.0221	1290	38.8
0.1708	0.8473	0.0267	1492	47.0
0.2153	0.9162	0.0284	1613	50.0
0.2628	0.9571	0.0296	1685	52.2
0.3185	0.9573	0.0296	1685	52.0
0.4251	0.9945	0.0306	1751	53.9
0.6077	1.0548	0.0329	1857	58.1
0.8777	1.1420	0.0356	2010	62.7
1.0000	1.2524	0.0374	2205	65.8

R=^{4}He/^{3}He

Supplemental Table 2a: Belgravia diffusion data modeled with single crystal activation energy

Belgravia	domains	Ea	$\ln(D_o/a^2)$						
	8	40.87	25.247						
gas fraction	0.022	0.112	0.117	0.176	0.058	0.140	0.210	0.163	
$\log(D_o/a^2)$	16.219	11.171	9.496	9.468	8.289	6.809	3.729	2.761	
closure temp (° C)	14	68	91	91	109	134	197	221	
step	temp	time	Fcum observed	Fcum modeled	10000/k	$\ln(D/a^2)$ modeled	delta modeled	delta observed	$\ln(D/a^2)$ observed
1	50	0.5	4.0E-05	8.5E-06	30.945	-33.296	-2.554	-4.116	-30.171
2	100	0.5	2.3E-03	6.0E-04	26.799	-24.783	-2.546	-3.880	-22.115
3	150	0.5	0.013	0.013	23.632	-18.677	-2.342	-2.378	-18.605
4	200	0.5	0.028	0.026	21.135	-17.455	-0.385	-0.422	-17.380
5	250	0.5	0.055	0.055	19.115	-16.019	0.975	0.983	-16.035
6	300	0.5	0.166	0.165	17.447	-13.552	1.456	1.453	-13.546
7	275	0.75	0.178	0.178	18.243	-15.652	1.688	1.705	-15.686
8	250	1.4	0.181	0.181	19.115	-17.546	1.738	1.790	-17.650
9	225	2	0.181	0.181	20.074	-19.547	1.752	1.908	-19.859
10	200	3	0.181	0.182	21.135	-21.734	1.754	2.126	-22.476
11	230	2	0.182	0.183	19.875	-19.149	1.758	1.913	-19.458
12	260	2	0.190	0.191	18.756	-16.919	1.793	1.827	-16.986
13	290	1	0.217	0.214	17.757	-15.130	1.927	1.836	-14.949
14	320	0.5	0.257	0.252	16.859	-13.765	2.168	2.135	-13.701
15	350	0.5	0.313	0.339	16.048	-12.630	2.435	2.675	-13.111
16	380	0.5	0.452	0.446	15.310	-12.019	2.887	2.771	-11.787
17	355	1	0.464	0.462	15.920	-14.360	3.431	3.584	-14.666
18	330	1.5	0.467	0.466	16.580	-16.168	3.656	3.916	-16.688
19	305	2.5	0.467	0.467	17.297	-17.786	3.728	4.133	-18.596
20	280	4	0.467	0.468	18.078	-19.443	3.753	4.225	-20.388
21	310	3	0.468	0.469	17.148	-17.597	3.786	4.252	-18.528
22	340	2	0.472	0.475	16.309	-16.097	3.899	4.110	-16.518
23	370	1	0.482	0.484	15.548	-14.917	4.092	3.991	-14.716
24	400	0.5	0.499	0.495	14.856	-13.863	4.277	4.104	-13.516
25	430	0.5	0.527	0.519	14.222	-13.105	4.550	4.470	-12.945
26	460	0.5	0.558	0.548	13.640	-12.828	5.010	4.949	-12.706
27	435	0.8	0.562	0.557	14.121	-14.350	5.276	5.643	-15.084
28	410	1.2	0.564	0.561	14.638	-15.558	5.348	5.943	-16.748
29	385	2	0.564	0.563	15.194	-16.764	5.380	6.108	-18.221
30	360	4	0.564	0.565	15.794	-18.030	5.395	6.117	-19.473
31	390	2.5	0.565	0.567	15.080	-16.601	5.416	6.157	-18.083
32	420	1.5	0.567	0.574	14.427	-15.348	5.461	5.950	-16.326
33	450	0.75	0.574	0.582	13.828	-14.264	5.534	5.673	-14.542
34	480	0.5	0.593	0.596	13.278	-13.362	5.649	5.496	-13.056
35	500	0.5	0.614	0.614	12.934	-13.048	5.846	5.777	-12.911
36	700	0.1667	0.653	0.679	10.276	-10.500	7.305	7.584	-11.056
37	750	0.1667	0.709	0.723	9.774	-10.683	7.914	7.830	-10.517
38	800	0.1667	0.780	0.778	9.318	-10.248	8.164	8.050	-10.019
39	850	0.1667	0.853	0.840	8.904	-9.810	8.372	8.267	-9.601
40	900	0.1667	0.902	0.898	8.524	-9.474	8.594	8.656	-9.597
41	950	0.1667	0.936	0.938	8.176	-9.405	8.918	8.992	-9.554
42	1000	0.1667	0.963	0.966	7.855	-9.195	9.143	9.185	-9.278
43	1050	0.1667	0.994	0.987	7.558	-8.696	9.199	8.874	-8.047
44	1100	0.1	0.998	0.995	7.283	-8.148	9.208	9.207	-8.146

Supplemental Table 2b: Belgravia diffusion data modeled with sample activation energy

Belgravia	domains	Ea	ln(Do/a^2)						
	8	44.728	25.247						
gas fraction	0.0220	0.1981	0.2296	0.0635	0.0893	0.1973	0.1017	0.0986	
log(D_o/a^2)	18.137	12.236	10.535	9.3467	8.0295	4.7675	3.9638	3.1766	
closure temp (° C)	23	86	109	127	149	215	234	255	
step	temp	time	Fcum observed	Fcum modeled	10000/k	ln(D/a^2) modeled	delta modeled	delta observed	ln(D/a^2) observed
1	50	0.5	4.0E-05	3.7E-06	30.945	-34.930	-4.741	-7.121	-30.171
2	100	0.5	2.3E-03	4.0E-04	26.799	-25.607	-4.736	-6.482	-22.115
3	150	0.5	0.013	0.012	23.632	-18.859	-4.546	-4.673	-18.605
4	200	0.5	0.028	0.025	21.135	-17.578	-2.375	-2.474	-17.380
5	250	0.5	0.055	0.048	19.115	-16.318	-0.732	-0.873	-16.035
6	300	0.5	0.166	0.165	17.447	-13.522	-0.253	-0.241	-13.546
7	275	0.75	0.178	0.178	18.243	-15.629	-0.095	-0.066	-15.686
8	250	1.4	0.181	0.181	19.115	-17.643	-0.070	-0.066	-17.650
9	225	2	0.181	0.182	20.074	-19.814	-0.064	-0.041	-19.859
10	200	3	0.181	0.182	21.135	-22.203	-0.063	0.074	-22.476
11	230	2	0.182	0.182	19.875	-19.369	-0.061	-0.017	-19.458
12	260	2	0.190	0.191	18.756	-16.885	-0.045	0.005	-16.986
13	290	1	0.217	0.222	17.757	-14.807	0.041	0.112	-14.949
14	320	0.5	0.257	0.274	16.859	-13.366	0.331	0.499	-13.701
15	350	0.5	0.313	0.342	16.048	-12.823	0.973	1.117	-13.111
16	380	0.5	0.452	0.439	15.310	-12.122	1.452	1.285	-11.787
17	355	1	0.464	0.459	15.920	-14.208	1.810	2.039	-14.666
18	330	1.5	0.467	0.463	16.580	-15.970	1.948	2.307	-16.688
19	305	2.5	0.467	0.465	17.297	-17.672	1.992	2.454	-18.596
20	280	4	0.467	0.465	18.078	-19.460	2.006	2.470	-20.388
21	310	3	0.468	0.467	17.148	-17.408	2.027	2.587	-18.528
22	340	2	0.472	0.476	16.309	-15.704	2.119	2.526	-16.518
23	370	1	0.482	0.489	15.548	-14.491	2.369	2.481	-14.716
24	400	0.5	0.499	0.502	14.856	-13.705	2.756	2.661	-13.516
25	430	0.5	0.527	0.527	14.222	-13.056	3.145	3.089	-12.945
26	460	0.5	0.558	0.554	13.640	-12.839	3.691	3.625	-12.706
27	435	0.8	0.562	0.561	14.121	-14.702	4.081	4.272	-15.084
28	410	1.2	0.564	0.563	14.638	-16.050	4.173	4.522	-16.748
29	385	2	0.564	0.564	15.194	-17.368	4.206	4.633	-18.221
30	360	4	0.564	0.565	15.794	-18.748	4.221	4.583	-19.473
31	390	2.5	0.565	0.567	15.080	-17.178	4.240	4.692	-18.083
32	420	1.5	0.567	0.570	14.427	-15.803	4.287	4.549	-16.326
33	450	0.75	0.574	0.577	13.828	-14.621	4.370	4.330	-14.542
34	480	0.5	0.593	0.587	13.278	-13.666	4.512	4.207	-13.056
35	500	0.5	0.614	0.600	12.934	-13.396	4.764	4.521	-12.911
36	700	0.1667	0.653	0.663	10.276	-10.589	6.352	6.586	-11.056
37	750	0.1667	0.709	0.716	9.774	-10.533	6.890	6.881	-10.517
38	800	0.1667	0.780	0.783	9.318	-10.061	7.166	7.145	-10.019
39	850	0.1667	0.853	0.852	8.904	-9.666	7.435	7.403	-9.601
40	900	0.1667	0.902	0.902	8.524	-9.573	7.816	7.828	-9.597
41	950	0.1667	0.936	0.936	8.176	-9.519	8.181	8.199	-9.554
42	1000	0.1667	0.963	0.963	7.855	-9.296	8.431	8.422	-9.278
43	1050	0.1667	0.994	0.981	7.558	-9.063	8.649	8.140	-8.047
44	1100	0.1	1.000	0.990	7.283	-8.582	8.718	8.500	-8.146

Supplemental Table 3a: Black Rock diffusion data modeled with single crystal activation energy

Black Rock	domains	Ea	$\ln(D_o/a^2)$						
	8	40.87	16.984						
gas fraction	0.012	0.024	0.047	0.198	0.218	0.102	0.260	0.139	
$\log(D_o/a^2)$	15.793	12.183	9.689	6.945	3.533	2.407	2.200	2.077	
closure temp (° C)	18	56	88	131	202	230	236	240	
step	temp	time	Fcum observed	Fcum modeled	10000/k	$\ln(D/a^2)$ modeled	delta modeled	delta observed	$\ln(D/a^2)$ observed
1	100	0.5	4.735E-04	2.0E-04	26.799	-26.959	-5.590	-6.446	-25.245
2	150	0.5	5.053E-03	4.6E-03	23.632	-20.687	-5.469	-5.553	-20.519
3	200	0.5	0.016	0.014	21.135	-18.531	-3.979	-4.059	-18.370
4	250	0.5	0.028	0.028	19.115	-17.420	-2.457	-2.429	-17.475
5	230	0.5	0.029	0.029	19.875	-19.528	-2.184	-2.223	-19.449
6	210	0.5	0.029	0.029	20.698	-21.276	-2.156	-2.433	-20.722
7	190	1	0.030	0.029	21.591	-23.126	-2.150	-2.614	-22.199
8	170	1	0.030	0.029	22.566	-25.133	-2.149	-2.912	-23.607
9	250	0.5	0.032	0.033	19.115	-18.215	-2.059	-1.833	-18.667
10	280	0.5	0.039	0.043	18.078	-17.148	-1.526	-1.351	-17.498
11	310	0.5	0.052	0.053	17.148	-16.902	-0.693	-0.796	-16.695
12	340	0.5	0.070	0.071	16.309	-16.015	-0.274	-0.252	-16.058
13	330	1	0.080	0.081	16.580	-17.130	0.006	0.011	-17.140
14	320	1	0.084	0.085	16.859	-18.008	0.158	0.108	-17.908
15	310	1	0.086	0.087	17.148	-18.745	0.229	0.132	-18.553
16	300	1	0.087	0.087	17.447	-19.435	0.266	0.103	-19.110
17	290	2	0.089	0.088	17.757	-20.124	0.292	0.069	-19.679
18	280	2	0.090	0.089	18.078	-20.824	0.312	0.053	-20.307
19	325	0.5	0.091	0.090	16.718	-18.094	0.346	0.295	-17.993
20	350	0.5	0.097	0.095	16.048	-16.960	0.468	0.354	-16.732
21	375	0.5	0.110	0.104	15.429	-16.239	0.744	0.522	-15.794
22	400	0.5	0.124	0.116	14.856	-15.749	1.089	0.992	-15.557
23	400	0.5	0.134	0.124	14.856	-16.049	1.239	1.103	-15.778
24	425	0.25	0.143	0.134	14.324	-15.140	1.331	1.302	-15.081
25	450	0.5	0.167	0.166	13.828	-14.454	1.497	1.619	-14.696
26	430	0.5	0.174	0.175	14.222	-15.509	1.620	1.785	-15.838
27	410	0.5	0.177	0.179	14.638	-16.440	1.658	1.826	-16.777
28	390	0.5	0.178	0.180	15.080	-17.376	1.671	1.782	-17.597
29	370	1	0.179	0.181	15.548	-18.354	1.678	1.721	-18.440
30	350	1	0.179	0.182	16.048	-19.388	1.682	1.656	-19.335
31	450	0.5	0.194	0.197	13.828	-14.913	1.727	1.770	-15.000
32	475	0.5	0.216	0.225	13.366	-14.211	1.851	1.963	-14.435
33	500	0.5	0.247	0.260	12.934	-13.781	2.081	2.175	-13.970
34	625	0.5	0.312	0.320	11.134	-13.020	3.551	3.538	-12.992
35	550	0.5	0.318	0.322	12.148	-16.205	4.100	3.587	-15.179
36	575	0.5	0.329	0.327	11.790	-15.538	4.135	3.695	-14.657
37	600	0.5	0.347	0.334	11.453	-14.957	4.192	3.717	-14.007
38	625	0.5	0.362	0.345	11.134	-14.460	4.271	4.109	-14.136
39	650	0.5	0.387	0.362	10.832	-14.032	4.368	4.128	-13.554
40	675	0.5	0.406	0.385	10.547	-13.654	4.472	4.516	-13.741
41	700	0.5	0.425	0.414	10.276	-13.309	4.579	4.757	-13.665
42	725	0.5	0.443	0.449	10.019	-12.989	4.683	5.016	-13.654
43	750	0.5	0.475	0.490	9.774	-12.690	4.785	4.929	-12.977
44	775	0.5	0.539	0.537	9.541	-12.414	4.887	4.734	-12.108
45	800	0.5	0.593	0.586	9.318	-12.181	4.999	4.953	-12.089
46	825	0.5	0.640	0.635	9.106	-12.009	5.132	5.145	-12.036
47	850	0.5	0.682	0.681	8.904	-11.903	5.287	5.330	-11.990
48	850	0.5	0.704	0.712	8.904	-12.165	5.418	5.572	-12.473
49	850	1	0.752	0.754	8.904	-12.370	5.520	5.477	-12.283
50	900	1	0.805	0.815	8.524	-11.765	5.608	5.691	-11.931
51	900	1	0.850	0.856	8.524	-11.869	5.660	5.643	-11.836
52	900	1	0.887	0.887	8.524	-11.916	5.684	5.596	-11.741
53	900	1	0.922	0.909	8.524	-11.969	5.710	5.453	-11.455
54	900	1	0.951	0.927	8.524	-12.002	5.726	5.356	-11.260
55	900	1	0.977	0.941	8.524	-12.025	5.738	5.112	-10.772
56	900	1	1.000	0.952	8.524	-12.043	5.747	3.810	-8.170

Supplemental Table 3b: Black Rock diffusion data modeled with sample activation energy

Black Rock	domains	Ea	$\ln(D_o/a^2)$						
	8	41.053	16.984						
gas fraction	0.027	0.085	0.156	0.049	0.222	0.115	0.223	0.124	
$\log(D_o/a^2)$	14.143	9.355	6.783	5.205	3.329	2.323	2.199	2.108	
closure temp (° C)	36	94	136	166	209	235	238	241	
step	temp	time	Fcum observed	Fcum modeled	10000/k	$\ln(D/a^2)$ modeled	delta modeled	delta observed	$\ln(D/a^2)$ observed
1	100	0.5	4.7E-04	5.8E-05	26.799	-29.435	-4.475	-6.570	-25.245
2	150	0.5	5.1E-03	1.5E-03	23.632	-22.925	-4.459	-5.662	-20.519
3	200	0.5	0.016	0.016	21.135	-18.200	-4.241	-4.156	-18.370
4	250	0.5	0.028	0.029	19.115	-17.370	-2.570	-2.517	-17.475
5	230	0.5	0.029	0.029	19.875	-21.193	-1.443	-2.315	-19.449
6	210	0.5	0.029	0.029	20.698	-22.942	-1.418	-2.528	-20.722
7	190	1	0.030	0.029	21.591	-24.798	-1.414	-2.713	-22.199
8	170	1	0.030	0.029	22.566	-26.814	-1.413	-3.016	-23.607
9	250	0.5	0.032	0.030	19.115	-19.828	-1.341	-1.921	-18.667
10	280	0.5	0.039	0.034	18.078	-18.221	-1.073	-1.435	-17.498
11	310	0.5	0.052	0.045	17.148	-17.026	-0.710	-0.875	-16.695
12	340	0.5	0.070	0.066	16.309	-15.960	-0.376	-0.327	-16.058
13	330	1	0.080	0.079	16.580	-16.925	-0.173	-0.065	-17.140
14	320	1	0.084	0.084	16.859	-17.697	-0.076	0.030	-17.908
15	310	1	0.086	0.087	17.148	-18.382	-0.032	0.053	-18.553
16	300	1	0.087	0.088	17.447	-19.044	-0.010	0.023	-19.110
17	290	2	0.089	0.089	17.757	-19.714	0.005	-0.012	-19.679
18	280	2	0.090	0.090	18.078	-20.400	0.016	-0.030	-20.307
19	325	0.5	0.091	0.092	16.718	-17.628	0.035	0.218	-17.993
20	350	0.5	0.097	0.101	16.048	-16.305	0.067	0.280	-16.732
21	375	0.5	0.110	0.117	15.429	-15.472	0.290	0.451	-15.794
22	400	0.5	0.124	0.133	14.856	-15.378	0.835	0.924	-15.557
23	400	0.5	0.134	0.139	14.856	-16.254	1.272	1.035	-15.778
24	425	0.25	0.143	0.145	14.324	-15.424	1.407	1.236	-15.081
25	450	0.5	0.167	0.167	13.828	-14.776	1.595	1.555	-14.696
26	430	0.5	0.174	0.174	14.222	-15.857	1.729	1.719	-15.838
27	410	0.5	0.177	0.177	14.638	-16.794	1.767	1.759	-16.777
28	390	0.5	0.178	0.178	15.080	-17.735	1.782	1.713	-17.597
29	370	1	0.179	0.178	15.548	-18.717	1.788	1.650	-18.440
30	350	1	0.179	0.179	16.048	-19.756	1.792	1.582	-19.335
31	450	0.5	0.194	0.190	13.828	-15.261	1.837	1.707	-15.000
32	475	0.5	0.216	0.211	13.366	-14.541	1.955	1.902	-14.435
33	500	0.5	0.247	0.241	12.934	-14.017	2.139	2.116	-13.970
34	625	0.5	0.312	0.329	11.134	-12.666	3.323	3.486	-12.992
35	550	0.5	0.318	0.332	12.148	-15.852	3.868	3.531	-15.179
36	575	0.5	0.329	0.337	11.790	-15.198	3.911	3.640	-14.657
37	600	0.5	0.347	0.347	11.453	-14.647	3.985	3.665	-14.007
38	625	0.5	0.362	0.361	11.134	-14.214	4.097	4.058	-14.136
39	650	0.5	0.387	0.379	10.832	-13.896	4.250	4.079	-13.554
40	675	0.5	0.406	0.400	10.547	-13.658	4.425	4.467	-13.741
41	700	0.5	0.425	0.425	10.276	-13.406	4.580	4.709	-13.665
42	725	0.5	0.443	0.455	10.019	-13.109	4.697	4.969	-13.654
43	750	0.5	0.475	0.491	9.774	-12.807	4.799	4.884	-12.977
44	775	0.5	0.539	0.533	9.541	-12.519	4.895	4.690	-12.108
45	800	0.5	0.593	0.581	9.318	-12.247	4.989	4.911	-12.089
46	825	0.5	0.640	0.631	9.106	-12.006	5.088	5.103	-12.036
47	850	0.5	0.682	0.682	8.904	-11.814	5.201	5.289	-11.990
48	850	0.5	0.704	0.716	8.904	-12.036	5.312	5.531	-12.473
49	850	1	0.752	0.761	8.904	-12.280	5.435	5.436	-12.283
50	900	1	0.805	0.820	8.524	-11.772	5.572	5.652	-11.931
51	900	1	0.850	0.858	8.524	-11.918	5.645	5.604	-11.836
52	900	1	0.887	0.887	8.524	-11.968	5.671	5.557	-11.741
53	900	1	0.922	0.908	8.524	-12.020	5.696	5.414	-11.455
54	900	1	0.951	0.926	8.524	-12.048	5.710	5.317	-11.260
55	900	1	0.977	0.939	8.524	-12.066	5.719	5.072	-10.772
56	900	1	1.000	0.950	8.524	-12.080	5.727	3.771	-8.170

Supplemental Table 4a: Beeshoek diffusion data modeled with single crystal activation energy

Beeshoek	domains	Ea	$\ln(D_o/a^2)$						
	8	40.870	17.020						
gas fraction	0.016	0.005	0.066	0.000	0.000	0.350	0.564	0.000	
$\log(D_o/a^2)$	9.706	8.088	5.663	3.579	1.869	1.639	1.534	1.467	
closure temp (° C)	88	112	155	201	245	252	255	257	
step	temp	time	Fcum observed	Fcum modeled	10000/k	$\ln(D/a^2)$ modeled	delta modeled	delta observed	$\ln(D/a^2)$ observed
1	100	1	1.0E-04	3.6E-07	26.799	-40.325	1.111	-4.527	-29.048
2	150	1	4.4E-04	9.2E-06	23.632	-33.812	1.112	-2.725	-26.138
3	200	0.5	9.1E-04	8.6E-05	21.135	-28.677	1.113	-1.124	-24.205
4	250	0.5	0.002	0.001	19.115	-24.542	1.123	0.181	-22.660
5	300	0.5	0.005	0.004	17.447	-21.218	1.176	0.934	-20.734
6	280	0.5	0.005	0.004	18.078	-22.590	1.213	1.101	-22.366
7	260	1	0.005	0.004	18.756	-24.003	1.222	1.109	-23.778
8	240	1	0.006	0.004	19.487	-25.514	1.225	0.987	-25.038
9	210	2	0.006	0.004	20.698	-28.004	1.226	0.892	-27.335
11	300	0.5	0.006	0.005	17.447	-21.356	1.244	1.315	-21.496
12	325	0.5	0.008	0.008	16.718	-20.006	1.320	1.551	-20.469
13	350	0.5	0.012	0.014	16.048	-19.014	1.513	1.779	-19.546
14	375	0.5	0.016	0.018	15.429	-18.748	2.017	2.128	-18.971
15	400	0.5	0.020	0.021	14.856	-19.169	2.817	2.595	-18.726
16	385	1	0.022	0.022	15.194	-20.387	3.077	2.917	-20.066
17	370	1	0.023	0.023	15.548	-21.287	3.163	3.073	-21.106
18	365	1	0.023	0.023	15.670	-21.615	3.202	3.151	-21.513
19	340	2	0.023	0.023	16.309	-22.976	3.225	3.192	-22.910
20	325	2	0.023	0.023	16.718	-23.839	3.236	3.168	-23.703
21	350	1	0.023	0.023	16.048	-22.478	3.245	3.253	-22.494
22	375	1	0.024	0.024	15.429	-21.259	3.272	3.261	-21.236
23	400	0.5	0.025	0.025	14.856	-20.184	3.324	3.342	-20.220
24	425	0.5	0.026	0.026	14.324	-19.286	3.422	3.419	-19.279
25	400	5	0.033	0.030	14.856	-20.785	3.624	3.237	-20.010
27	450	0.5	0.035	0.032	13.828	-18.996	3.786	3.772	-18.967
28	500	1	0.047	0.044	12.934	-17.612	4.014	3.975	-17.534
29	550	0.5	0.062	0.058	12.148	-16.462	4.247	4.196	-16.360
30	535	0.5	0.066	0.064	12.374	-17.194	4.381	4.608	-17.647
31	515	0.5	0.067	0.067	12.688	-17.951	4.437	4.721	-18.519
32	495	1	0.068	0.069	13.018	-18.697	4.470	4.906	-19.568
33	472	1	0.068	0.070	13.420	-19.569	4.493	4.930	-20.444
34	550	0.5	0.072	0.075	12.148	-17.051	4.542	4.778	-17.524
35	600	0.5	0.097	0.090	11.453	-15.996	4.729	4.439	-15.414
36	650	0.5	0.115	0.105	10.832	-15.635	5.187	5.069	-15.399
37	700	0.5	0.136	0.120	10.276	-15.553	5.719	5.475	-15.067
38	750	0.5	0.158	0.143	9.774	-14.940	5.928	5.878	-14.839
39	800	0.5	0.186	0.177	9.318	-14.305	6.079	6.154	-14.455
40	800	0.5	0.201	0.201	9.318	-14.475	6.164	6.379	-14.904
41	800	0.5	0.213	0.220	9.318	-14.561	6.207	6.470	-15.086
42	800	1	0.227	0.252	9.318	-14.637	6.245	6.680	-15.506
43	800	1	0.238	0.277	9.318	-14.701	6.277	6.745	-15.637
44	850	0.5	0.263	0.302	8.904	-13.893	6.300	6.409	-14.111
45	900	0.5	0.316	0.347	8.524	-13.162	6.325	6.313	-13.138
46	900	1	0.372	0.414	8.524	-13.223	6.355	6.522	-13.556
47	900	1	0.411	0.466	8.524	-13.270	6.379	6.616	-13.745
48	950	1	0.502	0.546	8.176	-12.594	6.399	6.418	-12.633
49	950	1	0.591	0.606	8.176	-12.628	6.416	6.271	-12.339
50	950	1	0.654	0.654	8.176	-12.649	6.426	6.307	-12.411
51	960	1	0.732	0.700	8.109	-12.526	6.433	6.133	-11.926
52	960	1	0.792	0.738	8.109	-12.536	6.438	6.123	-11.905
53	975	1	0.853	0.777	8.012	-12.347	6.444	6.040	-11.540
54	960	1	0.885	0.804	8.109	-12.559	6.450	6.104	-11.868
55	970	1	0.918	0.830	8.044	-12.432	6.453	6.027	-11.579
56	1300	0.5	1.000	0.981	6.357	-8.996	6.471	5.652	-7.359

Supplemental Table 4b: Beeshoek diffusion data modeled with sample activation energy

Beeshoek	**domains**	**Ea**	**ln(D_o/a^2)**						
	8	42.939	17.020						
gas fraction	0.010	0.009	0.010	0.000	0.064	0.036	0.018	0.852	
log(D_o/a^2)	11.014	9.207	7.473	7.347	6.021	2.035	2.031	1.941	
closure temp (° C)	87	113	142	144	169	266	266	269	
step	**temp**	**time**	**Fcum observed**	**Fcum modeled**	**10000/k**	**ln(D/a^2) modeled**	**delta modeled**	**delta observed**	**ln(D/a^2) observed**
1	100	1	1.0E-04	2.8E-07	26.799	-40.829	-0.032	-5.922	-29.048
2	150	1	4.4E-04	8.5E-06	23.632	-33.986	-0.032	-3.956	-26.138
3	200	0.5	9.1E-04	8.9E-05	21.135	-28.593	-0.030	-2.224	-24.205
4	250	0.5	0.002	0.001	19.115	-24.259	-0.014	-0.814	-22.660
5	300	0.5	0.005	0.004	17.447	-20.845	0.081	0.025	-20.734
6	280	0.5	0.005	0.005	18.078	-22.343	0.148	0.160	-22.366
7	260	1	0.005	0.005	18.756	-23.839	0.163	0.133	-23.778
8	240	1	0.006	0.005	19.487	-25.429	0.169	-0.027	-25.038
9	210	2	0.006	0.005	20.698	-28.046	0.170	-0.186	-27.335
11	300	0.5	0.006	0.006	17.447	-21.091	0.204	0.406	-21.496
12	325	0.5	0.008	0.010	16.718	-19.816	0.354	0.681	-20.469
13	350	0.5	0.012	0.013	16.048	-19.298	0.819	0.944	-19.546
14	375	0.5	0.016	0.016	15.429	-19.357	1.518	1.325	-18.971
15	400	0.5	0.020	0.020	14.856	-18.812	1.865	1.822	-18.726
16	385	1	0.022	0.022	15.194	-20.021	2.103	2.126	-20.066
17	370	1	0.023	0.023	15.548	-21.031	2.226	2.263	-21.106
18	365	1	0.023	0.023	15.670	-21.413	2.285	2.335	-21.513
19	340	2	0.023	0.023	16.309	-22.866	2.321	2.343	-22.910
20	325	2	0.023	0.023	16.718	-23.783	2.338	2.297	-23.703
21	350	1	0.023	0.024	16.048	-22.363	2.352	2.418	-22.494
22	375	1	0.024	0.024	15.429	-21.115	2.397	2.458	-21.236
23	400	0.5	0.025	0.025	14.856	-20.050	2.484	2.569	-20.220
24	425	0.5	0.026	0.027	14.324	-19.221	2.644	2.673	-19.279
25	400	5	0.033	0.030	14.856	-20.795	2.856	2.464	-20.010
27	450	0.5	0.035	0.032	13.828	-18.832	2.984	3.052	-18.967
28	500	1	0.047	0.046	12.934	-17.447	3.258	3.302	-17.534
29	550	0.5	0.062	0.060	12.148	-16.472	3.620	3.564	-16.360
30	535	0.5	0.066	0.065	12.374	-17.328	3.804	3.964	-17.647
31	515	0.5	0.067	0.067	12.688	-18.121	3.861	4.060	-18.519
32	495	1	0.068	0.069	13.018	-18.897	3.892	4.228	-19.568
33	472	1	0.068	0.070	13.420	-19.805	3.912	4.231	-20.444
34	550	0.5	0.072	0.075	12.148	-17.148	3.958	4.146	-17.524
35	600	0.5	0.097	0.089	11.453	-15.972	4.121	3.843	-15.414
36	650	0.5	0.115	0.109	10.832	-15.421	4.516	4.505	-15.399
37	700	0.5	0.136	0.123	10.276	-15.516	5.165	4.940	-15.067
38	750	0.5	0.158	0.145	9.774	-14.979	5.439	5.369	-14.839
39	800	0.5	0.186	0.178	9.318	-14.334	5.609	5.669	-14.455
40	800	0.5	0.201	0.201	9.318	-14.525	5.704	5.894	-14.904
41	800	0.5	0.213	0.219	9.318	-14.619	5.751	5.984	-15.086
42	800	1	0.227	0.248	9.318	-14.703	5.793	6.194	-15.506
43	800	1	0.238	0.272	9.318	-14.773	5.828	6.260	-15.637
44	850	0.5	0.263	0.297	8.904	-13.927	5.853	5.945	-14.111
45	900	0.5	0.316	0.343	8.524	-13.165	5.882	5.869	-13.138
46	900	1	0.372	0.411	8.524	-13.234	5.917	6.078	-13.556
47	900	1	0.411	0.462	8.524	-13.286	5.943	6.172	-13.745
48	950	1	0.502	0.544	8.176	-12.578	5.965	5.993	-12.633
49	950	1	0.591	0.605	8.176	-12.615	5.984	5.846	-12.339
50	950	1	0.654	0.654	8.176	-12.637	5.995	5.882	-12.411
51	960	1	0.732	0.701	8.109	-12.509	6.002	5.711	-11.926
52	960	1	0.792	0.740	8.109	-12.518	6.007	5.701	-11.905
53	975	1	0.853	0.779	8.012	-12.316	6.011	5.623	-11.540
54	960	1	0.885	0.806	8.109	-12.542	6.019	5.682	-11.868
55	970	1	0.918	0.833	8.044	-12.404	6.020	5.608	-11.579
56	1300	0.5	1.000	0.989	6.357	-8.786	6.034	5.321	-7.359

Supplementary Table 5: Khumani U-Th replicates

Sample Name	mass (ug)	U ppm	Th ppm
Kh1	460	0.40	0.79
Kh2	210	1.00	0.37
Kh3	370	0.73	0.75
Kh4	510	0.30	0.53
Kh5	310	0.47	0.74
Kh6	270	0.22	0.21
Kh7	540	0.22	0.33
Kh8	238	0.31	0.27
Kh9	490	0.83	2.08
Kh10	399	0.22	0.25
Kh11	637	0.56	0.69
Kh12	349	0.27	0.27
Kh13	248	0.95	1.18
Kh14	351	0.28	0.26
Kh15	416	0.23	0.27
Kh16	244	0.61	0.29
Kh17	250	0.46	0.40
Kh18	312	0.76	0.51
Kh19	355	0.30	0.27
Kh20	441	0.60	0.68
Kh21	357	0.22	0.24
Kh22	354	0.46	0.46

Chapter 4

COMBINED HEMATITE (U-TH)/HE AND (U-TH)/NE AGES AND ^{4}HE/^{3}HE THERMOCHRONOLOGY OF THABAZIMBI ORE, TRANSVAAL BASIN, SOUTH AFRICA

ABSTRACT

To determine the cadence and causes of mineralization, we implemented the combined (U-Th)/He and (U-Th)/Ne chronometers to hematite from two Transvaal Supergroup-hosted, Fe-ore localities in the Thabazimbi region of the Kaapvaal Craton, South Africa. The concordant He-Ne ages from the Donkerpoort Neck locality (Ne 1007 ± 96 Ma, He 1009 ± 36 Ma) suggest a significant ~1000 Ma tectono-thermal event occurred at this locality. ^{4}He/^{3}He age spectrum from the Donkerpoort Neck hematite suggests rapid cooling from 1000 to 900 Ma, followed by slow, nearly monotonic cooling to present in which the ore body remained within 2 km of the Earth's surface. This rapid cooling, in combination with concordant He-Ne ages, suggest a hot, oxidizing hydrothermal fluid triggered ~1000 Ma hematite recrystallization at the Donkerpoort Neck locality. The Donkerpoort West ore body, located 4 km along strike to the west of Donkerpoort Neck, yielded He-Ne ages uniquely young (Ne 121 ± 12 Ma, He 124 ± 5) compared to other Transvaal Supergroup hosted hematite ore deposits reported here. Mineralogical analysis by electron backscatter diffraction and spectroscopy, along with ^{4}He/^{3}He results, suggests this sample is a mixture of Proterozoic hematite and Cretaceous-Tertiary age goethite. The two-phase Donkerpoort West Fe-ore provides a cautionary example of the type of material

to avoid in Fe-oxide geo- and thermochronologic studies. Together, these samples provide insight into the origin of these economic deposits, and point to Paleoproterozoic age oxidative weathering.

I. INTRODUCTION

This study follows the path of the previous chapter, implementing (U-Th)/Ne and (U-Th)/He chronometry and $^{4}He/^{3}He$ thermochronology to investigate the timing of ore formation and subsequent thermal history from two mines, Donkerpoort Neck and Donkerpoort West, in the Thabazimbi region of the Transvaal Basin, South Africa (Figure 4.1). The Donkerpoort Neck and Donkerpoort West hematite ore bodies share many

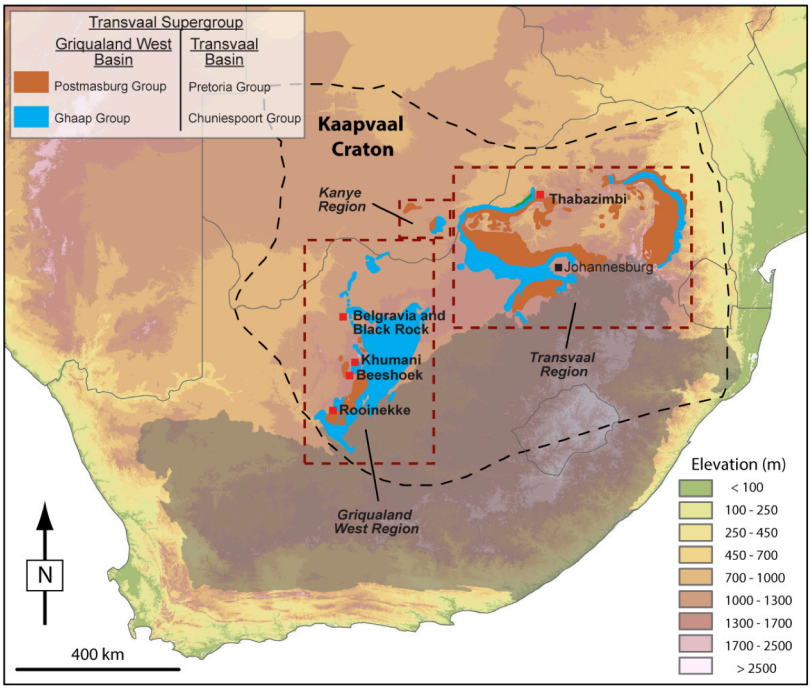

Figure 4.1: DEM of southern Africa showing a simplified geological map of the Transvaal Supergroup with sample locations (adapted from Eriksson et al., 2006; Smith and Beukes, 2016; Smith, 2018). Both the Donkerpoort Neck and Donkerpoort West ores from this chapter come from near the town of Thabazimbi, with the Griqualand West localities from the previous chapter shown for reference. The Donkerpoort Neck and Donkerpoort West ore bodies are both the result of Fe-upgrading of the Penge Iron Formation, a part of the Chuniespoort Group.

characteristics with the previously discussed suite of hematite samples from Griqualand West. The Transvaal and Griqualand West regions both preserve the Transvaal Supergroup, a late Archean through early Paleoproterozoic (~2.60 – 2.06 Ga) sequence of sedimentary and volcanic rocks (Eriksson et al., 2006; Sumner and Beukes, 2006; Beukes and Gutzmer, 2008).

Structurally-controlled hydrothermal upgrading of parent banded iron formation (BIF) has produced a series of ore bodies in the Northern and Southern ranges of the Thabazimbi region (Netshiozwi, 2002). These ore bodies, which have well-studied geologic histories but lack direct age determinations (Netshiozwi, 2002; Smith and Beukes, 2016), are well-suited to the application of the geo- and thermochronometric methods outlined in the previous chapter. Briefly, the (U-Th)/Ne and (U-Th)/He method is possible due to the incorporation of ~ppm levels of uranium and thorium, and high retentivity of He and Ne in hematite. These two chronometers allow for a pair of related ages to be obtained. The Ne age provides a high temperature constraint, possibly the formation age, of the specimen. The implementation of the $^{4}He/^{3}He$ method, which utilizes the polycrystalline structure commonly found in natural hematites, allows a time-temperature history to be obtained from a single sample over a broad range of geological temperatures.

While great strides have been made in our understanding of the mechanics of BIF deposition and subsequent Fe-upgrading (Rye and Holand, 1998; Webb et al., 2003; Clout and Simonson, 2005; Oliver et al., 2007; Morris and Kneeshaw, 2011; Rasmussen et al., 2016), the timing of ore genesis may not correlate with the expectation age inferred from

indirect age determinations (Rasmussen et al., 2007; Farley and McKeon, 2015). The massive hematite ores of Donkerpoort Neck and Donkerpoort West provide an excellent opportunity to apply the (U-Th)/Ne and (U-Th)/He chronometers and $^{4}He/^{3}He$ method to directly date the hematite and produce a time-temperature record for this region, potentially elucidating the thermal history over billion-year timescales.

II. GEOLOGIC BACKGROUND

The Transvaal Supergroup, present in both the Griqualand West and Transvaal region (Figure 4.1), hosts significant iron formations, that are exploited in large-scale, surface mining operations. In the Thabazimbi region, located in the northern part of the Transvaal Basin, Fe-enrichment of parent Penge Iron Formation (2.48 to 2.43 Ga), part of the Chuniespoort Group, has produced a series of tabular, strata-bound hematite ore bodies (Nelson et al., 1999; Smith and Beukes, 2016; Basson and Koegelenberg, 2017). Underlying the Penge is the Malmani Subgroup, containing a thick sequence of dolostones overlain by a thin shale bed (Walraven and Martini, 1995). The Penge Iron Formation in the Transvaal Basin is correlative to the Asbestos Hills Subgroup in Griqualand West, which hosts the parent BIFs of the hematite ore discussed in the previous chapter. The Bevets Conglomerate unconformably overlies the Penge Iron Formation, which marks the onset of Pretoria Group siliciclastic sediments (Walraven and Martini, 1995).

While the previous chapter discussed only the most distal effects of the Bushveld Igneous Complex (BIC), the emplacement of this massive 2.05 Ga granite body had significant metamorphic and structural effects in the Transvaal Basin due to the immediate

proximity of this massive igneous body and was the source of the largest known hydrothermal system on the planet (Eglington and Armstrong, 2004; Rajesh et al., 2013; Basson and Koegelenberg, 2017). BIC contact metamorphism expresses as andalusite and garnet-bearing assemblages in the shales of the Pretoria Group, while magnetite and grunerite are present in the Penge Iron Formation (Netshiozwi, 2002).

Predating BIC emplacement, an extensional regime triggered a series of normal faults in the Thabazimbi area, which removed some stratigraphy along the Penge-Malmani contact (Smith and Beukes, 2016). BIC emplacement tilted the Transvaal sequence to a dip of 50° S at Donkerpoort Neck and to 10 to 35° S at Donkerpoort West (Netshiozwi, 2002). Simultaneous with the emplacement of the main body of the BIC, a series of diabase sills intruded the surrounding Penge Iron formation, (Netshiozwi, 2002). At Donkerpoort Neck and Donkerpoort West, a single sill was emplaced parallel to BIF bedding (Netshiozwi, 2002). These diabase sills have a U-Pb titanite age of 2046.6 ± 3.4 Ma (Raejsh et al., 2013). The sill at Donkerpoort is interpreted to have predated Fe-ore enrichment, therefore providing a valuable maximum age of BIF Fe-enrichment (Netshiozwi, 2002; Beukes et al., 2003; Basson and Koegelenberg, 2017). The structural relationship between diabase sill and the Transvaal sedimentary units is shown in Figure 4.2. A geological map and cross section view of the Donkerpoort Neck and Donkerpoort West localities is shown in Figure 4.3 and Figure 4.4, respectively.

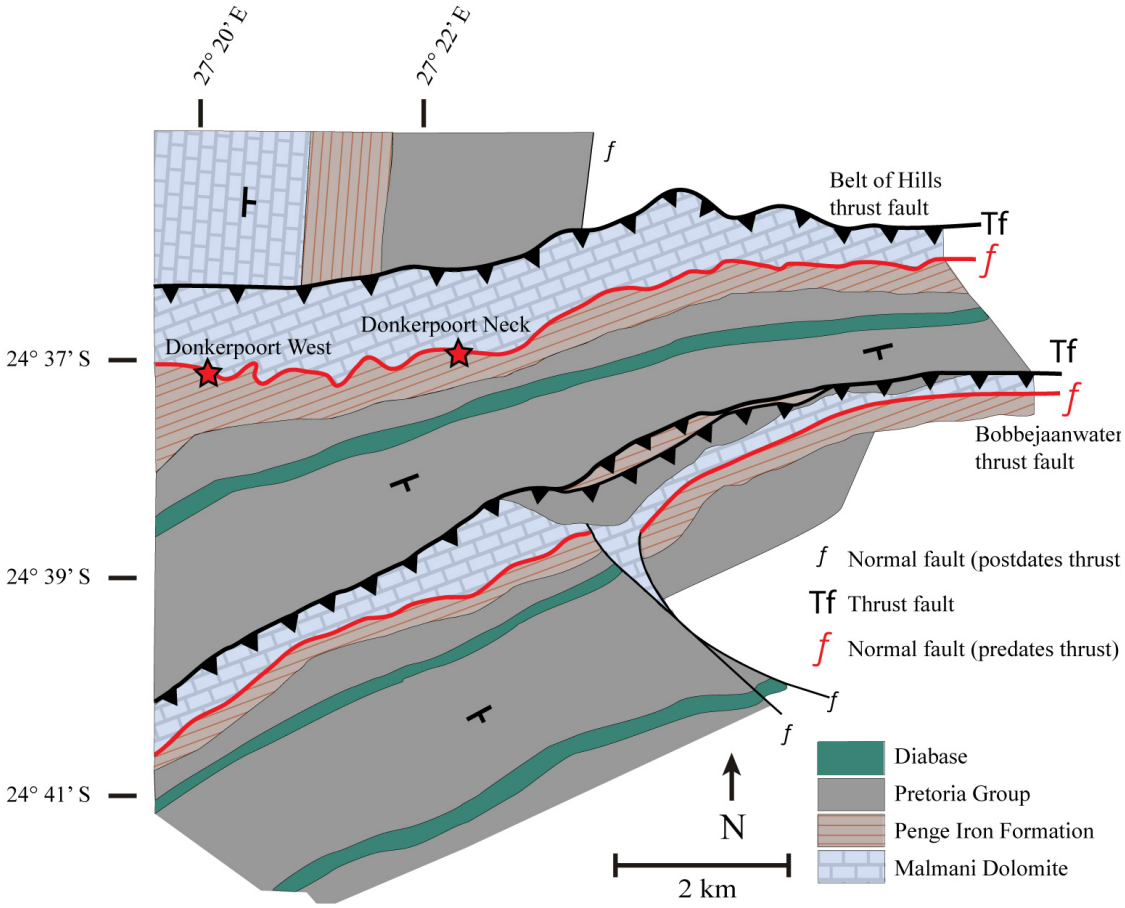

Figure 4.2: Geologic map of the northern and Southern Ranges in the Thabazimbi region (adapted from Netshiozwi, 2002; Gutzmer et al., 2006). Note the triplication of the sequence from thrust faulting. The boundary of the main body of the BIC lies just off map to the south.

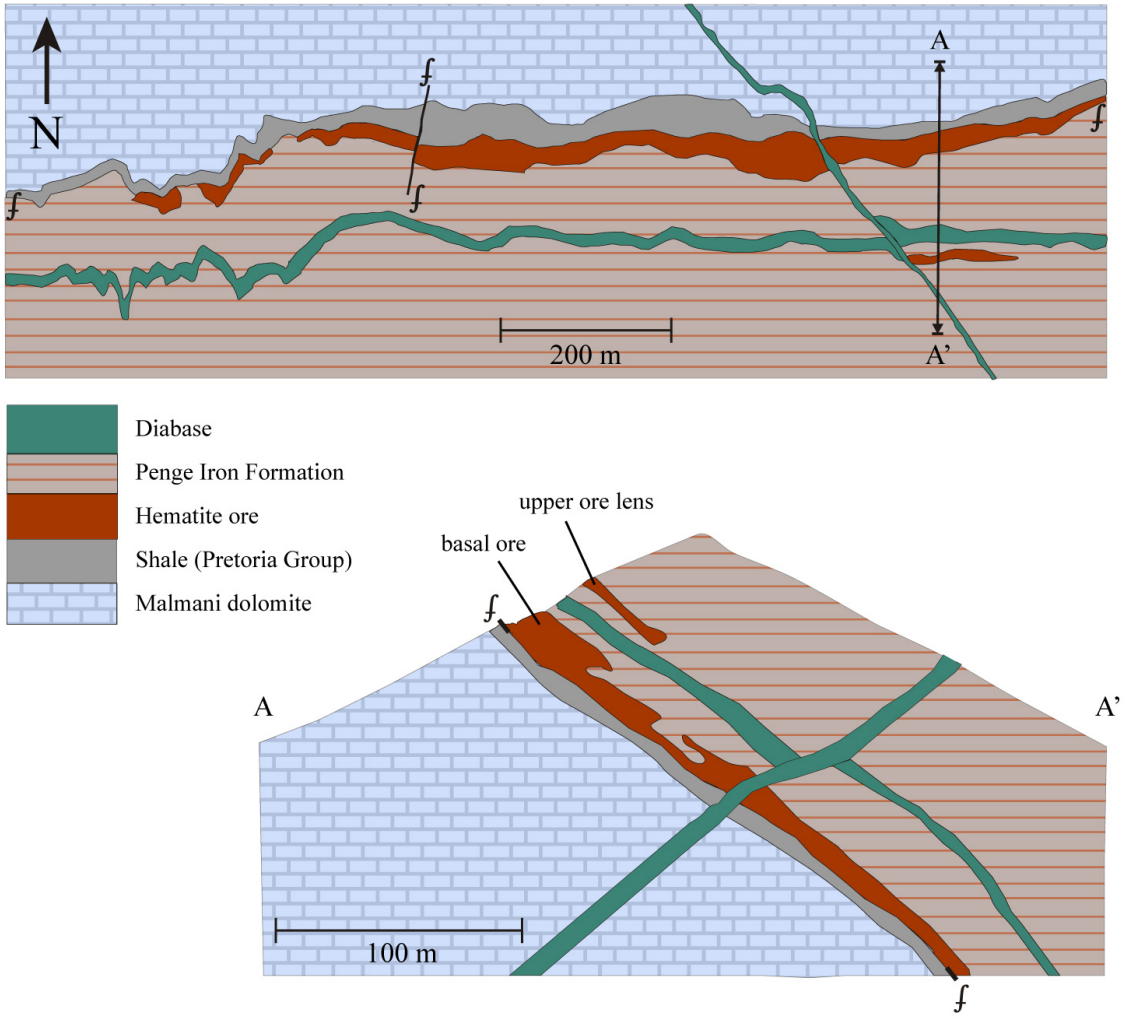

Figure 4.3: Geological map and cross section of the Donkerpoort Neck deposit, with the vertical line from A to A' shown in map view denoting the position of the cross section (adapted from Netshiozwi, 2002). The basal ore developed along the contact between Pretoria Group shale and Penge BIF is interpreted to be the result of fluid flow along this faulted contact (Netshiozwi, 2002). While an upper ore lens is developed above the diabase sill and interpreted to be the result of supergene weathering, thus representing a different ore forming process and event (Netshiozwi, 2002). The hematite sample from this study sourced from the basal, brecciated ore

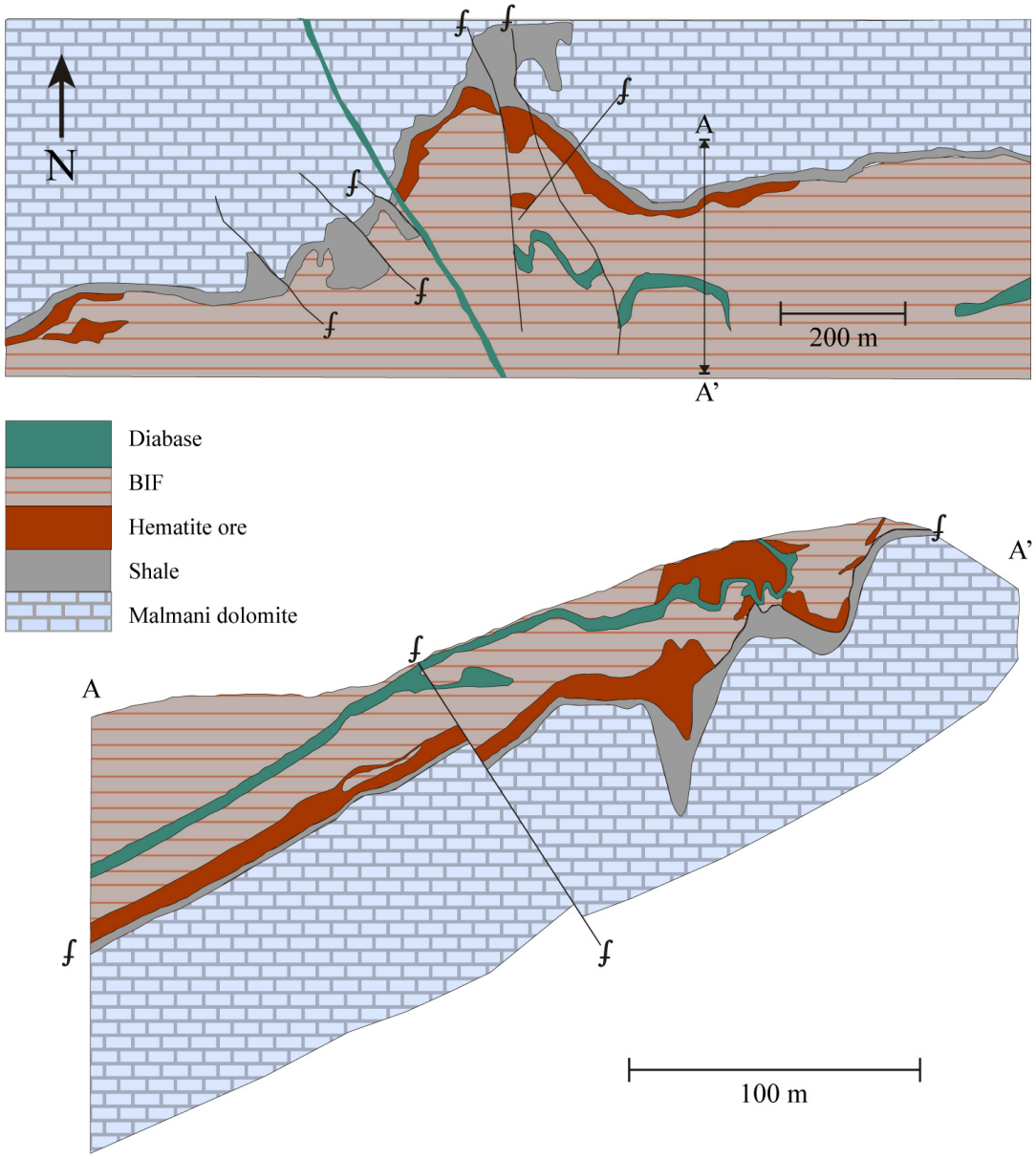

Figure 4.4: Geological map and cross section of the Donkerpoort West deposit, with the vertical line from A to A' shown in map view denoting the position of the cross section (adapted from Netshiozwi, 2002). Three generations of ore are hypothesized to have developed at Donkerpoort West. The first is the basal ore developed along the contact between Pretoria Group shale and Penge BIF (Netshiozwi, 2002). The second is the larger body of ore developed above the diabase sill (Netshiozwi, 2002). The third is a series of small lenticular bodies of ore near the topographic high of the Donkerpoort West deposit.

Next, a series of thrust faults duplicated the sequence at Donkerpoort Neck and Donkerpoort West, creating a series of km-scale east-west striking folds (Netshiozwi, 2002; Basson and Koegelenberg, 2017). At Donkerpoort Neck, initial Fe-upgrading along the basal contact with the Malmani Subgroup shale occurred prior to a final cross-cutting, dike intrusion (Netshiozwi, 2002; Smith and Beukes, 2016). The presence of hematite ore pebbles within the Waterberg Group (a sequence of siliciclastic sediments equivalent to the Olifantshoek Group in Griqualand West) indicates the initiation of ore formation occurred prior to deposition of the Waterburg Group (Netshiozwi, 2002). These sills have a baddeleyite U-Pb age of 1927 Ma, providing a minimum age for the Fe-enrichment of these hematite ore clasts (Hanson et al., 2004a). Using these ages, previous investigators have bracketed initial ore formation in the Thabazimbi area to between 2047 and 1927 Ma (Netshiozwi, 2002; Smith and Beukes, 2016; Basson and Koegelenberg, 2017). This age range is remarkably consistent with the proposed timing of initial ore formation between 2054 and 1930 Ma as determined by De Kock et al., (2008) using a paleomagnetic approach.

Fe-upgrading in the Thabazimbi area is interpreted to be the result of shallow crustal fluids utilizing the Penge Iron Formation as a conduit for fluid circulation, where the underlying Malmani shale and parallel-dipping, diabase sills act as less-permeable bounding layers for these hydrothermal fluids (Netshiozwi, 2002; Beukes and Smith, 2016). Manganese oxides are present where iron formation is in contact with carbonate and are interpreted to be the result of the same oxidation and mineralization (Johnson, 2015). The work presented here provides a direct constraint on the timing of

mineralization associated with the oxidation of iron formations and thereby may provide insight into the history of atmospheric O_2.

Existing constraints on this mineralization have been provided by fluid inclusion studies, which indicates two phases of hydrothermal circulation occurred in the Thabazimbi region (Netshiozwi, 2002). First, a high salinity brine triggered the oxidation of a large portion of ferrous minerals within the parent BIF, initiating hematite formation (Netshiozwi, 2002). This was followed by the circulation of a fluid of meteoric origin, triggering the leaching of remnant BIF-hosted chert (Netshiozwi, 2002). Halos of oxidized sediments suggest the initial, high-salinity brine affected a much larger volume of rock, and only where the meteoric fluid circulated, often directly on the shale-BIF contact, did the high-grade Fe ore develop (Netshiozwi, 2002).

Unlike in Griqualand West, which sat near the accreting margin of the plate, the northern portion of the Kaapvaal Craton was shielded from major tectono-thermal events for much of its remaining history by the Zimbabwe craton. The merger of these two cratons resulted in the Archean Limpopo belt, with orogenesis complete by ~2.0 Ga (Van Reenan et al., 2008). Post 2.0 Ga, a series of mafic intrusions were emplaced in both the Kaapvaal and Zimbabwe cratons between ~1.8 to ~1.7 Ga (Hanson et al., 2004a; Hanson et al., 2011). While the predominant interpretation is that little intraplate motion occurred between 1.8 and 1.1 Ga, paleomagnetic poles differ significantly between the Kaapvaal and Zimbabwe cratons, suggesting >2000 km of lateral movement may be accounted for in the Limpopo belt (Hanson et al., 2011). Finally, at least one other generation of igneous activity occurred in the Thabazimbi region. Dikes associated with the Umkondo large

igneous province were rapidly emplaced between 1112 and 1108 Ma, with the main pulse of volcanism occurring between 1109.8 ± 0.8 Ma and 1109.0 ± 1.3 Ma (Hanson et al., 2004b; de Kock et al., 2014). Although this event has not been previously linked to hematite ore formation, the development of the Umkondo LIP is associated with changing mantle convection during the assembly of Rodinia (Hanson et al., 2004b).

The Archean and Paleoproterozoic rocks discussed above are unconformably overlain by 300 – 180 Ma volcanic and sedimentary Karoo Supergroup, including the 185 – 180 Ma Karoo large igneous province (Catuneau et al., 2005; Jourdan et al. 2005). The modern topographic profile of the southern African Plateau is one with an elevated continental interior, separated from a low-elevation passive continental margin, by a high relief escarpment (Flowers and Schoene, 2010). A pulse of erosion in the Southern African Plateau interior occurred between 140 and 70 Ma (Tinker et al., 2008; Flowers and Schoene, 2010; Stanley et al., 2013; Stanley and Flowers, 2016). Along the western plateau margin, thermochronometric estimates of denudation range between <1 km and 1.5 km since the Cretaceous (Stanley et al., 2013; Wildman et al., 2015; Wildman et al., 2016; Wildman et al., 2017).

The topographic profile the southern African Plateau east of the Transvaal region largely resembles that of the southern and western Plateau margins (Flowers and Schoene, 2010). Fission track thermochronology estimates 1.7 km of erosion has taken place in the Lesotho Highlands (within the interior of the southern African Plateau, SE of Johannesburg) since 78 Ma (Brown et al., 2002). East of Johannesburg, (U-Th)/He thermochronology constrains Kaapvaal craton erosion to less than 850 meters since the

Cretaceous (Flowers and Schoene, 2010). Erosion estimates of relic Cretaceous African Land Surface landscapes northwest of Johannesburg (Partridge and Maud, 2000) produce Cenozoic rates of 3-5 meters erosion per million years (Dinks et al., 2010).

III. SAMPLE DESCRIPTION

The Donkerpoort Neck sample (Figure 4.5a) was collected in the Donkerpoort West open pit mine (GPS: -24.620 S, 27.375 E), ~6 km to the SW of the town of Thabazimbi. Figure 4.5a shows the brecciated BIF morphology of this hematite sample, a

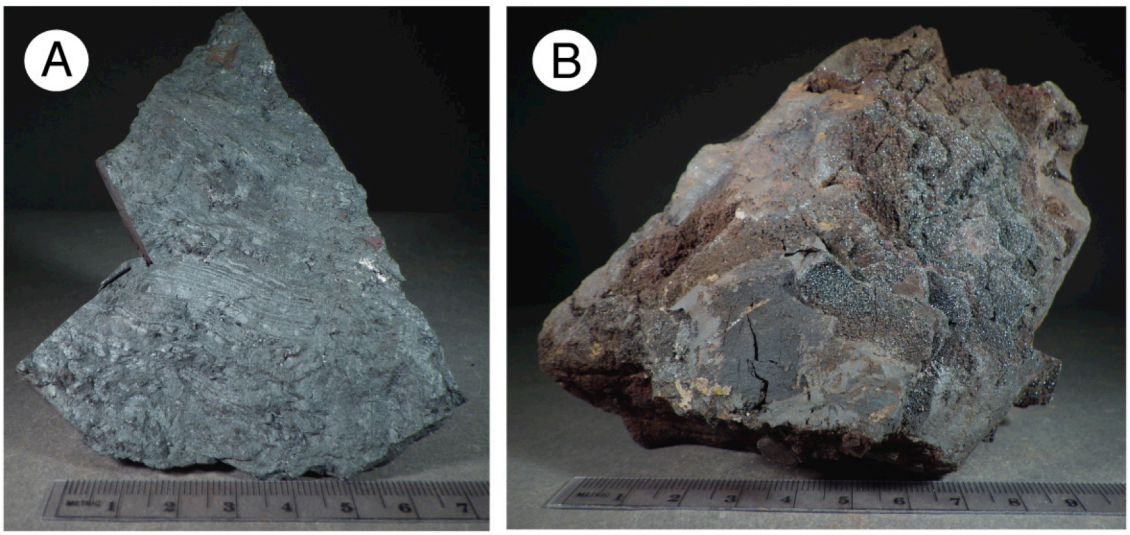

Figure 4.5: Photos of the Donkerpoort Neck (A) and Donkerpoort West (B) hand samples used in this study. Note the brecciated texture in the Donkerpoort Neck sample, typical of basal ore originating nearest to the shale contact. The Donkerpoort West sample displays a complicated morphology, with variable texture and color.

texture typical of ore near the shale-BIF boundary (Netshiozwi, 2002). While a few smaller ore bodies are developed above the diabase sill, the majority of ore, including this study's sample, is developed directly above the Malmani shale. The ore body grades from

brecciated ore, near the shale contact, to the massive ore, to hematized BIF below the diabase sill (Netshiozwi, 2002). We utilized a Scanning Electron Microscope (SEM) with an attached X-ray energy dispersive spectrometer (EDS) to assess sample purity. EDS mapping shows this sample ranges in Fe content from 67 to 71 wt%, with Al and Si content <0.5 wt%. EDS elemental analysis provides relative accuracy of a few wt% and small deviations in measured Fe contents from that of stoichiometric hematite should not, alone, cause concern for the He-Ne method. Furthermore, EDS mapping shows samples are free of mineralogical contaminants such as Mn-oxides, Fe-oxyhydroxides, and REE-rich accessory phases.

The Donkerpoort West sample (Figure 4.5b) was collected at the Doonkerpoort West open pit mine (GPS: -24.623 S, 27.329 E), ~4 km along strike to the west of the Donkerpoort Neck locality (Figure 4.2). Fe-ore at the Donkerpoort West locality displays a similar structure and morphology to that at the Donkerpoort Neck locality, with a gradation from brecciated ore, near the shale contact, to the massive ore, to hematized BIF below the diabase sill (Netshiozwi, 2002; Basson and Koegelenberg, 2017). However, at Donkerpoort West, a larger tabular ore body has developed above the diabase sill (Figure 4.4), thereby increasing the total volume of Fe-ore available here (Netshiozwi, 2002; Basson and Koegelenberg, 2017). The sample in this study was collected from this tabular ore body above the diabase sill.

Figure 4.5b shows the complicated morphology of this hematite sample, with both textural and color variation over handsample scale. EDS mapping of the Donkerpoort West sample shows greater variability in Fe content than the Doonkerpoort Neck sample,

or any of the samples discussed in the prior chapter from Griqualand West. The bulk of the Donkerpoort West sample ranges between a Fe content of 63 to 73 wt%, with Al and Si content <1.0 wt%. However, small portions of the sample display Fe-content as low as 58 wt%. Stoichiometric goethite is 63 wt% Fe, while hematite is 70% wt% Fe. Spectroscopic analysis by FTIR indicates the Donkerpoort West sample is indeed a mixture of hematite and goethite (Figure 4.6). Two texturally unique bands were analyzed by FTIR from the Donkerpoort West subsample. Comparing these two bands with the FTIR spectra for pure hematite, pure goethite, and 25:75, 50:50, and 75:25 mixtures (left panel Figure 4.6) indicates the Donkerpoort West sample varies between primarily hematite and ~50:50 hematite-goethite mixture. The ~50:50 hematite-goethite band makes of the majority of the sample volume.

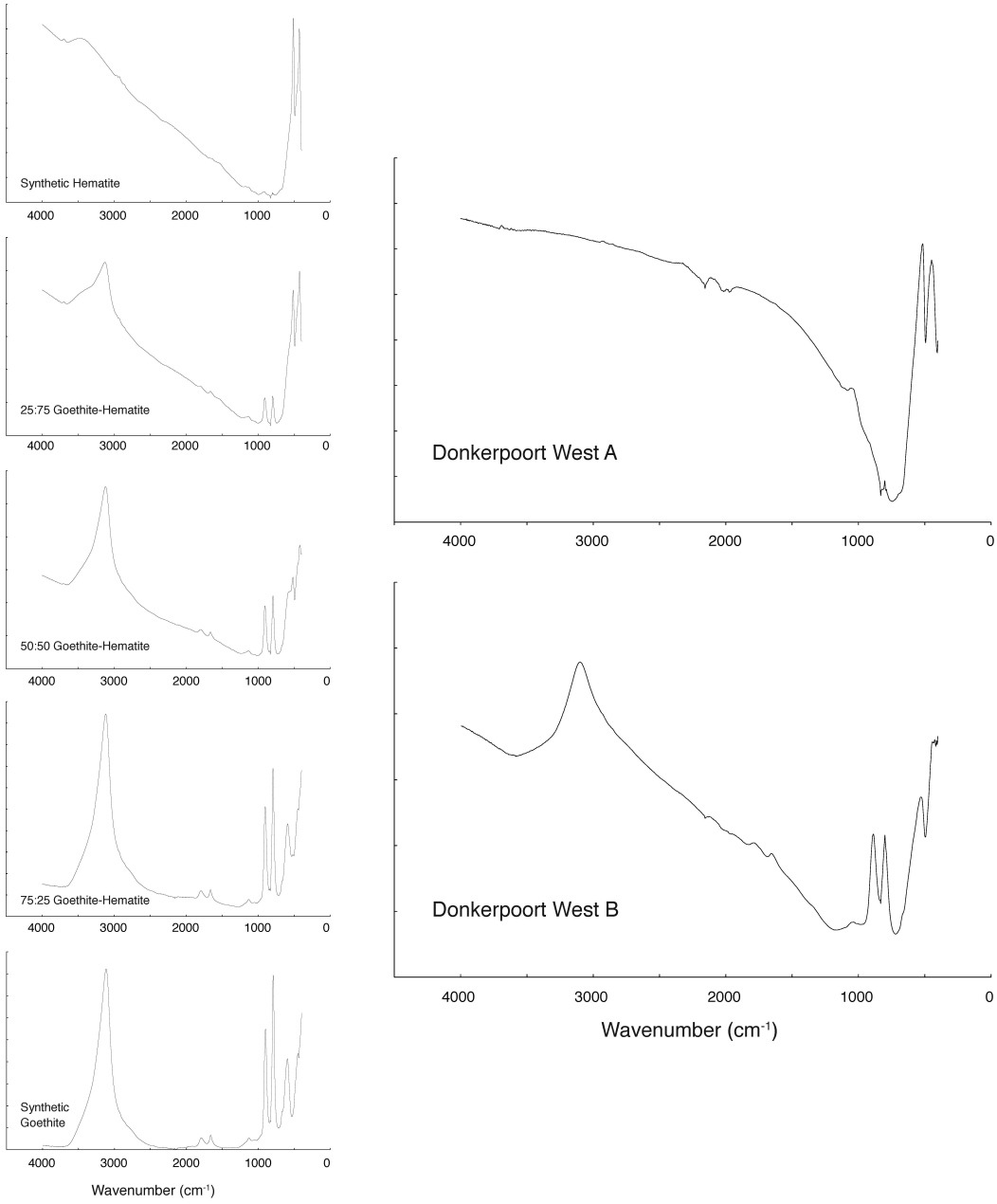

Figure 4.6: Spectroscopic analysis by FTIR of two bands of the subsample used to prepare material for $^{4}He/^{3}He$ analysis. Band A appears specular while band B has a more brown color and more massive texture. The left panel shows five spectra ranging from hematite (top), to goethite (bottom), along with 75:25, 50:50, and 25:75 mixtures of hematite-goethite.

IV. METHODS

The methods implemented in this study for He, Ne, U, and Th determination, along with those used in $^{4}He/^{3}He$ experiments, and the subsequent domain distribution and T-t modeling follows exactly as described in the previous chapter.

V. RESULTS

5.1 He and Ne ages

He, Ne, U and Th concentrations are shown in Table 4.1. Parent and daughter isotope concentrations were analyzed for each sample: a replicate pair of ~100 mg aliquots for He and Ne concentrations, along with a separate replicate pair of ~25 mg aliquots for U and Th concentration. The Donkerpoort Neck sample had mean U and Th concentrations of 0.44 and 0.36 ppm, respectively. The Donkerpoort West sample had mean U and Th concentrations of 2.12 and 2.40 ppm, respectively. The replicate U and Th concentrations varied by 3s within both samples. When combined with He concentrations of 1.8 to 3.1 nmol/g, He ages of 1009 and 124 Ma were determined for the hematite sample from Donkerpoort Neck and Donkerpoort West, respectively.

All aliquots analyzed for He were also analyzed for Ne. These measurements yielded ^{21}Ne concentrations between 36 and 64% nucleogenic ^{21}Ne ($^{21}Ne^{*}$). Notably, the proportion of $^{21}Ne^{*}$ in the two Donkerpoort West aliquots varied by nearly 25%, yet after isotopic deconvolution, the two aliquots yield $^{21}Ne^{*}$ concentrations within 2s of each other. Combining the above-mentioned parent isotope concentrations with $^{21}Ne^{*}$

concentrations of 0.052 to 0.097 fmol/g, ^{21}Ne ages of 1007 and 121 Ma were determined for the hematite sample from Donkerpoort Neck and Donkerpoort West, respectively.

5.2 He diffusivity

Both the Donkerpoort Neck and Donkerpoort West hematite samples were irradiated to allow for the application of the ^{4}He/^{3}He method. Figure 4.7 presents the results of the ^{3}He diffusion experiment carried out on the Donkerpoort Neck sample in the form of an

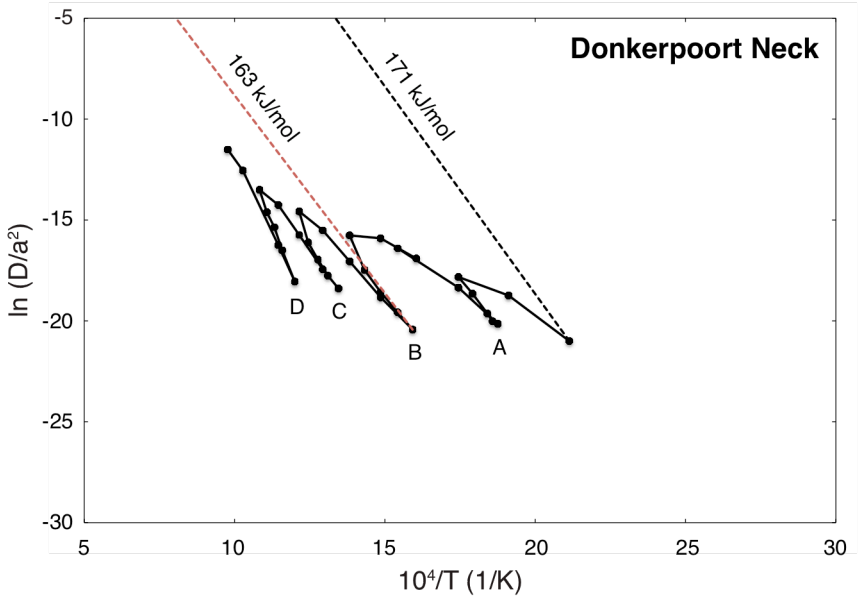

Figure 4.7: Arrhenius array from the ^{3}He diffusion experiment on the Donkerpoort Neck sample. The experiment progresses from lower right, along the solid black line connecting the calculated diffusivity from each heating step. The series of prograde and retrograde heating steps produce a zig-zag pattern. However, the retrograde sequences within each sample's Arrhenius array have a nearly identical slope (activation energy). The first few heating steps, where diffusivity rapidly changes, and the final fusion step are omitted. The dashed black line originating from the first plotted diffusion measurement reflects the activation energy from Farley (2018). This can be compared to the sample derived activation energy shown as a dashed red line. Each series of retrograde and prograde heating steps forms a limb in Arrhenius space and labeled A through D. The slope of the limbs steepens from A – D, with limbs A, B, and C having an average slope of 165 kJ/mol, similar to that of the dashed red line (163 kJ/mol) regressed through limb B.

Arrhenius plot. Just as with the Arrhenius plot presented in the previous chapter, the Donkerpoort sample shows declining diffusivity at any given temperature as the experiment progresses. A dashed black line is plotted through the first point in the Arrhenius array corresponding to an activation energy of 171 kJ/mol, as determined for hematite by Farley (2018). We also plot a line fit through a prograde and subsequent retrograde heating sequence, corresponding to an activation energy of 163 kJ/mol specific to the Donkerpoort Neck sample. The series of linear segments in Arrhenius space for the Doonkerpoort Neck sample have more variability in corresponding activation energy than the diffusion experiments presented in the previous chapter. Regressing through each the three prograde and retrograde heating sequences labeled A, B, and C on Figure 4.7 produces an average activation energy of 165 kJ/mol, yet with increasing values from 153 to 178 kJ/mol.

Figure 4.8 shows the Delta plot of the Donkerpoort Neck experimental results and model fit, implementing the activation energy of 171 kJ/mol as determined by Farley (2018). The results of the model are presented in Table 4.2, with a similar range in closure temperature (40 – 210° C) as the Griqualand West hematite ore samples discussed in the previous chapter. Figure 4.9 shows the $^{4}He/^{3}He$ age spectrum for the Donkerpoort Neck sample along with the corresponding bulk (U-Th)/Ne age and 2s error. The Donkerpoort Neck hematite shows rapidly increasing step age until $\Sigma F^{3}He \sim 0.1$, and then a long plateau age for the duration of the experiment. Three steps, between $\Sigma F^{3}He \sim 0.12$ and $\Sigma F^{3}He \sim 0.2$,

yield 2s He ages higher than the bulk Ne age of the Donkerpoort Neck sample. Age spectrum data is presented in Table 4.3.

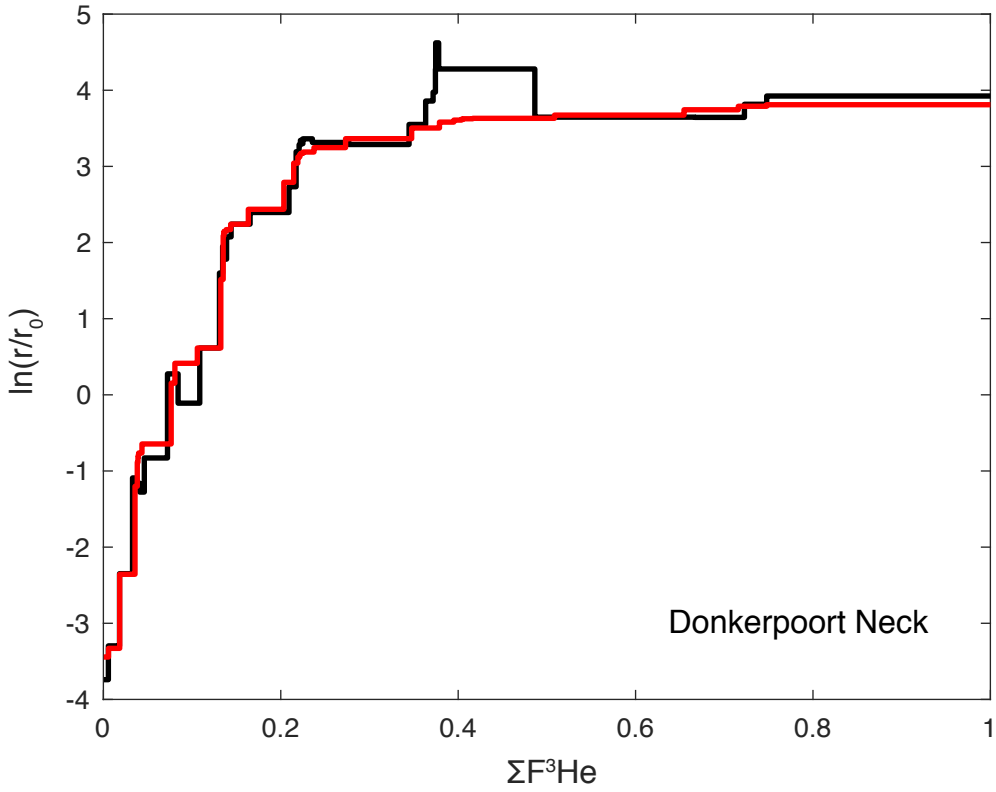

Figure 4.8: Delta plot for the Donkerpoort Neck sample. The black line shows the experimentally observed Delta array, while the red line is a best-fit model using hematite diffusion kinetics and eight discrete diffusion domains using the activation energy of 171 kJ/mol as calculated from heating experiments done on single domain hematite (Farley, 2018).

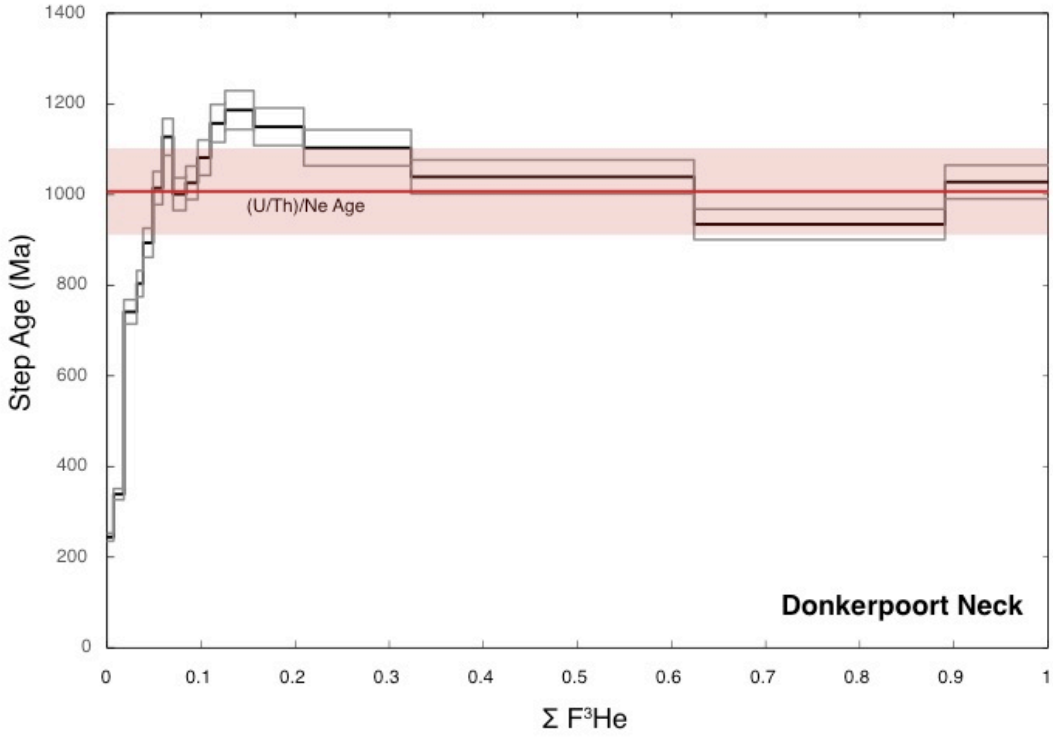

Figure 4.9: $^{4}He/^{3}He$ age spectrum for the Donkerpoort Neck sample. The (U-Th)/Ne age with 2s uncertainty is shown for reference.

The Donkerpoort West sample yielded $^{4}He/^{3}He$ results incompatible with the $^{4}He/^{3}He$ method almost certainly due to the presence of intermixed hematite and goethite in this sample. The $^{4}He/^{3}He$ age spectrum for the Doonkerpoort West sample is shown in Figure 4.10. Multiple step heating experiments were carried out with variable heating schedules yet yielded highly reproducible $^{4}He/^{3}He$ age spectra. By directly mounting the sample on a thermocouple and heating using a projector lamp apparatus (Farley et al., 1999), we observe nearly all ^{3}He diffusion below the $\Sigma F^{3}He$~0.5 increase in step age occurs in the first series of heating steps between 175° and 250° C.

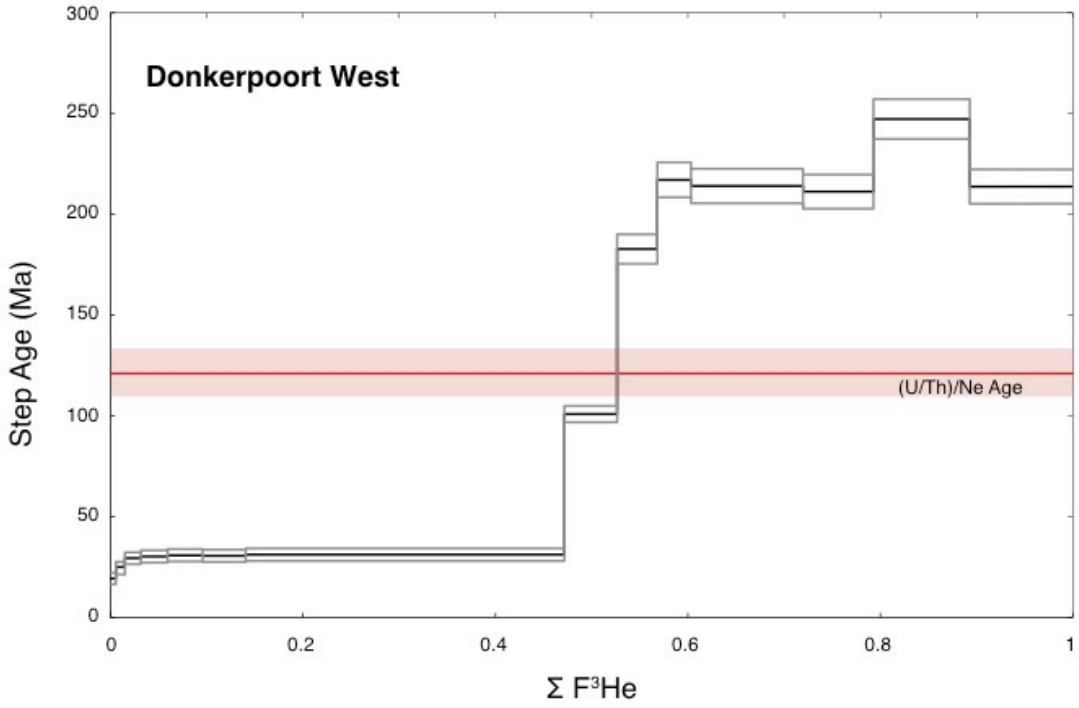

Figure 4.10: $^{4}He/^{3}He$ age spectrum for the Donkerpoort West sample. The (U-Th)/Ne age with 2s uncertainty is shown for reference. The rise in step age between the first and second plateau occurs immediately after the experiment progresses above the goethite dehydration temperature of ~225° C. This pattern is expected from the 2-component mixture deduced from SEM and FTIR.

VI. DISCUSSION

The hematite samples from Donkerpoort Neck (He 1009 Ma, Ne 1007 Ma) and Donkerpoort West (He 124 Ma, Ne 121 Ma) have He-Ne ages concordant within the given locality but dramatically different when compared to each other. Given the concordant He-Ne age from Donkerpoort Neck, the simplest conclusion is ~1000 Ma represents a formation age for the basal hematite ore at this locality. While we can hypothesize about the meaning of the ~120 Ma He-Ne age from Donkerpoort West, no definite conclusions can be drawn from this mixed mineralogy sample. Unlike in the hematite ores from our

Griqualand West suite, where many He-Ne ages fit geologic expectations, the results presented in this chapter do not correlate with the timing of any previously proposed ore forming events in the Thabazimbi region. As previously discussed, prior investigators have all concluded ore formation took place between 2050 and 1930 Ma in the Thabazimbi region (Netshiozwi, 2002; De Kock et al., 2008; Smith and Beukes, 2016), yet our hematite ages are dramatically younger than this expectation. The only regionally documented tectono-thermal event to have occurred in temporal proximity to the Donkerpoort Neck ~1000 Ma He-Ne age is the 1100 Ma Umkondo large igneous province (LIP) dikes (Hanson et al., 2004b; de Kock et al., 2014). An Umkondo LIP dike in the Buffelhoek-West mine (4 km SE of Donkerpoort West, 5 km SW of Donkerpoort Neck) yield a U-Pb baddeleyite age of 1110 ± 4 Ma (de Kock et al., 2014). Prior investigators have not proposed a link between Umkondo LIP dikes and ore formation.

The Donkerpoort Neck hematite ore genesis can be further understood with the time-temperature (T-t) modeling as an additional constraint to the bulk He-Ne ages. The results of the Donkerpoort Neck T-t modeling are shown in Figure 4.11. Of note is the pattern displayed in three steps between $\Sigma F^3He \sim 0.12$ and $\Sigma F^3He \sim 0.2$ (Figure 4.9), which yields 2s He step ages older than the final three steps of the experiment. In addition, these three steps yield 2s He ages older than the bulk Ne age of the Donkerpoort Neck sample. This behavior is hard to reconcile without invoking explanations averse to interpreting $^4He/^3He$ results (e.g., the degassing of a small detrital grain rich in ^4He or multiple generations of hematite within this single sample). Given the increase in age associated with these four steps is small and the spectrum meets the expectation shape from a sample

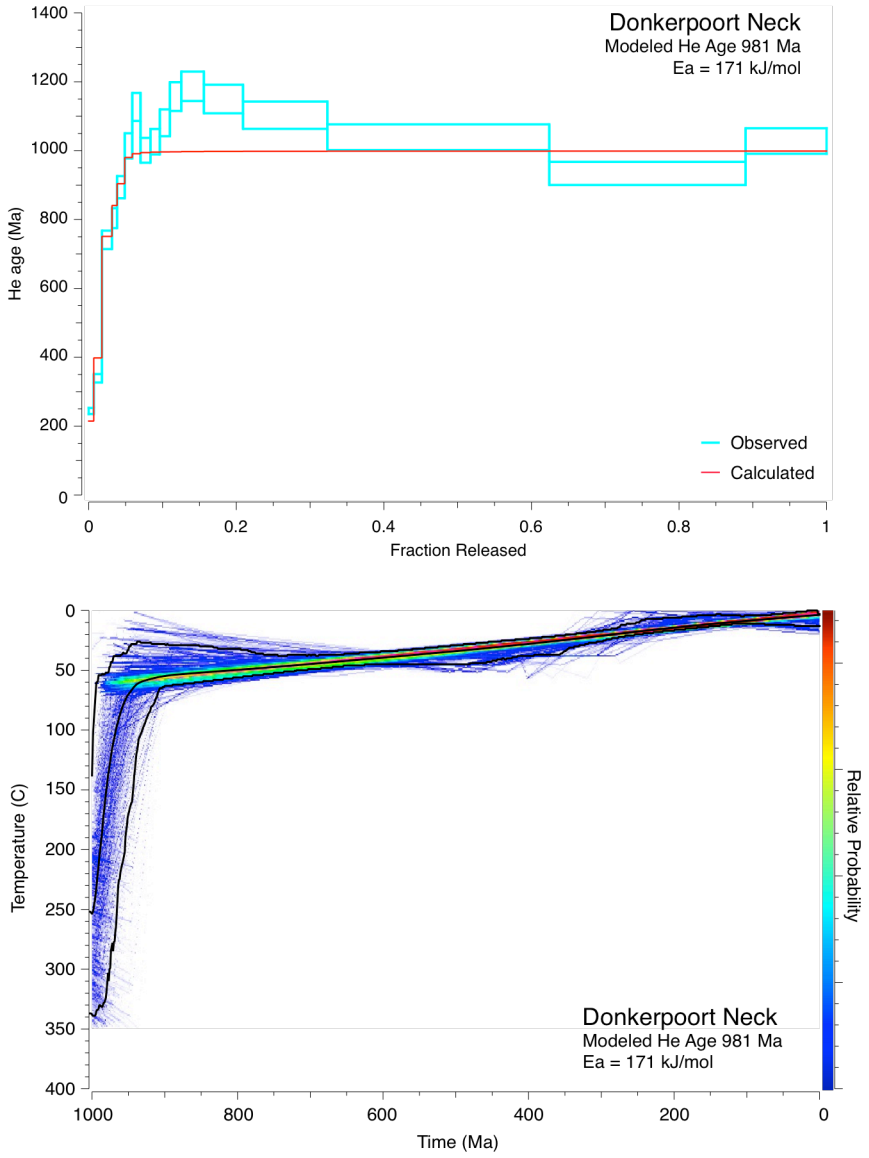

Figure 4.11: Time-temperature modeling results for the Donkerpoort Neck sample. The upper panel shows the age spectrum with measured data uncertainty bounds (blue lines) and the best-fit model age spectrum (red lines) obtained from the average (black line) time-temperature path shown in the lower panel.

with concordant He-Ne ages, we make the assumption these small deviations are an artifact inconsequential to the interpretation of the T-t modeling results.

Given the uncertainty in ore formation processes that may have taken place at Donkerpoort Neck at 1000 Ma, we allow the starting conditions for our T-t model to range between 0 and 400° C. The resulting T-t model has no constraint on initial temperature, although with a general trend of beginning hot and quickly cooling. By 900 Ma, the mean temperature path is ~50° C, in which steady cooling continues for the remainder of the sample's history. This post-900 Ma temperature history indicates the Donkerpoort Neck locality remained within a few km of the surface of the Earth for nearly all of the last billion years. While Karoo thickness is highly variable across the Kaapvaal, a burial depth of a few km is geologically likely given the Thabazimbi region was only on the margin of Springbok Basin, which is interpreted to have only accumulated a few km of Karoo sediments (Johnson et al., 1996; Catuneanu, 2004; McCarthy et al., 2018). Since the $^{4}He/^{3}He$ age spectrum does not display a He age plateau significantly older than the (U-Th)/Ne age, nor does it display He step ages which continually rise through the experiment, we can conclude that the ~1000 Ma He-Ne age at Donkerpoort Neck likely represents the formation age of Fe ore for this locality.

The Umkondo LIP dikes only slightly predate the He-Ne ages of the Donkerpoort Neck hematite (Hanson et al., 2011) and offer a possible source for hot, shallow crustal fluid circulation at this time. The 1100 Ma Umkondo LIP dike's age is within 2s uncertainty of the Ne age for Donkerpoort Neck. The initial T-t history of this sample suggests rapid cooling occurred at Donkerpoort Neck. It is geologically implausible the

Donkerpoort Neck ore was buried under a significant enough thickness of sediment to reset both the Ne and He age then exhumed rapidly enough to preserve a concordant He-Ne age. For these reasons we conclude the basal ore body hematite at Donkerpoort Neck experienced hydrothermally mediated hematite formation at ~1000 Ma, possibly triggered by hydrothermal fluids associated with the emplacement of Umkondo LIP dikes.

Prior investigators have proposed Fe-enrichment in the Thabazimbi region occurred between 2050 Ma and 1930 Ma (Netshiozwi, 2002; De Kock et al., 2008; Smith and Beukes, 2016). We do not believe the He-Ne chronology presented here is in conflict with a previous episode of Fe-enrichment occurring at this time. The presence of rounded, Fe-enriched hematite clasts within the Waterburg Group provides strong evidence for the occurrence of a phase of Paleoproterozoic Fe-enrichment (Netshiozwi, 2002; Hanson et al., 2004a). Direct age determinations on these detrital hematite clasts within the Waterburg utilizing the He-Ne method presented here could potentially further constrain the timing of this prior Fe-enrichment event.

While the Donkerpoort Neck results provide new evidence for Fe mineralization at ~1000 Ma, the Donkerpoort West sample proved much more challenging for the combined He-Ne and $^{4}He/^{3}He$ method. Two-phase mixtures are incompatible with the $^{4}He/^{3}He$ method, mainly due to the method requiring homogenous activation energy and U-Th concentrations. Furthermore, bulk sample He-Ne ages of two-phase mixtures cannot be interpreted for several reasons, but most importantly because the bulk age is meaningless if the distribution of U and Th is not uniform across both phases. The heating schedule suggests the transition from low-age plateau to the high-age plateau seen in the

$^{4}He/^{3}He$ spectrum occurs just after the phase transition from goethite to hematite (typically ~225° C). Given the FTIR spectrum from 'band A' indicates a nearly pure hematite composition, very careful sub-sampling of this material may allow for single aliquot age determinations to be made utilizing a newly developed method for sub-mg scale analyses (Hoffman, in prep).

Prior investigations have identified goethite within the Fe ore body at Donkerpoort West and interpreted this goethite to be secondary to initial hematite Fe ore development (Netshiozwi, 2002). The abundance of secondary goethite is correlated to the proximity of this ore body to the ancient African Land Surface, a Cretaceous-Tertiary age paleoweathering horizon (Van Niekerk et al., 1999; Partridge and Maud, 2000; Netshiozwi, 2002). At Donkerpoort West, karstic weathering of the underlying Malmani dolomite has created collapse features allowing for intensified meteoric fluid flow (Netshiozwi, 2002). Supergene alteration of the hematite ore body is interpreted to have led to the precipitation of African Land Surface age goethite in the cavities and pore spaces of these collapse features (Netshiozwi, 2002). These secondary goethites present an excellent target for future (U-Th)/He dating. In several ways, the Donkerpoort West sample utilized in this study was particularly poorly suited to the methods currently available to Fe-oxide geochronology. Pure hematite would have allowed for the methods of this study to be applied while pure goethite may be able provided an age constraint on the development of the African Land Surface in the Thabazimbi region. Instead, the mixture provides an age that is unlikely to correlate with any Fe-oxide forming geologic event. We can only speculate that the ~120 Ma He-Ne age is some mixture of a much

older generation of hematite and younger goethite. Based on the observed U-Th concentrations of other Transvaal hosted hematite ores (0.25 to 1.0 ppm), the U-Th concentration of the Donkerpoort West (2.07 to 2.43 ppm) sample is particularly high, suggesting the supergene goethite may be hosting the majority of parent nuclides.

VII. CONCLUSIONS

Application of the paired (U-Th)/Ne and (U-Th)/He chronometers, when combined with $^{4}He/^{3}He$ analysis, on hematite from the Donkerpoort Neck deposit in the Thabazimbi region of the Transvaal Basin provides new evidence for an ~1000 Ma event of hydrothermal fluid circulation. In this scenario, the faulted surface between the basal hematite ore deposit and underlying Malmani shale acted as a conduit for an oxidizing fluid, which drove recrystallization of the previously Fe-enriched ore. This hydrothermal fluid is possibly linked to the Umkondo LIP dikes, which were emplaced within 2s of the Donkerpoort Neck Ne age. While deep burial of a much older hematite sample followed by rapid erosion at ~1000 Ma could produce concordant He-Ne ages and the observed $^{4}He/^{3}He$ age spectrum, we find this interpretation less geologically likely.

While the Donkerpoort Neck results provide new evidence for Fe mineralization at 1000 Ma, the Donkerpoort West ore proved ill-suited for investigation by the paired He-Ne chronometer and $^{4}He/^{3}He$ method. We urge future investigators interested in the application of these methods to perform careful mineralogical analyses prior to investing effort in Fe-oxide chronometry, as two-phase mixtures yield un-interpretable results. Recent advances in the methodology of hematite dating allows for the analyses of sub-mg

mass aliquots where He and U-Th concentrations are measured on the same aliquot (Hoffman, in prep). Future application of this new method may allow the history of Proterozoic Fe-enrichment and Cretaceous-Tertiary supergene alteration to be parsed.

This study represents an additional effort to constrain the thermal and erosional history of the Kaapvaal Craton using hematite thermochronology. The Donkerpoort Neck and Donkerpoort West ore bodies were selected for their potential to record two billion-year histories. Rather, the 1000 Ma He-Ne age from Donkerpoort Neck provides further evidence for hematite ore's susceptibility to recrystallization (Rasmussen et al., 2007). Ore bodies developed along fault planes, such as those in the Thabazimbi region, may be particularly prone to recrystallization from shallow crustal fluid flow. Despite the differences between the chronology of ore formation proposed by previous investigators and the He-Ne ages reported in this study, we provide evidence the Donkerpoort Neck hematite ore body has remained within two kilometers of the Earth's surface for at least the last billion years. This result, when combined with the findings presented in the previous chapter, provides strong evidence for the particularly slow erosion rates in the Kaapvaal Craton.

REFERENCES

Basson IJ, and Koegelenberg C. (2017) Structural controls on Fe mineralization at Thabazimbi mine, South Africa. *Ore Geology Reviews*. **80**, 1056-71.

Beukes NJ, and Gutzmer J. (2008) Origin and paleoenvironmental significance of major iron formations at the Archean-Paleoproterozoic boundary. *Reviews in Economic Geology*. **15**, 5-47.

Braun J, Guillocheau F, Robin C, Baby G, and Jelsma H. (2014) Rapid erosion of the Southern African Plateau as it climbs over a mantle superswell. *Journal of Geophysical Research: Solid Earth*. **119**, 6093-6112.

Brown RW, Summerfield MA, Gleadow AJ. (2002) Denudational history along a transect across the Drakensberg Escarpment of southern Africa derived from apatite fission track thermochronology. *Journal of Geophysical Research: Solid Earth*. **107**, 1-18

Catuneanu O. (2004) Basement control on flexural profiles and the distribution of foreland facies: The Dwyka Group of the Karoo Basin, South Africa. *Geology*. **32**, 517-520.

Catuneanu O, Wopfner H, Eriksson PG, Cairncross B, Rubidge BS, Smith RMH, and Hancox PJ. (2005) The Karoo basins of south-central Africa. *Journal of African Earth Sciences*. **43**, 211-253.

Clout JMF, and Simonson BM. (2005) Precambrian iron formations and iron formation hosted iron ore deposits. In: Hedenquis JW, Thompson JFH, Goldfarb RJ, and Richards JP(eds) *Economic geology; one hundredth anniversary volume, 1905–2005*. Society of Economic Geologists. 643–679.

Eglington BM, and Armstrong RA. (2004) The Kaapvaal Craton and adjacent orogens, southern Africa: a geochronological database and overview of the geological development of the craton. *South African Journal of Geology*. **107**, 13-32.

Eriksson PG, Altermann W, and Hartzer FJ. (2006) The Transvaal Supergroup and its precursors. In: Johnson MR, Anhaeusser CR, and Thomas RJ (Eds), The Geology of South Africa, *Geological Society of South Africa and Council for Geoscience*, Johannesburg, 237-260.

De Kock MO, Evans DA, Gutzmer J, Beukes NJ, and Dorland HC. (2008) Origin and timing of banded iron formation-hosted high-grade hard hematite deposits—a paleomagnetic approach. In: Hagemann S, Rosiere C, Gutzmer J, and Beukes NJ (eds) Banded Iron Formation-Related High-Grade Iron Ore. 48-71.

De Kock MO, Ernst R, Söderlund U, Jourdan F, Hofmann A, Le Gall B, Bertrand H, Chisonga BC, Beukes N, Rajesh HM, and Moseki LM. (2014) Dykes of the 1.11 Ga Umkondo LIP, Southern Africa: clues to a complex plumbing system. *Precambrian Research.* **249**, 129-43.

Dirks PH, Kibii JM, Kuhn BF, Steininger C, Churchill SE, Kramers JD, Pickering R, Farber DL, Mériaux AS, Herries AI, King GC. (2010) Geological setting and age of Australopithecus sediba from southern Africa. *Science*. **328**, 205-8.

Farley KA. (2018) Helium diffusion parameters of hematite from a single-diffusion domain crystal. *Earth and Planetary Science Letters*. **231**, 117-129.

Farley KA, and McKeon R. (2015) Radiometric dating and temperature history of banded iron formation–associated hematite, Gogebic iron range, Michigan, USA. *Geology*. **43**, 1083–1086.

Flowers RM, and Schoene B. (2010) (U-Th)/He thermochronometry constraints on unroofing of the eastern Kaapvaal craton and significance for uplift of the southern African Plateau. *Geology*. **38**, 827–830, doi: 10.1130/G30980.1.

Hanson RE, Gose WA, Crowley JL, Ramezani J, Bowring SA, Bullen DS, Hall RP, Pancake JA, and Mukwakwami J. (2004a) Paleoproterozoic intraplate magmatism and basin development on the Kaapvaal Craton: Age, paleomagnetism and geochemistry of~ 1.93 to~ 1.87 Ga post-Waterberg dolerites. *South African Journal of Geology*. **107**, 233-54.

Hanson RE, Crowley JL, Bowring SA, Ramezani J, Gose WA, Dalziel IW, Pancake JA, Seidel EK, Blenkinsop TG, and Mukwakwami J. (2004b) Coeval large-scale magmatism in the Kalahari and Laurentian cratons during Rodinia assembly. *Science*. **304**, 1126-9.

Hanson RE, Rioux M, Gose WA, Blackburn TJ, Bowring SA, Mukwakwami J, and Jones DL. (2011) Paleomagnetic and geochronological evidence for large-scale post–1.88 Ga displacement between the Zimbabwe and Kaapvaal cratons along the Limpopo belt. *Geology*. **39**, 487-90.

Johnson, Jena Elaine (2015) Manganese: Minerals, Microbes, and the Evolution of Oxygenic Photosynthesis.Dissertation (Ph.D.), California Institute of Technology. doi:10.7907/Z9RF5S0X.

Johnson MR, Van Vuuren CJ, Hegenberger WF, Key R, and Show U. (1996) Stratigraphy of the Karoo Supergroup in southern Africa: an overview. *Journal of African Earth Sciences*. **23**, 3-15.

Jourdan F, Féraud G, Bertrand H, Kampunzu AB, Tshoso G, Watkeys MK, and Le Gall B. (2005) Karoo large igneous province: Brevity, origin, and relation to mass extinction questioned by new 40Ar/39Ar age data. *Geology*. **33**, 745-748.

McCarthy TS, Corner B, Lombard H, Beukes NJ, Armstrong RA, and Cawthorn RG. (2018) The pre-Karoo geology of the southern portion of the Kaapvaal Craton, South Africa. *South African Journal of Geology*. **121**, 1-22.

Morris RC, and Kneeshaw M. (2011) Genesis modeling for the Hamersley BIF-hosted iron ores of Western Australia: a critical review. *Australian Journal of Earth Sciences.* **58**, 417-51.

Nelson DR, Trendall AF, and Altermann W. (1999) Chronological correlations between the Pilbara and Kaapvaal cratons. *Precambrian Research*. **97**, 165–189.

Netshiozwi ST. (2002) Origin of high-grade hematite ores at Thabazimbi mine, Limpopo Province, South Africa (Doctoral dissertation, University of Johannesburg).

Oliver NH, Cleverley JS, Dipple GM, and Broadbent GC. (2007) Giant BIF-hosted hematite ores: Geochemical and isotopic modelling of meteoric and basinal fluid-rock reactions. In: Andrew et al. (eds) *Digging Deeper*. Proceedings of the Ninth Biennial SGA Meeting, Dublin. 1219-1222.

Partridge TC, and Maud RR. (2000) In: Partridge TC and Maud RR (eds) *The Cenozoic of Southern Africa*. Oxford Univ. Press, New York, 100-125.

Corner B, and Durrheim RJ. (2018) An Integrated Geophysical and Geological Interpretation of the Southern African Lithosphere. In: Siegesmund S, Basei M, Oyhantçabal P, and Oriolo S (eds) *Geology of Southwest Gondwana*. Regional Geology Reviews.19-61.

Rajesh HM, Chisonga BC, Shindo K, Beukes NJ, and Armstrong RA. (2013) Petrographic, geochemical and SHRIMP U–Pb titanite age characterization of the Thabazimbi mafic sills: Extended time frame and a unifying petrogenetic model for the Bushveld Large Igneous Province. *Precambrian Research*. **230**, 79-102.

Rasmussen B, Fletcher IR, Muhling JR, Thorne WS, and Broadbent GC. (2007) Prolonged history of episodic fluid flow in giant hematite ore bodies: Evidence from in situ U–Pb geochronology of hydrothermal xenotime. *Earth and Planetary Science Letters*. **258**, 249–259.

Rasmussen B, Muhling JR, Suvorova A, and Krapež B. (2016) Dust to dust: Evidence for the formation of 'primary' hematite dust in banded iron formations via oxidation of iron silicate nanoparticles. *Precambrian Research*. **284**, 49-63.

Rye R, and Holland HD. (1998) Paleosols and the evolution of atmospheric oxygen: a critical review. *American Journal of Science*. **298**, 621-672.

Smith AJB, and Beukes NJ. (2016) Paleoproterozoic Banded Iron formation-Hosted High Grade Hematite Iron Ore Deposits of Transvaal Supergroup, South Africa. *Episodes*. **39**, 269-284, doi: 10.18814/epiiugs/2016/v39i2/95778.

Stanley JR, and Flowers RM. (2016) Dating kimberlite emplacement with zircon and perovskite (U-Th)/He geochronology. *Geochemistry, Geophysics, Geosystems*. **17**, 4517–4533, doi: 10.1002/2016GC006519.

Stanley JR, Flowers RM, and Bell DR. (2013) Kimberlite (U-Th)/He dating links surface erosion with lithospheric heating, thinning, and metasomatism in the southern African Plateau. *Geology*. **41**, 1243–1246, doi: 10.1130/G34797.1.

Sumner DY, and Neukes NJ. (2006) Sequence stratigraphy development of the Neoarchean Transvaal carbonate platform, Kaapvaal Craton, South Africa. *South African Journal of Geology*. **109**, 11-22.

Tinker J, de Wit M, and Grotzinger J. (2002) Seismic stratigraphic constraints on Neoarchean-Paleoproterozoic evolution of the western margin of the Kaapvaal Craton, South Africa. *South African Journal of Geology*. **105**, 107-134.

Van Niekerk HS, Beukes NJ, Gutzmer J. (1999) Post-Gondwana pedogenic ferromanganese deposits, ancient soil profiles, African land surfaces and palaeoclimatic change on the Highveld of South Africa. *Journal of African Earth Sciences*. **29**, 761-81.

Van Reenen DD, Boshoff R, Smit CA, Perchuk LL, Kramers JD, McCourt S, and Armstrong RA. Geochronological problems related to polymetamorphism in the Limpopo Complex, South Africa. *Gondwana Research*. **14**, 644-62.

Webb AD, Dickens GR, and Oliver NH. (2003) From banded iron-formation to iron ore: geochemical and mineralogical constraints from across the Hamersley Province, Western Australia. *Chemical Geology*. **197**, 215-51.

Walraven F, and Martini J. (1995) Zircon Pb-evaporation age determinations of the oak tree formation, Chuniespoort group, Transvaal sequence: implications for Transvaal-Griqualand west basin correlations. *South African Journal of Geology*. **98**, 58-67.

Wildman M, Brown R, Watkins R, Carter A, Gleadow A, and Summerfield M. (2015) Post break-up tectonic inversion across the southwestern cape of South Africa: New

insights from apatite and zircon fission track thermochronometry. *Tectonophysics.* **654**, 30-55.

Wildman M, Brown R, Beucher R, Persano C, Stuart F, Gallagher K, Schwanethal J, and Carter A. (2016) The chronology and tectonic style of landscape evolution along the elevated Atlantic continental margin of South Africa resolved by joint apatite fission track and (U-Th-Sm)/He thermochronology. *Tectonics*. **35**, 511-45.

Wildman M, Brown R, Persano C, Beucher R, Stuart FM, Mackintosh V, Gallagher K, Schwanethal J, and Carter A. (2017) Contrasting Mesozoic evolution across the boundary between on and off craton regions of the South African plateau inferred from apatite fission track and (U-Th-Sm)/He thermochronology. Journal of Geophysical Research: *Solid Earth*. **122**, 1517-47.

Table 4.1: He, Ne, U and Th concentrations

Aliquot	Degassed mass (mg)	[4He] nmol/g	+/-	[21Ne*] fmol/g	+/-	Nucleogenic $^{21}Ne^*$ (%)	$^{21}Ne^*/^4He$	Ne age (Ma)	+/-	He age (Ma)	+/-
Donkerpoort Neck											
Donkerpoort Neck 1	100.2	3.10	0.08	0.097	0.004	42.49	3.13E-08	1034	68	1017	26
Donkerpoort Neck 2	93.9	3.05	0.09	0.092	0.004	36.34	3.01E-08	980	68	1000	27
Mean		3.08		0.094		39.42	3.07E-08	1007		1009	
2s		0.15		0.004				96		36	
% 2s		4.88		4.23				9.53		3.57	
Donkerpoort West											
Donkerpoort West 1	114.5	1.80	0.05	0.059	0.002	64.42	3.28E-08	128	8	123	3
Donkerpoort West 2	115.8	1.84	0.05	0.052	0.003	38.90	2.85E-08	114	9	125	4
Mean		1.82		0.056		51.66	3.06E-08	121		124	
2s		0.06		0.004				12		5	
% 2s		3.07		7.18				9.90		4.05	

Aliquot	Digested mass (mg)	U (ppm)	+/-	Th (ppm)	+/-	Sm (ppm)	+/-
Donkerpoort Neck							
Donkerpoort Neck A	24.15	0.42	0.01	0.34	0.01	0.40	0.02
Donkerpoort Neck B	24.04	0.45	0.01	0.37	0.01	0.41	0.02
Mean ppm		0.44	0.01	0.36	0.01	0.41	0.01
2s		0.02		0.02		0.00	
% 2s		3.45		4.23		1.23	
Donkerpoort West							
Donkerpoort West A	22.31	2.16	0.03	2.43	0.03	0.42	0.03
Donkerpoort West B	23.14	2.07	0.03	2.36	0.04	0.41	0.02
Mean ppm		2.12	0.03	2.40	0.04	0.42	0.02
2s		0.05		0.04		0.01	
% 2s		2.13		1.46		1.20	

Table 4.2: Donkerpoort Neck diffusion data modeled with single crystal Ea

Donkerpoort Neck	**domains**	**Ea**	**ln(Do/a^2)**						
	8	40.87	15.88						
gas fraction	0.013	0.022	0.077	0.047	0.155	0.147	0.262	0.276	
log(D_o/a^2)	13.296	10.735	8.421	6.249	3.707	3.455	3.352	3.161	
closure temp (° C)	43	74	107	144	198	204	206	211	
step	**temp**	**time**	**Fcum observed**	**Fcum modeled**	**10000/k**	**ln(D/a^2) modeled**	**delta modeled**	**delta observed**	**ln(D/a^2) observed**
1	150	1	6.7E-04	5.0E-04	23.632	-25.842	-3.443	-3.741	-25.247
2	200	1	5.6E-03	5.8E-03	21.135	-20.933	-3.329	-3.296	-20.999
3	250	1	0.018	0.018	19.115	-18.724	-2.357	-2.348	-18.740
4	300	1	0.033	0.036	17.447	-17.604	-1.201	-1.091	-17.825
5	285	1	0.038	0.038	17.916	-19.200	-0.886	-1.160	-18.652
6	270	1	0.039	0.039	18.411	-20.360	-0.814	-1.176	-19.637
7	265	1	0.040	0.039	18.582	-20.773	-0.784	-1.161	-20.019
8	260	1	0.041	0.040	18.756	-21.173	-0.763	-1.277	-20.145
9	300	1	0.046	0.044	17.447	-18.717	-0.645	-0.829	-18.349
10	375	1	0.072	0.076	15.429	-16.161	0.153	0.275	-16.405
11	350	1	0.084	0.081	16.048	-17.956	0.414	-0.109	-16.909
12	400	1	0.109	0.106	14.856	-15.906	0.615	0.615	-15.905
13	450	1	0.131	0.132	13.828	-15.594	1.515	1.600	-15.763
14	425	1	0.134	0.135	14.324	-17.758	2.088	1.950	-17.481
15	400	1	0.136	0.136	14.856	-18.936	2.130	1.947	-18.569
16	375	1	0.136	0.136	15.429	-20.139	2.142	1.863	-19.581
17	355	1	0.136	0.136	15.920	-21.156	2.146	1.781	-20.428
18	400	3	0.139	0.138	14.856	-19.016	2.170	2.074	-18.825
19	450	1	0.144	0.144	13.828	-17.045	2.241	2.242	-17.047
20	500	1	0.165	0.163	12.934	-15.597	2.437	2.395	-15.513
21	550	1	0.209	0.203	12.148	-14.689	2.791	2.733	-14.573
22	530	1	0.217	0.215	12.451	-15.816	3.043	3.193	-16.116
23	510	1	0.221	0.219	12.769	-16.631	3.124	3.284	-16.952
24	490	1	0.222	0.221	13.104	-17.388	3.158	3.343	-17.757
25	470	1	0.223	0.222	13.456	-18.141	3.172	3.298	-18.393
26	500	1	0.225	0.225	12.934	-17.101	3.189	3.362	-17.448
27	550	1	0.236	0.237	12.148	-15.600	3.246	3.314	-15.736
28	600	1	0.277	0.273	11.453	-14.405	3.364	3.287	-14.252
29	650	1	0.345	0.348	10.832	-13.409	3.504	3.551	-13.503
30	630	1	0.363	0.379	11.072	-14.057	3.581	3.858	-14.611
31	610	1	0.372	0.395	11.323	-14.626	3.608	3.974	-15.358
32	590	1	0.374	0.404	11.585	-15.191	3.620	4.275	-16.499
33	560	0.5	0.375	0.406	12.003	-16.059	3.625	4.623	-18.053
34	600	1	0.378	0.416	11.453	-14.939	3.631	4.279	-16.235
35	700	1	0.486	0.509	10.276	-12.603	3.673	3.647	-12.549
36	750	1	0.667	0.655	9.774	-11.711	3.744	3.644	-11.510
37	730	1	0.723	0.716	9.969	-12.203	3.789	3.816	-12.256
38	710	1	0.748	0.748	10.171	-12.661	3.810	3.924	-12.890
39	1300	1	1.000	1.000	6.357	-7.013	4.909	5.381	-7.957

Table 4.3: Donkerpoort Neck step age plot data

^{3}He Fcum	R_{step}/R_{bulk}	± R_{step}/R_{bulk}	Step Age	± Step Age
0.0068*	0.2420	0.0087	244	8.8
0.0179*	0.3358	0.0121	339	12.2
0.0315*	0.7346	0.0264	741	26.7
0.0384*	0.7963	0.0287	804	28.9
0.0488*	0.8857	0.0319	894	32.2
0.0590*	1.0053	0.0362	1014	36.5
0.0702*	1.1173	0.0402	1127	40.6
0.0837	0.9919	0.0357	1001	36.0
0.0964	1.0168	0.0366	1026	36.9
0.1100	1.0718	0.0386	1081	38.9
0.1255	1.1467	0.0413	1157	41.7
0.1559	1.1759	0.0423	1187	42.7
0.2091	1.1394	0.0410	1150	41.4
0.3232	1.0933	0.0394	1103	39.7
0.6240	1.0298	0.0371	1039	37.4
0.8907	0.9260	0.0333	934	33.6
1.0000	1.0185	0.0367	1028	37.0

$R=^4He/^3He$